

Technische Universität München  
Lehrstuhl für Aerodynamik und Strömungsmechanik

# **Alternative Air Brake Concepts for Transport Aircraft Steep Approach**

Ulrich Sebastian Jung

Vollständiger Abdruck der von der Fakultät für Maschinenwesen der Technischen Universität München zur Erlangung des akademischen Grades eines

Doktor-Ingenieurs

genehmigten Dissertation.

Vorsitzender: Univ.-Prof. Dr.-Ing. Manfred Hajek  
Prüfer der Dissertation: 1. apl. Prof. Dr.-Ing. Christian Breitsamter  
2. Univ.-Prof. Dr.-Ing. Mirko Hornung

Die Dissertation wurde am 20.10.2011 bei der Technischen Universität München eingereicht und durch die Fakultät für Maschinenwesen am 06.02.2012 angenommen.



# VORWORT

Die vorliegende Arbeit entstand während meiner Tätigkeit als wissenschaftlicher Mitarbeiter am Lehrstuhl für Aerodynamik und Strömungsmechanik der Technischen Universität München. All denen, die mich auf diesem Weg bis hierher unterstützt haben, möchte ich herzlich danken.

Besonders möchte ich mich bei meinem Doktorvater Herrn apl. Prof. Dr.-Ing. Christian Breitsamter für die ausgezeichnete Betreuung und die vielen wertvollen Ratschläge bedanken.

Ebenfalls bedanke ich mich bei Herrn Univ.-Prof. Dr.-Ing. Mirko Hornung, der die Aufgabe des Zweitprüfers übernommen hat, und Herrn Univ.-Prof. Dr.-Ing. Manfred Hajek für die Übernahme des Prüfungsvorsitzes.

Ein großer Dank geht an meine Kollegen, die meine Zeit am Lehrstuhl durch die großartige Atmosphäre sehr angenehm machten und mich mittels ausgiebiger Diskussionen fachlich voranbrachten.

Der Lehrstuhlwerkstatt gebührt ebenfalls Dank, insbesondere für die Hilfe bei den anspruchsvollen CNC-Fertigungsarbeiten und für die Wartung der Messtechnik.

Des Weiteren möchte ich mich herzlichst bei meiner Familie für all das bedanken, was sie mir auf den Weg gegeben hat.

Widmen möchte ich diese Arbeit meiner Frau Michaela Jung, die durch Ihre umfangreiche menschliche Unterstützung ganz maßgeblich zum Gelingen der Arbeit beigetragen hat.

Eching, März 2012

Ulrich Sebastian Jung



# ABSTRACT

With the exponential increase of commercial air traffic, methods for reducing perceived noise in airport vicinities are urgently required. Steep approaches have been identified as one feasible means of achieving the desired magnitude of noise reduction. In addition to this, steep approaches can help to increase airport capacities and enable operation into airports surrounded by large buildings or mountains. This thesis makes its contribution to the field by evaluating the applicability of four novel aerodynamic devices for use in steep approaches of commercial transport aircraft. It begins by unpacking the legislative and political conditions surrounding air traffic noise reduction and steep approach, surveying the leading edge research and outlining the thesis's specific contribution to the field. The necessary theoretical background knowledge is then gathered. Subsequently, experimental and numerical methods are introduced. The investigations conducted on the basis of these methods and the findings drawn from them are then reported on. The devices under investigation can all be seamlessly integrated into the wing of a commercial transport aircraft through a straight-forward modification of their existing aileron system and spoiler system, respectively. In order to evaluate the relevant steep approach parameters, they are compared with a Baseline configuration - the Baseline being defined as the approach configuration without deployed air brakes. Analogously, conventional spoilers are investigated to provide an additional basis for comparison. The steep approach effectiveness of the devices is evaluated through force measurements. To visualize the flow topology and thereby understand the flow physics underlying the achieved steep approach parameters, flow visualization methods and computational fluid dynamic simulations are utilized. The flow visualization methods utilized comprise tuft flow visualization, stereoscopic particle image velocimetry, and hot wire anemometry. All results gathered are evaluated in a synthesis section per results chapter. Taking these syntheses together, it is concluded that none of the investigated aerodynamic devices alone is best suited for conducting steep approaches. Instead, suitability depends on the desired additional descent angle and the acceptable penalty in approach velocity. For low values of both parameters, one of either novel aileron device is feasible. While for the higher values, one of the two spoiler devices under investigation, as well as the conventional spoiler are superior. To address the feasibility of using these devices with regard to possible horizontal tail plane buffet issues, a thorough investigation of the wing wake is also reported on. The main outcome from this wake investigation is that none of the investigated spoiler-devices pose a higher risk for horizontal tail plain buffet than the standard equivalents tested.



# ÜBERSICHT

Da der kommerzielle Luftverkehr exponentiell wächst, sind Maßnahmen zur Reduktion des dadurch verursachten Lärms in der Umgebung von Flughäfen dringend erforderlich. Als eine Maßnahme, die die erforderliche Größenordnung an Lärmreduktion bewirken kann, wird das Steilanflugverfahren betrachtet. Außerdem kann mit dem Steilanflugverfahren zusätzlich die Flughafenkapazität vergrößert werden und es ermöglicht Operationen an Flughäfen, die von hohen Gebäuden und Bergen umgeben sind. Zu Beginn dieser Arbeit werden die Gründe für Steilanflüge weiter herausgearbeitet und der Stand der Technik zusammengefasst. Anschließend wird der Beitrag dieser Arbeit zum Forschungsgebiet erläutert und die zugehörigen theoretischen Hintergrundinformationen erarbeitet. Die in der Arbeit angewandten experimentellen und numerischen Methoden werden erläutert. Auf Basis dieser Methoden wurden sowohl experimentelle, als auch numerische Untersuchungen durchgeführt, um die Eignung von neuartigen aerodynamischen Steuerflächen zur Durchführung von Steilanflügen durch Verkehrsflugzeuge zu bewerten. Alle untersuchten neuartigen Steuerflächen haben gemein, dass sie direkt in den Flügel einer bestehenden Verkehrsflugzeugkonfiguration integriert werden können. Dabei ersetzen sie vorhandene Spoiler und das Querruder. Um die Effektivität zur Durchführung von Steilanflügen zu bewerten, dienen Kraftmessungen im Windkanal. Auch die unveränderte Verkehrsflugzeugkonfiguration wurde vermessen und dient als Grundlage dieser Bewertung. Zusätzlich wurden konventionelle Spoiler als Vergleichsbasis untersucht. Um die durch die verschiedenen Steuerflächen verursachte Strömungstopologie zu untersuchen, wurde die Strömung mittels Fadensonden, stereoskopischer Particle Image Velocimetry und Hitzdrahtanemometrie vermessen. Außerdem dienten dazu die Untersuchungen mittels numerischer Strömungssimulation. Um beim Einsatz der untersuchten Steuerflächen auch das Risiko des Auftretens von Höhenleitwerks-Buffering zu bewerten, wurde der Nachlauf im Windkanal untersucht. Alle ermittelten Ergebnisse sind pro Kapitel jeweils in einer Synthese zusammengefasst. In Summe kann gefolgert werden, dass keine der untersuchten Steuerflächentypen in jedem Fall am besten abschneidet. Viel mehr kommt es darauf an, welche Größenordnung die wichtigsten Steilanflugparameter – Vergrößerung des Anflugwinkels und der Anfluggeschwindigkeit – erreichen sollen. Für jeweils niedrige Werte der beiden Parameter eignen sich die neuartigen Querruder am besten, bei höheren Werten schneiden die konventionellen Spoiler sowie einer der beiden unkonventionellen Spoilertypen am besten ab. Des Weiteren zeigen die Nachlaufuntersuchungen, dass keines der untersuchten Spoilersysteme ein erhöhtes Risiko für Höhenleitwerks-Buffering birgt.



# CONTENTS

<b>LIST OF FIGURES .....</b>	<b>VII</b>
<b>LIST OF TABLES .....</b>	<b>XV</b>
<b>NOMENCLATURE .....</b>	<b>XVII</b>
<b>1. INTRODUCTION .....</b>	<b>1</b>
1.1 Motivation and Purpose of the Study.....	1
1.2 Current Research into the Field .....	2
1.3 Contribution of This Work and Thesis Overview.....	5
<b>2. THEORETICAL BACKGROUND .....</b>	<b>7</b>
2.1 Steep Approach Operations .....	7
2.1.1 Approach Operations in General .....	8
2.1.2 Necessity to Conduct Steep Approaches .....	9
2.1.3 Requirements for Steep Approach Operations .....	10
2.1.4 Measures to Achieve Steep Approach Capabilities.....	11
2.1.5 Steep Approach Capable Aircraft.....	12
2.2 Transport Aircraft Wing.....	12
2.2.1 Cruise Flight Wing.....	12
2.2.2 High-Lift System of Contemporary Commercial Transport Aircraft.....	13
2.2.3 Aileron .....	14
2.2.4 Air Brake System.....	14
2.2.5 Multiple Device Allocation to Function .....	19
2.3 Aerodynamics .....	20
2.3.1 Similarity and Dimensionless Parameters .....	20
2.3.2 Derivation of Relevant Fluid Mechanic Quantities .....	21
2.3.3 Airfoil Aerodynamics .....	23
2.3.4 Drag Decomposition .....	24

2.3.5	High-Lift Aerodynamics .....	26
2.3.6	Stall Condition .....	30
2.3.7	Air Brake Aerodynamics .....	31
2.4	Flight Mechanics .....	32
2.4.1	Engine Thrust Ratings .....	32
2.4.2	Final Approach Conditions .....	33
2.4.3	Longitudinal Static Stability .....	35
2.5	Unsteady Aerodynamics .....	35
2.5.1	Strouhal Number .....	35
2.5.2	Buffet .....	36
<b>3.</b>	<b>EXPERIMENTAL METHODS .....</b>	<b>37</b>
3.1	Aerodynamic Simulation in Wind Tunnel .....	37
3.1.1	Low-Speed Wind Tunnel Simulation of High Reynolds-Number Problems .....	37
3.1.2	Feasibility of Half-Model Measurements .....	39
3.2	Measuring Methods .....	39
3.2.1	Balance Measurements .....	40
3.2.2	Tuft Flow Visualization .....	41
3.2.3	Stereo Particle Image Velocimetry .....	42
3.2.4	Constant Temperature Hot Wire Anemometry .....	44
3.3	Wind Tunnel Test Facility .....	49
3.4	Wind Tunnel Model .....	50
3.4.1	Model Nacelle .....	52
3.4.2	Laminar-Turbulent Tripping .....	53
3.5	Air Brake Model Parts .....	54
3.5.1	Conventional Spoiler .....	54
3.5.2	Adverse Spoiler .....	55
3.5.3	Advanced Adverse Spoiler .....	56
3.5.4	Deceleron .....	56
3.5.5	Split Aileron .....	57
3.6	Parameter Set-Up for Experiments .....	58
3.6.1	Balance Measurement Campaign .....	58
3.6.2	Flow Field Measurement Campaign .....	60

---

3.7	Post-Processing of Test Data .....	61
3.7.1	Aerodynamic Coefficients of Longitudinal Motion .....	61
3.7.2	Aerodynamic Coefficients of Lateral Motion.....	62
3.7.3	Parametric Decomposition of Aerodynamic Coefficients .....	63
3.7.4	Regression Analysis.....	63
3.7.5	Power Spectral Density Analysis.....	63
<b>4.</b>	<b>NUMERICAL METHODS.....</b>	<b>65</b>
4.1	Problem Definition.....	65
4.2	Choice of Feasible Computational Method .....	65
4.3	Computational Flow Solver CFX .....	72
4.4	Geometry Definition .....	72
4.5	Mesh Generation .....	73
4.5.1	Near Wall Mesh.....	75
4.5.2	Resolution of the Near Wake.....	76
4.5.3	SAS Grid.....	76
4.6	Computational Setup.....	77
4.6.1	Parameters for Transient Simulations.....	78
4.6.2	Boundary Conditions .....	78
4.7	Postprocessing.....	80
4.8	Validation of the Numerical Method .....	81
4.8.1	Validation Case RA16SC1 .....	82
4.8.2	Validation of RANS method.....	82
4.8.3	Validation of URANS method.....	85
4.8.4	Validation of SAS method.....	85
4.8.5	Grid Convergence Study.....	87
<b>5.</b>	<b>EVALUATION OF DEVICE PERFORMANCE.....</b>	<b>91</b>
5.1	Statistical Evaluation of the Force Measurement Uncertainty .....	91
5.1.1	Bias .....	91
5.1.2	Precision.....	92
5.1.3	Bias between the Campaigns .....	93
5.1.4	Accuracy Checks During Measurement Campaigns .....	93

5.1.5	Hysteresis Loop in Polars .....	93
5.1.6	Reynolds Number Effects .....	94
5.2	Evaluation of Devices Regarding Steep Approach Performance .....	95
5.2.1	Aerodynamic Force and Moment Coefficient Polars .....	96
5.2.2	Descent Velocity .....	103
5.2.3	Descent Angle .....	110
5.2.4	Nonlinear Interference Effects for Combined Usage of Spoiler Devices and Aileron Devices .....	115
5.3	Evaluation of Aileron Devices Regarding Lateral Control .....	116
5.3.1	Roll Control Effectiveness .....	117
5.3.2	Yaw Control Effectiveness .....	120
5.4	Effect of Devices on the Static Longitudinal Stability .....	121
5.5	Other Evaluation Fields .....	122
5.6	Synthesis .....	124
<b>6.</b>	<b>FLOW TOPOLOGY ANALYSIS .....</b>	<b>127</b>
6.1	Flow Topology Analysis by CFD Simulations .....	127
6.1.1	Flow Topology of Baseline Case .....	128
6.1.2	Flow Topology of High Lift Airfoil with Spoiler .....	133
6.1.3	Flow Topology of High Lift Airfoil with Adverse Spoiler .....	137
6.1.4	Flow Topology of High Lift Airfoil with Advanced Adverse Spoiler .....	140
6.1.5	Analysis of the Unsteadiness in the 2D URANS Simulations .....	144
6.1.6	Synthesis of URANS-Simulations .....	145
6.1.7	Flow Topology Analysis Based on SAS Simulation Results .....	147
6.2	Flow Topology Identification by Tuft Flow Analysis .....	155
6.3	Flow Topology Synthesis .....	160
<b>7.</b>	<b>INVESTIGATION OF THE NEAR WAKE .....</b>	<b>165</b>
7.1	Mean Flow Topology .....	166
7.2	Vertical Turbulence Distribution .....	171
7.3	Spectral Analysis of Vertical Turbulence .....	176

---

7.4 Synthesis .....177

**8. CONCLUSION .....179**

**REFERENCES.....183**



# LIST OF FIGURES

Figure 1-1:	Noise reduction objectives. ....	1
Figure 2-1:	Approach and Landing Phases. ....	8
Figure 2-2:	Relationship between altitude and slant distance for standard and steep approach. ...	9
Figure 2-3:	Landing distance available depending on approach path inclination. ....	10
Figure 2-4:	Approach categories with aircraft examples. ....	12
Figure 2-5:	Sectional view of an airfoil with deflected high lift devices. a) Leading Edge Slat and Fowler Flap. b) Leading Edge Slat and Aileron. ....	14
Figure 2-6:	Major air-brake types in current usage. a) Wing spoiler of a CTA; b) Posterior/tail-mounted split air brake; c) Fuselage mounted dorsal air brake on fighter aircraft; d) Double-decker Schempp-Hirth air-brake; e) Deceleron; f) Turning flap. ....	15
Figure 2-7:	Anatomical model (trout) underpinning naming of air brakes. ....	15
Figure 2-8:	Sectional view of investigated spoiler types. a) Conventional Spoiler, b) Adverse Spoiler, c) Advanced Adverse Spoiler. ....	17
Figure 2-9:	Sectional view of multifunctional aileron devices. a) Deceleron, b) Split Aileron. ....	19
Figure 2-10:	Example distribution of functions of a CTA's trailing edge devices. ....	19
Figure 2-11:	Example of typical pressure distribution of a transonic cruise airfoil [27]. ....	23
Figure 2-12:	Schematic lift over drag polar of baseline high-lift configuration and CS-configuration. ....	25
Figure 2-13:	Schematic lift over drag polar of baseline high-lift configuration and improved air-brake configuration. ....	26
Figure 2-14:	Drag composition dependent on flight velocity. ....	26
Figure 2-15:	Schematic pressure distribution for a generic high-lift configuration. ....	27
Figure 2-16:	Effect of Leading Edge Slat and Fowler Flap on lift curve. ....	28
Figure 2-17:	Illustration of high-lift flow phenomena with Schlieren flow visualization at approach angle of attack [110]. ....	29
Figure 2-18:	Areas of flow separations for CTA and interacting vortex systems. ....	31
Figure 2-19:	Schematic flow topology visualization by streamlines of a high-lift profile with deployed spoiler. ....	32
Figure 2-20:	Static equilibrium during a steady approach excluding the approach idle thrust force. ....	33
Figure 2-21:	Dependency of $Sr$ on $Re$ in wake of circular cylinder [86]. ....	36
Figure 3-1:	Drag polars for different $Re$ numbers of CTA EHLP configuration stage 3 [149]. ...	38
Figure 3-2:	Tuft stick used to investigate the flow. ....	42
Figure 3-3:	Stereo-PIV measurement in action. ....	44

Figure 3-4:	Block diagram of the HWA measurement chain [28].	45
Figure 3-5:	Sketch of the two-wire probe used in this investigation.	46
Figure 3-6:	Picture of the HWA probe and support used in the calibration process.	47
Figure 3-7:	Picture of HWA traverse support for the measurements.	48
Figure 3-8:	Wind Tunnel A. a) External view, b) Aerial drawing of the facility [176].	50
Figure 3-9:	Wind tunnel model in WTA.	51
Figure 3-10:	Sectional cut sketch of the through flow nacelle principle.	53
Figure 3-11:	CAD drawing of new shroud elements with spoiler cavity.	54
Figure 3-12:	Top view of outer wing with new shroud and conventional spoiler part.	55
Figure 3-13:	3D CAD view of Adverse Spoiler part.	55
Figure 3-14:	Installed novel spoiler models. a) Adverse Spoiler, b) Advanced Adverse Spoiler.	56
Figure 3-15:	Installed novel aileron parts. a) Deceleron, b) Split Aileron.	57
Figure 3-16:	Investigated deflection values. a) Aileron and Split Aileron, b) Aileron and Deceleron.	60
Figure 3-17:	Coordinate systems.	62
Figure 4-1:	Simulation quality over computational effort for different modeling strategies; those used in this work are in bold type and encircled in red: 2G URANS, URANS, and RANS.	66
Figure 4-2:	Reynolds-decomposition of flow quantities.	69
Figure 4-3:	Split of regions by SAS method, expected LES-regions encircled in red.	70
Figure 4-4:	Airfoil geometry generation for CFD simulations.	73
Figure 4-5:	RA16SC1 mesh with baseline blocking structure. a) Outer part; b) Inner part; c) Detail view of slat; d) Detail view of flap.	74
Figure 4-6:	Details of the 2.5D surface mesh of the RA16SC1-case. a) Slat cove region; b) Flap gap region.	77
Figure 4-7:	Boundary conditions illustration for 2.5D-SAS simulations; farfield is downscaled.	79
Figure 4-8:	Boundary conditions illustration for 2D RANS/URANS simulations; farfield is downscaled.	80
Figure 4-9:	Pressure coefficient on the surfaces of the RA16SC1 airfoil. Experimental results of DLR; own RANS simulation results for $\alpha_{num} = 10^\circ$ and $\alpha_{num} = 11^\circ$ , $U_\infty = 54\text{m/s}$ , $Re_\infty = 1.8 \cdot 10^6$ .	83
Figure 4-10:	Velocity distribution around RA16SC1 airfoil, $U_\infty = 54\text{m/s}$ , $Re_\infty = 1.8 \cdot 10^6$ . a) PIV measurements by DLR; b) own $\alpha_{num} = 11^\circ$ RANS simulation.	84
Figure 4-11:	Pressure coefficient on the surfaces of the RA16SC1 airfoil. Experimental results of DLR, own RANS and URANS simulation results at $\alpha_{num} = 11^\circ$ , $U_\infty = 54\text{m/s}$ , $Re_\infty = 1.8 \cdot 10^6$ .	85
Figure 4-12:	Isosurfaces of the Q-criterion for the RA16SC1 simulation, slat area, $U_\infty = 54\text{m/s}$ , $Re_\infty = 1.8 \cdot 10^6$ . a) SAS method, $Q = 3.3 \cdot 10^6 \text{ s}^{-2}$ ; b) Zonal LES by Deck [52].	86

Figure 4-13:	Isosurfaces of the Q-criterion for the RA16SC1 simulation, flap area, $U_\infty = 54\text{m/s}$ , $Re_\infty = 1.8 \cdot 10^6$ . a) SAS method $Q = 3.3 \cdot 10^6 \text{ s}^{-2}$ ; b) Zonal LES by Deck [52].	86
Figure 4-14:	Absolute mean velocity distribution $\bar{U}/U_\infty$ in symmetry plane, $U_\infty = 50 \text{ m/s}$ , $Re_\infty = 1 \cdot 10^6$ .	88
Figure 4-15:	Grid convergence study for lift, drag, and pitching moment coefficients.	89
Figure 5-1:	Time series of lift coefficients for $n = 100$ repeated measurements with constant configuration baseline at $\alpha = 5^\circ$ and Conventional Spoiler with $\delta_S = 30^\circ$ at $\alpha = 20^\circ$ .	92
Figure 5-2:	$C_L$ - $\alpha$ -polar for forward and backward $\alpha$ -sweep.	94
Figure 5-3:	Lift over drag polar for Baseline, $Re_\infty \approx 5 \cdot 10^5$ , $Re_\infty \approx 8 \cdot 10^5$ and $Re_\infty \approx 1 \cdot 10^6$ .	95
Figure 5-4:	Polars for BL and CS; a) $C_L$ over $C_D$ , b) $C_M$ over $C_L$ .	96
Figure 5-5:	Polars for BL and AS; a) $C_L$ over $C_D$ , b) $C_M$ over $C_L$ .	97
Figure 5-6:	Polars for BL and AAS; a) $C_L$ over $C_D$ , b) $C_M$ over $C_L$ .	98
Figure 5-7:	Polars for BL, CS, AS, and AAS; a) $C_L$ over $C_D$ , b) $C_M$ over $C_L$ .	98
Figure 5-8:	Polars for DC and SA with zero mean deflection angle $\delta_A = 0^\circ$ and fixed absolute differential deflection angle of $\delta_A =  90^\circ $ ; a) $C_L$ over $C_D$ , b) $C_M$ over $C_L$ .	99
Figure 5-9:	Polars for DC with zero mean deflection angle $\delta_A = 0^\circ$ and differential deflection angles of $\delta_A = 20^\circ$ , $\delta_A = 60^\circ$ , and $\delta_A = 90^\circ$ ; a) $C_L$ over $C_D$ , b) $C_M$ over $C_L$ .	100
Figure 5-10:	Polars for SA with zero mean deflection angle $\delta_A = 0^\circ$ and differential deflection angles of $\delta_A = 20^\circ$ , $\delta_A = 60^\circ$ , and $\delta_A = 90^\circ$ ; a) $C_L$ over $C_D$ , b) $C_M$ over $C_L$ .	100
Figure 5-11:	Polars of DC with $\delta_A = +60^\circ$ for different mean deflection angles; $\delta_A = -30^\circ$ , $\delta_A = 0^\circ$ , $\delta_A = +30^\circ$ ; a) $C_L$ over $C_D$ , b) $C_M$ over $C_L$ .	101
Figure 5-12:	Polars of SA $\delta_A = -60^\circ$ , $+60^\circ$ for different mean deflection angles; $\delta_A = -30^\circ$ , $\delta_A = +0^\circ$ , $\delta_A = +30^\circ$ ; a) $\delta_A = -60^\circ$ $C_L$ over $C_D$ , b) $\delta_A = -60^\circ$ $C_M$ over $C_L$ , c) $\delta_A = +60^\circ$ $C_L$ over $C_D$ , d) $\delta_A = +60^\circ$ $C_M$ over $C_L$ .	102
Figure 5-13:	$C_L$ over $C_D$ for the devices CS, AS, AAS, DC, SA; $\delta_S = 30^\circ$ , $\delta_A = -90^\circ$ , $\delta_A = +90^\circ$ . An exemplarily value of $\Delta C_{L,max}$ is included in the plot for the AS case.	103
Figure 5-14:	Relative descent velocity $V_S/V_{S,ref} - 1$ over relative approach velocity $V_{app}/V_{app,ref} - 1$ for BL and CS with various $\delta_S$ for the range of minimum feasible approach velocities.	104
Figure 5-15:	Relative descent velocity $V_S/V_{S,ref} - 1$ over relative approach velocity $V_{app}/V_{app,ref} - 1$ for BL and AS with various $\delta_S$ for the range of minimum feasible approach velocities.	105
Figure 5-16:	Relative descent velocity $V_S/V_{S,ref} - 1$ over relative approach velocity $V_{app}/V_{app,ref} - 1$ for BL and AAS with various $\delta_S$ for the range of minimum feasible approach velocities.	105

- Figure 5-17: Relative descent velocity  $V_S/V_{S,ref} - 1$  over relative approach velocity  $V_{app}/V_{app,ref} - 1$  for BL and DC with various differential deflection angles  $\delta_A$  for the range of minimum feasible approach velocities. .... 106
- Figure 5-18: Relative descent velocity  $V_S/V_{S,ref} - 1$  over relative approach velocity  $V_{app}/V_{app,ref} - 1$  for BL and SA with various differential deflection angles  $\delta_A$  for the range of minimum feasible approach velocities. .... 106
- Figure 5-19: Relative descent velocity  $V_S/V_{S,ref} - 1$  over relative approach velocity  $V_{app}/V_{app,ref} - 1$  of BL and DC with  $\delta_A = 60^\circ$ , mean deflection angles  $\delta_A = -30^\circ$ ,  $\delta_A = -15^\circ$ ,  $\delta_A = 0^\circ$ ,  $\delta_A = 15^\circ$ ,  $\delta_A = 30^\circ$  for the range of minimum feasible approach velocities. .... 107
- Figure 5-20: Relative descent velocity  $V_S/V_{S,ref} - 1$  over relative approach velocity  $V_{app}/V_{app,ref} - 1$  of BL and SA with  $\delta_A = 60^\circ$  and  $\delta_A = -60^\circ$ , mean deflection angles  $\delta_A = -30^\circ$ ,  $\delta_A = 0^\circ$ ,  $\delta_A = 30^\circ$  for the range of minimum feasible approach velocities. .... 108
- Figure 5-21: Relative descent velocity  $V_S/V_{S,ref} - 1$  over relative approach velocity  $V_{app}/V_{app,ref} - 1$  for the range of minimum feasible approach velocities, comparison of all investigated air-brake types with  $|\delta_A| = 90^\circ$  for the aileron devices and  $\delta_S = 30^\circ$  for the spoiler devices. Data points for  $V_{app} \approx V_{app,min}$  are highlighted by ellipses. .... 108
- Figure 5-22: Relative descent velocity  $V_S/V_{S,ref} - 1$  over relative approach velocity  $V_{app}/V_{app,ref} - 1$  for the range of minimum feasible approach velocities, example for a flight envelope and reasonable configurations extracted from the graph. .... 109
- Figure 5-23: Relative descent angle  $\gamma/\gamma_{ref} - 1$  over relative approach velocity  $V_{app}/V_{app,ref} - 1$  for BL and CS with various  $\delta_S$  for the range of minimum feasible approach velocities. .... 110
- Figure 5-24: Relative descent angle  $\gamma/\gamma_{ref} - 1$  over relative approach velocity  $V_{app}/V_{app,ref} - 1$  for BL and AS with various  $\delta_S$  for the range of minimum feasible approach velocities. .... 111
- Figure 5-25: Relative descent angle  $\gamma/\gamma_{ref} - 1$  over relative approach velocity  $V_{app}/V_{app,ref} - 1$  for BL and AAS with various  $\delta_S$  for the range of minimum feasible approach velocities. .... 111
- Figure 5-26: Relative descent angle  $\gamma/\gamma_{ref} - 1$  over relative approach velocity  $V_{app}/V_{app,ref} - 1$  for BL and DC with various  $\delta_A$  for the range of minimum feasible approach velocities. .... 112
- Figure 5-27: Relative descent angle  $\gamma/\gamma_{ref} - 1$  over relative approach velocity  $V_{app}/V_{app,ref} - 1$  for BL and SA with various  $\delta_A$  for the range of minimum feasible approach velocities. .... 112
- Figure 5-28: Relative descent angle  $\gamma/\gamma_{ref} - 1$  over relative approach velocity  $V_{app}/V_{app,ref} - 1$  for BL and DC with  $\delta_A = 60^\circ$  and various mean deflection angles of  $\delta_A = -30^\circ$ ,  $\delta_A = -15^\circ$ ,  $\delta_A = 0^\circ$ ,  $\delta_A = 15^\circ$ ,  $\delta_A = 30^\circ$  for the range of minimum feasible approach velocities. .... 113

Figure 5-29:	Relative descent angle $\gamma/\gamma_{ref} - 1$ over relative approach velocity $V_{app}/V_{app,ref} - 1$ for BL and SA with $\delta_A = -60^\circ$ and $\delta_A = +60^\circ$ ; various mean deflection angles of $\delta_A = -30^\circ$ , $\delta_A = 0^\circ$ , $\delta_A = 30^\circ$ for the range of minimum feasible approach velocities. ....	113
Figure 5-30:	Relative descent angle $\gamma/\gamma_{ref} - 1$ over relative approach velocity $V_{app}/V_{app,ref} - 1$ for the range of minimum feasible approach velocities: Comparison of all investigated air-brake types at $ \delta_A  = 90^\circ$ and $\delta_S = 30^\circ$ . ....	114
Figure 5-31:	a) Relative descent angles $\gamma/\gamma_{ref} - 1$ of the investigated air-brake configurations over $ \delta_A $ , $\delta_S$ at $V_{app,min}$ . b) Relative approach velocity $V_{app,min}/V_{app,min,ref} - 1$ of the investigated air-brake configurations over $ \delta_A $ , $\delta_S$ . ....	115
Figure 5-32:	Achievable descent angle $\gamma/\gamma_{ref} - 1$ over approach velocity $V_{app}/V_{app,ref} - 1$ . Comparison of discrete deployment of DC and AS with combined deployment and linear superposition. ....	116
Figure 5-33:	Angle of attack $\alpha$ over control surface deflection angle $\delta_A$ , $\delta_S$ for a constant lift coefficient $C_L = 1.5$ . a) Configurations A and CS. b) Configurations A, DC, and SA. ....	117
Figure 5-34:	Relations of $C_l$ over $\delta_A$ , $\delta_S$ . Exemplarily plotted for some deflection configuration of the investigated devices at fixed $C_L = 1.5$ . a) Configurations A and CS. b) Configurations SA. c) Configurations DC. ....	118
Figure 5-35:	a) Relations of $ C_{l\delta_A,S} $ over $\delta_A$ . Plotted for all investigated aileron devices and CS at fixed $C_L = 1.5$ . b) Relations of $ C_{l\delta_A,S} $ over $C_L$ . Plotted for CA, DC, SA configurations at $C_L = 1$ , $C_L = 1.25$ , and $C_L = 1.5$ . ....	120
Figure 5-36:	Relations of $C_n$ over $\delta_A$ , exemplarily plotted for some deflection configurations of the investigated devices at fixed $C_L = 1.5$ . a) Configurations SA. b) Configurations DC. ....	121
Figure 5-37:	$C_M$ over $C_L$ for the devices CS, AS, AAS, DC, SA; $\delta_S = 30^\circ$ , $\delta_A = -90^\circ$ , $\delta_A = +90^\circ$ . ....	122
Figure 5-38:	Relative descent angles $\gamma/\gamma_{ref} - 1$ over relative $V_{app,min}/V_{app,min,ref} - 1$ for all investigated air-brake configurations with Pareto frontier. ....	125
Figure 6-1:	Sketch of periodic vortex shedding areas and the associated characteristic length scales for the CS-case. ....	128
Figure 6-2:	Average surface pressure coefficient distributions. URANS result of BL-case at $\alpha = 0^\circ$ , $\alpha = 10^\circ$ , and $\alpha = 15^\circ$ , $U_\infty = 50$ m/s, $Re_\infty = 1 \cdot 10^6$ . ....	129
Figure 6-3:	Distribution of mean total velocity in symmetry plane. URANS result of BL-case at $\alpha = 10^\circ$ , $U_\infty = 50$ m/s, $Re_\infty = 1 \cdot 10^6$ . ....	130
Figure 6-4:	Areas of reverse velocity in symmetry plane. Averaged URANS result of BL-case at $\alpha = 10^\circ$ , $U_\infty = 50$ m/s, $Re_\infty = 1 \cdot 10^6$ . ....	131

Figure 6-5:	Distribution of mean total pressure loss coefficient $K_L$ in symmetry plane. URANS result of BL-case at $\alpha = 10^\circ$ , $U_\infty = 50$ m/s, $Re_\infty = 1 \cdot 10^6$ . .....	131
Figure 6-6:	Distribution of total velocity in symmetry plane. URANS result of BL-case at $\alpha = 10^\circ$ , $U_\infty = 50$ m/s, $Re_\infty = 1 \cdot 10^6$ . a) $t_1 = 134,7$ ms; b) $t_2 = 136$ ms.....	132
Figure 6-7:	Distribution of mean total velocity in symmetry plane. Averaged URANS result of CS-case with $\delta_S = 30^\circ$ at $\alpha = 10^\circ$ , $U_\infty = 50$ m/s, $Re_\infty = 1 \cdot 10^6$ .....	134
Figure 6-8:	Distribution of mean total pressure loss in symmetry plane. Averaged URANS result of CS-case with $\delta_S = 30^\circ$ at $\alpha = 10^\circ$ , $U_\infty = 50$ m/s, $Re_\infty = 1 \cdot 10^6$ . .....	135
Figure 6-9:	Distribution of total velocity in symmetry plane. URANS results of CS-case with $\delta_S = 30^\circ$ at $\alpha = 10^\circ$ , $U_\infty = 50$ m/s, $Re_\infty = 1 \cdot 10^6$ . a) $t_1 = 130$ ms; b) $t_2 = 132.9$ ms. .	136
Figure 6-10:	Distribution of mean total velocity in symmetry plane. Averaged URANS result of AS-case with $\delta_S = 30^\circ$ at $\alpha = 10^\circ$ , $U_\infty = 50$ m/s, $Re_\infty = 1 \cdot 10^6$ . .....	137
Figure 6-11:	Distribution of mean total velocity in symmetry plane. Averaged URANS result of AS-case with $\delta_S = 30^\circ$ at $\alpha = 20^\circ$ , $U_\infty = 50$ m/s, $Re_\infty = 1 \cdot 10^6$ . .....	138
Figure 6-12:	Distribution of mean total pressure loss in symmetry plane. Averaged URANS result of AS-case with $\delta_S = 30^\circ$ at $\alpha = 10^\circ$ , $U_\infty = 50$ m/s, $Re_\infty = 1 \cdot 10^6$ . .....	139
Figure 6-13:	Distribution of total velocity in symmetry plane. URANS results of AS-case with $\delta_S = 30^\circ$ at $\alpha = 10^\circ$ . a) $t_1 = 224.96$ ms; b) $t_2 = 228.96$ ms, $U_\infty = 50$ m/s, $Re_\infty = 1 \cdot 10^6$ . .....	140
Figure 6-14:	Distribution of mean total velocity in symmetry plane. Averaged URANS result of AAS-case with $\delta_S = 30^\circ$ at $\alpha = 10^\circ$ , $U_\infty = 50$ m/s, $Re_\infty = 1 \cdot 10^6$ . .....	141
Figure 6-15:	Distribution of mean total velocity in symmetry plane. Averaged URANS result of AAS-case with $\delta_S = 30^\circ$ at $\alpha = 20^\circ$ , $U_\infty = 50$ m/s, $Re_\infty = 1 \cdot 10^6$ . .....	141
Figure 6-16:	Distribution of mean total pressure loss in symmetry plane. Averaged URANS result of AAS-case with $\delta_S = 30^\circ$ at $\alpha = 10^\circ$ , $U_\infty = 50$ m/s, $Re_\infty = 1 \cdot 10^6$ . .....	142
Figure 6-17:	Distribution of total velocity in symmetry plane. URANS results of AAS-case with $\delta_S = 30^\circ$ at $\alpha = 10^\circ$ , $U_\infty = 50$ m/s, $Re_\infty = 1 \cdot 10^6$ . a) $t_1 = 151.7$ ms; b) $t_2 = 155.52$ ms. .....	143
Figure 6-18:	Lift coefficient spectra gathered by FFT. URANS results of configurations BL, CS with $\delta_S = 30^\circ$ , AS with $\delta_S = 30^\circ$ , and AAS with $\delta_S = 30^\circ$ , each at $\alpha = 10^\circ$ , $U_\infty = 50$ m/s, $Re_\infty = 1 \cdot 10^6$ . .....	144
Figure 6-19:	Distribution of total velocity in symmetry plane. SAS results of BL-case at $\alpha = 10^\circ$ , $U_\infty = 50$ m/s, $Re_\infty = 1 \cdot 10^6$ . a) $t_1 = 37.5$ ms; b) $t_2 = 43.26$ ms.....	148
Figure 6-20:	Turbulent structures around the BL-airfoil, visualized by ISO surfaces of Q-criterion $Q = 1.2 \cdot 10^7$ s <sup>-2</sup> colored by the ratio of the eddy viscosity to the molecular viscosity, $t = 43.26$ ms, $U_\infty = 50$ m/s, $Re_\infty = 1 \cdot 10^6$ . .....	149

Figure 6-21: Distribution of total velocity in symmetry plane. SAS results of CS-case with $\delta_S = 30^\circ$ at $\alpha = 10^\circ$ , $U_\infty = 50$ m/s, $Re_\infty = 1 \cdot 10^6$ . a) $t_1 = 19.79$ ms; b) $t_2 = 27.35$ ms. .....	150
Figure 6-22: Turbulent structures around the CS-airfoil with $\delta_S = 30^\circ$ at $\alpha = 10^\circ$ , visualized by ISO surfaces of Q-criterion $Q = 1.2 \cdot 10^7$ s <sup>-2</sup> colored by the ratio of the eddy viscosity to the molecular viscosity, $t = 27.35$ ms, $U_\infty = 50$ m/s, $Re_\infty = 1 \cdot 10^6$ .....	151
Figure 6-23: Distribution of total velocity in symmetry plane. SAS results of AS-case with $\delta_S = 30^\circ$ at $\alpha = 10^\circ$ , $U_\infty = 50$ m/s, $Re_\infty = 1 \cdot 10^6$ . a) $t_1 = 24.33$ ms; b) $t_2 = 27$ ms. .	152
Figure 6-24: Turbulent structures around the AS-airfoil with $\delta_S = 30^\circ$ at $\alpha = 10^\circ$ , visualized by ISO surfaces of Q-criterion $Q = 1.2 \cdot 10^7$ s <sup>-2</sup> colored by the ratio of the eddy viscosity to the molecular viscosity, $t = 27$ ms, $U_\infty = 50$ m/s, $Re_\infty = 1 \cdot 10^6$ .....	153
Figure 6-25: Distribution of total velocity in symmetry plane. SAS results of AAS-case with $\delta_S = 30^\circ$ at $\alpha = 10^\circ$ , $U_\infty = 50$ m/s, $Re_\infty = 1 \cdot 10^6$ . a) $t_1 = 43.2$ ms; b) $t_2 = 50.8$ ms.	154
Figure 6-26: Turbulent structures around the AAS-airfoil with $\delta_S = 30^\circ$ at $\alpha = 10^\circ$ , visualized by ISO surfaces of Q-criterion $Q = 1.2 \cdot 10^7$ s <sup>-2</sup> colored by the ratio of the eddy viscosity to the molecular viscosity, $t = 50.8$ ms, $U_\infty = 50$ m/s, $Re_\infty = 1 \cdot 10^6$ .....	155
Figure 6-27: Overall view for cases BL (a) and CS with $\delta_S = 30^\circ$ (b) at $\alpha = 0^\circ$ .....	156
Figure 6-28: Overall view for cases AS with $\delta_S = 30^\circ$ (a) and AAS with $\delta_S = 30^\circ$ (b) at $\alpha = 0^\circ$ . .....	157
Figure 6-29: Overall view for cases BL (a) and CS with $\delta_S = 30^\circ$ (b) at MVAP. ....	158
Figure 6-30: Overall view for cases AS with $\delta_S = 30^\circ$ (a) and AAS with $\delta_S = 30^\circ$ (b) at MVAP. .....	158
Figure 6-31: View for cases BL (a) and CS, $\delta_S = 30^\circ$ (b) in the stall angle range at $\alpha = 22^\circ$ .....	159
Figure 6-32: Overall view for cases AS with $\delta_S = 30^\circ$ (a) and AAS with $\delta_S = 30^\circ$ (b) in the stall angle range at $\alpha = 22^\circ$ . ....	159
Figure 6-33: Flow topology sketch of the approach situation for the Baseline. a) View from below; b) view from above.....	161
Figure 6-34: Flow topology sketch of the approach situation with deployed Conventional Spoiler. a) View from below; b) view from above. ....	162
Figure 6-35: Flow topology sketch of the approach situation with deployed Adverse Spoiler. a) View from below; b) view from above. ....	163
Figure 6-36: Flow topology sketch of the approach situation with deployed Advanced Adverse Spoiler. a) View from below; b) view from above. ....	164
Figure 7-1: Velocity distribution in plane x1 ( $x_1/b = 0.12$ ). a) BL; b) CS with $\delta_S = 30^\circ$ .....	166
Figure 7-2: Velocity distribution in plane x1 ( $x_1/b = 0.12$ ). a) AS with $\delta_S = 30^\circ$ ; b) AAS with $\delta_S = 30^\circ$ .....	167
Figure 7-3: Velocity-distribution in plane x2 ( $x_2/b = 0.92$ ). a) BL; b) CS with $\delta_S = 30^\circ$ .....	169

---

Figure 7-4:	Velocity distribution in plane x2 ( $x_2/b = 0.92$ ). a) AS with $\delta_S = 30^\circ$ ; b) AAS with $\delta_S = 30^\circ$ .....	170
Figure 7-5:	Vertical turbulence intensity distribution in plane x1 ( $x_1/b = 0.12$ ). a) BL; b) CS with $\delta_S = 30^\circ$ .....	172
Figure 7-6:	Vertical turbulence intensity distribution in plane x1 ( $x_1/b = 0.12$ ). a) AS with $\delta_S = 30^\circ$ ; b) AAS with $\delta_S = 30^\circ$ .....	173
Figure 7-7:	Vertical turbulence intensity distribution in plane x2 ( $x_2/b = 0.92$ ). a) BL; b) CS with $\delta_S = 30^\circ$ .....	174
Figure 7-8:	Vertical turbulence intensity distribution in plane x2 ( $x_2/b = 0.92$ ). a) AS with $\delta_S = 30^\circ$ ; b) AAS with $\delta_S = 30^\circ$ .....	175
Figure 7-9:	Spectral power density over reduced frequency distribution for measurement point TIP. a) BL; b) CS with $\delta_S = 30^\circ$ ; c) AS with $\delta_S = 30^\circ$ ; d) AAS with $\delta_S = 30^\circ$ .....	177

# LIST OF TABLES

Table 3-1:	Operating data of the balance [125].	41
Table 3-2:	Parameters of the tuft flow visualization.	42
Table 3-3:	Stereo PIV components.	44
Table 3-4:	Flow parameters for the HWA calibration.	47
Table 3-5:	Hot wire anemometry parameters.	48
Table 3-6:	Operating data of Wind Tunnel A [176].	49
Table 3-7:	Deflection values of the high-lift devices.	51
Table 3-8:	Parameters of the wind tunnel model.	52
Table 3-9:	Parameter overview.	58
Table 3-10:	Polar parameters for balance measurements.	59
Table 3-11:	Values of deflection and gap for spoiler-based devices.	59
Table 3-12:	Ranges of deflection for aileron-based devices.	60
Table 4-1:	Numerical parameters for simulations.	77
Table 4-2:	Numerical parameters for inner loop of transient simulations.	78
Table 4-3:	Boundary condition parameters.	80
Table 4-4:	Mesh parameters for mesh convergence study.	87
Table 4-5:	Mesh parameters for mesh convergence study.	88
Table 5-1:	Linear interval identification, coefficients of linear regression and quality of linear regression; $C_L = 1.5$ for all configurations.	119
Table 6-1:	Aerodynamic force coefficient trends relative to BL.	146
Table 6-2:	Maximum vertical extent of wake ( $K_L > 0.02$ ) and separation positions on main wing and flap ( $\bar{u} < 0$ at the wall) for the investigated spoiler cases.	147



# NOMENCLATURE

## Roman Symbols

$\mathcal{R}$	[-]	aspect ratio
$b$	[m]	wingspan
$c$	[m]	wing mean aerodynamic chord
$c_\infty$	[m/s]	ambient speed of sound
$C_D$	[-]	absolute drag coefficient
$C_{D0}$	[-]	zero lift drag coefficient
$C_{Di}$	[-]	induced drag coefficient
$C_{DL}$	[-]	lift-dependent drag coefficient
$C_f$	[-]	friction coefficient
$c_{FL,proj}$	[m]	streamwise projected flap chord length
$c_{FL,Sp,proj}$	[m]	streamwise projected characteristic length of flap and spoiler
$C_p$	[-]	pressure coefficient
$C_l$	[-]	rolling moment coefficient
$C_{l\delta A,S}$	[1/°]	roll control effectiveness
$C_{l0}$	[-]	offset in rolling moment for zero deflection of the device
$C_L$	[-]	lift coefficient
$C_{L,app}$	[-]	approach lift coefficient
$C_{L,app,max}$	[-]	maximum approach lift coefficient
$C_{L,max}$	[-]	maximum lift coefficient
$C_{L\alpha}$	[1/°]	lift curve slope
$C_m$	[-]	pitching moment coefficient
$C_n$	[-]	yawing moment coefficient
$C_p$	[-]	pressure coefficient
$C_p^*$	[-]	critical pressure coefficient
$C_Y$	[-]	side force coefficient
$C_x$	[-]	aerodynamic force coefficient with regard to dimension $x$
$d$	[m]	cylinder diameter; tuft diameter; flap gap; nacelle diameter at inlet
$d_{Karb}$	[ $\mu\text{m}$ ]	grain-diameter of Karborundum
$D$	[N]	drag
$f$	[Hz]	frequency
$F_x, F_y, F_z$	[N]	components of balance force in coordinate system of the balance
$h$	[m]	height of the model's péniche; cell edge length

$k$	[-]	reduced frequency
$k_{krit}$	[ $\mu\text{m}$ ]	critical height of tripping strip
$K_L$	[-]	total pressure loss coefficient
$l$	[m]	characteristic length scale; length of tufts; length of fuselage; length of nacelle
$l$	[N · m]	rolling moment
$L$	[N]	lift
$L$	[m]	global length scale
$L_{vK}$	[m]	von Karman length scale
$L/D$	[-]	aerodynamic efficiency
$(L/D)_C$	[-]	aerodynamic efficiency for transonic cruise flight
$m$	[N · m]	pitching moment
$Ma$	[-]	Mach number
$M_x, M_y, M_z$	[N · m]	components of balance moments in coordinate system of the balance
$M_{x,max}$	[N · m]	maximum permitted moment around the $x$ -axis of the balance
$n$	[-]	number of sub measurements per angle of attack; number of time steps
$n_L$	[-]	number of necessary mesh points per global length scale
$n_T$	[-]	number of time steps
$N_z$	[-]	number of cells in spanwise direction
$p$	[Pa]	static pressure
$p_t$	[Pa]	total pressure
$p_{t,\infty}$	[Pa]	freestream total pressure
$q_\infty$	[Pa]	freestream dynamic pressure
$Q$	[1/s <sup>2</sup> ]	second invariant of the velocity gradient tensor
$R$	[N]	resulting force
$R$	[m]	radius of model bottom leading edge
$R^2$	[-]	regression quality
$Re$	[-]	Reynolds number
$S$	[m <sup>2</sup> ]	wing reference area
$s_i$	[m]	span of inner part of Split Aileron
$s_o$	[m]	span of outer part of Split Aileron
$S_{w'}$	[(m/s) <sup>2</sup> /Hz]	power spectral density of $w'$
$Sr$	[-]	Strouhal number
$t_1, t_2$	[s]	points in simulation time
$t_{idle}$	[s]	idle time between measurements
$Tu$	[-]	turbulence intensity
$Tu_x$	[-]	turbulence intensity of the axial velocity fluctuation
$Tu_y$	[-]	turbulence intensity of the lateral velocity fluctuation
$Tu_z$	[-]	turbulence intensity of the vertical velocity fluctuation

$u, v, w$	[m/s]	local axial, lateral, and vertical velocities
$u^*, v^*, w^*$	[-]	nondimensional axial, lateral, and vertical velocity components
$u^*$	[m/s]	friction velocity
$u', v', w'$	[m/s]	fluctuation value of axial, lateral, and vertical velocities
$U$	[m/s]	total velocity
$U$	[-]	uncertainty
$U_\infty$	[m/s]	freestream velocity
$V_{app}$	[m/s]	approach velocity
$V_{ref}$	[m/s]	landing reference speed at Minimal Velocity Approach Point
$V_s$	[m/s]	descent velocity
$V_{S,max}$	[m/s]	maximum feasible value of descent velocity
$V_{st}$	[m/s]	level flight stall velocity
$V_\theta$	[m/s]	cross flow velocity
$W/S$	[-]	wing loading
$W$	[N]	weight force
$x, y, z$	[m]	coordinates in axial, lateral, and vertical directions according to the aerodynamic coordinate system, German standard DIN 9300
$x^*, y^*, z^*$	[-]	non-dimensional x, y, z coordinates
$y^+$	[-]	non-dimensional distance from a wall

## Greek Symbols

$\alpha$	[°]	aircraft angle of attack
$\alpha_{max}$	[°]	angle of attack, for which lift coefficient becomes maximum; maximum used angle of attack for experiments
$\alpha_{min}$	[°]	minimum used angle of attack for experiments
$\gamma$	[°]	descent angle
$\gamma$	[-]	ratio of specific heats
$\Gamma$	[°]	dihedral angle
$\delta$	[°]	deflection angle of aerodynamic device
$\delta_{Ai}$	[°]	inner segment deflection angle of Split Aileron
$\delta_{Al}$	[°]	lower segment deflection angle of Deceleron
$\delta_{Ao}$	[°]	outer segment deflection angle of Split Aileron
$\delta_{Au}$	[°]	upper segment deflection angle of Deceleron
$\delta_\Delta$	[°]	differential deflection angle of Deceleron/Split Aileron
$\Delta$	[m]	filter size
$\Delta t$	[s]	outer time step

---

$\Delta x, \Delta y, \Delta z$	[m]	cell size in the three coordinate directions
$\varepsilon$	[W/kg]	average rate of energy dissipation per unit mass
$\eta_K$	[m]	Kolmogorov length scale
$\vartheta_c$	[°]	semi-apertural flow angle
$\kappa$	[-]	von Karman constant
$\lambda$	[-]	taper ratio
$\lambda$	[kg/m/s]	bulk viscosity
$\mu$	[-]	engine bypass ratio
$\mu$	[kg/m/s]	dynamic viscosity
$\mu$	[-]	mean value
$\nu$	[m <sup>2</sup> /s]	kinematic viscosity
$\rho$	[kg/m <sup>3</sup> ]	air density
$\xi$	[-]	axial dimensionless vorticity
$\sigma_{ij}$	[N/m <sup>2</sup> ]	viscous stress tensor
$\sigma$	[-]	standard deviation
$\tau_{ij}^R$	[N/m <sup>2</sup> ]	Reynolds stress tensor
$\tau_w$	[N/m <sup>2</sup> ]	shear stress
$\varphi$	[°]	turning angle of balance bogie, extrusion angle
$\varphi_{25\%}$	[°]	sweep angle at 25% chord length
$\varphi_{50\%}$	[°]	sweep angle at 50% chord length
$\vec{\omega}$	[1/s]	rotation vector

## Other Symbols

### Subscripts

<i>a</i>	aircraft
<i>A</i>	aileron
<i>app</i>	approach
<i>c</i>	calibration
<i>E</i>	total energy
<i>exp</i>	experimental
<i>F</i>	flap
<i>m</i>	wind tunnel model
<i>M</i>	measurement
<i>MW</i>	main wing
<i>num</i>	numerical
<i>ref</i>	reference point, baseline configuration at the MVAP
<i>S</i>	spoiler
<i>Sl</i>	slat
<i>T</i>	temperature
<i>W/T</i>	wind tunnel
$\infty$	ambient, freestream

### Superscripts

—	mean value
'	fluctuation value
*	non-dimensional value

### Frequently Used Abbreviations

2D	two-dimensional
2.5D	two-and-a-half dimensional
3D	three-dimensional
A	Aileron
AS	Adverse Spoiler

---

AAS	Advanced Adverse Spoiler
BL	Baseline configuration
CAD	computer aided design
CCD	charge-coupled device
CFD	computational fluid dynamics
CFX	CFD-program CFX version 12 of ANSYS, Inc.
CM	coarsened mesh
CS	Conventional Spoiler
CTA	commercial transport aircraft
DC	Deceleron
DLR	German Aerospace Center
DNS	direct numerical simulation
EHLP	European High-Lift Project
ENS	engine nacelle strakes
FAR	Federal Aviation Regulations
FM	refined mesh
HAI	high or approach idle thrust
HTP	horizontal tail plane
HWA	constant temperature hot wire anemometry
LCY	London City Airport
LES	large eddy simulation
MCT	maximum continuous thrust
MTO	maximum takeoff thrust
MVAP	minimal velocity approach point
PIV	stereo particle image velocimetry
PM	production mesh
PSD	power spectral density
RANS	Reynolds-averaged Navier Stokes
RG	research grid
SA	Split Aileron; Spalart Allmaras turbulence model
SAS	scale adaptive simulation
SSA	slow steep approach
SST	shear stress transport turbulence model
TFN	through-flow nacelle
TUM-AER	Institute of Aerodynamics and Fluid Mechnics, Technischen Universität München
URANS	unsteady Reynolds-averaged Navier Stokes
WTA	Wind Tunnel Facility A of TUM-AER
x1, x2	wake plane designations
ZLES	zonal large eddy simulation

# 1. INTRODUCTION

## 1.1 Motivation and Purpose of the Study

Since the 1950s air transport has become a major means of mass transportation - its mean growth since that time has been more or less consistently exponential [139]. A consequence of this growth is ever-increasing noise pollution in the vicinity of airports. Various studies have shown negative effects on the comfort and health of the population exposed to such noise pollution [134], [162], [72]. As a means to avert airport noise pollution, a growing number of noise restrictions for departing and approaching transport aircraft have been and continue to be instated [88]. A list of current restrictions and noise abatement procedures for specific airports is given in [8] and these are reviewed in detail by Girvin in [78]. Within their Vision 2020 proposal, the EU Advisory Council for Aeronautical Research in Europe (ACARE) asks for a reduction in noise impact by one half per operation relative to technology of the year 2000 [13]. NASA has set similar goals. Their Quiet Aircraft Technology Program (QAT) aims to achieve a reduction in perceived noise impact of future aircraft by one half relative to technology of the year 1997 within 10 years and by three quarters (-20 dB) within 25 years [130]. Both these objectives are illustrated in Figure 1-1.

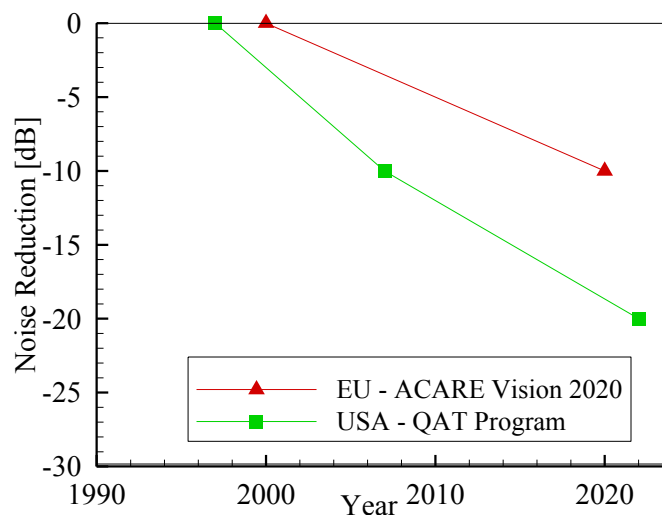


Figure 1-1: Noise reduction objectives.

The ACARE postulation was endorsed in 2008 by an addendum [4]. In order to meet these aircraft noise requirements new operational procedures are needed in addition to reductions in source noise. First and foremost among these new operational procedures are

steeper approach paths, potentially combined with the continuous descent approach technique.

The aerodynamic requirements for the steep approach performance are manifold. First and foremost, they demand a sufficiently high maximum lift coefficient and a sufficiently low glide ratio in order to provide adequate properties of flight mechanics. Indeed, the approach setting's aerodynamic performance of conventional Commercial Transport Aircraft (CTA) is not sufficient to permit steep approaches. Thus, deployment of some kind of air-brake device is required. However, the use of air brakes leads to a vortical and turbulent CTA wake. Thus, wing mounted air brakes can create another, more indirect aerodynamic challenge for steep approach, namely: Horizontal Tail Plane (HTP) buffet.

Despite these issues, steep approaches still have many advantages over standard approaches beside noise reduction: they enable to operate into airports surrounded by large buildings or mountains and they might lead to an increase of airport capacity by reduction of separation through avoidance of leading aircraft wake by conducting a steep approach of the follower. In addition, improvement to the aerodynamic performance of a CTA's approach configuration could allow reduced landing velocities and with it, further reduced noise and decreased landing length. This would make aircraft landing performance compatible with existing runway facilities.

Based on these circumstances and challenges, the investigations covered by this thesis focus on the performance regarding slow steep approach (SSA) capabilities of different novel air-brake concepts for CTA. It does not take into account source noise.

One can envisage different types of air brakes to fulfill the SSA requirements; Mertol, for example, investigates the feasibility of fuselage air-brakes in Ref. [122], while Flaig et al. postulate a "high-lift system of minimum complexity" [67]. This infers a modified CTA air-brake system of the same dimensions as the standard high-lift devices in current usage, namely, the spoiler and aileron systems. These considerations have led the author to investigate modified spoiler and aileron air-brake systems, potentially capable of fulfilling the requirements for SSA, while adding minimal complexity to the CTA.

## 1.2 Current Research into the Field

Recognition of the importance of environmental issues surrounding aviation is now widespread; with many research programs addressing these issues directly. The €1.6 billion European initiative Clean Sky is one of the largest [43]. Since its inception in 2008 it has identified and addressed the steps needed to be taken to meet the Vision 2020 -goals set by ACARE [13]. One part of the Clean Sky initiative is the Green Regional Aircraft program which is centered on the subjects low aerodynamic noise landing gear and high-lift devices. It focuses on advanced concepts that meet desired functions such as steep approach. It also addresses source noise issues including: passive acoustic treatment such as brush-like devices and the use of porous materials or serrations to reduce noise from

flap side edge vortices and slat upper trailing edge vortex shedding. The program's ideas for unconventional aerodynamic devices feature leading-edge gapless or drooped nose architectures, and kinematics to reduce noise caused by tracks and slots while maintaining high-lift performance [169].

Dobrinsky gave a résumé of noise research in the past 40 years in Ref. [54]. He outlined that with the introduction of fuel saving, high-bypass ratio engines around 1970, a significant reduction in jet noise was simultaneously achieved. Consequently, approach phase airframe noise, which came to the fore by the throttled-down engines, became a concern. Thus, substantial research efforts into airframe noise started after 1970. Based on theoretical work into aeroacoustics of the 1960s, most of the basic source noise reduction technologies had been invented by 1975. These included porous edge extensions [24], perforated edge extensions and edge serrations [87], [65], porous leading edge inserts [65], and porous edge replacements [65]. Subsequent developments include trailing-edge brushes, covers, fillers, liners, side-edge fences, brushes, and porous inserts for the slat cove, as well as moldline technology for hinged flaps and the application of streamlined fairings. Dobrinsky also referred to the potential of applying spoilers to enable steep noise abatement approach procedures and to contribute to wake vortex alleviation. He underlines the long term necessity for new aircraft configurations featuring short landing gears and enhanced lift capabilities for reduced approach speed [54].

Generally, noise research is concerned with either source noise or procedures that reduce perceived source noise. Both lines of enquiry were addressed by the German national research project 'Strategien zur Lärminderung an der Quelle unter Einschluss operationeller Möglichkeiten, speziell für den Nachtflug' [Translation: 'Strategies to Reduce Source Noise Including Operational Options, Specifically for Night Flight'] [131].

Research into source noise of CTA, can be further split into two categories: the first covers all the sources generated by the propulsion system, the second, the noise sources associated with the airframe. On modern CTA, airframe and propulsion noise are approximately of the same magnitude during approach and landing [22].

Wesley and Gliebe address in Refs. [117] and [79] the noise reduction of jet engine propulsion systems. The reduction of source noise generated by the high lift system has been investigated in recent years by experimental [22] and numerical methods [142], [143]. Model scale tests [39], flyover noise measurements [40] and computations [116] have identified the leading-edge slat as a prominent source of airframe noise during approach, in particular the air-brake devices used, these being sources of low frequency noise, outlined in Ref. [54]. De Bruin et al. present in Ref. [51] a noise prediction environment that combines the simulation of aircraft trajectory, attitude, speed and thrust with a simulation of the corresponding noise characteristics of the engine noise, thereby aiding the development of abatement flight procedures.

Recent research on CTA spoiler aerodynamics has mainly concentrated on the use of spoilers as a trailing-vortex-alleviation device. Extensive experimental wind tunnel research in this field has been performed [48], [50]. Flight tests with ground-based sensor measurements have also been conducted [33], [91], [49]. Such spoiler usage is significant for the present research as the interaction of the wake produced by the devices deployed with the HTP and leading to potential tail buffet issues is a shared topic. In this context, spoilers with base openings were shown to redirect the flow away from the CTA's tail. It ensures that the vortex wake flow of the inboard wing has reduced impact on the HTP, thereby facilitating steeper descent capability [6]. Seoud et al. investigate in Ref. [155] the production of noise and vibrations upon deployment of air brakes made of porous plates of high multi-scale porosity, known as fractal grids. They are capable of allowing independent and variable control of pressure drop and turbulence intensity alongside the ability to heavily dampen vibrations. As such, they have the potential to provide a foundation for silent air brakes.

To investigate the aero-acoustics of spoilers, low speed wind tunnel experiments were conducted in Ref. [151], where Sakaliyski et al state that 'one of the most critical tasks in noise reduction is to develop technologies to increase drag in quiet ways'.

Besides the reduction of source noise, new operational procedures are essential in order to meet the aircraft noise requirements. Among these, the combination of steep approach and continuous descent approach techniques shows great promise. Investigations into the benefits of this technology can be found, for instance, in Refs. [42], [166], [93], and [64]. Many aircraft manufacturers conducted trials leading to clearance to operate into London City Airport by means of steep approach in 2009. These trials indicate the significant demand for conducting steep approaches with CTA. The development of approach procedures for silent aircraft is shown in [93], albeit with regard to a blended wing body configuration.

In terms of the noise reduction potential of steep approach procedures, the following was identified: A descent angle of  $\gamma = 5^\circ$  instead of  $\gamma = 3^\circ$  leads to an approximate halving of the noise footprint. Antoine et al. estimate in Ref. [12] the noise reduction of a transport aircraft steep approach to be in the region of 7.7 dB. They specify a twofold advantage to this: first, the steeper flight path increases the propagation distance between the aircraft and the ground; second, the engines can be throttled back because the amount of thrust required to maintain the approach velocity is reduced, which, in turn, decreases engine noise. Regarding the second advantage, one must consider the indirect requirements of the Federal Aviation Regulations (FAR) (formerly, Joint Aviation Requirements) and EASA Certifications Specifications (CS) (formerly, Joint Aviation Requirements) regarding the minimum thrust setting needed to ensure the performance of a go-around procedure in the face of an abortive landing [60], [35]. Nevertheless, reduction in perceived noise for the steep approach procedure is assured.

Besides noise reduction potential, Filippone lists the following additional benefits to steep approach: shorter approach maneuver time, lower fuel consumption, and obstacle-clearing approaches [64]. Filippone [63] has also investigated the increased maneuver capabilities of novel spoiler types used for steep approach.

### 1.3 Contribution of This Work and Thesis Overview

As outlined above, extensive research has been conducted regarding the noise produced by CTA in all its facets. To contribute to this field, the author has chosen to investigate four novel air-brake types for CTA and their suitability to the enhancement of CTA steep approach performance. In order to measure and assess the efficacy of the novel air brakes two baseline cases are provided for comparison. In the first, the control test, the experimental configuration without air brakes of any kind was measured. In the second, the experimental configuration with conventional spoilers (CS) was measured. The CS test provides an indication of the current standard configuration, as such spoilers are utilized today in the approach phase, albeit in rare cases. The theoretical background, which is needed for the discussion of the results, is given in chapter 2. The operational particulars connected with steep approach and the principles of high-lift design are presented herein in the same way associated aerodynamics and flight mechanics.

To benchmark air-brake types in terms of steep approach, one must consider many aspects. This work focuses on specific aspects of aerodynamics and flight mechanics, namely: flight mechanics performance arising from the aerodynamic force and moment coefficients; the flow topologies characterized by the different configurations; and the evaluation of the wake linked to air-brake type, which potentially can lead to tail buffet, and, in turn, can indirectly narrow the steep approach performance. This work touches only briefly on other, no less important, non-aerodynamic/flight mechanic aspects.

The aerodynamic coefficients of each model configuration are evaluated by force measurements taken in low speed wind tunnel experiments. For this purpose, a detailed CTA half model was equipped with different specifically constructed air-brake model components. These include two types of multifunctional aileron devices and two types of novel spoilers, as well as a conventional spoiler. All the experimental investigations were conducted in the low-Reynolds number region at  $Re_{\mu} \approx 1 \cdot 10^6$  based on mean aerodynamic chord for angles of attack ranging from low negative values to post-stall values. The air-brake deflection settings are extensively varied. The details of the experiments are summarized in chapter 3.

Experimental and numerical investigations were conducted to evaluate the flow topology connected to the spoiler configuration. To visualize the wall adjacent flow, tufts were put on to the model's upper surfaces. The tuft pictures inform about mean flow direction, and consequently, areas of attached and separated flow; thereby making increased turbulence levels clearly identifiable. Two dimensional (2D) Reynolds Averaged

Navier Stokes (RANS) and first and second generation two-and-a-half dimensional (2.5D) Unsteady RANS (URANS) simulations of the mid-spoiler-sections allowed investigation of the flow topology generated by the three investigated spoiler types. All the numerical parameters of these simulations are given in chapter 4.

The main part of this work, the analysis and discussion of the assembled data, spans chapters 5 to 7. Chapter 5 focuses on the discussion of air-brake effectiveness regarding steep approach performance and lateral control of the configurations investigated here. The steep approach performance of a specific device cannot be examined in isolation from other control functions of the aerodynamic surfaces of a CTA. When showing that a device is capable of the required steep approach performance, it must also be shown that the other functions of the control surfaces, principally, lateral control ability, are maintained. Thus, both aspects - steep approach and lateral control effectiveness - are evaluated concurrently in this chapter.

Chapter 6 provides a comprehensive flow analysis of the different spoiler device configurations under investigation. It comprises an evaluation and discussion of the flow physics phenomena in the immediate experimental surroundings of the devices. The data for this analysis comes from the high-fidelity CFD simulations and the wool tuft flow visualization conducted in the wind tunnel experiments.

The flow analysis spreads to the influence of the spoiler device configuration on the near wake flow, which is discussed in chapter 7. Herein, the horizontal tail buffet characteristics of the CTA configurations are discussed. The air-brake wake potentially exhibits concentrations of turbulent kinetic energy at characteristic frequencies attributed to the air-brake vortex shedding. To counter this, power spectral density distributions are presented and discussed. These data are one major input to evaluate tail plane buffet. The results presented here make use of turbulent flow field data based on advanced Hot-Wire Anemometry (HWA) alongside flow field turbulence measured by Stereo Particle Image Velocimetry (PIV). Horizontal tail plane buffet is but one of many lines of enquiry open when investigating wake. Also of interest are flow topology and vortical structures which aid evaluation of the possible hazard for following aircraft.

Chapter 8 provides a closing summary of the investigation and its corresponding findings and concludes with some remarks on possible future developments and applications.

## 2. THEORETICAL BACKGROUND

This chapter provides the necessary background knowledge to evaluate the devices under investigation in this thesis. It starts with the requirements of steep approach operations, followed by the principles of CTA wing design including high lift and air-brake systems. In the sections on aerodynamics, flight mechanics and unsteady aerodynamics the relevant physical quantities are introduced.

### 2.1 Steep Approach Operations

A steep approach operation is defined as a situation where a descent angle is steeper than the conventional angle of  $\gamma = 3^\circ$ . Steep approach operations have been daily business for many years at both commercial and military airports that are surrounded by obstacles. London City Airport (LCY), for example, is surrounded by high buildings [7]. On closer inspection it becomes clear that the commercial sector has always been limited to smaller regional aircraft. Nevertheless, there is a significant demand to incorporate larger mainline CTA into commercial airports, where steep approach is mandatory. For instance, in June 2007, Airbus obtained certification for its A318 aircraft to operate into LCY with a descent angle of  $\gamma = 5.5^\circ$  [5]. This is the largest CTA to be certified for steep approach operations to date. As a result, air carrier British Airways plc started to utilize this CTA type at LCY in 2009 [31]. Other aircraft manufacturers followed suit in conducting trials. This led to clearance to operate their CTA types (including the Embraer E-190 and ATR-72 [102]) into LCY by means of steep approach in 2009. Thus, LCY can serve as a reference airport regarding steep approach operations of CTA; as could Lugano airport, where descent angles of  $\gamma = 6^\circ$  are mandatory [150].

Closely related to steep approach is Continuous Descent Arrival [21]. In this procedure the approaching aircraft's descent angle is not set to a specific value, but flexible depending on each individual aircraft's capabilities to realize a continuous low noise descent [147]. Here, descent angle can range up to values that are also applicable for steep approach [115].

After introducing the general approach operations in the following subsection, the necessary requirements and measures for conducting steep approaches are presented. Additionally, an overview of the range of current aircraft capable of conducting steep approach is given.

### 2.1.1 Approach Operations in General

The CTA's approach operation marks the period between the end of cruise flight and landing and is divided into three phases. These are descent, final approach, and flare. Descent (which combines initial and intermediate approach) begins with the aircraft leaving cruise flight altitude. Through deceleration it shifts into final approach when the aircraft performs a straight flight along the Instrument Landing System (ILS) glide slope path. Deceleration to approach velocity  $V_{app}$  must be completed upon reaching a certain altitude limit, typically 1000ft. Final approach is then continued as a stationary flight at approach velocity  $V_{app}$ , known as 'stabilized approach'. An 'unstabilized approach', in contrast, is an approach with either a too low and/or slow flight path (and is linked to a deficit in kinetic energy), or it is an approach with a too high and/or fast flight path (linked to an excess of kinetic energy). These cases may result in approach and landing incidents, such as a loss of control, short and/or hard landing, tail strike, and a runway excursion and/or overrun [71]. When talking generally about 'approach', it is this stationary final approach phase that is meant. The last section of the final approach is sometimes referred to as the 'short final'.

The rotation of an aircraft's nose upwards serves to arrest the descent rate before touchdown and is referred to as 'flare'. While performing steep approach, the flare has to be initiated at a much higher altitude than normal due to the steeper approach angle and higher rate of descent. Figure 2-1 illustrates the approach and landing phases between cruise flight and stop.

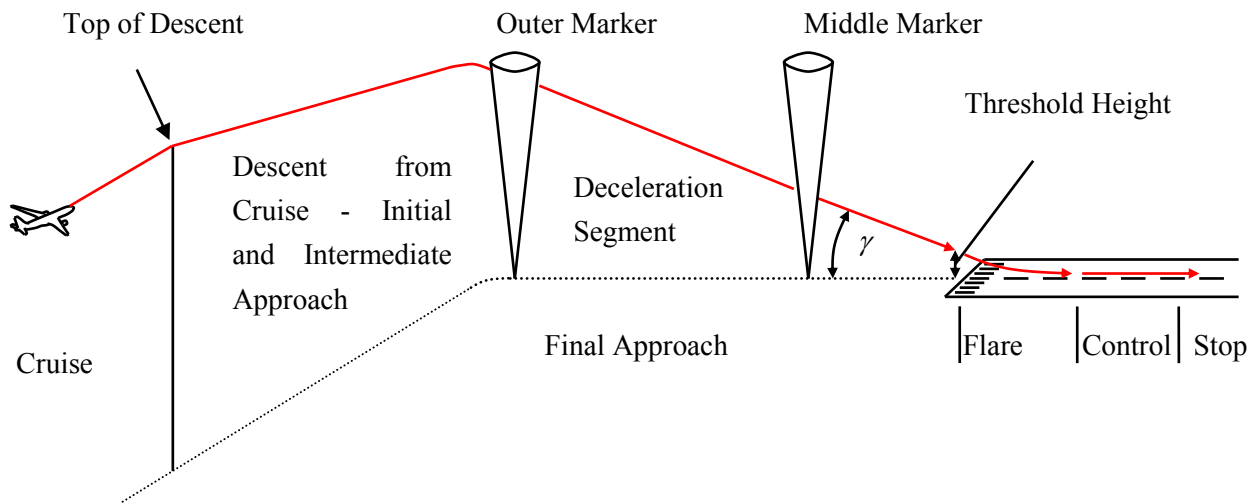


Figure 2-1: Approach and Landing Phases.

Decelerating on a glide path without deploying air brakes is usually not possible [71], thus the deployment of air brakes is necessary. However, the use of air brakes is not recommended for standard approaches beginning less than 1000 ft above airfield elevation and/or in the landing flaps configuration [71]. However, the use of air brakes is necessary for conducting steep approach.

As a means to increase the aircraft landing rate, Air Traffic Control (ATC) at high-density airports frequently request pilots to maintain high airspeed in final approach [71]. This contradicts the legislative demand to lower approach speeds so as to minimize noise.

### 2.1.2 Necessity to Conduct Steep Approaches

The necessity to conduct steep approaches is not limited to the current principal motive of being able to operate into airports surrounded by obstacles, such as LCY. In future, and in harness with the above motive, steep approaches should be able to make a major contribution to noise reduction, as stated in section 1.2. The principle means to reduce noise is thereby to increase the slant distance between the approaching aircraft and the noise receiver. This is illustrated in Figure 2-2, where the standard approach path is contrasted by the steep approach path, making visible the increase in slant distance.

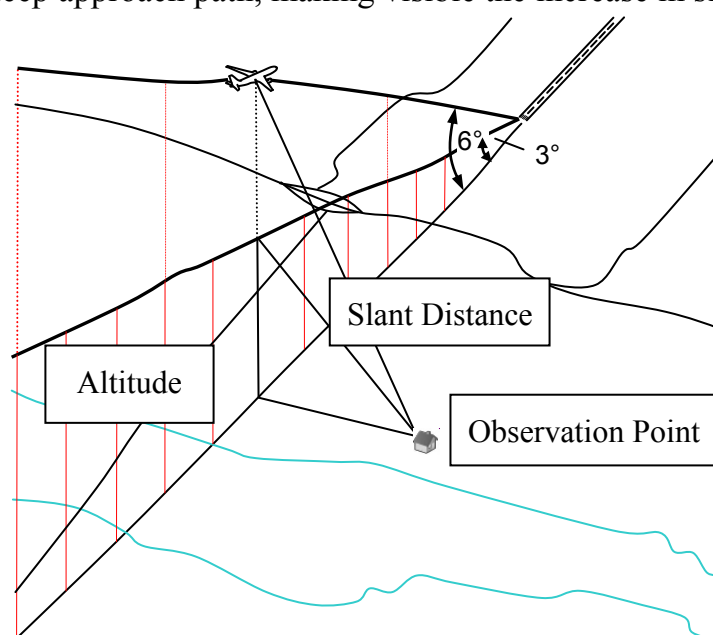


Figure 2-2: Relationship between altitude and slant distance for standard and steep approach.

Furthermore, the forecasted growth in worldwide civil air transport is limited by the traffic-slot-capacity of the major airports. This capacity can be increased by improving the approach procedures, as well as through traffic decentralization, i.e. making greater use of smaller airports for long range operations. Therefore, in terms of airfield performance the descent capabilities of future CTAs needs to be increased towards those of military transport aircraft [70].

Steep approach is import to the military sector for an additional reason: the need to get into so-called 'hot landing zones', where hostility is present around the airport, with increased ease. This enables military aircraft, for example, a tactical air lifter, to remain above the range of small-arms fire until close to the airfield [77].

### 2.1.3 Requirements for Steep Approach Operations

There are three major demands subsumed in the JAR Certification Requirements to conduct a steep approach:

First, the aircraft must be capable of maintaining the steep descent angle of  $\gamma = 5.5^\circ$  (or steeper) compared with the standard value of  $\gamma = 3^\circ$  in the most limited configuration (including, for example, the anti-icing setting of the engines). The precise descent angle  $\gamma$  is dependent on the individual airport. The aircraft must demonstrate that there is a further margin of  $\Delta\gamma = 2^\circ$  in the approach angle to provide maneuver capability. Maneuver agility is also assessed, this being the speed with which an aircraft is able to regain its flight path. These parameters are, for the greater part, defined by the aircraft's drag margin, meaning the surplus drag achievable by deploying the air brakes at maximum setting.

The second demand is the ability to flare. It is equivalent to the ability to quickly change the lift of the aircraft. This is achieved by a steep lift-slope gradient, slow approach speed and high elevator effectiveness. The transient issues of flare lie beyond the scope of this work and so are not addressed in detail.

The third demand is the ability to stop in the distance available. The main parameter to minimize, and thereby optimize, to this end is the approach speed. This demand is not necessarily associated with steep approaches, but in most cases steep approaches are used on limited length runways. Steep approach also leads to the possibility of optimizing the landing distance in that landing points may be moved closer to surrounding obstacles [16]. This is illustrated in Figure 2-3.

Other JAR requirements include demonstration of a landing with a lowered approach velocity  $V_{app} = V_{ref} - 5\text{kt}$ , a single engine landing and go-around, and a good flight deck visibility.

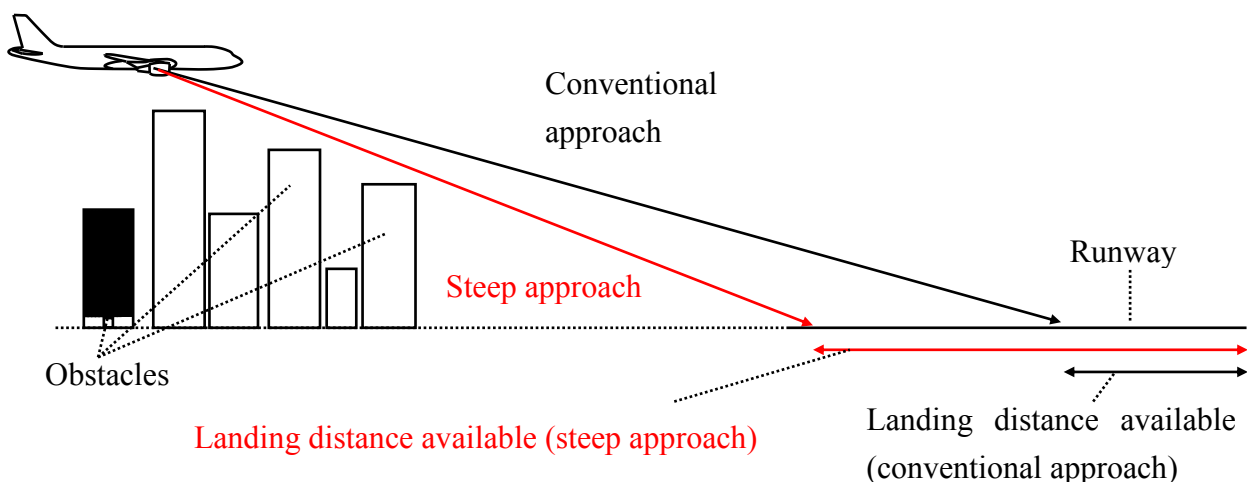


Figure 2-3: Landing distance available depending on approach path inclination.

A very important aspect for commercial flight operations is safety: Fatal accident figures have decreased globally over the last few decades of commercial air transportation.

Nevertheless, safety is still a big issue due to stagnation in accident rates in recent years [113]. The last decade's fatal accidents and onboard fatalities by phase of flight have been analyzed in Ref. [163]. Consulting these statistics, final approach and landing combined are the most critical phases of flight. Thus, when dealing with steep approach technologies, which affect final approach and landing, safety aspects call for serious attention.

One accident in 2007 linked to steep approach was reported in Ref. [103]. In this case a wind shift, combined with below-target approach speeds, led to a sudden sink before touchdown. This accident led the airline to reassess the risk level of its steep approach operations, amend some of its procedures, and introduce additional simulator training.

#### 2.1.4 Measures to Achieve Steep Approach Capabilities

The primary measures to achieve steep approach capabilities comprise the deployment of air brakes. The main disadvantage of conventional spoilers used for steep approaches is that they reduce maximum lift while increasing drag. But as Mertol states in Ref. [123], an increased drag coefficient is not the only air-brake requirement for steep approach usage. Also called for are an increased maximum lift coefficient, a non-increase in the mass of the aircraft, and no change in the contour of the aircraft, in order that cruise drag is not increased. Propeller aircraft can use a variation of their propeller pitch for a negative thrust in addition to air brakes [77].

Software modifications are sometimes necessary to achieve the required steep approach characteristics [58]. Rosa states for aircraft manufacturer Airbus in [136], that he has identified further aft center of gravity limits to reduce approach speed and 'anti-droop' aileron positions to improve braking performance as measures for steep approaches. Landing after a steep approach can potentially be harder than a normal approach. As a means to compensate for this, regional aircraft manufacturer Fokker developed a means to reduce the precharged pressure in the main landing gear (MLG) struts of their Fokker 100 aircraft, thereby providing increased cushioning [55].

German Aerospace Center DLR made use of a Ground Based Augmentation System in their campaign to investigate new approach procedures including steep approach [76], [101]. This campaign also investigated the perceived noise reduction potential of the new approach procedures.

A head up display is reported to be in the process of being introduced in large military aircraft designed to conduct steep approaches in battlefield conditions [144]. Helicopter manufacturers Sikorsky and Bell installed small chin windows in their helicopters by the pilot's feet for evaluation during helicopter steep approaches [83], [84]. Other more unorthodox methods include Tail Chutes, and the helicopter-capabilities of a hybrid helicopter/fixed wing aircraft [85].

### 2.1.5 Steep Approach Capable Aircraft

This subsection lists specific aircraft types already conducting steep approaches. The list makes no claim to be complete.

Regional turboprop aircraft comprise de Havilland Canada DHC-7, Dornier Do 228, Saab 2000 [150], Dornier 328 [94], and ATR 72 [75] Regional jet aircraft (RJA) comprise Dornier 328 JET [44], BAe 146/Avro RJ series, Fokker 70 [76], Fokker 100, Fokker 28, Embraer 170 [114], and most recently (since 2010), the Embraer 190 [80]. These capabilities are also planned for a future RJA, the Sukhoi Superjet [127]. Business jets include Challenger 605 and 850 [152], Piaggio P180 [46], and Cessna Skyhawk [160].

The only mainline CTA to date certified steep approach capable is the Airbus A318. By using spoilers three and four of each wing as air brakes, the aircraft's steep approach capabilities were achieved with minimal alterations to its standard configuration [172]. NASA has reported on its extensive research into a steep approach capable transport aircraft, named Quiet Short-Haul Research Aircraft (QSRA), in [158]. The Airbus A400M is an example of a military transport aircraft capable of conducting extra steep approaches [128]. The Lockheed Martin F-35A is a military fighter type aircraft in current usage that is able to conduct vertical landings. Figure 2-4 shows the spectrum of approach types with values of descent angle as well as aircraft examples for each segment.

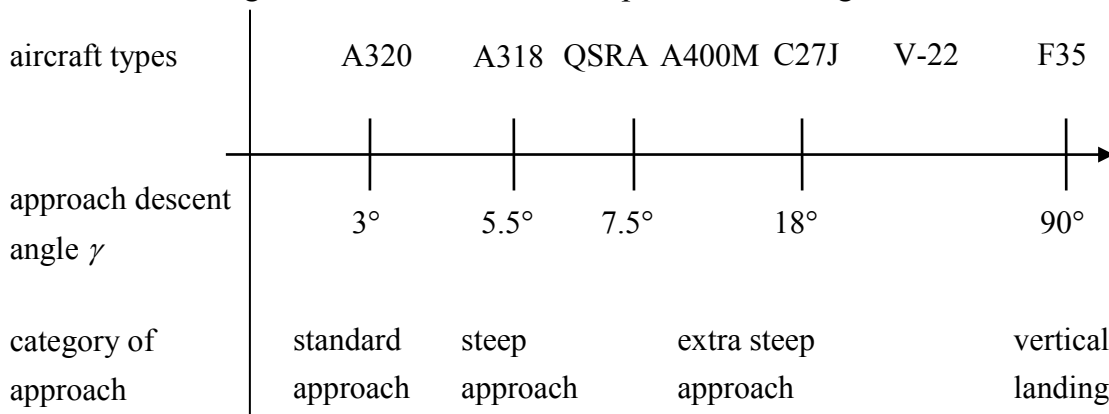


Figure 2-4: Approach categories with aircraft examples.

## 2.2 Transport Aircraft Wing

As all the devices under investigation are to be integrated into a CTA's wing, the wing, including its high-lift system, is outlined in this section.

### 2.2.1 Cruise Flight Wing

A CTA's wing must comply with completely different objectives and constraints for each of the various flight phases and related conditions, in which it will operate. The fundamental design aim for cruise flight is to generate sufficient lift to balance the weight force while keeping weight and drag to a minimum in order to minimize fuel burn and

maximize range. However, for a wing these are often conflicting requirements, because the minimum drag design is not the minimum weight design, and vice-versa. To complicate the challenge, the landing gear has to be retractably integrated into the wing for cruise flight. Finally, the wing is also the main fuel tank of the aircraft, so it must be large enough to hold enough fuel for the flight while also having enough spare capacity to allow for future developments of the aircraft, such as longer range versions. And yet, a too large wing would trigger compatibility problems at airports, not least in terms of maneuvering around the airports and having sufficient space available at the loading gates [25].

These cruise flight objectives differ considerably from those of approaching flight conditions – the focus of this work. When designing a wing for steep approach, the objectives and, more importantly, the constraints for cruise flight conditions must provide its foundation. Put simply, one starts with the wing design for cruise flight conditions. For the next stage, one integrates various retractable and deployable devices into this design. These are allocated to the wing's leading and trailing edges, and thus are labeled leading edge devices, trailing edge devices and control surfaces. Together they are called the high-lift system, and include the air-brake system. Rigid constraints relating to mechanical retractability further limit the aerodynamicist's freedom in terms of both the shape and orientation of the high-lift system's elements.

### 2.2.2 High-Lift System of Contemporary Commercial Transport Aircraft

The wing is designed to change in shape and size so as to alter its aerodynamics and the flight characteristics of the airplane while in flight. The reason for this is to increase the flight maneuvering envelope and thereby provide adequate aerodynamic characteristics for the design points Take off, Maneuvering, Approach and Landing. Additional special design points exist, such as Short Takeoff and Steep Approach. Kiefner summarizes in Ref. [106] that further main objectives of CTA high-lift technologies are the reduction of noise and emissions, increase of airport capacity, passenger comfort, safety and aircraft efficiency, minimization of maintenance effort and finally, an increase in system availability. Overviews of the high lift system design process for large CTAs, including the legal requirements defined in JAR 25.333, are given by the authors of Refs. [67], [70], [145], and [171].

As noted above, the high-lift system includes leading and trailing edge devices. Contemporary CTA leading edge device types comprise 'Leading Edge Slat', 'Krüger Flap', and 'Droop Nose Device'. Contemporary CTA trailing edge device types include 'Plain Flap' and 'Fowler Flap'. A downward deflection of any of these devices is defined to be of positive direction  $\delta > 0$ .

The most common high-lift system devices are installed on the wind tunnel model used in this study: Leading Edge Slats spanning almost from root to tip of the wing's leading edge, Fowler Flaps inboard and outboard at the wing's trailing edge and Ailerons

outboard at the wing's trailing edge. Sectional views of these device types are illustrated in Figure 2-5, where the deflection definition of the devices is also given.

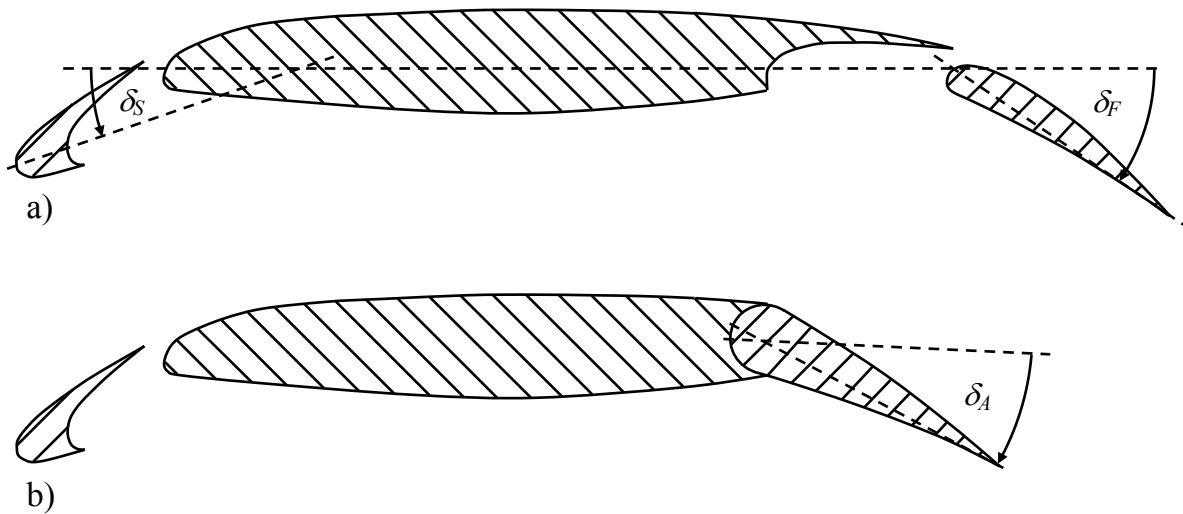


Figure 2-5: Sectional view of an airfoil with deflected high lift devices. a) Leading Edge Slat and Fowler Flap. b) Leading Edge Slat and Aileron.

Less common devices such as leading edge root extensions and blown flaps also exist. Generally they are divided into powered and unpowered devices. Current CTA utilize only unpowered devices due to regulatory reasons.

### 2.2.3 Aileron

Contemporary CTA, such as the configuration investigated here, do have an all speed aileron. This is realized by plain flaps positioned at the most outboard trailing edges of each wing. These ailerons are used to deliver roll control by deflecting the starboard and port side one differentially. It can also be deflected symmetrically in positive rotating direction for both wings to provide additional lift. In this case, it is considered to be a high-lift system component. Zero deflection  $\delta_A = 0$  means the aileron is flush with the adjacent wing segments inboard and outboard of the aileron.

### 2.2.4 Air Brake System

Air brakes are defined as deployable devices which increase aerodynamic drag, thereby decelerating an aircraft. Their main objective is to decrease air speed in the flight phases of descent and approach, and to decrease landing distance. Military aircraft make extensive use of air brakes for tactical maneuvering. The use of air brakes when conducting steep approach is, at present, essential. Although the term air brake is sometimes used to refer to a specific type of vertically extending air brake, it also refers to any brake system that uses air flow to fulfill its duty. It is the latter, wider definition that is appealed to in this work. The range of major air-brake types in current usage is shown in Figure 2-6.

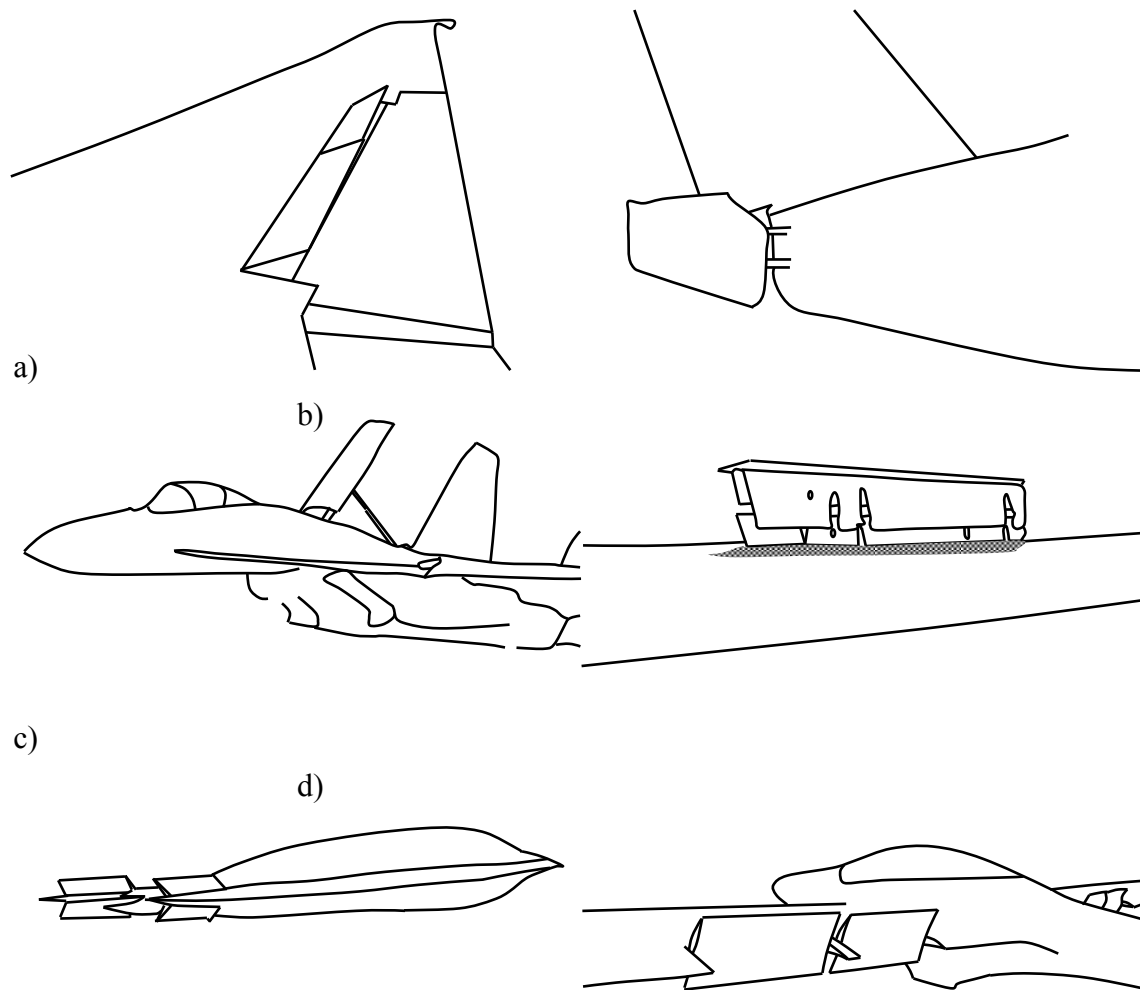


Figure 2-6: Major air-brake types in current usage. a) Wing spoiler of a CTA; b) Posterior/tail-mounted split air brake; c) Fuselage mounted dorsal air brake on fighter aircraft; d) Double-decker Schempp-Hirth air-brake; e) Deceleron; f) Turning flap.

The naming of air brakes is dependent on their position and is underpinned by an anatomical model, illustrated in Figure 2-7.

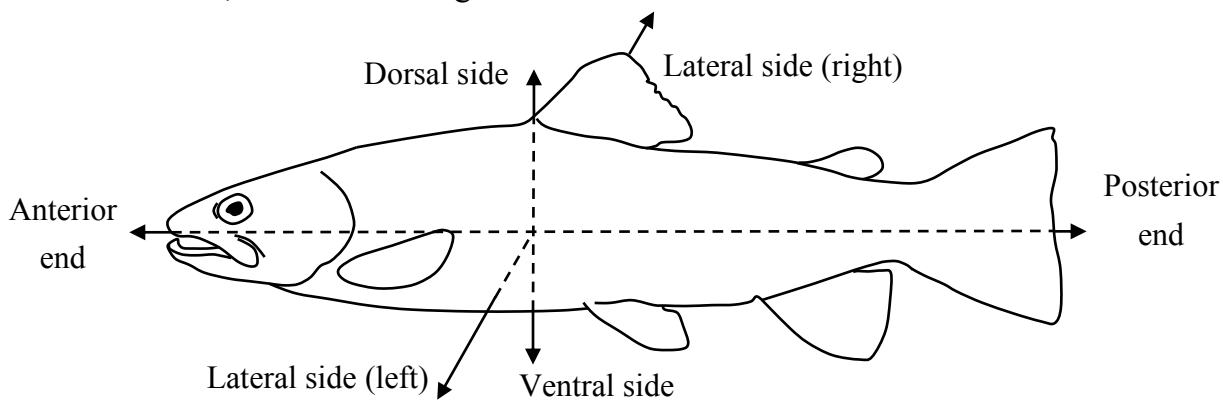


Figure 2-7: Anatomical model (trout) underpinning naming of air brakes.

The majority of air-brake types are wing-based. The most common are conventional Wing Spoilers (CS). These are used with nearly every contemporary CTA. Fowler Flaps are also used as air brakes with every contemporary CTA. Although their principal function is to increase the lift coefficient, they act as air brakes in their highest setting: their flap-extension range occupies half of their capability, generating lift proportional to induced drag. As the flaps extend beyond halfway, the inverse occurs, because profile drag at constant lift increases with profile camber and flap deflection [69]. Schempp-Hirth air-brakes, often found on gliders, are flat, sometimes perforated plates that extend perpendicular to the wing's surface. Some designs extend above and below the wing.

When investigated for their role in steep approaches, Mini Trailing Edge Devices (TEDs) have shown to carry an air-braking effect, in addition to lift increase [131]. Examples of other integrated air-brake high-lift concepts include an integrated spoiler and flap system described in Ref. [138] and drooped spoilers with trailing-edge wedges [170].

Fuselage mounted air-brake systems have also been developed. The Embraer E-170 has a ventral air brake installed at the wing/fuselage fairing for use in steep approach [114]. Dorsal air brakes are mainly used by fighter aircraft such as the Eurofighter Typhoon [173] or MiG-29 [59]. While Posterior or tail-mounted split air brakes are used by the BAE 146-300 [16], and the Fokker F-28 for steep approach.

Some more detailed information about spoiler- and aileron-based air-brake concepts, which are to be investigated in this work, follows.

#### 2.2.4.1 Spoiler Based Concepts

Conventional wing spoilers (CS) are plates on the top surface of a wing or segments of the wing shroud's trailing edge, which are hinged upwards, thereby decrease the section's camber and disturb the trailing edge airflow. This leads to a lift reduction and a drag increase of the respective wing section. CS differ from other air brakes in the way that other air brakes are designed to mainly increase drag while making little change to lift, while CS greatly reduce lift while increase drag. The CS's hinge axis is located inside the spoiler and parallel to its leading edge. They are common on nearly every contemporary CTA and classified as secondary flight controls. Most CTA have several CS distributed along the wingspan. The individual CS are allocated to one or more of the following tasks: They are used as ground spoilers to assist in slowing the aircraft. Hereby, the increase in drag created by the CS directly assists the braking effect. However, the real gain comes here as the CS cause a loss of lift and hence the weight of the aircraft is transferred from the wings to the undercarriage, allowing the wheels to be mechanically braked with much less chance of skidding. Other allocations are to use them as flight spoilers to descend and in combination with ailerons to control lateral motion. The usage for lateral control is primarily to reduce adverse yaw when rudder input is limited by higher speeds. For such CS the term Spoileron has been coined.

Concerning actuation CS usually make use of hydraulic actuation, but an electromechanical actuator for a transport aircraft spoiler surface was also investigated [74]. CS require holding open as the airflow tends to blow them closed. Some CS feature breather slots, e.g. the ones of the Airbus A300 and Sud Aviation Caravelle.

Two novel spoiler based concepts are investigated in this work. The first is designated Adverse Spoiler (AS) and was patented by Mertol in 2008 [123]. The second one is a modified version of AS and designated as Advanced Adverse Spoiler (AAS). These spoilers distinguish from CS in that manner, that the hinge line is moved back to the trailing edge of the spoiler respectively wing shroud. When deploying the AS a vent is opened between the bottom and top side of the wing, where the spoiler is located. The AAS follows the same principle as the AS, but the just mentioned AS's vent is closed by a flat cross-piece connecting the main wing and the trailing edge of the AAS. A sectional view sketch of CS, AS and AAS with the deflection definition can be found in Figure 2-8.

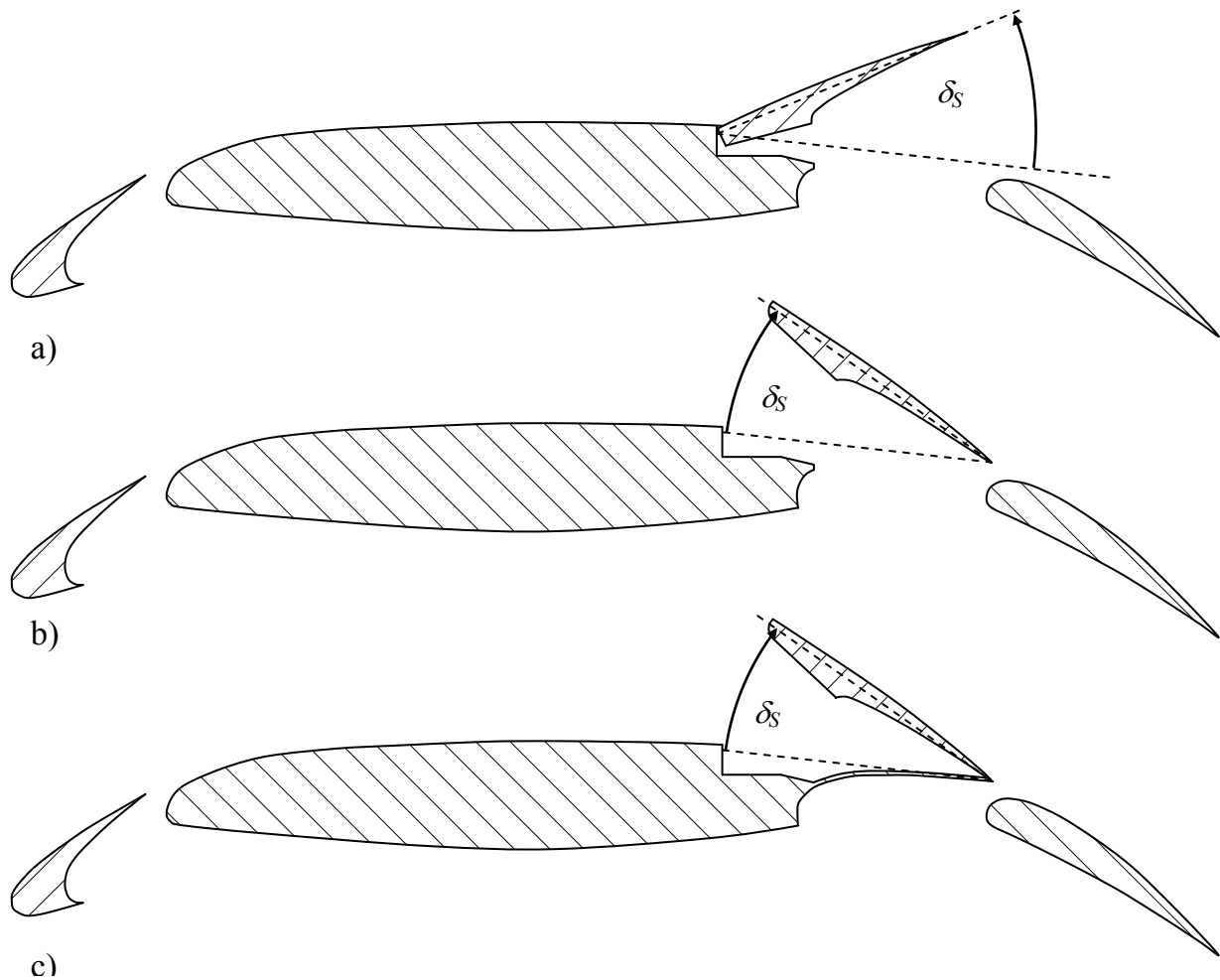


Figure 2-8: Sectional view of investigated spoiler types. a) Conventional Spoiler, b) Adverse Spoiler, c) Advanced Adverse Spoiler.

More geometrical details of the actual implementation of the devices into the wind tunnel model follow in the air-brake model parts subsections 3.5.1 to 3.5.3.

### 2.2.4.2 Aileron Based Concepts

Besides spoiler based CS, AS, and AAS air-brakes types, two aileron based air-brake concepts are investigated in this work. They combine the functions of braking, lifting, rolling and yawing motion control. One of their advantages against the spoiler based concepts should be that they potentially do not disturb the Fowler Flap devices' flow as much if at all due to their spatial distance outboard of these devices. Descriptions of the investigated aileron based devices follow in the next two paragraphs.

#### *Deceleron*

The Deceleron (DC) was patented in Ref. [47] by aviation company Northrop. It is defined to be a Plain Flap which splits into upper and lower halves to serve as speed brake. It can be operated in one piece the same way as a conventional aileron, but can also be deflected differentially to serve as air brake. This differential deflection  $\delta_A$ , which is the difference of upper and lower segment deflection angle, is superposed by the deflection of the mean deflection angle  $\delta_A$ .  $\delta_A$  again is defined as the arithmetic mean of upper segment deflection angle  $\delta_{Au}$  and lower segment deflection angle  $\delta_{Al}$ :  $\delta_A = (\delta_{Au} + \delta_{Al})/2$ .

For usage as split flap the lower half of the DC can be drooped down to serve as an outboard extension of the outboard Fowler flap. The Northrop F-89 was the first airplane to use the DC exclusively as its air brake. The reason for applying the DC on the F-89 was that its thin wing prevented the installation of CSs. No CTA was equipped with it until today. Other aircraft, which have a DC installed, comprise for instance Northrop Grumman B-2, Fairchild Republic A-10, and Northrop XF-8. Aerodynamic investigations of an aircraft equipped with DCs were conducted by Butler [34]. A similar device with the difference, that it is implemented as subsystem into a Plain Flap was patented [156].

#### *Split Aileron*

The Split Aileron (SA) is a laterally segmented Plain Flap. The two segments can be deflected differentially. By this, the SA can be used like the DC as multifunctional aerodynamic device. A system for providing this kind of differential motion to deployable lift devices is patented in Ref. [81].

The SA's aileron deflection angle  $\delta_A$  is defined as the arithmetic mean of outer segment deflection angle  $\delta_{Ao}$  and inner segment deflection angle  $\delta_{Ai}$ :  $\delta_A = (\delta_{Ao} + \delta_{Ai})/2$ . The differential deflection angle  $\delta_A$  is defined by the difference of outer and inner segment deflection angle:  $\delta_A = \delta_{Ao} - \delta_{Ai}$ . A sectional view sketch of the two multifunctional aileron devices can be found in Figure 2-9.

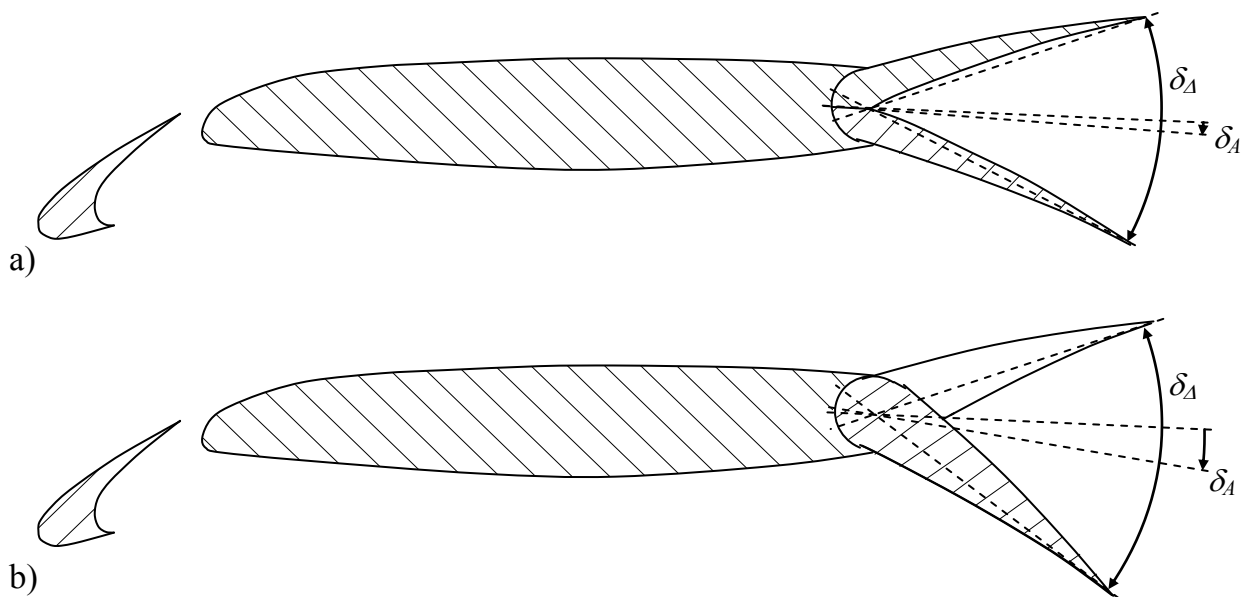


Figure 2-9: Sectional view of multifunctional aileron devices. a) Deceleron, b) Split Aileron.

More geometrical details of the actual implementation of these devices into the wind tunnel model again follow in the air-brake model parts subsections 3.5.4 and 3.5.5.

### 2.2.5 Multiple Device Allocation to Function

Besides adapting the wing’s aerodynamics to be able to conduct maneuvering, takeoff, approach and landing, another function of the movable wing devices, especially the trailing edge flaps and spoilers, can be the gust and maneuver load alleviation, where a change in lift distribution is utilized for loads management [133], [107]. Typically, each function is allocated to a set of trailing edge devices. An exemplary allocation of CTA’s trailing edge devices for their functions is illustrated in Figure 2-10.

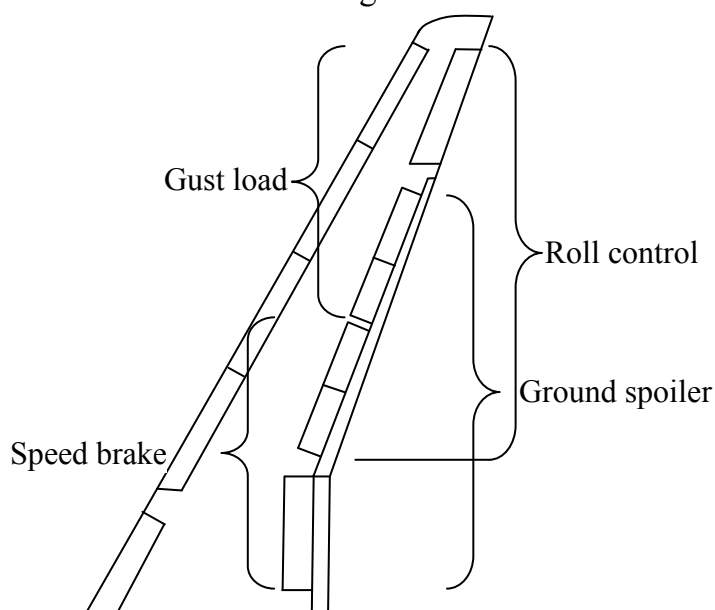


Figure 2-10: Example distribution of functions of a CTA’s trailing edge devices.

## 2.3 Aerodynamics

After introducing the relevant dimensionless parameters and fluid mechanic quantities, airfoil, high-lift, and air-brake aerodynamics are outlined in this section. Drag decomposition is discussed as well.

### 2.3.1 Similarity and Dimensionless Parameters

Dimensionless parameters are essential to bear analogy of flow fields and thus to be able to convey experimental results to the original. Flow analogy is obtained only if geometrical and the relevant physical quantities correspond to a fixed ratio for any correspondent position of both flow fields as defined by Truckenbrodt in Ref. [168]. For experimental simulations only the most relevant quantities can be considered. These quantities and the resulting relevant dimensionless parameters have to be determined previously to the experiment.

Mach number  $Ma$  and Reynolds number  $Re$  are regarded most relevant for an investigation of CTA aerodynamics. Reynolds number gives a measure of the ratio of inertial forces to viscous forces. Mach number gives a measure of the ratio of inertial to elastic forces. Additionally, Strouhal number  $Sr$  is useful for characterizing unsteady flow phenomena. It represents a measure of the ratio of inertial forces due to the unsteadiness of the flow to the inertial forces due to changes in velocity from one point to another in the flow field. The definition of these three parameters is the following:

$$Re = \frac{U_\infty \cdot l}{\nu_\infty} \quad (2.1)$$

$$Ma = \frac{U_\infty}{c_\infty} \quad (2.2)$$

$$Sr = \frac{f \cdot l}{U_\infty} \quad (2.3)$$

where  $U_\infty$  is the freestream velocity,  $l$  a characteristic length scale,  $\nu_\infty$  the freestream kinematic viscosity,  $c_\infty$  the ambient speed of sound, and  $f$  the frequency. Approach of CTA is happening exclusively at low Mach numbers. For example, the nominal approach velocity of a Boeing B737-800 series CTA is  $V_{app} = 130 \text{ kt} = 66.9 \text{ m/s}$  [23], resulting in a Mach number of  $Ma_{B737} \approx 0.195$ . The wind tunnel's test section inflow Mach number is  $Ma_{WT} \approx 0.146$  resulting from the consistently used inflow velocity  $U_\infty = 50 \text{ m/s}$ . Both Mach numbers are in the subsonic region by fulfilling the criterion  $Ma < 0.3$ . Therefore, the flow can be considered incompressible, with a negligible relative change in density of  $\Delta\rho/\rho_\infty < 5\%$ . The Mach number similarity is taken for granted. This Mach number limit

criterion can be derived from the compressible Euler equations using scale analysis of non-dimensional quantities.

Reynolds number  $Re$  represents the most important dimensionless quantity for viscous flow phenomena to ensure dynamic similarity [141]. Reynolds number similarity can not be obtained within the conducted wind tunnel tests, as by scaling down the real aircraft to the model size, the wind tunnel test Reynolds number becomes  $Re_{W/T} \approx 1 \cdot 10^6$ . It is at least one order of magnitude smaller than the Reynolds number for an approaching CTA. The range for typical freestream Reynolds numbers of approaching CTA is  $Re_{CTA} \approx 2 \cdot 10^7 \div 5 \cdot 10^7$ . To address this issue, the transition of the boundary layer from laminar to turbulent state is tripped at positions, where transition is anticipated for the real aircraft. Nevertheless, the model boundary layer is too thick compared to the real aircraft and shear stress profiles are not compatible. More details about the tripping follow in subsection 3.4.2.

The previously given dimensionless parameter values are based on the thermo-physical properties defined by ICAO's international standard atmosphere [95]. The actual conditions in the wind tunnel test section and in real flight vary in each case slightly, but this does not affect the magnitude of the dimensionless parameters.

### 2.3.2 Derivation of Relevant Fluid Mechanic Quantities

All fluid mechanic quantities are discussed in this work in their non-dimensional form, which gives the opportunity to transfer these quantities to real flying conditions. The definition of all the discussed quantities is given in this subsection. Pressure  $p$  is expressed in its dimensionless form as pressure coefficient  $C_p$ ,

$$C_p = \frac{p}{\rho_\infty / 2 \cdot U_\infty^2} = \frac{p}{q_\infty} \quad (2.4)$$

where  $\rho_\infty$  is the freestream density and  $q_\infty$  is the freestream dynamic pressure. The forces lift  $L$  and drag  $D$  as well as the rolling moment  $l$  and pitching moment  $m$  are also discussed in their non-dimensional form:

$$C_L = \frac{L}{q_\infty \cdot S}, C_D = \frac{D}{q_\infty \cdot S} \quad (2.5)$$

$$C_l = \frac{l}{q_\infty \cdot S \cdot b/2}, C_m = \frac{m}{q_\infty \cdot S \cdot c} \quad (2.6)$$

where  $S$  is the reference area,  $c$  the wing mean aerodynamic chord, and  $b$  the wingspan. The exclusively used coordinate system is orientated with respect to the aerodynamic coordinate system according to German standard DIN 9300 [53]. Thus, the x-coordinate points in streamwise direction, the z-coordinate upwards perpendicular to the x-direction in

the model's plane of symmetry, and the y-coordinate starboard, perpendicular to the x- and z-direction. All three linear dimensions in their dimensionless form  $x^*$ ,  $y^*$ , and  $z^*$  are referenced to the half span  $b/2$  of the wind tunnel model:

$$x^* = \frac{x}{b/2}, y^* = \frac{y}{b/2}, z^* = \frac{z}{b/2}. \quad (2.7)$$

The coordinate system is related to the Wing Reference Point (WRP), namely the most outboard position of the wing trailing edge. The coordinate values at WRP are  $x^* = 0$ ,  $y^* = 1$ , and  $z^* = 0$ .

Dimensionless mean flow velocities  $u^*$ ,  $v^*$ , and  $w^*$  are obtained by time averaging the velocity components  $u$ ,  $v$ ,  $w$ , which are the axial, lateral and vertical velocities with respect to the aerodynamic coordinate system and relating them to the inflow velocity. The time averaging is symbolized by an overbar:

$$u^* = \bar{u}/U_\infty, v^* = \bar{v}/U_\infty, w^* = \bar{w}/U_\infty. \quad (2.8)$$

The local cross flow velocity  $V_g$  is obtained by

$$V_g = \sqrt{\bar{v}^2 + \bar{w}^2} / U_\infty. \quad (2.9)$$

Vortical flows are characterized by the rotation vector  $\vec{\omega}$ :

$$\vec{\omega} = \nabla \times \vec{u}. \quad (2.10)$$

The axial dimensionless vorticity  $\xi$  is obtained by relating the axial component of  $\vec{\omega}$  to the inflow velocity  $U_\infty$  and wing half span  $b/2$ ,

$$\xi = \left( \frac{\partial \bar{w}}{\partial y} - \frac{\partial \bar{v}}{\partial z} \right) \cdot \frac{b/2}{U_\infty}. \quad (2.11)$$

The mean of the squared velocity fluctuation values marked with an apostrophe symbol are obtained by

$$\begin{aligned} \overline{u'^2} &= \lim_{T \rightarrow \infty} \frac{1}{T} \int_{t_0}^{t_0+T} [u(t) - \bar{u}]^2 dt \\ \overline{v'^2} &= \lim_{T \rightarrow \infty} \frac{1}{T} \int_{t_0}^{t_0+T} [v(t) - \bar{v}]^2 dt \\ \overline{w'^2} &= \lim_{T \rightarrow \infty} \frac{1}{T} \int_{t_0}^{t_0+T} [w(t) - \bar{w}]^2 dt \end{aligned} \quad (2.12)$$

The root mean square of the fluctuation values related to the freestream velocity  $U_\infty$  defines the turbulence intensity

$$Tu = \frac{\sqrt{1/3 \cdot (\overline{u'^2} + \overline{v'^2} + \overline{w'^2})}}{U_\infty} \quad (2.13)$$

and its Cartesian components

$$Tu_x = \frac{\sqrt{\overline{u'^2}}}{U_\infty}, Tu_y = \frac{\sqrt{\overline{v'^2}}}{U_\infty}, Tu_z = \frac{\sqrt{\overline{w'^2}}}{U_\infty}. \quad (2.14)$$

The turbulence intensity of the freestream velocity  $Tu_\infty$  at the inflow is a parameter for a wind tunnel's flow quality and a boundary condition parameter for the inflow of CFD computations. The vertical turbulence intensity component  $Tu_z$  of the flow in the vicinity of the CTA's tail is a parameter to evaluate horizontal tail buffet.

### 2.3.3 Airfoil Aerodynamics

Airfoils are wing sections at span wise positions. Pressure and friction forces act on wings in air flow. The pressure distribution on the wing surface can be regarded as being composed of one two-dimensional pressure distribution per airfoil. Airfoils for CTA are designed to maximize the aerodynamic efficiency  $(L/D)_C$  of transonic cruise flight. This is done by optimizing the design of the airfoils' contour and, consequently, the resulting pressure distribution of the cruise flight design point conditions. Figure 2-11 illustrates typical pressure distribution of a supercritical cruise wing airfoil.

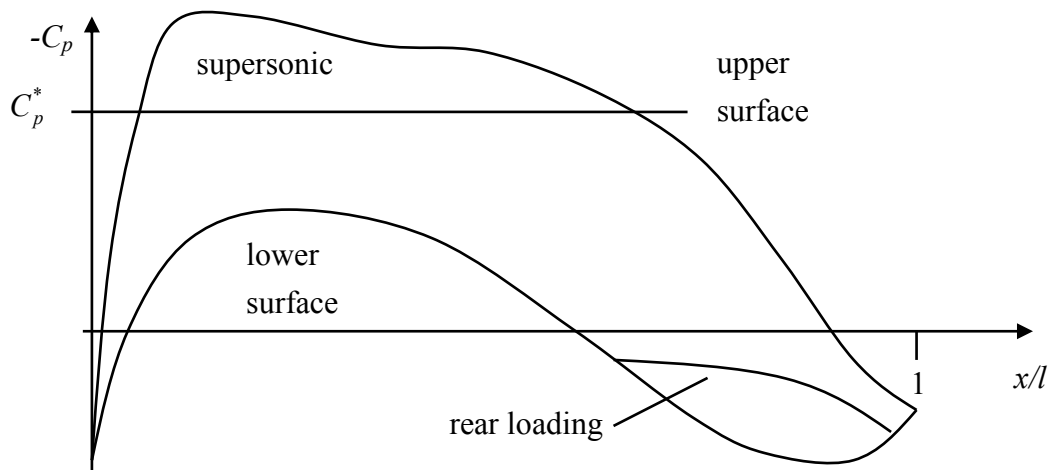


Figure 2-11: Example of typical pressure distribution of a transonic cruise airfoil [27].

The integral value of the pressure and shear forces over the wetted area gives the resulting force  $R$ . It is decomposable into the streamwise component, drag  $D$ , and the component perpendicular to the freestream (velocity vector), lift  $L$ .

### 2.3.4 Drag Decomposition

Drag can be related to production mechanism. It may also be divided into components in other ways. There is sometimes confusion around the terminology, since several effects contribute to each of the drag components. The definition used in this work is as follows: Overall drag is split into zero lift drag  $C_{D0}$  and lift-dependent drag  $C_{DL}$ :

$$C_D = C_{D0} + C_{DL} \quad (2.15)$$

#### *Zero Lift Drag*

Zero lift drag  $C_{D0}$  is the drag at  $C_L = 0$  and is approximately independent from the lift coefficient per configuration. It can be further subdivided into profile drag, wave drag and interference drag. Profile drag consists of skin friction drag, vortex drag due to wing twist, drag due to fuselage upsweep, drag due to control surface gaps, nacelle base drag, and pressure drag. Skin friction drag arises from the shear stresses at the surface of a body due to viscosity. It accounts for most of the drag of a transport aircraft in cruise.

Parasite drag refers to the grouping of non-lifting skin friction and pressure drag, fuselage upsweep drag, control surface gap drag, and nacelle base drag. Air brakes primarily aim to increase parasite drag by creating additional pressure drag.

Wave drag is the increment in drag associated with increases in Mach number and is produced by the presence of supersonic regions at transonic speeds, which does not apply to CTA approach flight phase.

#### *Lift-Dependent Drag*

The largest part of lift-dependent drag is covered by induced drag, which is created by wake vortices. The energy this phenomenon expends is directly responsible for the induced drag. But it also includes lift wave drag and steering drag, together with lift-dependent components of skin friction and pressure drag. The induced drag coefficient  $C_{Di}$  is calculated by

$$C_{Di} = \frac{C_L^2}{\pi \cdot AR \cdot e} \quad (2.16)$$

where  $AR$  is the aspect ratio, and  $e$  the Oswald factor. It can be deduced from Eq. (2.16) that the contribution of induced drag to overall drag can be very large for CTA at high-lift, low-speed flight conditions. One can take advantage of this high induced drag for steep approach because the lift-to-drag ratio decreases approximately linearly at low speeds.

Another drag item that is sometimes considered separately is trim drag, the drag increment associated with the tail load (HTP negative lift) required to trim the aircraft in pitch. Trim drag does not appear in this investigation, because no HTP was used in the wind tunnel experiments or computational investigations. Drag coefficient increments are

commonly given in drag-count units equaling an increment in drag coefficient of  $\Delta C_D = 10^{-4}$  [96]. A lift count corresponds to  $\Delta C_L = 10^{-3}$ .

The two lift over drag polar comparisons in Figure 2-12 and Figure 2-13 clarify the different drag components. There are two polars in each Figure which qualitatively show the two types of air-brakes' modes of functioning in comparison with a baseline deployment using no air-brakes. Figure 2-12 illustrates the functioning of a CTA's conventional spoiler (CS). Figure 2-13, the same, with an improved air brake. The CS reduces  $C_{L,max}$  and increases  $C_{D0}$ . Due to the reduction in lift the new  $C_{L,app}$  with CS has to be decreased. The corresponding relation  $C_{L,app} \leq C_{L,max}/1.23^2$  is reviewed in subsection 2.4.2. One can see that, as a result, the increase in  $C_{D0}$  is partly cancelled out by the reduced  $C_{Di}$  due to lift loss.

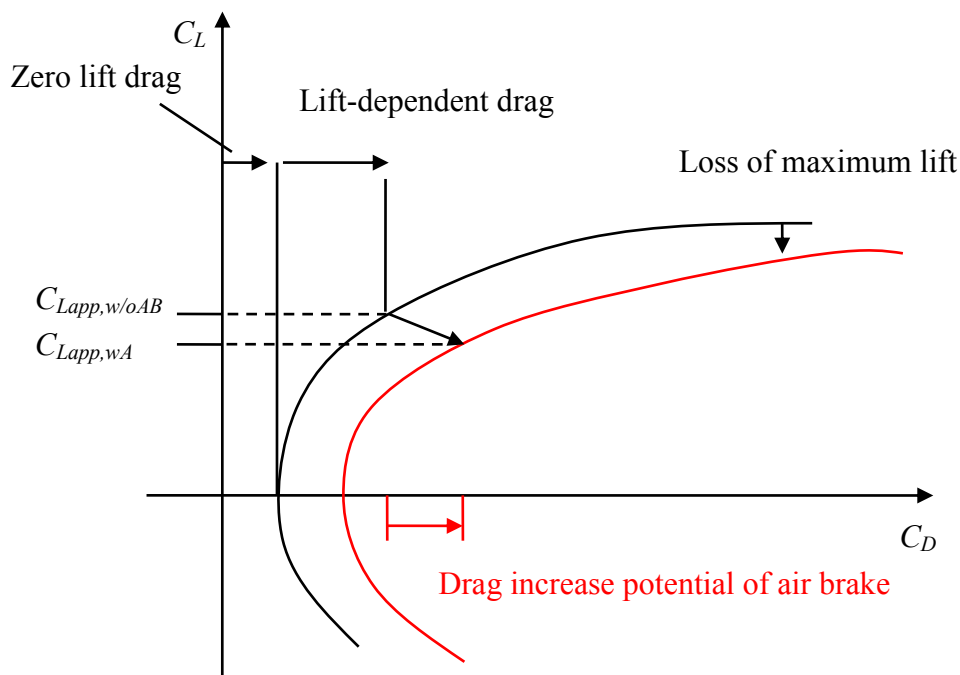


Figure 2-12: Schematic lift over drag polar of baseline high-lift configuration and CS-configuration.

The improved air-brake concept, by contrast, increases  $C_{L,max}$  leading to an increased  $C_{L,app}$  that benefits from an increase in  $C_{Di}$  in addition to the increase in  $C_{D0}$ .

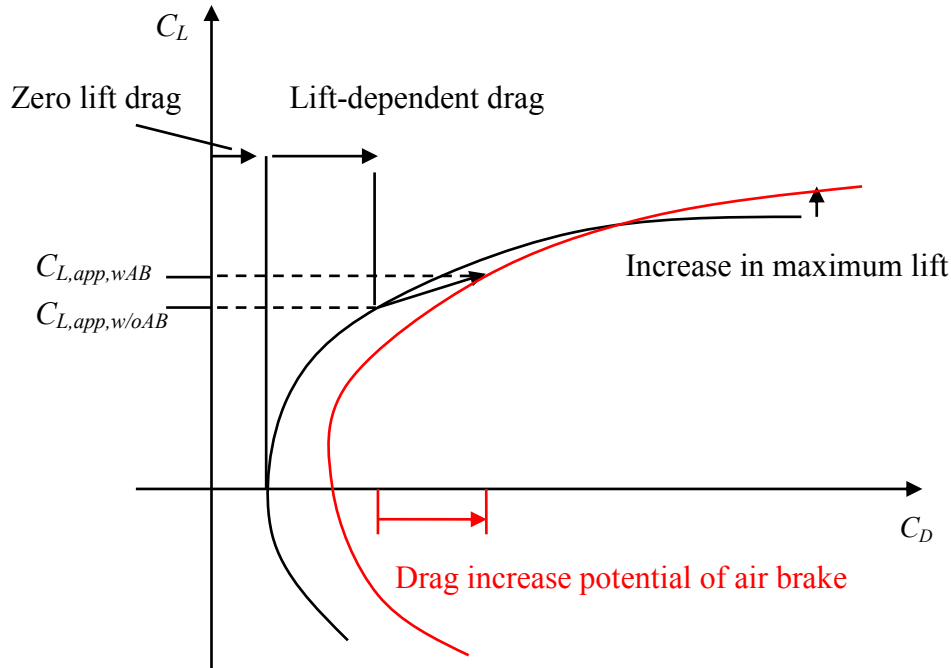


Figure 2-13: Schematic lift over drag polar of baseline high-lift configuration and improved air-brake configuration.

The relative contribution of lift-dependent drag and zero lift drag to the overall drag dependent on flight velocity is illustrated in Figure 2-14.

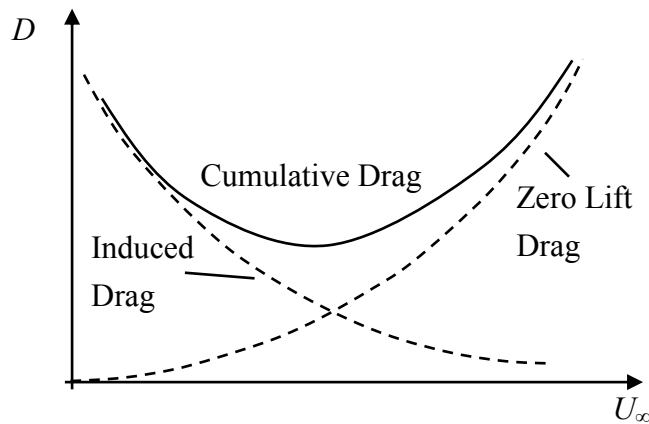


Figure 2-14: Drag composition dependent on flight velocity.

### 2.3.5 High-Lift Aerodynamics

When deploying leading edge and trailing edge high-lift devices simultaneously, the existing cruise flight airfoil pressure distribution (Figure 2-11) is reshaped, generating three suction peaks; one at the leading edges of each element. Each suction peak is followed by a recompression region extending to the respective trailing edge. This is illustrated in a schematic graph presenting pressure distribution over chord length, Figure 2-15.

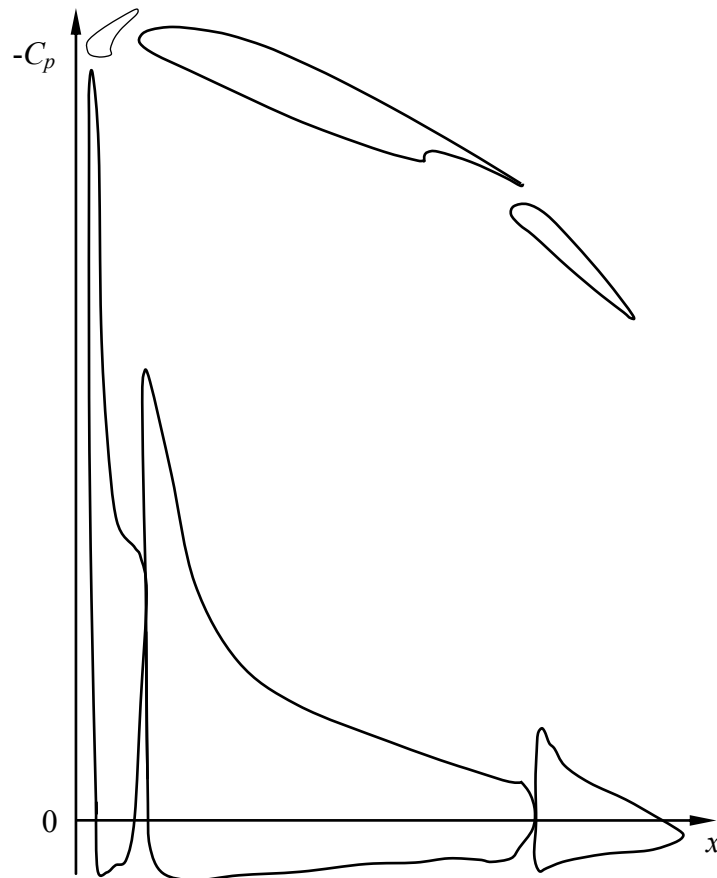


Figure 2-15: Schematic pressure distribution for a generic high-lift configuration.

The primary aerodynamic function of the leading edge devices is to decrease the suction peak magnitude at the leading edge of the main wing relative to the suction peak of the cruise airfoil at the same angle of attack. It also has positive effects on the main wing's boundary layer, which result in a decrease in the gradient of the recompression behind the suction peak and lead to another deferral of flow separation on the main wing's upper surface to a higher angle of attack  $\alpha_{max}$  and a higher maximum lift coefficient  $C_{L,max}$ . When deploying a leading edge device, the lift curve slope  $C_{L\alpha}$  is approximately retained, compared to the cruise airfoil.

The basic aerodynamic functional mode of a plain flap is to increase the section camber. This is also the case for the Fowler flap, which also increases the wing area, leading to an increase in zero-lift coefficient  $C_{L0}$ . For the Fowler flap, this is obtained in combination with a positive effect on the Fowler Flap's suction side boundary layer by the high energy flow coming from the main wing's lower side through the gap between main wing and Fowler Flap. Because the lift curve slope  $C_{L\alpha}$  is approximately retained when deploying the trailing edge devices, these effects lead to an upward shift in the lift curve. A combined deflection of both leading edge and trailing edge devices leads to an approximately linear accumulation of the effects of both types of device. Figure 2-16 illustrates the effects of a Leading Edge Slat and a Fowler Flap on the lift coefficient

curve. More details on the aerodynamic functional modes of high lift elements can be found, for instance, in Ref. [159].

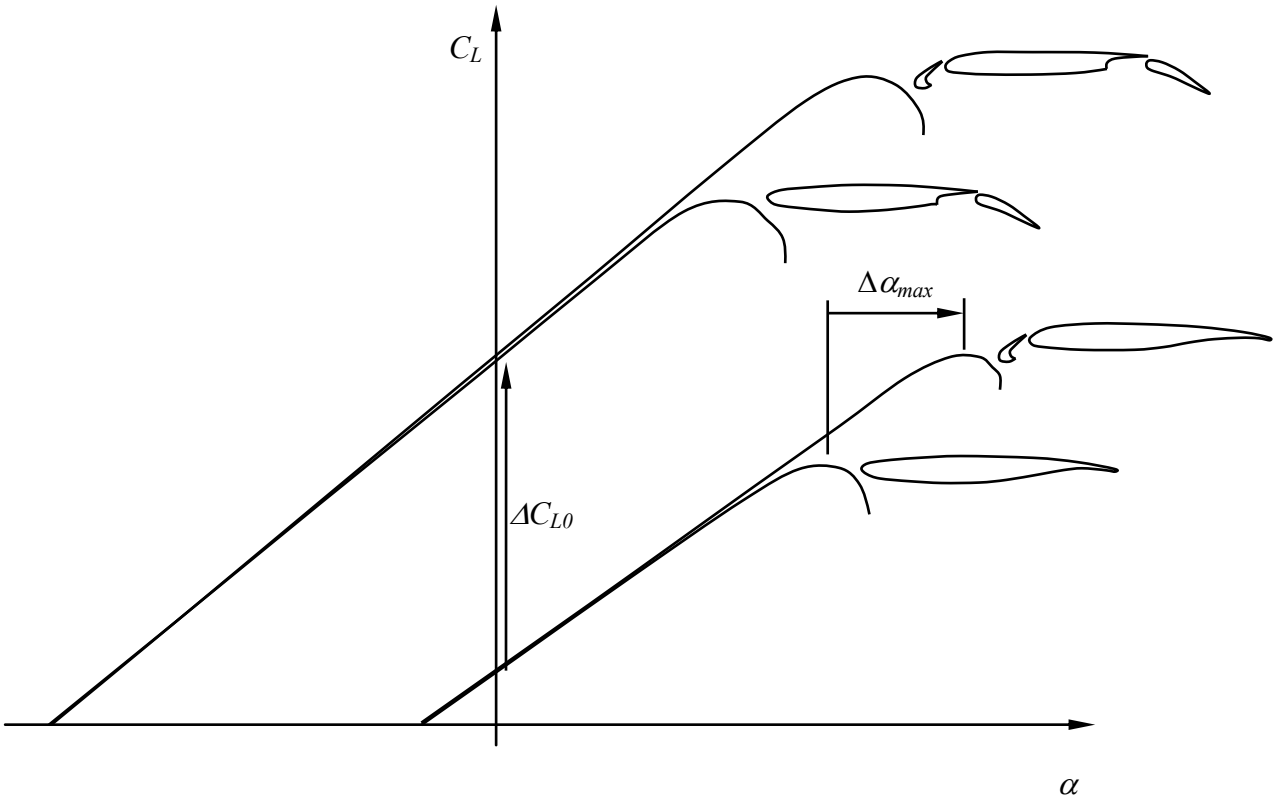


Figure 2-16: Effect of Leading Edge Slat and Fowler Flap on lift curve.

There are usually at least two different high-lift settings for the CTA flight-phases of takeoff and approach. In the approach setting, the Fowler Flaps are generally deployed at a higher rotating angle  $\delta_F$  than in the takeoff setting. The two high-lift settings also have different aerodynamic objectives to that of cruise configuration. For the approach configuration the objective is to obtain the highest possible maximum lift coefficient  $C_{L,max}$ , while the drag coefficient  $C_D$  is constrained to a sufficiently high value. In contrast, a maximized lift over drag ratio  $L/D$  is the main objective of the takeoff configuration so as to fulfill the legal requirements of the second climb segment [67], [171].

From here on, this work focuses solely on the approach setting. Assessment and improvement of the approach high-lift setting's properties requires the identification, localization, and understanding of the effects and flow features that determine the maximum attainable lift coefficient  $C_{L,max}$ . For high-aspect ratio wings,  $C_{L,max}$  is directly related to the occurrence of flow separation on the wing. When increasing the angle of attack  $\alpha$  above a certain value, flow separation covers a sufficiently large portion of the wing and overcompensates the lift gain in portions of the wing where the flow remains attached. This situation is called stall.

Rudnik et al. state in Ref. [149] that the aerodynamic characteristics of CTA high-lift configurations pose a great challenge to the reliability of simulations, whether created in a

wind tunnel or using numerical methods. The reason for this is the variety of different flow phenomena and the geometric complexity of the high-lift configuration. Important flow phenomena are pressure- and geometry-induced flow separations, interactions of wall bounded and free shear layers, strong pressure gradients, and high flow curvature. The aerodynamics are very sensitive to small variations in the gap size and overlap between the various elements [171]. The phenomena also have an impact on each other. Regarding this matter, Haines states in [90] that ‘in the competitive state of aircraft design it is not sufficient to avoid adverse aerodynamic interference; one must positively aim for favorable interference. Experience shows that this is a realistic aim’ and that ‘this is perhaps the most severe challenge to the aerodynamicist’.

The high-lift airfoil flow phenomena and flow interaction mechanisms that appear at an approach angle of attack have been investigated experimentally in [126]. They are illustrated in Figure 2-17 by a Schlieren flow visualization and discussed below in streamwise order.

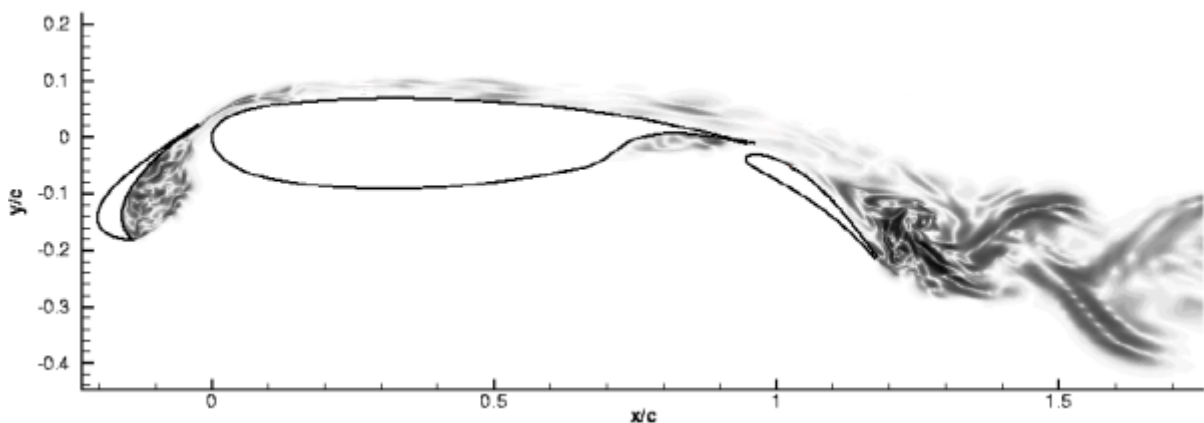


Figure 2-17: Illustration of high-lift flow phenomena with Schlieren flow visualization at approach angle of attack [110].

On the bottom side of the slat, vortices are shedding from the lower side slat leading edge, where the flow separates, creating a highly unsteady recirculation region in the slat cove. In the slat region most of the unsteadiness develops in the shear layer between the low velocity fluid in the recirculation region and the high velocity fluid that passes through the gap between slat trailing edge and main wing leading edge [116]. The top and bottom flow of the slat merges at the slat trailing edge and form the slat wake shear layer. The slat wake intensity is a measure of the slat source noise [157]. On the top and bottom surfaces of the main wing, boundary layers develop. The top boundary layer and the slat wake gradually fuse in a mixing layer. On the main wing’s bottom side, the flow separates at the front face of the flap cove and a recirculation zone is formed in the flap cove. It is here, that the bottom boundary layer arises and gradually fuses with the main wing wake flow in the flap mixing layer. A trailing edge flow separation may occur on the flap, unless it is suppressed

through the use of an active flow control, for example, investigated by Becker et al. [19], among others. In contrast to the CTA takeoff setting, where there is little or no separation zone, a CTA approach configuration applies a high flap deflection angle or flap separation zone to the majority of the flap, resulting in a large, highly unsteady turbulent wake region extending behind the flap. This leads to a strong increase in drag compared to the non-separated take-off flap setting. Unsteady excursions of the flap separation point cause the overall lift to change.

For higher, near stall angles of attack, the main difference in flow topology is that the flow detachment at the trailing edge of the slat mitigates or even completely disappears. Based on the established knowledge of high-lift flow phenomena detailed in this subsection, chapter 6 presents these phenomena in more detail, focusing on this work's specific configurations.

### 2.3.6 Stall Condition

As stated above, the main objective of the CTA approach configuration is to raise the maximum lift coefficient  $C_{L,max}$ . This is even more the case for steep approach.  $C_{L,max}$  is limited by stall at a certain angle of attack  $\alpha_{max}$ . Flaig et al. in [68] show the two typical areas that are endangered by flow separations for beginning stall conditions of CTA: top side of the wing behind the fuselage wing junction and top side of the wing behind the engine nacelles. The separation tendency interacts here with vortex systems created by the inboard slat end and the engine nacelle strakes (ENS). ENS are specifically installed to improve this separation tendency on the wing behind the nacelles. The ENS installed on the model under investigation are discussed in subsection 3.4.1. For a wing without twist, there would also be a separation tendency on the top side of the aileron. This is caused by the tapering of the wings due to the high local outboard aerodynamic loading that is exacerbated by backward sweep. Aileron flow separation must be avoided under all circumstances due to the categorical regulations regarding the need for lateral manoeuvrability. Actual wing designs take account of such circumstances by a design with wing twist to make the wing root stall before the wing tips. The separation zones and interacting vortex systems are illustrated in Figure 2-18.

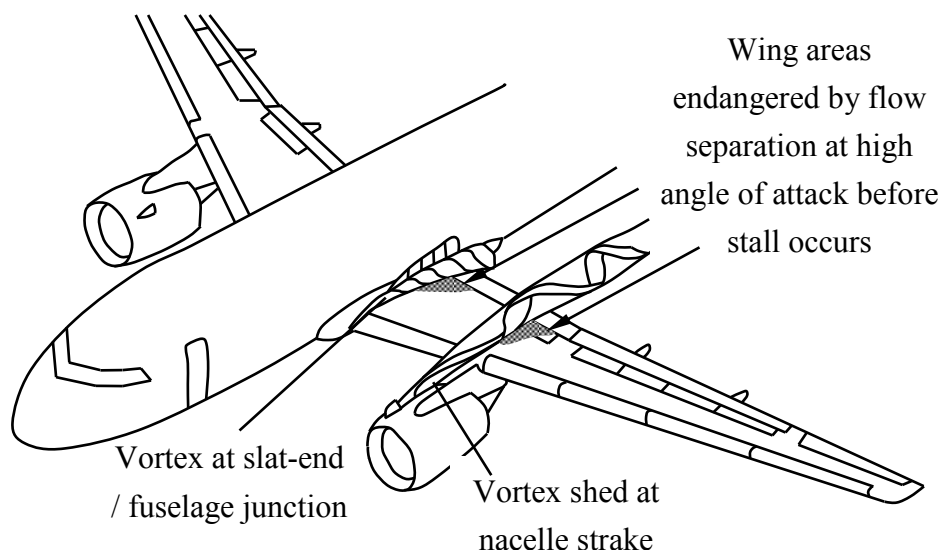


Figure 2-18: Areas of flow separations for CTA and interacting vortex systems.

The phenomenon Pitch-Up usually accompanies the stall of a CTA's wing. When flow separation starts at the wingtips, this results in a considerable forward shift of the center of pressure and consequently in an increase of the pitching moment [41]. Expressed the other way around: observation of an increase in pitching moment near  $\alpha_{max}$  is a clear indication of wing tip stall.

### 2.3.7 Air Brake Aerodynamics

Contrary to the high-lift systems discussed above, where the main objective is to increase the lift coefficient  $C_L$ , the main objective of air brakes is to increase the drag coefficient  $C_D$  and thereby decrease the glide ratio  $L/D$ . The primary means by which virtually all air-brake types achieve this drag increase is by creating parasite pressure drag through intentional flow separation that leads to a low pressure region at the trailing part of the air brake.

#### *Spoiler Aerodynamics*

Figure 2-17 illustrates the flow topology of a high-lift airfoil with deployed conventional spoiler (CS).

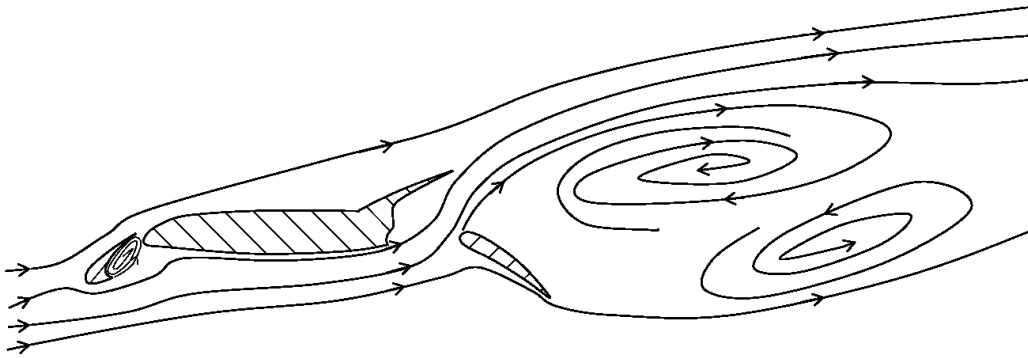


Figure 2-19: Schematic flow topology visualization by streamlines of a high-lift profile with deployed spoiler.

The main wing upper flow is deflected upwards by the CS. In addition to this, the lower side main wing flow is deflected upwards behind the trailing edge of the main wing. It is directed into a complex low pressure zone behind spoiler and Fowler flap containing recirculation bubbles. This happens because the lower side main wing flow is no longer guided by the wing shroud as the shroud has been deflected upwards to form the CS. This also leads to a change in the inflow to the flap, leading again to a stronger separation of the flap flow, located further upstream.

## 2.4 Flight Mechanics

After looking into CTA thrust and assessing its magnitude for approach settings in the following subsection, it becomes feasible to neglect approach thrust when introducing the flight mechanical parameters necessary to evaluate the steep approach performance of the devices under investigation. The theoretical background for longitudinal static stability is then provided as this can potentially be affected by deployment of air brakes.

### 2.4.1 Engine Thrust Ratings

Engines are certified to deliver specific standard thrust ratings. A rating is a selectable predefined power setting appropriate for a particular flight condition. Rating terminology differs between civil and military aircraft, reflecting the different requirements. The following thrust ratings are used for CTA: Maximum Takeoff Thrust (MTO), Maximum Continuous Thrust (MCT), Maximum Climb Thrust, Maximum Cruise Thrust, Flight Idle Thrust, High or Approach Idle Thrust (HAI), and Ground Idle Thrust. The aircraft manufacturer and engine supplier must declare two of these as principal ratings to the certifying authorities since these define the safe limits of operation of the engine and aircraft. These are the MTO and the MCT ratings. The relevant engine thrust rating for approach is HAI and is much lower than MTO. In the final phase of approach it is important to be able to provide high thrust rapidly if required. To ensure this, there are maximum response time requirements in FAR part 25 and part 33 for MTO thrust to be reached from HAI thrust if the landing has to be aborted. This requires the engine to run at

a higher speed than is ideal for approach. In Ref. [71] is shown that a typical CTA's HAI thrust level is about 5% of the MTO thrust level.

#### 2.4.2 Final Approach Conditions

The final approach stage is regarded with the thrust set and maintained at HAI. In this paragraph's account of approach flight mechanics thrust force has been excluded because HAI ranges are around one order of magnitude lower than other occurring forces and therefore can be neglected. The stabilized approach phase can be considered a steady state. Figure 2-20 shows the equilibrium of forces at work in this phase.

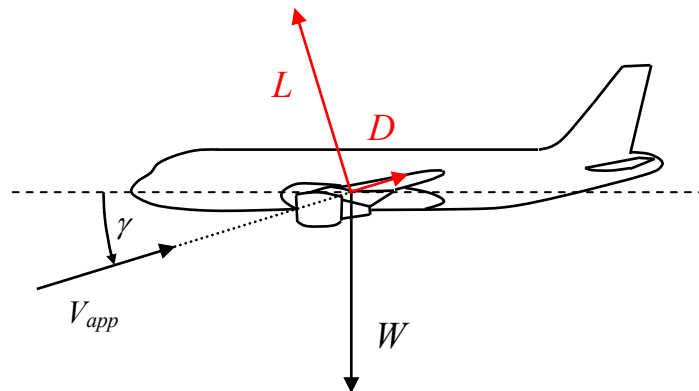


Figure 2-20: Static equilibrium during a steady approach excluding the approach idle thrust force.

The descent velocity  $V_s$  is defined as

$$V_s = V_{app} \sin(\gamma). \quad (2.15)$$

We can now use the trigonometrical dependency between  $C_L$ ,  $C_D$  and  $\gamma$  apparent in Figure 2-20. Presuming typical lift to drag ratios for a transport aircraft high-lift configuration of  $L/D \sim 10$  and, thus,  $C_D \ll C_L$ ,  $\sqrt{C_L^2 + C_D^2} \approx C_L$ , leads to

$$\sin(\gamma) = \frac{C_D}{\sqrt{C_L^2 + C_D^2}} \approx \frac{C_D}{C_L}. \quad (2.16)$$

Using the same approximation, the approach velocity  $V_{app}$  can be calculated by

$$V_{app} \approx \sqrt{\frac{2}{\rho}} \sqrt{\frac{W}{S}} \frac{1}{\sqrt{C_L}}. \quad (2.17)$$

Finally, the descent velocity  $V_s$

$$V_s = \sqrt{\frac{2}{\rho}} \sqrt{\frac{W}{S}} \frac{1}{\sqrt{C_L}} \sqrt{\frac{C_D^2}{C_L^2 + C_D^2}} \approx \sqrt{\frac{2}{\rho}} \sqrt{\frac{W}{S}} \frac{C_D}{C_L^{3/2}} \quad (2.18)$$

and the descent angle  $\gamma$

$$\gamma \approx \sqrt{\frac{2}{\rho}} \sqrt{\frac{W}{S}} \frac{C_D}{C_L^{3/2}} \frac{1}{V_{app}} \approx \frac{C_D}{C_L} \quad (2.19)$$

is obtained. On the right hand side of Eqs. (2.17) and (2.18) one can distinguish the first two factors as fixed values. The density is prescribed by the atmospheric conditions. The second term is determined by the wing loading  $W/S$ , an aircraft configuration parameter. The proportions of the aerodynamic lift and drag coefficients define the other factor. These can be manipulated by means of high-lift device configuration and setting.

The approach velocity  $V_{app}$  is limited to 1.23 times the level flight stall velocity  $V_{st}$ , defined in FAR part 25/125 [61] and in CS part 25/125 (former JAR25) [36]:

$$V_{app} > 1.23 \cdot V_{st} \quad (2.20)$$

With the small-angle approximation for  $\gamma$ , this leads to

$$\frac{W}{S} \approx C_{L,app} \frac{\rho}{2} V_{app}^2 = C_{L,max} \frac{\rho}{2} V_{st}^2 \Rightarrow C_{L,app} \leq \frac{C_{L,max}}{1.23^2}. \quad (2.21)$$

Thus, we reach the maximum approach lift coefficient  $C_{L,app,max}$  directly from the respective maximum lift coefficient  $C_{L,max}$ . The Minimal Velocity Approach Point (MVAP) is defined for the angle of attack  $\alpha$ , where  $C_L = C_{L,max}/1.23^2$ . Using a baseline configuration (BL) at the MVAP as a reference, indicated by the subscript ‘ref’, three operational parameters arising from Eqs. (2.17), (2.18), and (2.19) can be defined:

$$\frac{V_{app}}{V_{app,ref}} - 1 = \frac{\sqrt{C_{L,ref}}}{\sqrt{C_L}} - 1 \quad (2.22)$$

$$\frac{V_S}{V_{S,ref}} - 1 = \frac{C_{L,ref}^{3/2}}{C_{D,ref}} \frac{C_D}{C_L^{3/2}} - 1 \quad (2.23)$$

$$\frac{\gamma}{\gamma_{ref}} - 1 = \left( \frac{C_L}{C_D} \right)_{ref} \frac{C_D}{C_L} - 1 \quad (2.24)$$

These parameters are dedicated to evaluating the relative steep approach performance of different air-brake configurations. Of the three, the descent parameter  $V_S/V_{S,ref} - 1$  is limited to a maximum. This maximum must be equal to the standard approach’s magnitude for two reasons. First, following Dobrzynski, passenger comfort should limit descent velocity to approximately  $V_{S,max} = 1100 \text{ ft/min} = 5.59 \text{ m/s}$  [54]. Second, FAR part 25/723 [62] defines  $V_{S,max} = 12 \text{ ft/s} = 3.66 \text{ m/s}$  as a maximum for the landing descent velocity for landing gear stability reasons. Neither reason is compelling: The first is not related to any

regulation framework, while the second could be met, for example, by a two segment landing strategy. Such a strategy would comprise a steep approach followed by a switch to standard approach with lower descent velocity close to touchdown [122].

More important than  $V_S/V_{S,ref} - 1$  is the descent angle parameter  $\gamma/\gamma_{ref} - 1$  defined in Eq. (2.24). It must be maximized to achieve the steepest approach path possible. This can be obtained by maximizing the descent factor  $C_D / C_L^{3/2}$ , as well as by minimizing  $V_{app}$ .

### 2.4.3 Longitudinal Static Stability

The ease of maintaining static trim is related to a property of the equilibrium state, which is known as static stability. The static stability of any equilibrium state is related to the response of the system to any small disturbance in the equilibrium state. If a system in an equilibrium state returns to equilibrium following a small disturbance, is said to be a stable equilibrium [137]. To ensure static pitch stability the following inequation applies in the relevant region around  $C_{L,app}$  with  $C_{m0} > 0$

$$dC_m / dC_L < 0. \quad (2.25)$$

To evaluate the influence of the air-brake types on the static pitch stability, the moment curve slope  $dC_m/dC_L$  between the different investigated configurations is compared in the results chapter 5.

## 2.5 Unsteady Aerodynamics

The use of wing based air brakes in flight is often limited, due to the turbulent airflow that develops behind them and causes noticeable noise and vibration. This again may cause discomfort to passengers. More severely it may lead to horizontal tail plane (HTP) buffet. Thus, in this work, the aerodynamic analysis of the models' wing wake is primarily used to deliver input data for tail flutter analysis. The foundation for the later discussion of these unsteady aerodynamic wake effects is laid in this section.

### 2.5.1 Strouhal Number

All bodies moving through air trail an unsteady wake. For blunt bodies, for instance a cylinder, this phenomenon is called vortex shedding. Investigations into vortex shedding were initiated by Strouhal, who concentrated on the dominant frequencies found in the wake of circular cylinders [164]. He introduced the Strouhal number  $Sr$  (Eq. 2.3) to characterize the dependency of the wake's dominating characteristic frequency  $f$  on the configuration parameters inflow velocity  $U_\infty$  and cylinder diameter  $d$ .  $Sr$  is also dependent on  $Re$  to a minor extent. This dependency is illustrated in Figure 2-21 for circular cylinders.

Configurations which are closer to typically flat shaped air-brake geometries have also been investigated: Norberg in [132] investigated the wake of rectangular cylinders

having angles of incidence relative to the upcoming flow; and Chen et al. in [37] investigated the Strouhal numbers of inclined flat plates.

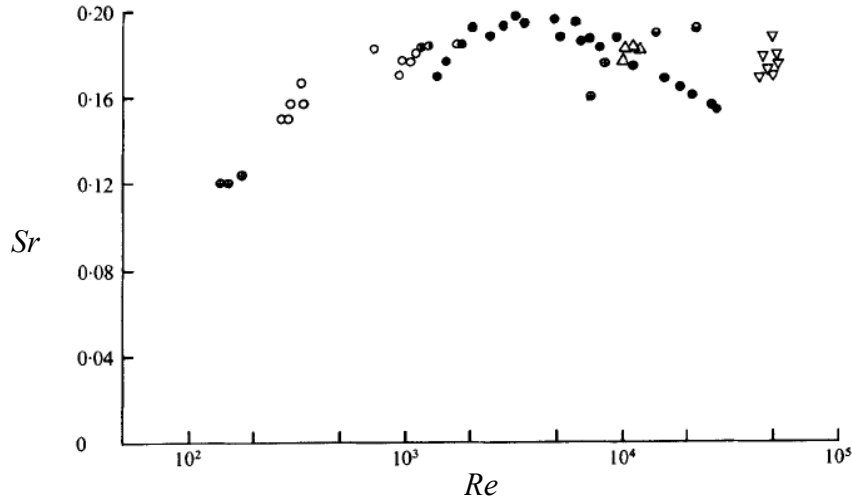


Figure 2-21: Dependency of  $Sr$  on  $Re$  in wake of circular cylinder [86].

### 2.5.2 Buffet

The general definition of buffet is a shaking of airplane surfaces. One distinguishes between three types of buffet based on their causes. The first is an excitation by turbulent incoming airflow (dynamic response problem). The second is an excitation by partially detached flow on the wing at high angles of attack and is called Low Speed Buffet. Here, the flow detachment moves periodically upstream and downstream. The third is transonic buffet, also called High Speed Buffet. Here the moving shock wave interacts with the boundary layer leading to an oscillating separation. Of exclusive relevance for this work is the first cause, where the turbulent wake flow of the wing – including the air brake and high-lift system – excites the HTP, potentially leading to buffet at the HTP. The wake imparts its energy in the form of turbulent flow and can be characterized by the power spectral density (PSD) of the wake flow. Frequency scaling entails matching model and aircraft Strouhal numbers:

$$Sr_m = \frac{f_m L_m}{U_{\infty, m}} = \frac{f_a L_a}{U_{\infty, a}} = Sr_a \quad (2.26)$$

The impact of the turbulent wake flow on the HTP leads to unsteady pressures on the HTP and subsequently to excitation of its structural modes. The high dynamic response shortens the fatigue life of the impacted structures and potentially damages them. An investigation of the reworking of a glider due to the consequences of tail buffet can be found in Ref. [154]. Investigations in the field of air-brake wake optimization of CTA have been conducted through the research programme AWIATOR [38], among others.

## 3. EXPERIMENTAL METHODS

Despite continuous progress in CFD, wind tunnel tests are still seen as an irreplaceable investigation technology, especially with regard to high-lift design and its complex flow topology, already touched on in subsection 2.3.5. Clarifying the role of the different technologies involved in the contemporary industrial high-lift design process, Reckzeh et al. state in Ref. [146] that initial CFD designs of the high-lift system are validated by wind tunnel tests, with the final performance of the real aircraft derived by extrapolation.

All circumstances, methods and materials applied to the wind tunnel tests performed within the framework of this investigation are covered in this chapter. It outlines the general boundary conditions of performing wind tunnel simulations before introducing the measurement methods used, the test facility, and the wind tunnel model – including the air-brake elements under examination. The chapter closes with an account of the actual experimental setup for the tests and the analysis methods used to post process the data gained.

### 3.1 Aerodynamic Simulation in Wind Tunnel

In wind tunnel simulations geometrically similar but downscaled models are used to investigate the aerodynamics of a real aircraft. While, the real aircraft moves through approximately still air, the stationary, experimental model is exposed to the air circulated through the wind tunnel. Common factors that affect wind tunnel simulations include wind tunnel blockage or creating a static pressure gradient in the test section. The effect of these factors on the aerodynamic coefficients can be counteracted by correction methods. No correction methods are applied in this investigation as the absolute values of the aerodynamic coefficients are not needed when evaluating air-brake configurations relative to the baseline configuration. For the experimental investigations conducted it was assumed that 1) low speed wind tunnel tests and 2) a half-model can adequately simulate real aircraft high Reynolds-number aerodynamics. These two assumptions are addressed in the following.

#### 3.1.1 Low-Speed Wind Tunnel Simulation of High Reynolds-Number Problems

The approach of CTA is a high Reynolds-number flow situation. Nevertheless, due to budget and availability constraints the wind tunnel tests conducted within the frame of this investigation were conducted exclusively in a low Reynolds number wind tunnel facility. Within the European High-Lift Projects (EHLPI and II), CTA high-lift configurations were tested at a range of Reynolds-numbers [149]. The range started at  $Re = 6.5 \cdot 10^6$ ,

which is larger than the one achieved in this investigation, but still much lower than those found in real flight. The range went up to the value of  $Re = 25.5 \cdot 10^6$ , which is a typical value for approaching CTA. The EHLP configuration with the highest degree of geometric complexity, designated as ‘stage 3’, is comparable in its level of details to the wind tunnel model used for this investigation. Drag over lift polars of stage 3 wind tunnel tests under different Reynolds numbers are compared in Figure 3-1.

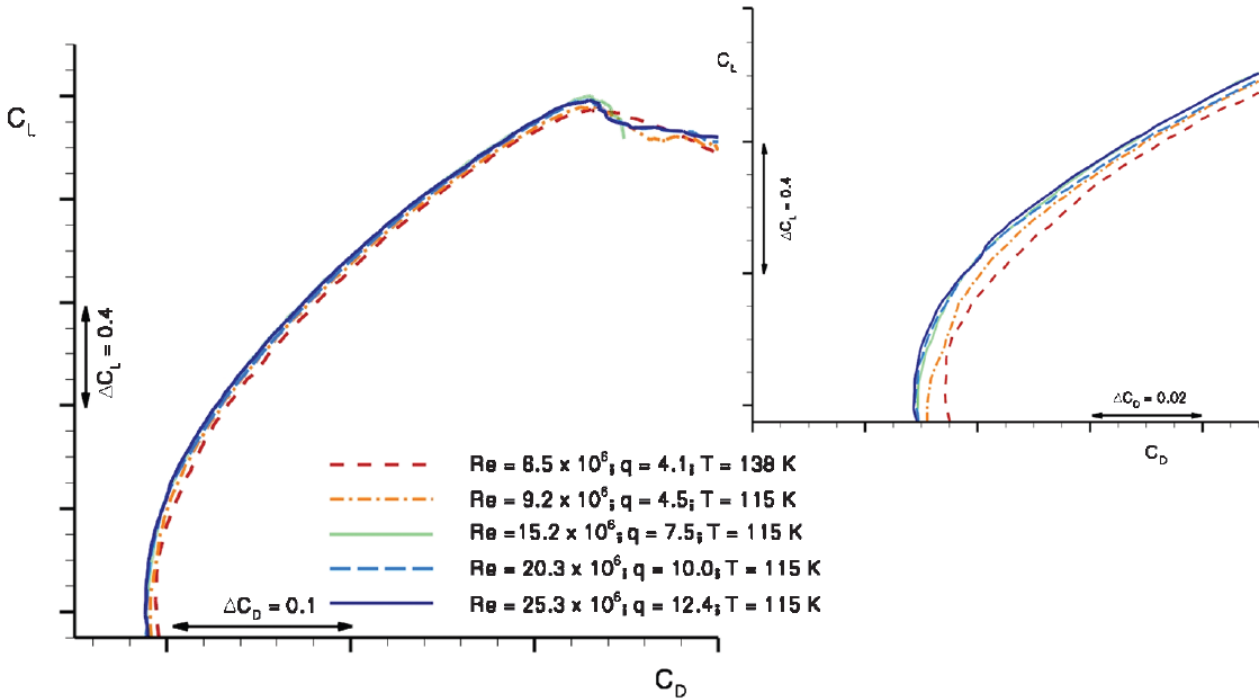


Figure 3-1: Drag polars for different  $Re$  numbers of CTA EHLP configuration stage 3 [149].

The EHLP test results suggest that for moderate angles of attack the lift coefficient  $C_L$  is nearly independent from  $Re$ , whereas the drag coefficient  $C_D$  shows a much higher dependency on  $Re$  in the moderate  $\alpha$ -region. The drag coefficient  $C_D$  is consistently overpredicted by the lowest  $Re = 6.5 \cdot 10^6$  test compared to the highest  $Re = 25.5 \cdot 10^6$  test by  $\Delta C_D \approx 0.006$  over the moderate angles of attack range. For the stall area, the maximum lift coefficient  $C_{L,max}$  is underpredicted by the low  $Re$  test by about  $\Delta C_{L,max} \approx 0.06$ . These errors result in error percentages of  $\sim 2.5\%$  for the  $C_D$  and  $C_{L,max}$  predictions if one takes the typical published values of the aerodynamic coefficients of approaching aircraft [171]. The characteristic of the polar curve is also very different for the various  $Re$  numbers in the stall region. The curve is rounded off for the low  $Re$  test compared to a more edged shape for the high  $Re$  test. Thus, the aerodynamic characteristics of both  $C_{L,max}$  and  $L/D$  for moderate  $\alpha$ , so important in evaluating the steep approach performance, are affected to some extent by the Reynolds number. From the results of the EHLP investigations one can derive that the experimental results of this investigation overpredict absolute  $C_D$  for moderate  $\alpha$  and thereby underpredict  $L/D$  for moderate  $\alpha$ . They ought also to misjudge the exact shape of the stall behavior and the values of  $\alpha_{max}$  and  $C_{L,max}$ . Here, all aerodynamic

coefficients will be evaluated per air-brake case relative to the baseline, namely the case without a deployed airbrake. Following this *modus operandi*, one can assume that the incremental changes in the aerodynamic coefficients following minor changes in the geometry are much more precise compared to the absolute values of the aerodynamic coefficients from the wind tunnel tests. This approach makes the low Reynolds number wind tunnel test a feasible method for this investigation.

Regarding extrapolation of the low Reynolds number wind tunnel test data to free flight conditions, one has to be extremely careful, particularly with regard to stall phenomena, where viscous effects dominate the flow. Nevertheless, in the industrial design process stall characteristics are examined in low-speed wind tunnel tests. For example, the stall characteristics of contemporary aircraft HondaJet were evaluated in low-speed wind tunnel tests in Ref. [75].

To compensate for the effect of a too low Reynolds number to overpredict the laminar boundary layer propagation length, transition roughness bands are used to change the nature of the boundary layer from laminar to turbulent at particular locations on the model surface when conducting low  $Re$  wind tunnel tests. The bands are made from tiny grains of sand embedded in a thin strip of paint. The grains introduce disturbances into the boundary layer which trip the boundary layer flow changing it from laminar to turbulent. All strips are fixed at positions which are representative of the approach flight case of the real CTA. More details about the tripping are given in subsection 3.4.2.

### 3.1.2 Feasibility of Half-Model Measurements

In order to use a model as large as possible for a given wind tunnel test section, a half model was opted for. It allows a larger length ratio of model to real aircraft  $L_m/L_a$  [167], and thereby a convergence of model  $Re_m$  towards real aircraft  $Re_a$ . On the other hand, the aerodynamic characteristics might be compromised to a certain extent by this technique, in particular, regarding the existence of a boundary layer on the reflection plane. Earnshaw et al. in Ref. [56] specifically investigated the feasibility of using a half-model with *péniche* for high-lift wind tunnel tests instead of a full model. They conclude that it is possible to gather appropriate results for stall angle of attack  $\alpha_{max}$  as well as  $C_L$ ,  $C_D$  and  $C_m$  values. They underline that the drag coefficient has a high accuracy in the range of  $\Delta C_D = 15$  drag counts, equaling  $\Delta C_D = 0.0015$ . This is certainly beneficial for an investigation concerning air-brake aerodynamics using similar equipment. Thus, half-model tests are considered feasible for this investigation.

## 3.2 Measuring Methods

Four measurement methods were used in the wind tunnel investigations: Balance measurements serve to obtain the aerodynamic coefficients. Tuft pictures visualize the surface flow topology and complement the CFD results to describe the flow topology

associated with the different configurations. To evaluate the wake flow topology, Stereo Particle Image Velocimetry (PIV) and advanced Constant Temperature Hot-Wire Anemometry (HWA) were the methods of choice.

### 3.2.1 Balance Measurements

By using a six-component balance all three mutually perpendicular Cartesian forces and all three moments around mutually perpendicular axes can be gathered. The challenge for the balance is that it has to accurately present small differences in large forces. Furthermore, the forces and moments vary widely in value.

Wind Tunnel Facility A's (WTA) external six-component balance was used exclusively for this investigation. The balance is a strain gauge balance, capable of measuring all six steady state force and moment components. It is arranged below the test section of WTA and incorporates a bogie, which allows turning of the test object – which is attached to the balance – in the test section's floor plane. In the case of this investigation, the model's fuselage was attached, therefore the bogie enables varying the model's angle of attack  $\alpha$ .

To compensate for the mass forces of each configuration and angle of attack  $\alpha$ , the load for a measurement under wind off conditions was recorded and later subtracted from the actual measurement under wind. The balance's sampling rate is  $f_M = 200$  Hz. For each sub-measurement the balance values are averaged over one second. To obtain the final measurement value the arithmetic mean  $\bar{y}$  is calculated from  $n$  sub-measurements  $y_i$ :

$$\bar{y} = \frac{\sum_{i=1}^n y_i}{n}$$

The parameters for the specific measurement campaigns are detailed in subsection 3.6.1. The operating data of the balance is summarized in Table 3-1. It must be pointed out that the balance's maximum permitted moment around the  $x$ -axis  $M_{x,max} = 700$  Nm limits the freestream velocity for the conducted tests to  $U_\infty = 50$  m/s.

Table 3-1: Operating data of the balance [125].

Balance parameter	
Longitudinal force	$ F_x  < 1500 \text{ N}$
Side force	$ F_y  < 3000 \text{ N}$
Normal force	$ F_z  < 3000 \text{ N}$
Moment around $x$ -axis	$ M_x  < 700 \text{ Nm}$
Moment around $y$ -axis	$ M_y  < 500 \text{ Nm}$
Moment around $z$ -axis	$ M_z  < 700 \text{ Nm}$
Precision of measurements	0.025% (Based on entire measuring range)

### 3.2.2 Tuft Flow Visualization

A relatively simple means for investigating the flow close to a solid wall is the tuft flow visualization. Short tufts are fastened to the surface at one end. The alignment and motion of the freely movable part of the tufts gives some information about the local flow. If the local flow has a low turbulence level and is attached, the tufts indicate the mean direction of the local flow by a still alignment along the direction of the local flow. If the tufts exhibit a floundering unsteady motion, this may be taken as an indicator for the turbulence intensity of the local flow. A more pronounced motion of the tufts, a tendency to lift away from the surface and a reversal of the tuft alignment direction in a direction opposite to the freestream flow direction, may indicate a separated flow regime [124]. By fastening many tufts on a complete surface, the separation line can be identified and the stalling behavior can be characterized by recording the tuft behavior for an incremental increase in the model's angle of attack  $\alpha$ .

Tuft flow visualization has been used successfully in many aerodynamic studies and is mainly used in flight tests as a standard method for in-flight flow visualization [66]. It features in scientific flight test research, such as the the Cranked-Arrow Wing Aerodynamics Project International study [148]. Tuft flow visualization is also common in wind tunnel investigations, for example Ref. [111].

The tufts used in this investigation consist exclusively of white cotton. They are fastened on the model's upper surface by means of a thin transparent adhesive tape. The tufts are arranged onto the model's upper surfaces in span wise rows at constant local chord positions. To capture the findings, photographs were taken with a charge-coupled device (CCD) camera. The parameters of the tuft pictures are summarized in Table 3-2.

Table 3-2: Parameters of the tuft flow visualization.

Parameter	
Tuft material	cotton
Tuft diameter	$d \approx 1$ mm
Length of the tufts	$l = 20$ mm
Lateral/span wise spacing of tufts	$\Delta y = 30$ mm
Mean streamwise position of tuft rows	Slat: $x/l_{Sl} \approx 0.5$
	Flap: $x/l_F \approx 0.6$
	Main Wing: $x/l_{MW} \approx 0.05, 0.3, 0.5, 0.75, 0.95$
CCD camera	Pentax *istDs

Obviously, tufts of the size used and the corrugation caused by fixing them onto the model affect the surface conditions and thus, the flow. However, it is assumed that the global near wall flow characteristics can nevertheless be identified. This is because the diameter of the tufts is low enough to ensure that their geometric extension perpendicular to the surface does not exceed the boundary layer thickness for the most part of the surface.

As a simple means to examine the flow surrounding the model a tuft stick is used. Fixed to the end of this stick is a tuft with a length of  $l \approx 100$  mm. By placing the tuft stick into the flow, the local flow direction and turbulence can be evaluated in the same way as the fastened tufts. Figure 3-2 shows the author using the tuft stick in WTA to examine the flow features.

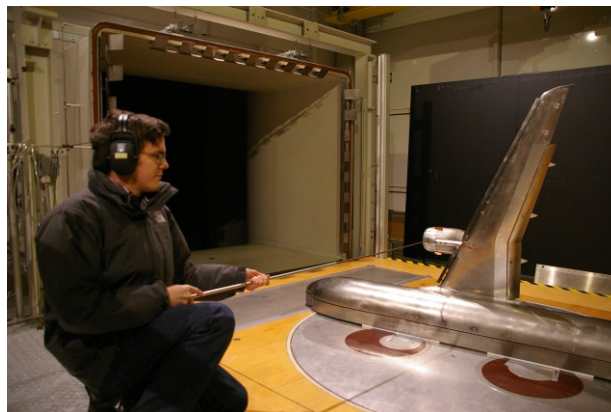


Figure 3-2: Tuft stick used to investigate the flow.

### 3.2.3 Stereo Particle Image Velocimetry

The Stereo Particle Image Velocimetry (Stereo-PIV) system allows one to simultaneously measure the distribution of all three instantaneous velocity components in a planar trapezoidal field perpendicular to the inflow velocity. Because it is an optical measurement

system, no disturbances of any kind are caused by a supporting system. The PIV's mode of operation may be summarized as follows:

A laser device produces a thin vertically expanded laser sheet in the measurement plane. Seeding particles composed of oil are injected into the air flow. The position of the particles in the measurement field, which are illuminated by the laser light, are recorded twice with a short interval between the records by two cameras located upstream and downstream of the measurement plane laterally to the model. By means of cross correlation based on Fast Fourier Transformation, the three-components of the instantaneous velocity distribution in the measurement field can then be computed from the four camera records with a high spatial resolution.

The chosen sampling rate  $f$  of the PIV measurements is the highest possible for this system with  $f = 5$  Hz. A number of  $n = 388$  double image samples are recorded per measurement and camera. From this data both the mean velocity components and the root mean square of the velocity components are obtained. Pseudo turbulence intensities  $Tu_x$ ,  $Tu_y$ ,  $Tu_z$  are then derived from these root mean squares. The measurement field's height is  $\Delta y \approx 170$  mm and its width is  $\Delta z \approx 250$  mm, reflecting the distance of the cameras from the measurement field position as well as the focal length of the camera lenses.

To investigate the near wake of the model's wing, two streamwise wake plane positions  $x_1$  and  $x_2$  were defined. Their exact positions are introduced in subsection 3.6.2. For each plane, the measurement field position was changed incrementally to capture the complete wake of the wing. Ten overlapping spanwise positions and between one and two overlapping vertical positions were used per plane.

A picture of the system in action can be found in Figure 3-3. Here, the laser system unit is visible on the right hand side. The green laser light sheet is directed toward the left hand side of the picture, crossing the wake of the model's wing. The cameras are installed on each side of the laser sheet lens on a shared beam.  $Tu_x$  is visualized in false color for a sample configuration to represent the two wake planes under investigation.

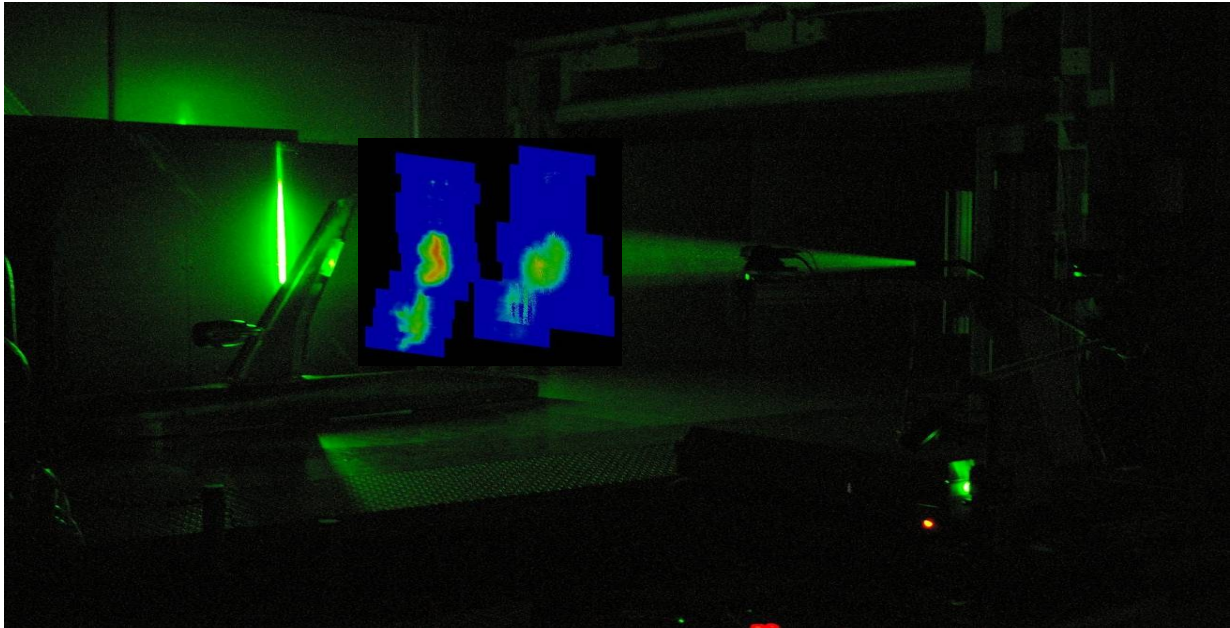


Figure 3-3: Stereo-PIV measurement in action.

Table 3-3 gives a summary of the properties of the PIV system's components. A detailed description of the system can be found in Ref. [82].

Table 3-3: Stereo PIV components.

Component	Name	Commentary
Seeding	Bis(2-ethylhexyl)-sebacat	
Laser	Spectra-Physics GCR PIV-200	Type Nd:YAG
CCD Cameras	FlowSense M2 8bit	1185 x 1599 Pixel
System-Hub	Dantec dynamics - Flow Map	
Software – Data analysis	Dantec dynamics – Flow Manager	Version 4.50.17

### *Computation of Vorticity and other Differential Quantities from PIV Data*

When calculating differential quantities from PIV Data, for example the three vorticity components, one has to be very careful. As Willert states in Ref. [175] the vorticity values obtained from PIV data can only act as estimates for the actual vorticity field. Actual vorticity magnitudes may be much higher, as vorticity is only a local average of an already locally averaged velocity field and not a point measurement.

#### 3.2.4 Constant Temperature Hot Wire Anemometry

The Constant Temperature Hot Wire Anemometry (HWA) used in this investigation is based on convective heat transfer from a heated wire probe that traverses the flow on a

support. Any change in the flow conditions that affects the probe's heat transfer is detected instantaneously by the connected constant temperature HWA system. The HWA's high time resolution gives it a big advantage over other measurement systems, including, for example, the PIV system introduced above. Most significantly, it allows one to evaluate the spectral properties of the investigated flow. A detailed summary of the HWA's theoretical background is given by Bruun in Ref. [32]. In the following paragraphs the HWA measurement chain, HWA probes, calibration process and measurement process are described.

### HWA Measurement Chain

The HWA measurements are conducted by means of an A. A. Lab Systems AN-1003 anemometer [1]. A block diagram of the HWA measurement chain used is given in Figure 3-4. Control of the measuring process – from the anemometer signal into the computer via the chain – is managed by National Instrument's DIAdem software which is also used for the data collection. A program developed at the Institute of Aerodynamics at Technische Universität München (TUM-AER) [30] is then used to compute the actual velocity data from the voltage time series data, followed by a statistical analysis of that data. The program uses the look-up tables created in the calibration process to deliver the velocity time series, the mean velocity, Reynolds stresses and turbulence intensity components.

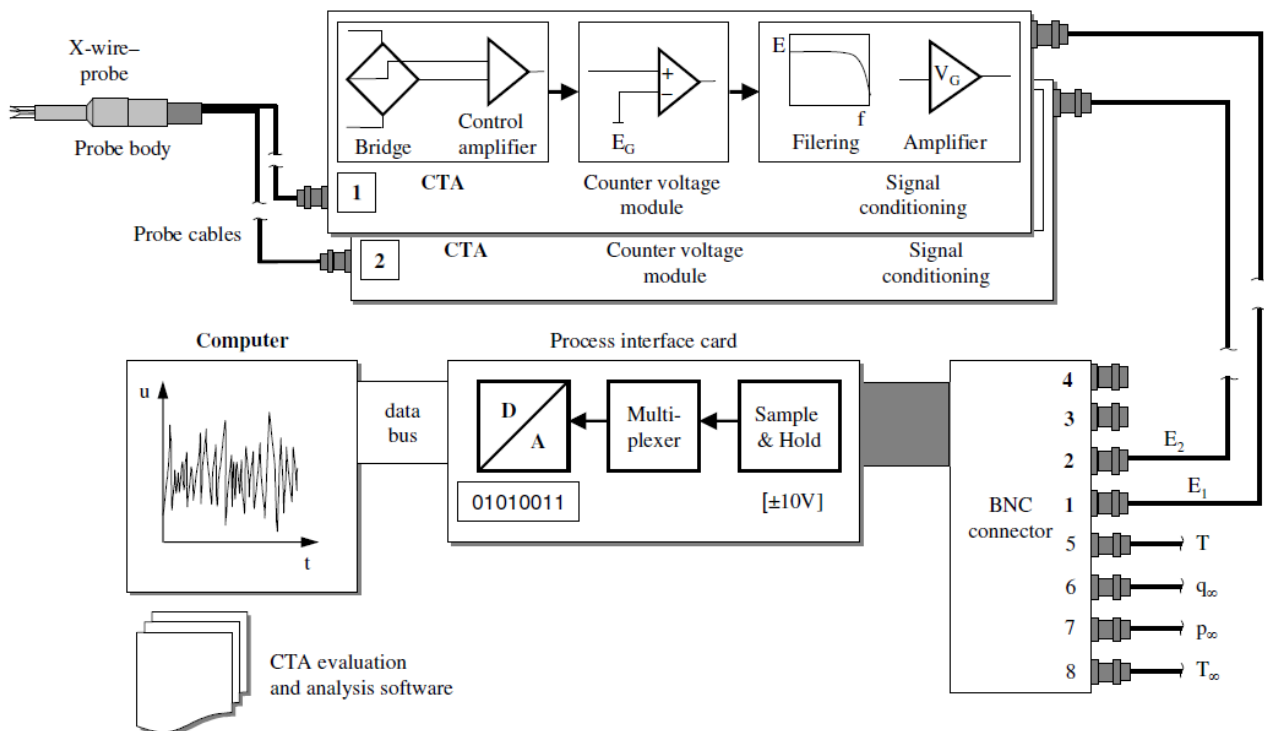


Figure 3-4: Block diagram of the HWA measurement chain [28].

### Hot Wire Probe

Hot-wire probes with one or more wires are widely available. They allow simultaneous measurement of one, two, or all three components of the velocity vector at a single position in the flow field. While three-wire probes allow one to measure all three velocity components and Reynolds-stresses simultaneously, they have the disadvantage of a small semi-apertural angle  $\mathcal{G}_c$ . As a consequence, the likelihood that the results of the data analysis are ambiguous is considerably higher than with two-wire probes: The semi-apertural angle is  $\mathcal{G}_c \approx 45^\circ$  for a two-wire probe compared to  $\mathcal{G}_c \approx 35^\circ$  for a three-wire probe. As the flow angles in the near wake of the wing can be predictably higher than maximum values typical for three-wire probes, exclusive use of a two wire probe has been opted for (referred to from here on simply as the probe). Figure 3-5 shows a schematic view of this x-type probe.

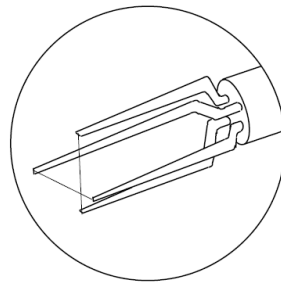


Figure 3-5: Sketch of the two-wire probe used in this investigation.

### Calibration and Data Interpretation

Such probes never have perfect geometrical accuracy and their wires, as well as their holding pins, have mutual interference effects. As a consequence, one can note an effect on the adjacent flow. Furthermore, the response behavior of a HWA probe is always non-linear. A calibration method is therefore needed to account for this non-linear response and the interference effects in order to arrive at valid velocity and flow angle measurements. For this investigation a look-up table method was chosen to do so [9]. To conduct the calibration, the probe is traversed from negative to positive flow angles  $\mathcal{G}_c$  in incremental steps  $\Delta\mathcal{G}_c$  by means of a probe support for one inflow velocity  $\bar{U}_c$ . In between each movement a record is made. Having moved through all angles  $\mathcal{G}_c$ , the next inflow velocity  $\bar{U}_c$  is set and the angle variation is repeated. The whole process is repeated for a series of inflow velocities, spanning near still air to high velocities considerably exceeding the highest velocities required for the actual investigation. The values chosen for the inflow velocities  $\bar{U}_c$  and angles  $\mathcal{G}_c$ ,  $\Delta\mathcal{G}_c$  are summarized in Table 3-4. The calibration took place in the same wind tunnel facility as the measurements. The facility is equipped with a support system which is used to position the probe for the calibration process.

Table 3-4: Flow parameters for the HWA calibration.

Flow parameter	Values
Inflow velocity span	$4.9 \text{ m/s} \leq \bar{U}_c \leq 59.8 \text{ m/s}$
Specific inflow velocity values	$\bar{U}_c = 4.9, 7.6, 10.3, 14.8, 17.9, 25.5, 30.3, 35.6, 40.0, 46.3, 50.5, 55.0, 59.8 \text{ [m/s]}$
Flow angle span	$-45^\circ \leq \vartheta_c \leq +45^\circ$
Angle increment	$\Delta\vartheta_c = 5.0^\circ$

The calibration method is conducted for static inflow conditions, but it is assumed that it is also valid for unsteady flow conditions. Figure 3-6 shows a picture of the probe and support installed and ready for calibration.

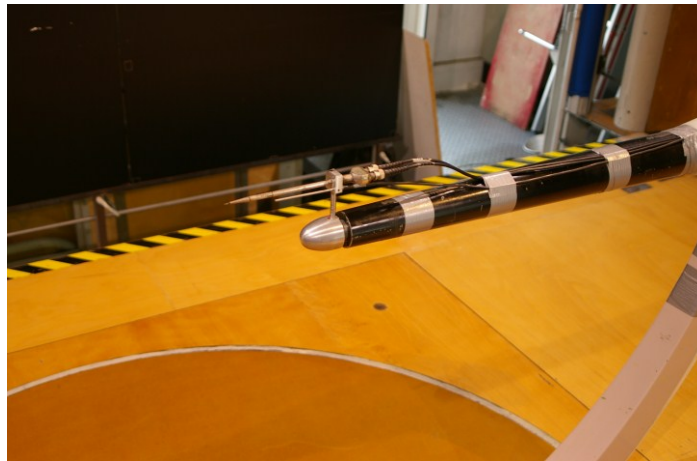


Figure 3-6: Picture of the HWA probe and support used in the calibration process.

The anemometer parameters, which are used for the HWA measurements as well as the probe calibration process, are summarized in Table 3-5.

#### *HWA Measurement Setup*

HWA was utilized to examine the instantaneous velocity components in the model's wake at two discrete positions. Both positions were deliberately selected to occupy measurement planes  $x_1$  and  $x_2$ . The probe's support system was kept simple. The probe's traversal was done manually. The HWA measurement setup, including the probe support, is illustrated in Figure 3-7. The anemometer parameters for the actual measurements were the same as for the calibration (Table 3-5). The accuracy of the complete HWA measurement chain was in the magnitude of 1% for mean values, 2.5% for turbulence intensities and 4% for power spectral densities.

Table 3-5: Hot wire anemometry parameters.

Parameters	
HWA anemometer type designation	A. A. Lab Systems – AN-1003
Gain	1
Countervoltage	2.2 V
Overheat ratio	1.8
Sample rate	3000 Hz
Measurement period	6.4 s
Number of measured values	19200
Separation frequency – Low-pass filter	1000 Hz
Digitization precision	16 bit

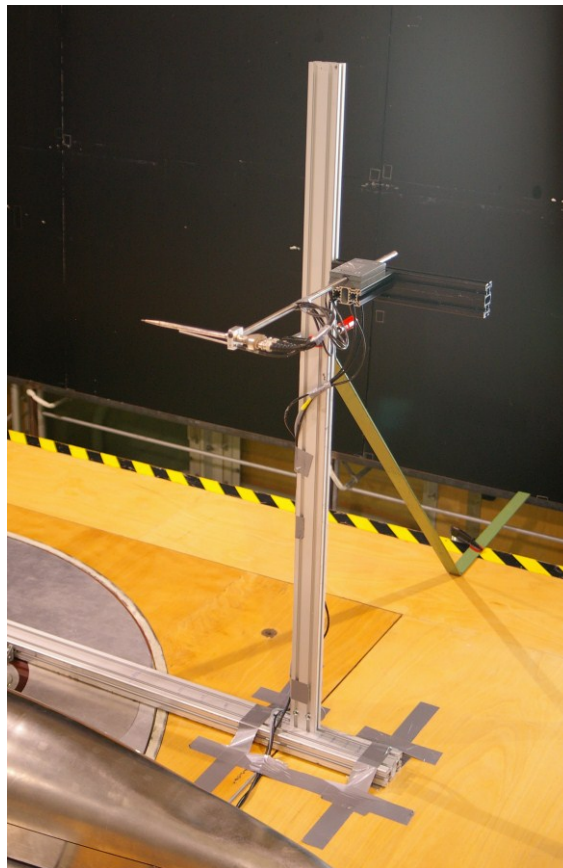


Figure 3-7: Picture of HWA traverse support for the measurements.

### 3.3 Wind Tunnel Test Facility

TUM-AER operates three large sub-sonic model wind tunnel facilities. The largest and most powerful – Wind Tunnel A (WTA) – was used exclusively in this work. It is Göttingen-type wind tunnel designed for continuous operation. The facility features a closed circuit. The test section can be operated open or closed with fixed straight walls. The open test section was used exclusively in this investigation. This option was chosen so as to benefit from free optical access and to minimize wall interference error which is much higher for closed test sections without adaptive walls. This is due to the missing of three walls. The fourth wall, namely the floor, is maintained and represents the symmetry wall when conducting half-model tests. The operating data of WTA can be found in Table 3-6.

Table 3-6: Operating data of Wind Tunnel A [176].

Wind Tunnel Parameter	
Cross-section	1.80 m x 2.40 m
Nozzle contraction	7 : 1
Test section length	4.80 m
Fan effective power	420 kW
Maximum velocity	65 m/s
Turbulence intensity	$Tu_x = Tu_y = Tu_z < 0.4\%$
Deviation of flow direction	$\Delta\alpha = \Delta\beta < 0.2^\circ$
Deviation of static pressure	$\Delta p/q_\infty \leq 0.4\%$
Temporal deviation of freestream velocity $x = 1.5 \text{ m}, r \leq 0.8 \text{ m}$	$U_\infty \leq 20 \text{ m/s}: \Delta U_\infty \leq 0.12 \text{ m/s}$ $U_\infty > 20 \text{ m/s}: \Delta U_\infty \leq 0.0067 U_\infty$
Spatial deviation of freestream velocity $x = 1.5 \text{ m}, r \leq 0.8 \text{ m}$	$U_\infty \leq 20 \text{ m/s}: \Delta U_\infty \leq 0.12 \text{ m/s}$ $U_\infty > 20 \text{ m/s}: \Delta U_\infty \leq 0.0067 U_\infty$

In the settling chamber, upstream of the nozzle, screens are installed to improve the dynamic pressure uniformity and reduce the flow turbulence level. Guide vanes are also installed in the tunnel corners to reduce the turbulence created in the corners and thereby reduce losses in the backflow circuit, where the fan is installed. The nozzle exit edges are equipped with Seiferth wings. These prevent low frequency instabilities. It is taken that this kind of passive flow control increases the level of turbulence of the shear layer and

induces high frequency disturbances into the shear layer [112]. An external view of WTA's backflow circuit and an aerial drawing of its components are given in Figure 3-8.

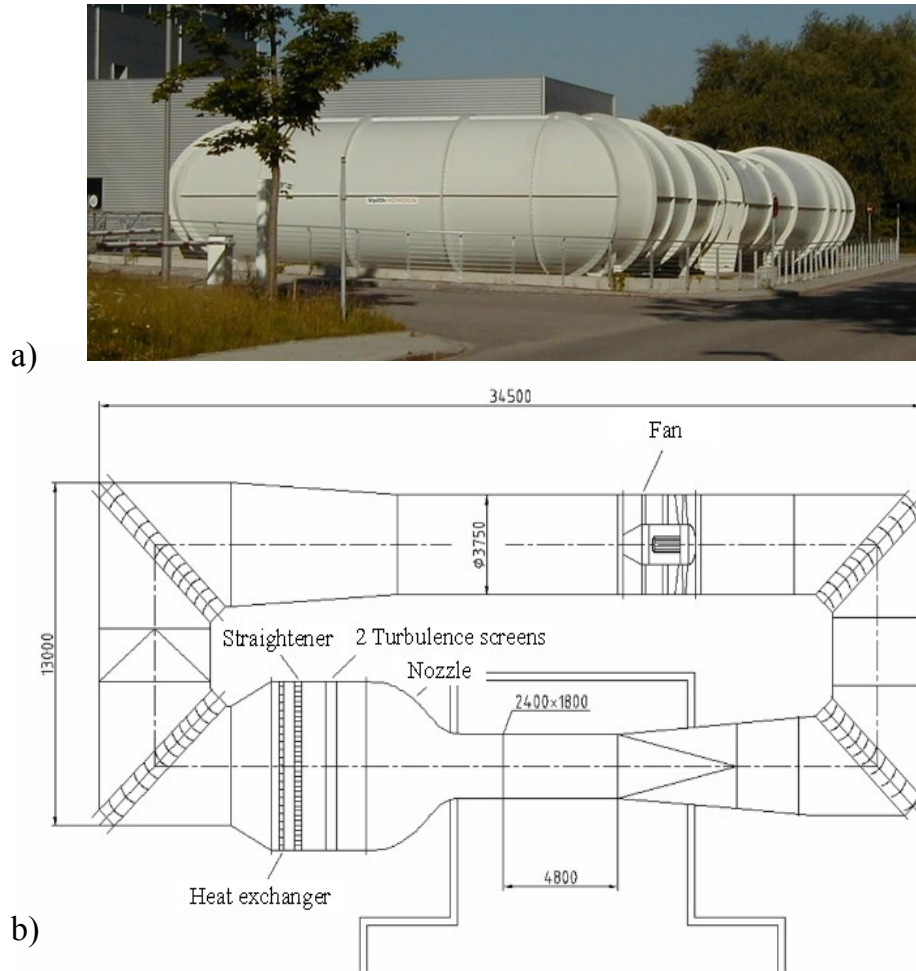


Figure 3-8: Wind Tunnel A. a) External view, b) Aerial drawing of the facility [176].

### 3.4 Wind Tunnel Model

A single model representing a contemporary CTA configuration's starboard wing with high-lift devices, half fuselage and engine nacelle was used for this investigation (subsequently referred to as the model). The model consists of a metal main wing structure with detachable leading and trailing edges to allow mounting of various high-lift devices. The high-lift-device configuration was representative for contemporary CTA. It consisted of full-span leading edge slats, discontinuous only by a cut-out at the nacelle pylon mount, and both inboard and outboard single slotted Fowler flaps. At the trailing edge outboard of the outer Fowler flap, there was the all speed aileron. The slats were attached to the main wing using twelve slat tracks. The flaps were mounted to the main wing by five flap tracks. The inner flap edge was fixed at the fuselage. The flap tracks were covered by flap track fairings. At the inner slat end, an onklet served as a fairing between wing leading edge and fuselage. The inner slat side edge was equipped with a slat horn. The deflection of the high-lift devices was chosen to represent an approach configuration. This configuration,

with no air-brake deflection, served as the baseline for the investigation, and is here entitled *Baseline Configuration (BL)*. The high-lift device deflections can be found in Table 3-7.

Table 3-7: Deflection values of the high-lift devices.

Parameter		
Fowler deflection angle	$\eta_F =$	34°
Fowler gap		28%
Slat deflection angle	$\eta_S =$	26°
Aileron deflection angle	$\eta_A =$	10°

The wing tip is equipped with a wing tip device. A picture of the half-model installed in WTA in the BL configuration can be found in Figure 3-9.

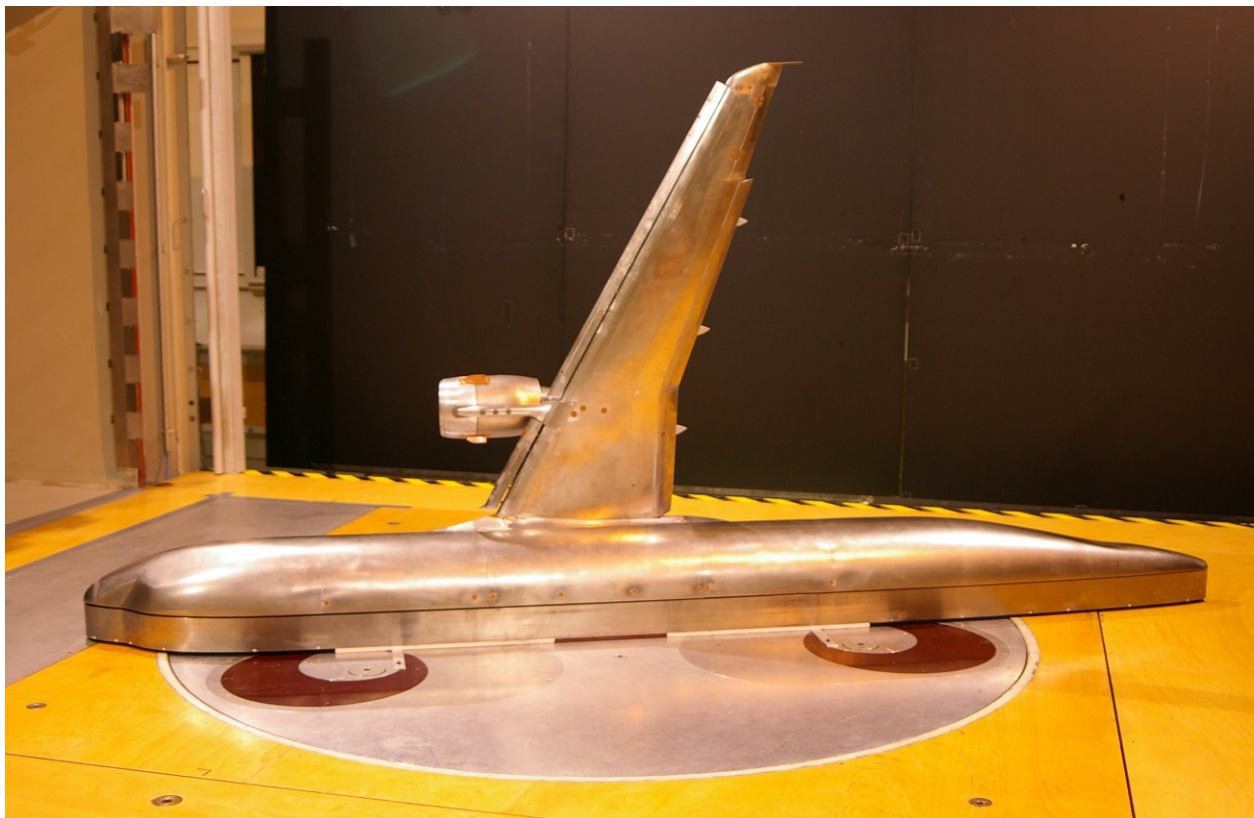


Figure 3-9: Wind tunnel model in WTA.

To reduce the interaction of the wind tunnel floor boundary layer with the aerodynamics of the model, the model is installed with small clearance directly above an earthed péniche, which has the same outline as the fuselage. To ensure that there is no mechanical contact between the péniche and the model fuselage four flat towing arms are installed. The gap

between fuselage and péniche is aerodynamically closed by adjacent labyrinth seals. The péniche is equipped with brush strips adjacent to the test section floor to ease the gliding movement when the angle of attack is changed. The effective height of the péniche is  $h \approx 0.09$  m. The parameters of the wind tunnel half model are summarized in Table 3-8.

Table 3-8: Parameters of the wind tunnel model.

Parameter		
Scale		1:13.6
Half span	$b/2 =$	1246.81 mm
Fuselage length	$l =$	2762.73 mm
Wing reference area	$S =$	0.3309 m <sup>2</sup>
Wing mean aerodynamic chord	$c =$	0.308 m
Aspect ratio	$\mathcal{AR} =$	9.396
Taper ratio	$\lambda =$	0.246
Sweep angle at 25% chord length	$\varphi_{25\%} =$	24.96°
Sweep angle at 50% chord length	$\varphi_{50\%} =$	22.5°
Dihedral angle	$\Gamma =$	5.11°
Material		Inconell 718

### 3.4.1 Model Nacelle

To simulate a CTA jet engine the model incorporates a through flow nacelle (TFN). This TFN is equipped with two engine nacelle strakes consisting of metal sheets with tapered leading edges. They are attached in flow direction and rectangular to the outside of the TFN and can lead to a reduction in interference drag, an increase in  $C_{L,max}$  and  $L/D$  at high  $\alpha$ , a broader range of high  $C_L$ , and less abrupt stall characteristics [174]. The TFN is mounted at  $y \approx 0.33 \cdot b/2$ . It represents a contemporary high-bypass-ratio engine with a bypass ratio of  $\mu \approx 5.9$  with external mixing. The TFN diameter at inlet is  $d = 125$  mm, and the overall length amounts to  $l = 237$  mm. It is closely coupled to the wing. The TFN has an internal corebody nacelle and an internal pylon. A sectional cut sketch of the through flow nacelle principle is given in Figure 3-10.

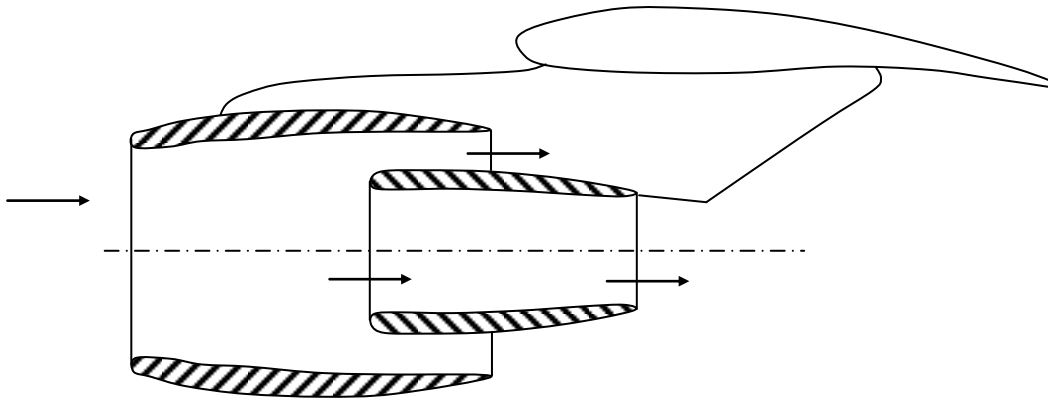


Figure 3-10: Sectional cut sketch of the through flow nacelle principle.

Other TFNs with increased by-pass ratios compatible with the model also exist. Investigations into the influence of these high by-pass ratio nacelles on the model's aerodynamics can be found in Refs. [100] and [99].

### 3.4.2 Laminar-Turbulent Tripping

As discussed in subsections 2.3.1 and 3.1.1, the wind tunnel test Reynolds number  $Re_m$  is at least one order of magnitude lower than the real CTA approach Reynolds number  $Re_a$ . To achieve aerodynamic conditions representative of actual CTA approach in the wind tunnel tests, transitions from laminar to turbulent boundary layers were tripped by roughness strips at positions where transition can be anticipated for the real aircraft. Roughness strips were used around the leading edge of the nacelles as well as at the nose of the fuselage. The pressure distribution on the wing with deployed slats provokes a natural transition at or near the leading edge. This makes an artificial transition unnecessary on the wing [89]. The strips consisted of Karborundum K120 powder, commonly used for this purpose. For example, Abbott et al. used it for a series of well known wind tunnel experiments of airfoils by NACA [2]. The powder was attached to the surfaces using wet lacquer. The Fuselage nose strip had a width of 15 mm and was positioned 25 mm downstream of the fuselage nose. The Nacelle strip had a width of 4 mm and was positioned 10 mm downstream of the nacelle's leading edge.

This specific powder type with its specific grain diameter was selected in light of the Reynolds numbers and the consequential specific thickness required of the boundary layer. On one hand, complete tripping demands a minimum strip height, and thus grain diameter; on the other, a too thick strip would create unreasonably high additional drag. The optimal height  $k_{krit}$  is given by Breitsamter in Ref. [29]:

$$k_{krit} = 26x^{1/4} \left( \frac{\nu}{U_\infty} \right)^{3/4} \quad (3.1)$$

Parameter  $x$  refers to the wall length upstream of the strip. For the chosen wind tunnel inflow velocity of  $U_\infty = 50$  m/s the critical height becomes  $k_{krit} = 111$   $\mu\text{m}$ . This corresponds sufficiently with the Karborundum 120 grain-diameter of between  $d_{Karb} = 90$   $\mu\text{m}$  and  $d_{Karb} = 125$   $\mu\text{m}$ .

### 3.5 Air Brake Model Parts

All air-brake device model parts were designed specifically for this investigation using Dassault Systèmes' Computer Aided Design (CAD) program package CATIA V5. The parts were made out of the aluminum alloy CERTAL and manufactured in the TUM-AER workshops with the help of computer controlled milling machines.

As stated earlier, all of the air-brake device model parts corresponded solely with the existing aileron-related wing and spoiler system geometry. The two novel aileron devices replaced the conventional aileron and the two novel spoiler devices covered the two most outboard spoiler positions. The model came with a removable aileron, which is deflectable by replaceable connectors. Thus, the original aileron could easily be replaced by the specifically designed novel ailerons, providing their connectors were compatible with the existing ones. No conventional spoilers were incorporated into the model. Thus the original one-piece wing shroud model element had to be replaced by a newly designed one. The new shroud element contained a cavity where the two most outboard spoilers are located. It consisted of three parts in contrast to the original one-part shroud element. Figure 3-11 shows a CAD drawing of the new wing shroud elements.

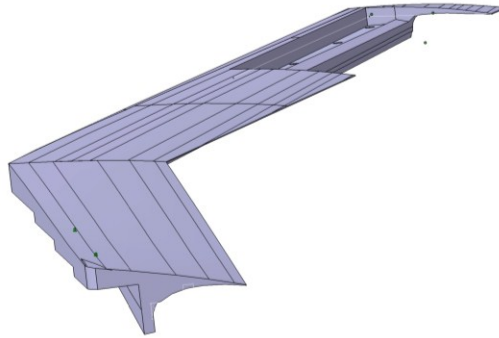


Figure 3-11: CAD drawing of new shroud elements with spoiler cavity.

For all the air-brake devices several connectors were constructed to simulate a number of discrete deflections  $\delta_s$  of the continuous deflection movement of the real devices.

#### 3.5.1 Conventional Spoiler

As no conventional spoiler (CS) part was available for the model, a new one – carrying the same shape as the wing shroud – was designed. The only difference was that the spoiler part's top leading edge had to be rounded to allow for deflection. The corresponding connectors were placed in-between the shroud cavity base and the spoiler's lower side

joint plane. The spoiler was then fixed by three screws. Figure 3-12 shows a top view of the outboard wing part with the spoiler installed.

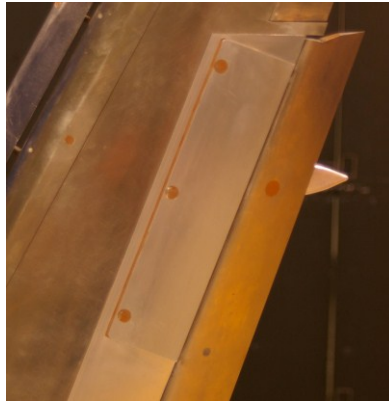


Figure 3-12: Top view of outer wing with new shroud and conventional spoiler part.

### 3.5.2 Adverse Spoiler

An adverse spoiler (AS) differs from a CS insofar as the hinge line is moved from the front part of the spoiler to the trailing edge. However, the AS model part carried the same upper surface shape as the CS. The lower side front part, which is covered inside the wing when the spoiler is not deployed, was defined by a generic sloped planar face. The part's bottom leading edge was chamfered by a radius of  $R = 2$  mm, and the upper surface merged with the front face at around  $90^\circ$ . Figure 3-13 shows a 3D CAD view of the AS part.

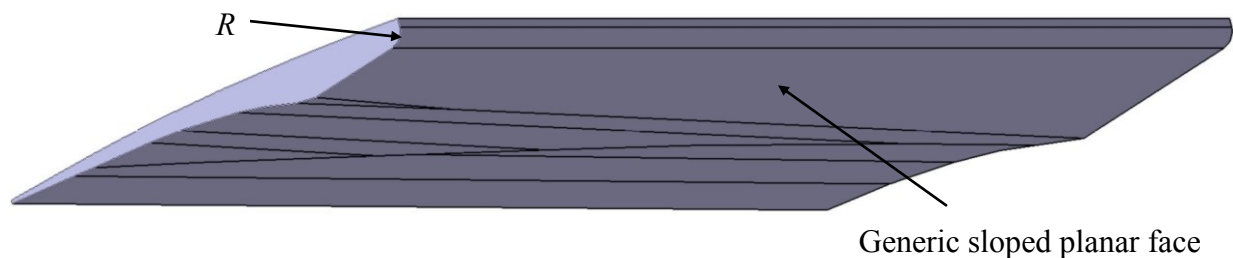


Figure 3-13: 3D CAD view of Adverse Spoiler part.

The AS's thin trailing edge was unable to give enough structural support for the mounting of the AS part to the wing. Thus, connectors comprising two narrow crosspieces were created to mount the front of the AS part to the main wing and define the deflection angle  $\delta_{AS}$ . The crosspieces were located near the inboard and outboard edges of the AS model and fixed by screws to the shroud cavity base and the AS model's lower side. The AS model had joint notches as a counterpart to the bottom connectors which served to support it laterally. One connector was constructed for each deflection angle under investigation. Figure 3-14a shows a photograph of the AS model installed at the model's wing.

### *Gap Variation*

To be able to vary the gap between the AS's trailing edge and the flap spacers were constructed. The default gap value is defined as that which is given when the AS trailing edge is flush against the adjacent main wing trailing edge. With spacers the gap can be reduced to 70% of the default value or increased to 150%. The high aerodynamic potential of a variation in the gap between the flap and the main wing trailing edge is evidenced by Airbus's use of a drooped spoiler to control this gap for its newest high efficient CTA programme A350 [107].

### 3.5.3 Advanced Adverse Spoiler

In contrast to AS, where a vent opens between AS and the main wing by deflecting the AS upwards, this vent is closed for the Advanced Adverse Spoiler (AAS). All other parameters are the same and therefore the parts produced for the AS were reused. The vent was closed by fixing a flat, fitted metal sheet plate over it. The sheet was then sealed to ensure that the vent was completely closed. A picture of the installed AAS model can be found in Figure 3-14b.

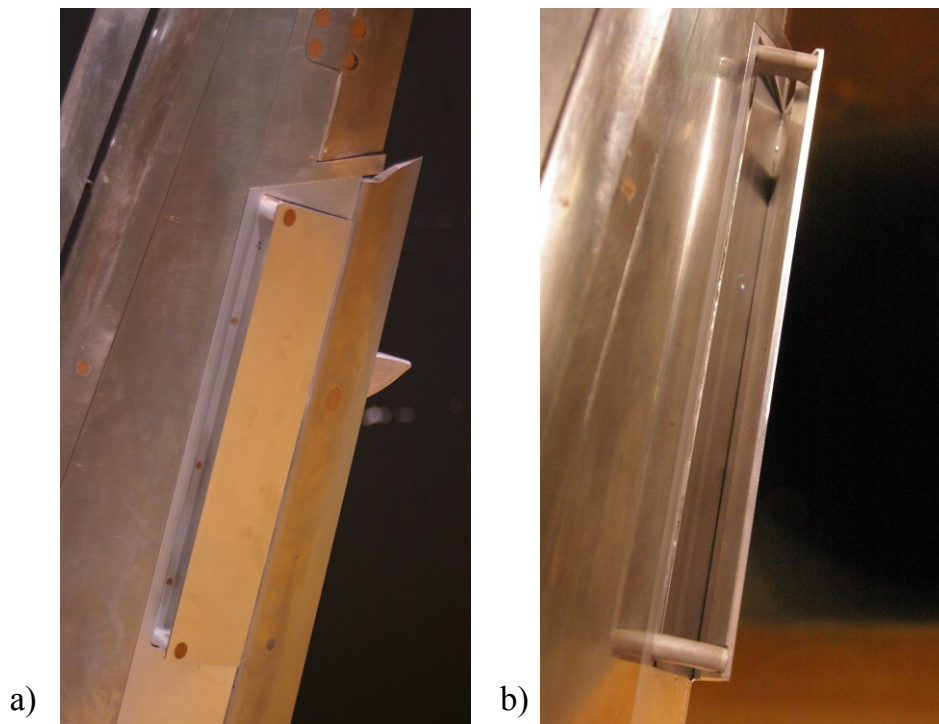


Figure 3-14: Installed novel spoiler models. a) Adverse Spoiler, b) Advanced Adverse Spoiler.

### 3.5.4 Deceleron

The Deceleron (DC) consists of an upper and a lower part which correspond geometrically with the original aileron divided in half lengthways. To realize the DC upper part's deflection, two connectors were fixed by screws at the two original aileron joint notches of the main wing and at two joint notches in the top side of the upper DC part. The lower DC

part was then connected to the upper one. This was realized by spacers that were inserted between the two DC parts. The specific spacer defines and maintains the differential deflection angle  $\delta_A$  between lower and upper part of the DC. Various connectors and spacers were constructed to simulate various combinations of lower and upper DC part deflections. Figure 3-15a shows the installed DC parts.

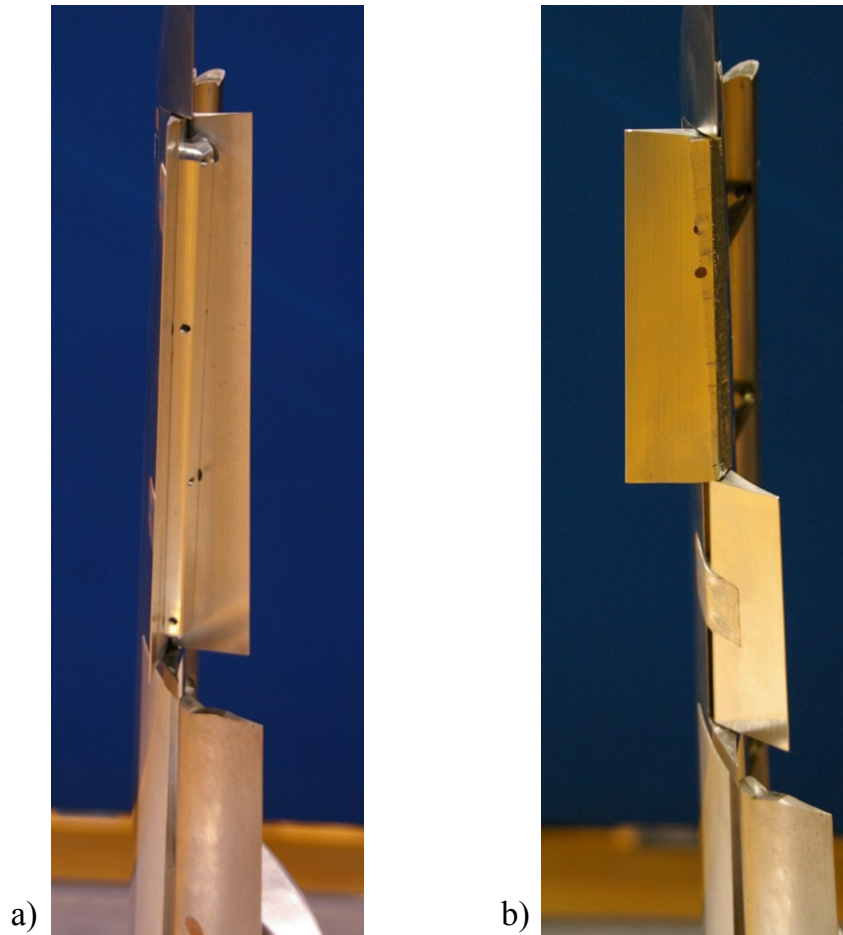


Figure 3-15: Installed novel aileron parts. a) Deceleron, b) Split Aileron.

### 3.5.5 Split Aileron

The Split Aileron (SA) was created by laterally segmenting the original aileron geometry into an inner and an outer part. Together, both SA parts cover the same dimensions as the conventional aileron. The cut spreads parallel to the lateral edges of the aileron. The lateral position of the cut could have been chosen following three methods: Retaining same span for inner and outer part, retaining same projected area for inner and outer part, or aiming to have the same aerodynamic load for inner and outer part. Because the SA's breaking functionality should be available approximately decoupled from the roll control function, the third method was chosen as the potentially most suitable option for this requirement. To gain the same aerodynamic load requirement, an elliptic aerodynamic load distribution along the model's wingspan was assumed. This leads to the inner SA part's span of  $s_i = 97.86$  mm and the outer SA part's span of  $s_o = 115.14$  mm for a total aileron span of

$s_{ai} = 213$  mm. To realize the deflection of inner and outer SA parts, two connectors were fixed by screws at the two original aileron joint notches of the main wing and at a joint notch in the top side of each SA part. A picture of the SA model parts installed at the model can be found in Figure 3-15b.

### 3.6 Parameter Set-Up for Experiments

A parameter study was conducted with respect to the air-brake configurations. For the given multi-dimensional parameter space this lead to various individual parameter combinations to be investigated in addition to the baseline (BL). Each of these parameter combinations is designated as a configuration. Table 3-9 gives an overview of the varied parameters.

Table 3-9: Parameter overview.

Subject of investigation	Designation	Device deflection parameters
Aileron	Aileron (A)	Aileron deflection angle $\delta_A$
Spoilers	Conventinal Spoiler (CS)	Spoiler deflection angle $\delta_S$
	Advanced adverse Spoiler (AAS)	
	Adverse Spoiler (AS)	Spoiler deflection angle $\delta_S$ Flap gap $d$
Novel Ailerons	Deceleron (DC)	Aileron deflection angle $\delta_A$
	Split Aileron (SA)	Differential deflection angle $\delta_\Delta$

For all tests, excluding the Reynolds number sensitivity study, the freestream velocity was kept at a constant value of  $U_\infty = 50$  m/s. The model was positioned at various inclines to simulate different angles of attack  $\alpha$ . For example, a zero angle of attack,  $\alpha = 0^\circ$ , was defined by pointing the model fuselage's longitudinal axis along the wind tunnel's inflow direction. The parameter values chosen for the balance measurement campaign and the ones for the flow-field measurement campaign are given in the next subsections.

#### 3.6.1 Balance Measurement Campaign

All balance measurements were conducted by running angle of attack polars for each configuration investigated. The parameters for these  $\alpha$ -polars remained the same for all measurements of the parameter study. This excludes the measurements that were conducted to determine their statistical repeatability (section 5.1.2). In contrast to the high-

$\alpha$  domain, where wing flow is subject to large areas of separation associated with non-linear characteristics, doubled angle of attack increments  $\Delta\alpha$  were chosen for moderate  $\alpha$  where linear aerodynamics dominated. Each polar measurement was recorded twice so as to be able to check their repeatability. The polar parameters are summarized in Table 3-10.

Table 3-10: Polar parameters for balance measurements.

Polar parameter	
Minimum angle of attack	$\alpha_{min} = -10^\circ$
Maximum angle of attack	$\alpha_{max} = 25^\circ$
Angle of attack increment	$-10^\circ \leq \alpha < 15^\circ : \Delta\alpha = 1^\circ$ $15^\circ \leq \alpha \leq 25^\circ : \Delta\alpha = 0.5^\circ$
Number of sub measurements per $\alpha$	$n = 10$
Idle time before each measurement starts	$t_{idle} = 5 \text{ s}$

The deflection and, where relevant, gap of the air-brake devices was varied extensively. The values chosen for the spoiler-based devices are listed in Table 3-11 and the range of the parameters chosen for the aileron-based devices in Table 3-12. Figure 3-16 gives an overview of all specific deflection combinations for DC and SA.

Table 3-11: Values of deflection and gap for spoiler-based devices.

Device	Deflection angle values	Gap values
Baseline Configuration (BL)	$\delta_A = 10^\circ, \delta_S = 0^\circ$	100%
Conventional Spoiler (CS)	$\delta_A = 10^\circ;$ $\delta_S = 5^\circ, 10^\circ, 15^\circ, 20^\circ, 30^\circ, 45^\circ, \text{ and } 60^\circ$	100%
Adverse Spoiler (AS)	$\delta_A = 10^\circ;$ $\delta_S = 2^\circ, 5^\circ, 10^\circ, 15^\circ, 20^\circ, 30^\circ, 45^\circ, \text{ and } 60^\circ$	70%, 100%, 150%
Advanced Adverse Spoiler (AAS)	$\delta_A = 10^\circ;$ $\delta_S = 2^\circ, 5^\circ, 10^\circ, 15^\circ, 20^\circ, 30^\circ, 45^\circ, \text{ and } 60^\circ$	100%

Table 3-12: Ranges of deflection for aileron-based devices.

Device	Deflection range	Differential deflection values
Conventional Aileron (A)	$\delta_A = -30^\circ \div +60^\circ$	N/A
Deceleron (DC)	$\delta_A = -50^\circ \div +60^\circ$	$\delta_A = 20^\circ, 40^\circ, 60^\circ, 90^\circ$
Split Aileron (SA)	$\delta_A = -45^\circ \div +45^\circ$	$\delta_A = -120^\circ \div +120^\circ$

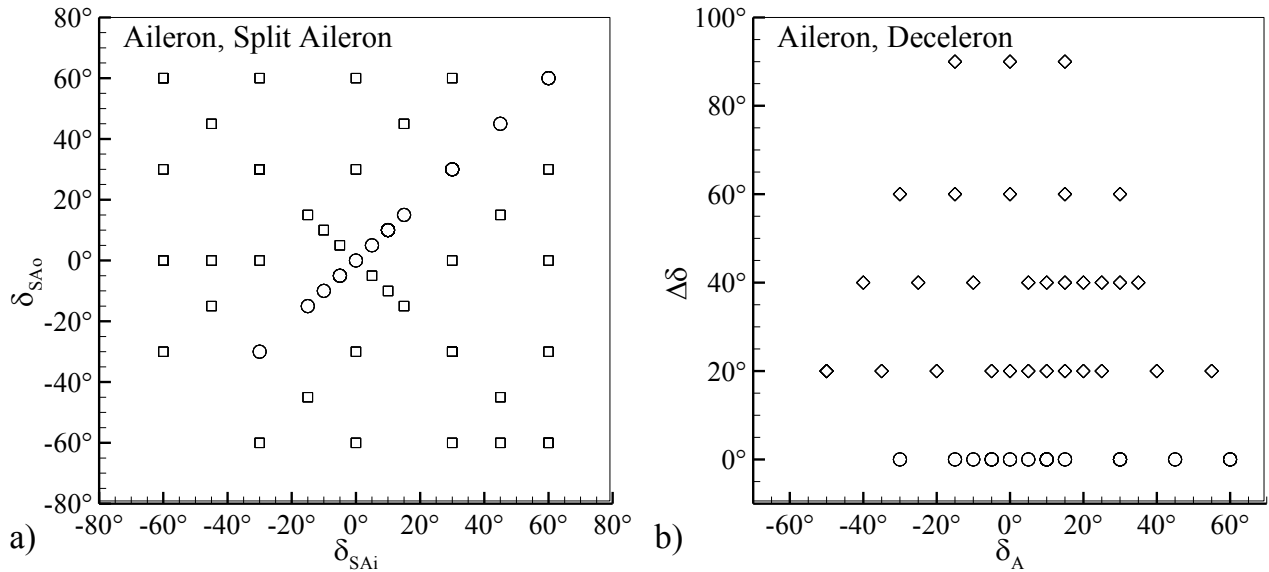


Figure 3-16: Investigated deflection values. a) Aileron and Split Aileron, b) Aileron and Deceleron.

### 3.6.2 Flow Field Measurement Campaign

Flow field measurements comprise the measurement of the velocity field in the near wake by HWA and PIV and the visualization of the wing adjacent flow by tufts. The flow field measurements were conducted exclusively for BL, CS, AS and AAS configurations.

#### *PIV and HWA in the Wake*

As mentioned in subsections 3.2.3 and 3.2.4, all wake flow field measurements are conducted in two planes in the near wake of the half-model's wing, designated x1 and x2. The upstream plane x1 is defined as being located at  $x_1/b = 0.12$  and represents the immediate near field wake of the wing. The downstream plane x2 is treated as representative of the leading edge of the HTP which is not included in the wind tunnel model. It is positioned at  $x_2/b = 0.92$ . For all three spoiler configurations the spoiler deflection angle is fixed to a value of  $\delta_s = 30^\circ$ . The angle of attack  $\alpha$  is restricted to one value per investigated device. These  $\alpha$ -values correspond in each case to a consistent lift coefficient of  $C_L = 1.5$ .

### Tuft Pictures

To illustrate the development of the wall adjacent flow as a function of  $\alpha$ , pictures of the model with attached tufts were taken for a range of angles of attack between  $\alpha_{min} = -10^\circ$  and  $\alpha_{max} = 25^\circ$ . Additional pictures, where the tuft stick is used, were taken to illustrate some specific flow features of the configurations under investigation. This was also done for some aileron-based device configurations.

## 3.7 Post-Processing of Test Data

This section details the post-processing method applied to the raw test data to produce the final results, to be discussed in Chapters 5 to 7.

### 3.7.1 Aerodynamic Coefficients of Longitudinal Motion

No horizontal tail plane was used in the experiments. Consequently, trim-lift and trim-drag are excluded from this investigation. Thus, the aerodynamic coefficients of lift  $C_L$ , drag  $C_D$ , and pitching moment  $C_m$  are calculated directly from the measured forces of balance  $F_X$ ,  $F_Y$  and the moment of balance  $M_Z$  as well as the logged dynamic pressure  $q$  and the model's reference area  $S$ . Due to the fact that the balance coordinate system turns when rotating the balance's bogie by the turning angle  $\varphi$ , the forces and moments in the aerodynamic coordinate system are gathered by:

$$\begin{bmatrix} L \\ D \\ m \end{bmatrix} = \begin{bmatrix} -\sin\varphi & -\cos\varphi & 0 \\ -\cos\varphi & \sin\varphi & 0 \\ 0 & 0 & -1 \end{bmatrix} \cdot \begin{bmatrix} F_X \\ F_Y \\ M_Z \end{bmatrix} \quad (3.2)$$

$$\begin{bmatrix} C_L \\ C_D \\ C_m \end{bmatrix} = \frac{1}{q \cdot S} \begin{bmatrix} L \\ D \\ m/c \end{bmatrix} \quad (3.3)$$

Figure 3-17 illustrates the forces measured in the system of balance coordinates and the resulting aerodynamic forces in the aerodynamic system of coordinates.

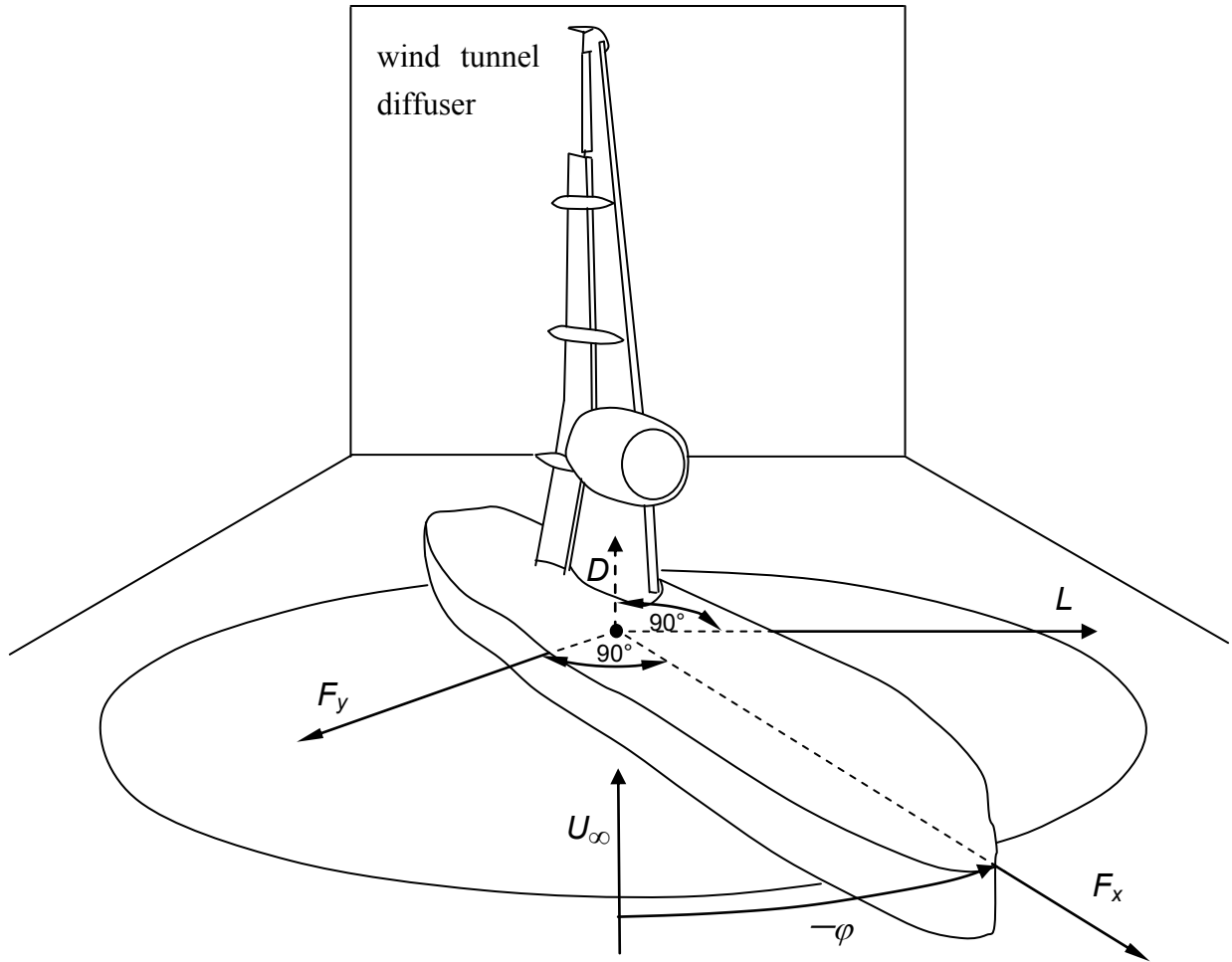


Figure 3-17: Coordinate systems.

### 3.7.2 Aerodynamic Coefficients of Lateral Motion

Contrary to the coefficients of longitudinal motion for half model measurements, the lateral motion's coefficient of side force  $C_Y$ , rolling moment  $C_l$  and yawing moment  $C_n$  can only be deduced indirectly. To do so, the force and moments of the baseline configuration marked with index  $BL$  are subtracted from the values of the respective configuration. By this method, only aerodynamic values with a zero angle of yaw  $\beta = 0^\circ$  can be deduced.

$$\begin{bmatrix} \Delta Y \\ \Delta l \\ \Delta n \end{bmatrix} = \begin{bmatrix} -1 & 0 & 0 \\ 0 & 1 & 0 \\ 0 & 0 & 1 \end{bmatrix} \cdot \begin{bmatrix} F_Z - F_{Z,BL} \\ M_X - M_{X,BL} \\ M_Y - M_{Y,BL} \end{bmatrix} \quad (3.4)$$

$$\begin{bmatrix} C_Y \\ C_l \\ C_n \end{bmatrix} (\beta = 0^\circ) = \frac{1}{q \cdot 2S} \begin{bmatrix} \Delta Y \\ \Delta l / b \\ \Delta n / b \end{bmatrix} \quad (3.5)$$

For the definition of these coefficients the reference area is doubled to  $2S$ . This is due to the fact that both the half wing area of the respective configuration  $S$  and the Baseline half wing area  $S$  are taken into account.

### 3.7.3 Parametric Decomposition of Aerodynamic Coefficients

For moderate angles of attack  $\alpha$ , CTA aerodynamics is considered linear. At the same time, for moderate device deployment angles  $\delta$ , the corresponding aerodynamics are considered linear, too. Under these conditions, the aerodynamic coefficients can be considered two-dimensionally linear and presented by a two dimensional linear superposition:

$$C_x = C_{x0} + \frac{\partial C_x}{\partial C_L} \cdot C_L + \frac{\partial C_x}{\partial \delta} \cdot \delta = C_{x0} + C_{xL} \cdot C_L + C_{x\delta} \cdot \delta \quad (3.6)$$

Here, the derivatives  $C_{x\delta}$  are designated the device effectiveness of the coefficient  $C_x$ .

### 3.7.4 Regression Analysis

When conducting a regression analysis of the parametric measurement data to gather Eqs. (3.6), one has to limit the population of data points to a valid range to receive a high regression quality. Therefore, the populations are divided into two intervals. Interval I is characterized by linear behavior, Interval II, with non-linear behavior. The regression is then carried out using only the data from interval I. This assures that the linearized device effectiveness values derived by the regression analysis reflect the original aerodynamic behavior to a high fidelity. The regression quality  $R^2$  is assessed by the sum of the error square of the approximated coefficient plane:

$$R^2 = \frac{\sum_{i=1}^n (y_{lin,i} - \bar{y})^2}{\sum_{i=1}^n (y_i - \bar{y})^2} \quad (3.7)$$

With this definition, a value of  $R^2 = 1$  represents a perfect fit. The quality of each regression analysis is stated explicitly. In accordance with Ref. [153], interception at the origin is not forced on the data, as the interception of straight-line data is always inherent in the data and should be allowed to express itself. In terms of a good identifiability, a model with minimal parameters, which achieves a high quality value, is preferable [108]. This is assured by the exclusive use of linear regression analysis.

### 3.7.5 Power Spectral Density Analysis

Time-resolved velocity information of the wing wake was obtained using the HWA measurements. The spectral information of these time dependent velocity signals gives

important information regarding the dominant frequencies of the flow. To arrive at this information the one-sided power spectral density (PSD) was established using a Fourier-transformation of the velocity fluctuations  $\bar{u}'$  [20]. The transformed function  $X_{\bar{u}'}(\omega)$  was deduced from the velocity fluctuation time series  $\bar{u}'(t)$  by

$$X_{\bar{u}'} = \lim_{T \rightarrow \infty} \int_0^T \bar{u}'(t) e^{-i\omega t} dt. \quad (3.8)$$

The power spectral density was calculated by multiplying of the Fourier transform  $X_{\bar{u}'}(\omega)$  with its conjugate-complex number  $X_{\bar{u}'}^*(\omega)$

$$S_{\bar{u}'}(\omega) = \lim_{T \rightarrow \infty} \frac{2}{T} X_{\bar{u}'}^*(\omega) X_{\bar{u}'}^T(\omega). \quad (3.9)$$

The reduced frequency parameter  $k$  is defined as relating to the frequency  $f$  to  $U_\infty$  and the characteristic length scale  $l$

$$k = \frac{f \cdot l}{U_\infty}; \quad f = \frac{1}{T} = \frac{\omega}{2\pi}. \quad (3.10)$$

Using the parameters introduced in Eqs. (3.9) and (3.10), the related power spectral density distributions  $S_{\bar{u}'}^N$  are defined by Breitsamter [30]:

$$S_{\bar{u}'}^N(k) = S_{\bar{u}'} \left( \frac{1}{\bar{u}'} \right) \left( \frac{\Delta k U_\infty}{l} \right), \quad (3.11)$$

$$\Delta k = \frac{\Delta f l}{U_\infty}, \quad \Delta f = \frac{f_m}{2n_b}. \quad (3.12)$$

To calculate the spectra, a linear band averaging with  $n_b = 1024$  frequency bands is applied. Thus, the frequency resolution becomes  $\Delta f = 1.46$  Hz for  $f_m = 3000$  Hz. For all other parameters of the CTA, see Table 3-5.

# 4. NUMERICAL METHODS

Besides wind tunnel and flight tests, a third approach to investigating aircraft aerodynamics has been established in recent decades: computational fluid dynamics (CFD) simulation aided by computers. The process of performing a CFD calculation requires the engineer to perform a number of tasks: define the problem; select the solution strategy; select an available computational flow solver or develop a new one; and, finally, conduct analysis and interpretation of the results in post processing. Each step is potentially error prone or subject to some degree of uncertainty. There is no universally accepted means of identifying or classifying errors, which can range from human or user errors to inadequacies in the modeling strategy or model equations. The European Research Community on Flow, Turbulence and Combustion's best practice guidelines adopt, for example, the following classification based on seven different sources of error and uncertainty: Model error and uncertainties, discretization or numerical error, iteration or convergence error, round-off error, application uncertainties, user errors, and code errors [177]. To minimize these errors and uncertainties, the author paid great attention to the careful preparation and execution of the operations related to the simulations. All the required steps are documented in this chapter.

## 4.1 Problem Definition

The object of the CFD-investigations conducted was to analyze the flow topology and phenomena associated with the different spoiler device configurations under investigation. To succeed in this task a suitable computational model had to be identified. This was done in two parts. First, the capabilities of the different available methods were evaluated using the relevant literature. This is covered in section 4.2. Second, a validation of the chosen numerical methods was conducted in order to test their capabilities and limits. This is covered in section 4.8. The validation case chosen, which is designated RA16SC1, is representative of the class of problem under investigation and for which there is comprehensive experimental and numerical data available. All the framework conditions for the simulations performed are resolved in this chapter.

## 4.2 Choice of Feasible Computational Method

When choosing a feasible method to solve an unsteady fluid mechanic problem, one has to consider which physical phenomena can be factored out, so as to simplify the governing equations which have to be solved. The starting point in this case are the Navier Stokes equations, which exhaustively describe unsteady viscous compressible continuum flows.

When rejecting any simplifications, one has to solve the Navier Stokes equations directly. This method is designated Direct Numerical Simulation (DNS). By applying simplifications to the equations or by modeling the unsteady component of the flow instead of resolving it, one comes to the following CFD methods in descending order of degree of required computational effort: Large Eddy Simulation (LES), Second Generation Unsteady Reynolds Averaged Navier Stokes (2G URANS) Simulation. Lower effort is required for the Reynolds Averaged Navier Stokes (RANS) Simulation and its unsteady implementation, the Unsteady Reynolds Averaged Navier Stokes (URANS) Simulation. And finally Euler Simulation and Potential Flow Simulation need an even lower effort. These methods for predicting flows are opposed in Figure 4-1 and classified by the anticipated quality of their representation of the flow physics and their computational effort. Three of these methods, which have an intermediate level in both categories, were chosen for this work: 2G URANS, URANS, and RANS.

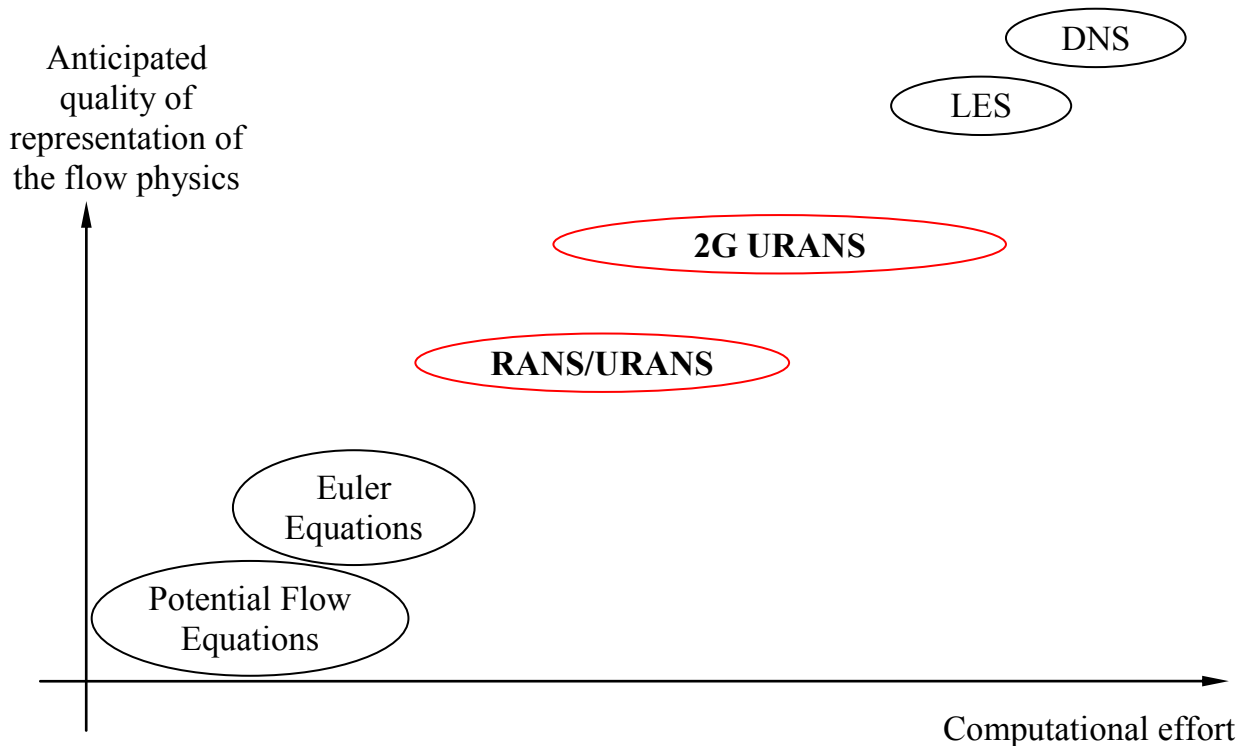


Figure 4-1: Simulation quality over computational effort for different modeling strategies; those used in this work are in bold type and encircled in red: 2G URANS, URANS, and RANS.

The process on which the selection of these three methods is based on is discussed below.

### *Navier-Stokes Equations*

The Navier-Stokes equations state the laws of conservation of mass, momentum, and energy for the flow of a fluid in thermodynamic equilibrium. In the Cartesian tensor notation, let  $x_i$  be the coordinates,  $p$ ,  $\rho$ ,  $T$ , and  $E$  the pressure, density, temperature, and total energy, and  $u_i$  the velocity components. Each conservation equation has the form

$$\frac{\partial w}{\partial t} + \frac{\partial F}{\partial x_j} = 0. \quad (4.1)$$

For the mass equation, we have

$$w = \rho, F_j = \rho u_j. \quad (4.2)$$

For the  $i$  momentum equations, we have

$$w_i = \rho u_i, F_{ij} = \rho u_i u_j + p \delta_{ij} - \sigma_{ij}, \quad (4.3)$$

where  $\sigma_{ij}$  is the viscous stress tensor, which is proportional to the rate of strain tensor and the bulk dilatation. If  $\mu$  and  $\lambda$  are the coefficients of dynamic viscosity and bulk viscosity then

$$\sigma_{ij} = \mu \left( \frac{\partial u_i}{\partial x_j} + \frac{\partial u_j}{\partial x_i} \right) + \lambda \delta_{ij} \left( \frac{\partial u_k}{\partial x_k} \right). \quad (4.4)$$

Based on Stokes Hypothesis,  $\lambda = -2\mu/3$ . For the energy equation, we have

$$w = \rho E, F_j = (\rho E + p)u_j - \sigma_{jk}u_k - \kappa \frac{\partial T}{\partial x_j}, \quad (4.5)$$

where  $\kappa$  is the coefficient of heat conduction. The pressure  $p$  is related to the density  $\rho$  and energy  $E$  by equation of state

$$p = (\gamma - 1)\rho(E - 1/2u_i u_i), \quad (4.6)$$

in which  $\gamma$  is the ratio of specific heats.

### *Euler and Potential Equations*

If two key parameters of the fluid mechanic problem to be solved can be factored out, the Navier-Stokes Equations become simpler mathematical models. First, when viscosity is neglected, the outcome is the Euler Equations. If vorticity is excluded, the outcome is the Potential Equations. Both of these simplified models have been applied on high-lift flows by others. Referring to this, Flaig et al. state in Ref. [67] that these models are insufficient for predictions regarding aerodynamic high-lift flow, stall characteristics and total drag of a CTA configuration because significant interactions between boundary layer and wake/vortex flow are not considered. Khare et al in Ref. [104] also reject these simplified models on the grounds that the complexities of flow physics for high-lift flows includes attachment line transition, relaminarization, viscous wake interactions, confluent boundary layers, separation and reattachment. Thus, these two simplified models are considered

inapplicable to the present problem and are discarded. Instead, the Navier-Stokes equations are to be solved.

### *Direct Numerical Simulation*

As mentioned above, when solely using the Navier-Stokes Equations to compute the flow, one would have to perform a DNS. Here, the largest as well as the smallest scale flow structures have to be resolved by the computational mesh. The smallest flow structures' size decreases the higher the Reynolds number becomes. A measure for the smallest flow structures of a specific flow problem is the Kolmogorov length scale  $\eta_K = (\nu^3 / \varepsilon)^{1/4}$ , where  $\varepsilon$  is the average rate of energy dissipation per unit mass, and  $\nu$  is the kinematic viscosity of the fluid [105]. A measure for the largest scales is the global length scale  $L$  of the flow problem. The number of necessary mesh points per global length scale  $n_L$  thus becomes  $n_L \sim L / \eta_K = Re^{3/4}$ . With the Courant-Friedrichs-Levy stability condition for explicit time integration,  $n_L \sim n_T$  follows the effort for conducting a DNS to be  $n_L \cdot n_T \sim Re^3$ . For a CTA flight Reynolds number of  $Re \approx 10^6$  to  $10^8$  this would lead to extremely fine necessary spatial and temporal discretization and consequently to a huge computational effort. To compute the answer to the problem that concerns us in this way is not feasible at present; nor will it be for several decades.

### *Large Eddy Simulation*

Performing a LES instead of a DNS provides the opportunity to reduce the computational effort. Here, the large flow structures – ‘Large Eddies’ –, which have to be resolved by the mesh, are treated in DNS manner. Meanwhile, the behavior of the unresolved smaller flow structures and their dissipation process is modeled by a sub-grid scale turbulence model. The split into large and small scales is achieved by low-pass filtering. Scales are then resolved from the domain size  $L$  down to the filter size  $\Delta$ . Thereby, a major portion of the turbulent fluctuations has to be resolved. Compared to a DNS, the computational effort is vastly reduced, but is still not affordable and thus is not considered for this work.

### *Reynolds Averaged Navier-Stokes Method*

After rejecting DNS and LES, the next step to reduce the computational effort to an affordable degree is the RANS simulation. Here, the turbulent motion of the flow is not resolved by simulation, but is modeled by a turbulence model. The flow quantities are therefore decomposed by the Reynolds decomposition into temporal mean  $\bar{u}$  and fluctuation part  $u'$ :

$$u = \bar{u} + u', \quad \bar{u} = \frac{1}{\Delta T} \int_t^{t+\Delta T} u(\bar{x}, t) dt \quad (4.7)$$

The Reynolds decomposition of the flow quantities is illustrated in Figure 4-2.

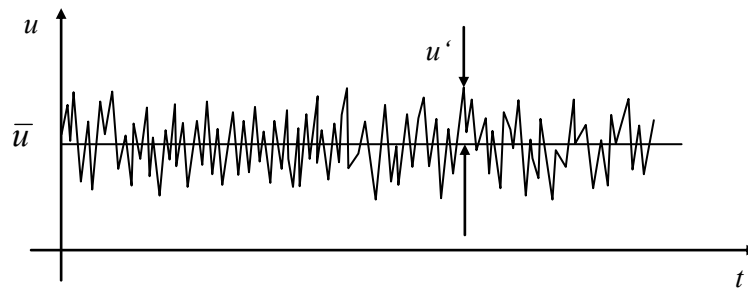


Figure 4-2: Reynolds-decomposition of flow quantities.

By applying the Reynolds decomposition to the Navier-Stokes equations one arrives at the RANS equations

$$\frac{\partial \rho \bar{u}_i}{\partial t} + \frac{\partial (\rho \bar{u}_j \bar{u}_i)}{\partial x_j} = -\frac{\partial \bar{p}}{\partial x_i} + \frac{\partial}{\partial x_j} \left( \mu \frac{\partial \bar{u}_i}{\partial x_j} - \rho \overline{u'_i u'_j} \right) \quad (4.8)$$

with the Reynolds stress tensor

$$\overline{\rho u'_i u'_j} = \tau_{ij}^R. \quad (4.9)$$

Here, we have ten unknowns, but only four equations. To close this system of equations, the Reynolds stress tensor is modeled by turbulence models. These solve the closure problem by using half-empirical formulations. The aim of RANS computations is to determine the mean flow with acceptable precision.

### *Unsteady RANS Method*

When a RANS model is employed for flows dominated by large scale vortical structures, as is the case for wakes of blunt bodies and also the flow past a spoiler (see subsection 2.3.7), the average quantities are often less satisfactory due to the inherently unsteady nature of the flow [73]. This is reflected in an unsatisfactory converging process of the simulation towards a steady solution. In such cases, Unsteady RANS methods (URANS) provide a means to include the flow-unsteadiness in the calculations while avoiding the high expenses of a LES or DNS. The computed solution then becomes time-dependent.

### *Second Generation URANS Method*

Froehlich et al. show in Ref. [73] that the results from URANS calculations have to be taken with a pinch of salt, as it is the internal instabilities of the flow that are the cause of the flow unsteadiness. In some cases, not even the Strouhal numbers given by experiments testing the underlying flow are captured by the URANS method. ‘Second Generation URANS’ methods have been introduced as a means to overcome the weaknesses of the URANS method. One of the Second Generation URANS methods is URANS combined

with the Scale Adaptive Simulation (SAS) [120]. SAS was chosen for this particular investigation; it resolves the flow in regions with large-scale turbulence. Everywhere else, it switches to a RANS mode as this reduces the computational effort compared to a flow resolution in the complete computational domain. This split into two regions is illustrated qualitatively for the spoiler case in Figure 4-3.



Figure 4-3: Split of regions by SAS method, expected LES-regions encircled in red.

When creating the computational mesh for the SAS simulations one must be sure to refine the mesh in the expected large-scale turbulence regions so that the turbulent structures are adequately resolved. The SAS method is to a large extent comparable to the Detached Eddy Simulation (DES).

The SAS model is characterized by the adding of the von Karman length scale,  $L_{vK}$ , to the scale-determining equation of RANS turbulence models.  $L_{vK}$  is defined as the ratio of the first velocity derivative divided by the second derivative times the von Karman constant  $\kappa = 0.41$ :

$$L_{vK} = \kappa \left| \frac{U'}{U''} \right|; U'' = \sqrt{\frac{\partial^2 U_i}{\partial x_k^2} \frac{\partial^2 U_i}{\partial x_j^2}}; \quad (4.10)$$

$$U' = S = \sqrt{2 \cdot S_{ij} S_{ij}}; S_{ij} = \frac{1}{2} \left( \frac{\partial U_i}{\partial x_j} + \frac{\partial U_j}{\partial x_i} \right)$$

Herein,  $U_i$  is the velocity vector. The background of this approach is a theory developed by Rotta [121]. He proposed an exact transport equation for the turbulent length scale in which higher velocity derivatives appear and the von Karman length scale is the leading order term for inhomogeneous flows.  $L_{vK}$  allows the turbulence model to identify resolved scales in unstable flows. This alters the eddy-viscosity to a level that allows the formation of a turbulent spectrum. Simultaneously, attached boundary layers are treated in RANS mode [57].

In Ref. [121] the theory and rationale behind the SAS methodology combined with Menter's Shear Stress Transport (SST) turbulence model [119] is given in detail. The test cases in that article focus on generic flows suitable for demonstrating the basic behavior of the concept. In contrast, Ref. [57] aims at providing a wider range of test cases, with an emphasis on industrial applications, for example, an airfoil flow with massive separation. The limitations of the formulation are discussed in detail in Ref. [121]. The SAS emerges

as mainly suitable for flows featuring strong flow instabilities typically associated with large separated zones behind bluff bodies or flows with vortical instabilities. Computation cases, which include a high-lift airfoil with or without a spoiler device, are therefore assumed to be very suitable for the SAS model. The SAS model is to be combined with a turbulence model in the same way as they are in RANS simulations. The range of turbulence models is discussed below.

### *Turbulence Modeling*

Turbulence models were first developed using algebraic models (which imply the least additional computational cost). Nowadays, one- and two-equation turbulence models have proved to be a good compromise between accuracy and computational cost and are most popular. For these models, one or two additional transport equations for modeling the turbulence are solved besides the five equations of state. Different turbulence models and their applicability to technical flows have been investigated by Klement in Ref. [109], among others. CFD results obtained by employing one-equation turbulence models were compared against experimental data, as well as results of algebraic and two-equation turbulence models by Mani et al. [118]. They found that for most engineering problems the one-equation turbulence models provide accurate solutions. They are more accurate than algebraic models and more efficient and robust than two-equation models. However, two equation models, including the SST-model [119] proved to be more feasible for free shear layers than one-equation models. One example of a popular one-equation model is the Spalart Allmaras (SA) model. As flow interaction between the shear layer of a leading wing element and a trailing one - for example slat and main wing - is a crucial flow phenomenon associated to high-lift flows, two equation models should be advantageous for this kind of problem. Murayama et al. show in Ref. [129], that two commonly used turbulence models, SA and SST, produce similar aerodynamic forces at lower angles of attack when simulating the flow around a three-element high-lift configuration. At higher angles of attack, the SST model gives better results for their computations. They also found that the maximum lift and the angle of attack where the stall occurs are very sensitive to the turbulence model. For these reasons the SST turbulence model was chosen to be used exclusively for all the simulations performed in this work. Efforts to modify the  $k-\omega$  turbulence model to make it better suited to the typical requirements of high-lift aerodynamics have been made by Hellsten [92]. For this work, however, the original SST model is used.

### *Two Dimensional and Two and Half Dimensional Simulations*

One way to reduce the computational effort involved is to reduce the real three-dimensional (3D) problem to a two-dimensional (2D) one. This is done by excluding the spanwise dimension. Simulations conducted in the MEGAflow research project showed that 2D RANS simulations deliver valid results for high lift configurations [15]. In this

work all RANS and URANS simulations are performed in 2D. The SAS simulation is only valid in 3D because the resolved turbulence structures are by nature three-dimensional. Thus, the domain for the SAS simulations is created by extruding the 2D RANS-mesh in spanwise direction. The resulting mesh is labeled two and half dimensional (2.5D) due to the fact that while the flow domain is 3D, it is based purely on 2D geometry. Further details of the 2.5D mesh design follow in subsection 4.5.3.

### 4.3 Computational Flow Solver CFX

The commercial CFD program CFX (version 12) was used for all simulations performed. All the theoretical foundations upon which CFX is based are given in the ANSYS CFX-Solver Theory Guide [10].

### 4.4 Geometry Definition

All computations conducted were based on a two-dimensional extraction of the respective wing. A streamwise section of the RA16SC1 wing was used for the validation study and an airfoil wing section of the CTA model was used for the spoiler investigations. The chosen airfoil for the spoiler investigations needed to be representative of the flow characteristics under investigation. Therefore, a section of the model wing at a spanwise position that corresponds with the mid-section of the two outer spoilers used in the wind tunnel experiments was chosen. The nominal chord length in this section is  $c = 0.164$  m. It must be pointed out that through this method the simulations are reduced to a quasi 2D case, lacking the 3D flow effects at the lateral edges of the devices under investigation and which do not span the complete wing. Nevertheless, it is assumed that the principle flow topology in the spoiler mid-section can be adequately reproduced in the simulations. The airfoil generation for the spoiler investigation based on the wind tunnel model geometry is illustrated in Figure 4-4. Sectional cut A-A shows the computational geometry.

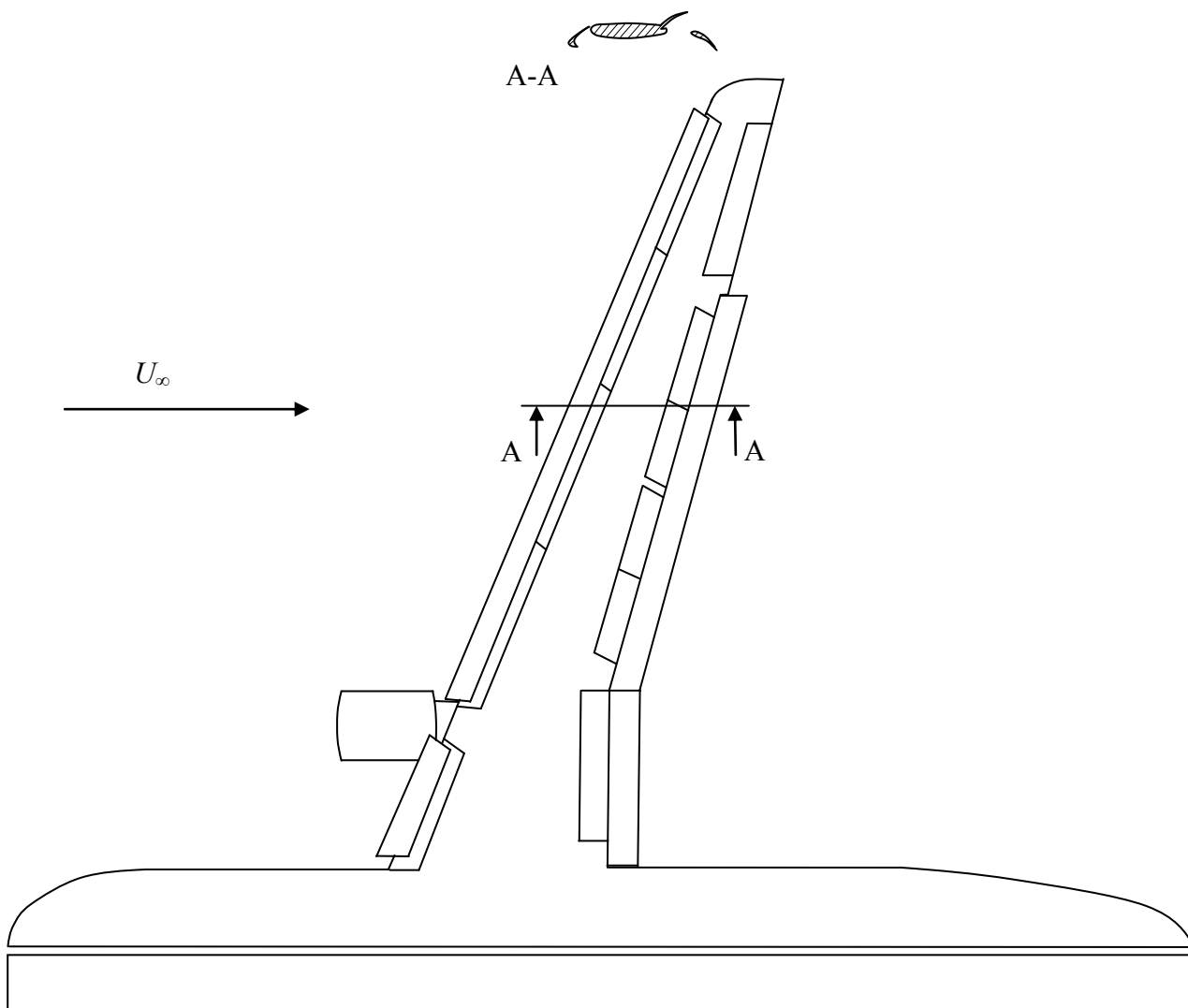


Figure 4-4: Airfoil geometry generation for CFD simulations.

## 4.5 Mesh Generation

The fluid properties are calculated at discrete spatial positions. The distribution of these positions is defined by the computational mesh. There are two different types of mesh scheme: structured and unstructured. The structured meshes are also designated as grids. Grids differ from unstructured meshes in that they are comprised of hexahedral elements that follow a uniform pattern. Unstructured meshes do not have a uniform pattern. In this work structured meshes are used exclusively. The high-lift wing geometry is complex, making grid generation difficult and time consuming.

All grids used were created using the commercial meshing software ANSYS ICEM CFD – Hexa [11]. A mature grid topology allows the grid points to be minimized while maintaining the required level of accuracy. Thus, the author paid great attention to the maturity of the grids used.

The global structure of the mesh is designated blocking. For all grids used the blocking is divided into an outer part, treating the farfield of the flow, and an inner part

that maps the wing elements and is wrapped by the outer blocking. The outer part has an O-structure. The inner part's structure is much more complex and accounts for the complex geometry, totaling 91 blocks. The blocking is maintained for both the RA16SC1 and wind tunnel model grids, and is designated as the Research Grid (RG) in both its baseline and conventional spoiler configurations. For the adverse and advanced adverse spoiler set-ups the inner grid structure had to be adapted in the region where the spoiler is located by a minimal change in the blocking. The RA16SC1 mesh with the baseline blocking structure is illustrated in Figure 4-5.

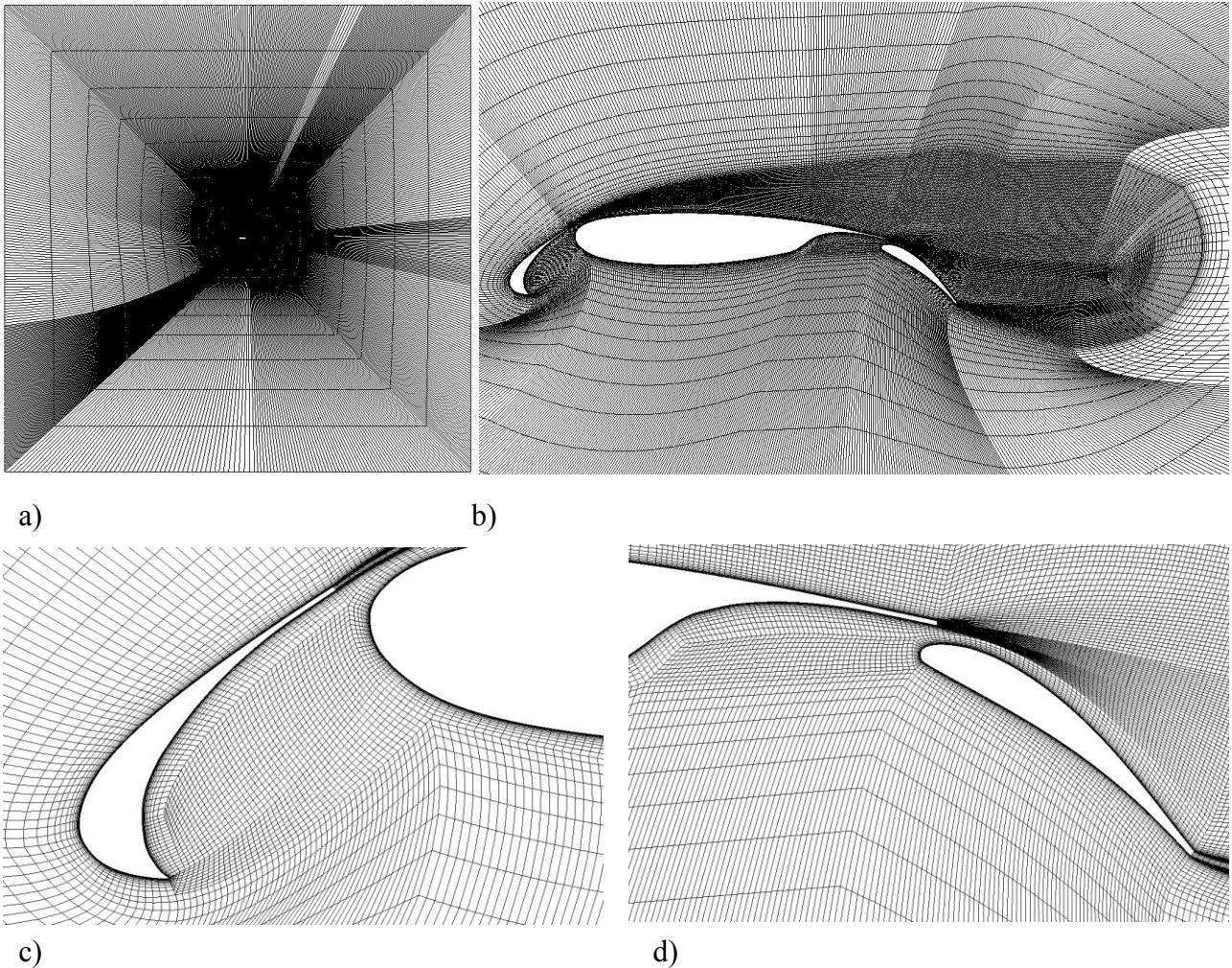


Figure 4-5: RA16SC1 mesh with baseline blocking structure. a) Outer part; b) Inner part; c) Detail view of slat; d) Detail view of flap.

The outer edge of the mesh has the form of a square and has a length of 40 times the nominal chord length. The leading edge of the airfoil is aligned with the center of this square.

### 4.5.1 Near Wall Mesh

The resolution of the wall boundary layers by the mesh is of great importance to the quality of the solution. To achieve optimal resolution, the layers' characteristics are defined thus. The non-dimensional distance from a wall  $y^+$  is defined by:

$$y^+ \equiv \frac{y \cdot u^*}{\nu} = \frac{y \cdot \sqrt{\frac{\tau_w}{\rho}}}{\nu} = \frac{y \cdot \sqrt{\frac{1}{2} U_\infty^2 \cdot C_f}}{\nu} \quad (4.11)$$

$$u^* = \sqrt{\frac{\tau_w}{\rho}} \quad (4.12)$$

$$\tau_w = \frac{1}{2} \rho U_\infty^2 \cdot C_f \quad (4.13)$$

where  $u^*$  is the friction velocity,  $\tau_w$  the shear stress, and  $C_f$  the friction coefficient. By this parameter  $y^+$ , the boundary layer fluid domain can be subdivided into three sub-domains. The first, designated viscous sub-layer, starts from the wall up to  $y^+ < 5$ . This is followed by the Buffer Layer sub-domain between  $5 < y^+ < 30$ . The Logarithmic/Outer Region sub-domain is characterized by  $y^+ > 30$ .

CFX automatically turns on wall functions if the boundary layer is not adequately resolved by the mesh. However, this treatment of the boundary layer by wall-functions is considered by far not as high by the standard of quality as the treatment of the boundary layers by resolving them by the mesh. To ensure an adequate spatial resolution of the boundary layers, one has to resolve the flow domain so close to the walls that even the viscous sub-layer is resolved by some cells. For an accurate reproduction of a turbulent boundary layer, a general rule is that the first grid point off the wall should have a maximum distance of  $y^+ < 1$  from the wall. For a smooth mesh with an adequate expansion factor of the cells, around 5-10 grid points are then positioned in the viscous sub-layer.

$y^+$ -values are pre-estimated by empirical wall friction coefficients for the fully-turbulent flow of a flat plate in free air. After the computation is complete, it can be shown that the  $y^+$ -values of the cells closest to the wall are low enough to accurately reproduce the actual calculation of the velocity profile. For the relevant  $Re \approx 1 \cdot 10^6$ , an estimated friction coefficient of  $c_f = 4.5 \cdot 10^{-3}$  leads to a maximum absolute height of the cell nearest the wall of

$$y_{y^+=1} = \frac{y^+ \cdot \nu}{\sqrt{\frac{1}{2} U_\infty^2 \cdot C_f}} \approx 6 \times 10^{-6} \text{ m} . \quad (4.14)$$

Depending on the off-wall distance, the cell height in the boundary layer is set to increase with a maximum cell expansion factor of  $y_{n+1}/y_n \approx 1.3$ . This leads to around 35 cells occupying the boundary layer. This is considered reasonable for the logarithmic layer to be accurately resolved [161].

#### 4.5.2 Resolution of the Near Wake

By continuing the boundary layer point clustering behind the trailing edges of the slat, main wing and flap elements a fine resolution of the wake of each element is generated. Through this technique, confluence of the elements' wakes is treated with the necessary care. The wake refinement zones of slat and flap are merged behind the wing. With this mesh topology a refined region rises up to about two and a half times the flap chord length in inflow direction behind the flap's trailing edge (Figure 4-5b).

#### 4.5.3 SAS Grid

The design of a 2.5D grid for the SAS simulations by extruding the 2D RANS grid requires the specification of two main grid parameters. The first is the cell size  $\Delta z$  in the extruding direction. The second covers the complete span size of the domain  $L_z = N_z \cdot \Delta z$ , where  $N_z$  is the number of cells in spanwise direction. The extruded cells are programmed to be uniformly distributed. Cell size in the span direction is chosen to ensure that cells have similar edge lengths  $\Delta x \approx \Delta y \approx \Delta z$  in the regions where large scale turbulence is expected, which is preferable when using the SAS method. This leads to values of  $\Delta z_{RA16SC1} = 1.5$  mm for the validation-case and  $\Delta z_{RG} = 0.7$  mm for the research-case. The number of cells  $N_z$  has to be sufficiently large to enable the turbulent structures to develop. A number of  $N_z = 100$  is considered reasonable and thus used for all simulations.

The extruding direction is chosen to represent the sweep of the wing to be simulated. For the validation-case this leads to an extruding direction perpendicular to the airfoil-plane as the RA16SC1 validation-case features no sweep. For the research grids, the extrusion is performed in the  $x$ - $z$ -plane with an extrusion angle of  $\varphi = 24.5^\circ$ . This represents the  $\frac{1}{4}$ -chord sweep of the wind tunnel models outer wing. Figure 4-6 shows details of the 2.5D grid used for the RA16SC1-case. The two regions where the flow is assumed to be dominated by large scale turbulence are shown in Figure 4-6: the slat cove region in Figure 4-6a, and the flap gap region in Figure 4-6b.

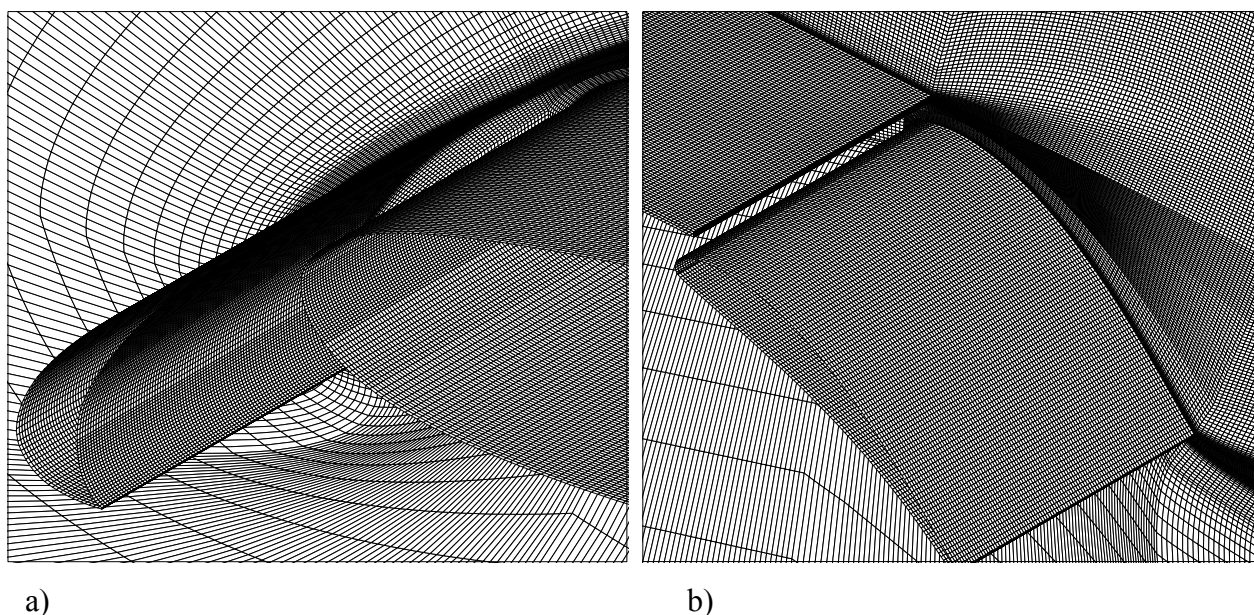


Figure 4-6: Details of the 2.5D surface mesh of the RA16SC1-case. a) Slat cove region; b) Flap gap region.

## 4.6 Computational Setup

CFX offers the possibility to choose values for a limited number of simulation parameters. It surely focuses more on usability than customization opportunities. The parameters chosen for the RANS simulations in this work are summarized in Table 4-1.

Table 4-1: Numerical parameters for simulations.

Parameter	Value
Temporal Discretization	Second order backward Euler scheme
Advection scheme	High Resolution
Problem type	Single Phase
Fluid	Air Ideal Gas
Heat transfer	Total Energy
Turbulence model	Shear Stress Transport
Reference pressure	1 atm
Fluid temperature	293 K
Buoyancy	non

The chosen advection scheme option *High Resolution* is a second order discretization of the convective terms. This discretization scheme is bounded and follows the boundedness principle used by Barth and Jespersen [18]. All computations were performed with double precision.

#### 4.6.1 Parameters for Transient Simulations

The parameters for the transient URANS and SAS simulations are essentially the same as those used for the steady RANS calculations. They differ in that the transient URANS and SAS simulations carry additional parameters related to the inner loop and outer time step. The outer time step was set to be equal to 3% of the convective time scale of the mean chord of the shortest wing element, i.e. the slat. Thus, the connected unsteady flow phenomena could be resolved through the simulation. For the research-case the outer time step  $\Delta t$  became

$$\Delta t = 3\% \cdot \frac{c_{Slat}}{U_\infty} = 3\% \cdot \frac{0.034 \text{ m}}{50 \text{ m/s}} = 2 \cdot 10^{-5} \text{ s}. \quad (4.15)$$

For the validation case RA16SC1 the outer time step  $\Delta t$  became

$$\Delta t = 3\% \cdot \frac{c_{Slat}}{U_\infty} = 3\% \cdot \frac{0.125 \text{ m}}{54 \text{ m/s}} = 7 \cdot 10^{-5} \text{ s}. \quad (4.16)$$

This timestep, combined with the fine mesh resolution, led to a Courant number of approximately unity for cells in the slat cove. The parameters for the inner loop of the transient simulations were kept constant at all times and are summarized in Table 4-2.

Table 4-2: Numerical parameters for inner loop of transient simulations.

Transient Parameter	Value
Minimum number of inner loops per outer time step	4
Maximum number of inner loops per outer time step	12
Residual Type	maximum
Residual Target	$5 \cdot 10^{-4}$

A minimum of four and a maximum of twelve inner loops are conducted to establish accuracy. If, after twelve loops, the residuals of the inner loop's calculation do not decline to values lower than the target value, the inner loop is aborted. The reason for this is that it is assumed the residual target will not be obtained by conducting more loops.

#### 4.6.2 Boundary Conditions

Two different boundary condition set-ups were used, one for the 2D RANS and URANS simulations and one for the 2.5D SAS-simulations. For the SAS-simulations, four different CFX-derived boundary conditions were applied: *Inlet* for the far field borders of the mesh in front of and below the airfoil; *Outlet* for the far field borders of the mesh behind and above the airfoil; *Wall* for the surfaces of slat, main wing, spoiler and flap; and *Domain interface* at the spanwise borders of the mesh to realize the translational periodicity of the

mesh in spanwise direction. Preselected values of the Cartesian velocity components at the inlet defined the angle of attack. This technique makes it unnecessary to create a new mesh every time  $\alpha$  is changed. Instead, only the preselected velocity components are adapted. Average static pressure is set over the outlet faces. An overview of the arrangement of this boundary condition set-up is illustrated in Figure 4-10.

For the RANS/URANS simulations, this boundary-condition set-up led to low frequency oscillations in the far-field of the mesh. As a consequence of this, the following boundary condition set-up was used instead: *Inlet* applied to the far field borders of the mesh in front of the airfoil; *Outlet* to the far field borders of the mesh behind the airfoil; *Opening* conditions set above and below the airfoil in the far-field; *Domain interface* to the spanwise borders of the mesh to realize the translational periodicity of the mesh in spanwise direction, in this case to enable the 2D setting; and *Wall* applied to the surfaces of slat, main wing, spoiler and flap. The preselected values of the velocity at the inlet carry only an  $x$ -component. Thus, the inner mesh had to be changed, in this case to realize the angles of attack for each angle to be investigated. At the opening, the relative pressure was set to zero, along the outlet the average pressure was set to atmospheric pressure. This is illustrated in Figure 4-9. The parameters for the boundary conditions are summarized in Table 4-3.

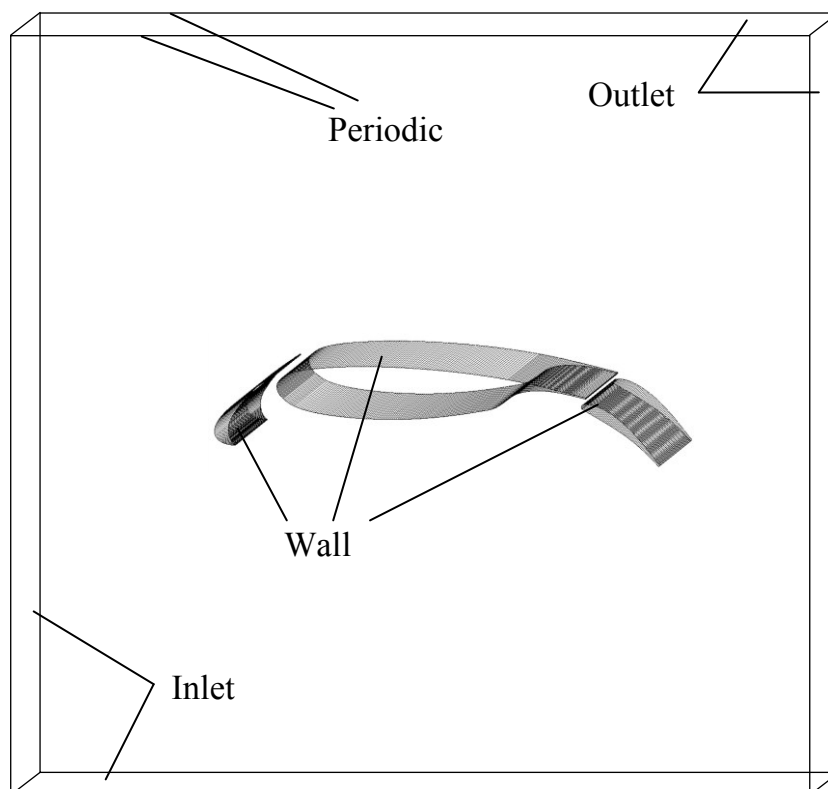


Figure 4-7: Boundary conditions illustration for 2.5D-SAS simulations; farfield is downscaled.

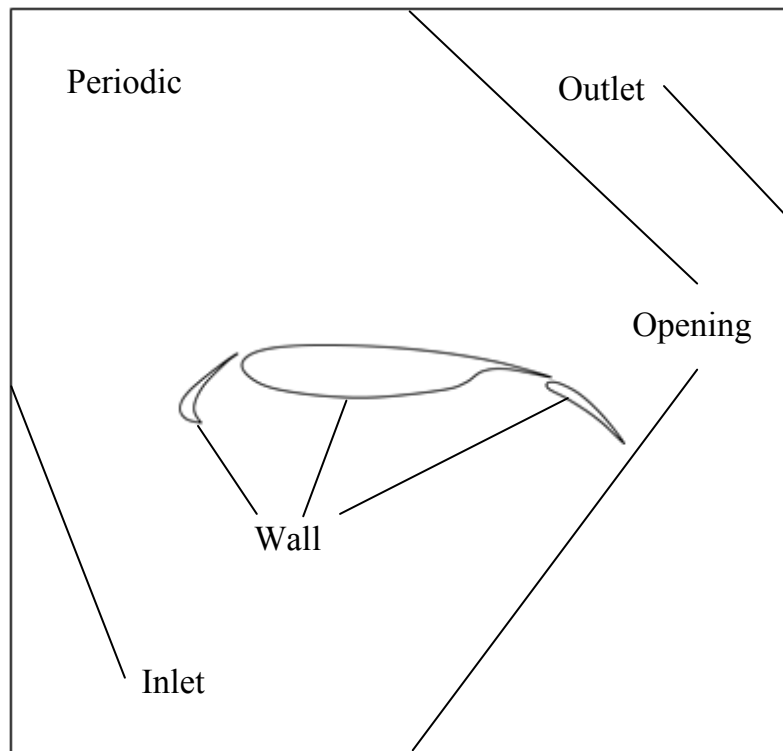


Figure 4-8: Boundary conditions illustration for 2D RANS/URANS simulations; farfield is downscaled.

Table 4-3: Boundary condition parameters.

Boundary condition	Parameter	Value
Inlet	Flow regime	subsonic
	Turbulence intensity	5% (Default)
	Velocity	Inflow Velocity
Outlet	Flow regime	subsonic
	Average static pressure	1 atm
Opening	Pressure	1 atm
	Flow direction	orthogonal
Wall	Boundary type	no slip
Domain interface	Translational periodicity	-

## 4.7 Postprocessing

This subsection sets out the mathematical foundations of the more sophisticated postprocessing techniques used in this investigation.

### *Vortex Core Visualization by $Q$ -criterion Isosurface*

A common method for visualizing the vortical structures in highly turbulent flow fields is to highlight the isosurfaces of the second invariant of the velocity gradient tensor  $Q$ . This is defined by

$$Q = -\frac{1}{2} \frac{\partial \bar{u}_i}{\partial x_j} \frac{\partial \bar{u}_j}{\partial x_i} = -\frac{1}{2} (\overline{S_{ij} S_{ij}} - \overline{\Omega_{ij} \Omega_{ij}}). \quad (4.17)$$

This method was used for the SAS simulations to point out the turbulent structures.

### *Streamlines*

Streamlines serve to display flow topology. They chart the path a small, neutrally buoyant particle would take through the flow domain, assuming the displayed solution to be in a steady state. The streamlines are defined by

$$\frac{d\bar{x}_s}{ds} \times \bar{u}(\bar{x}_s) = 0, \quad (4.18)$$

where  $\bar{x}_s$  is the parametric representation of one streamline at a moment in time.

### *Total Pressure Loss*

The local degree of distortion or spoiling of the flow is expressed by the total pressure loss coefficient  $K_L$

$$K_L = \frac{p_{t,\infty} - p_t}{p_{t,\infty}}, \quad (4.19)$$

where  $p_t$  is the local total pressure and  $p_{t,\infty}$  the mean freestream total pressure.

## 4.8 Validation of the Numerical Method

Before the chosen CFD methods can be used for the flow topology analysis of the research case they have to be validated. This is done to show the capabilities and limits of the different methods when applied to this type of flow problem. The validation comprises two parts: First, CFD simulations are executed using the RA16SC1-case. This case has similar high-lift geometry as the research case; however, extensive experimental data has been published for an evaluation of the results [14]. This first part makes clear that the chosen method is valid to simulate the flow structures typical for this type of geometry. The second part comprises a mesh convergence study to show that the produced results are second order convergent in terms of mesh resolution.

#### 4.8.1 Validation Case RA16SC1

The airfoil RA16SC1 used for the validation is representative of a high-lift airfoil in approach setup. It comprises slat, main wing and Fowler flap. The RA16SC1-airfoil has received extensive experimental investigation [14]. Many numerical investigations have also been conducted [52]. The experimental data from a measurement campaign by DLR in cooperation with Airbus Germany in LSWT Bremen was used to validate the CFD methods chosen for this investigation. Pressure tabs are distributed all over the surfaces of slat, main wing and flap to assess the pressure distribution on all surfaces, while PIV measurements were used to provide flow field data in the vicinity of the airfoil.

#### 4.8.2 Validation of RANS method

The DLR wind tunnel tests studied different angles of attack. For the validation, angle of attack  $\alpha_{exp} = 12^\circ$  was chosen exclusively. As the presence of wind tunnel walls affects flow, the angle of attack under assessment cannot easily be transferred to the numerical setup. This means that the angle of attack set for the numerical simulations is evaluated by systematically varying the angle of attack until the suction peaks of slat and main wing are matched. Figure 4-9 shows the pressure distribution on the slat, main wing and flap surfaces gathered by DLR in the  $\alpha_{exp} = 12^\circ$  tests, as well as the results from the  $\alpha_{num} = 10^\circ$  and  $\alpha_{num} = 11^\circ$  angle 2D RANS simulations. By comparing the results from the two tests it was found that in the 2D RANS simulation an angle of  $\alpha_{num} = 11^\circ$  best represents the experimental case.

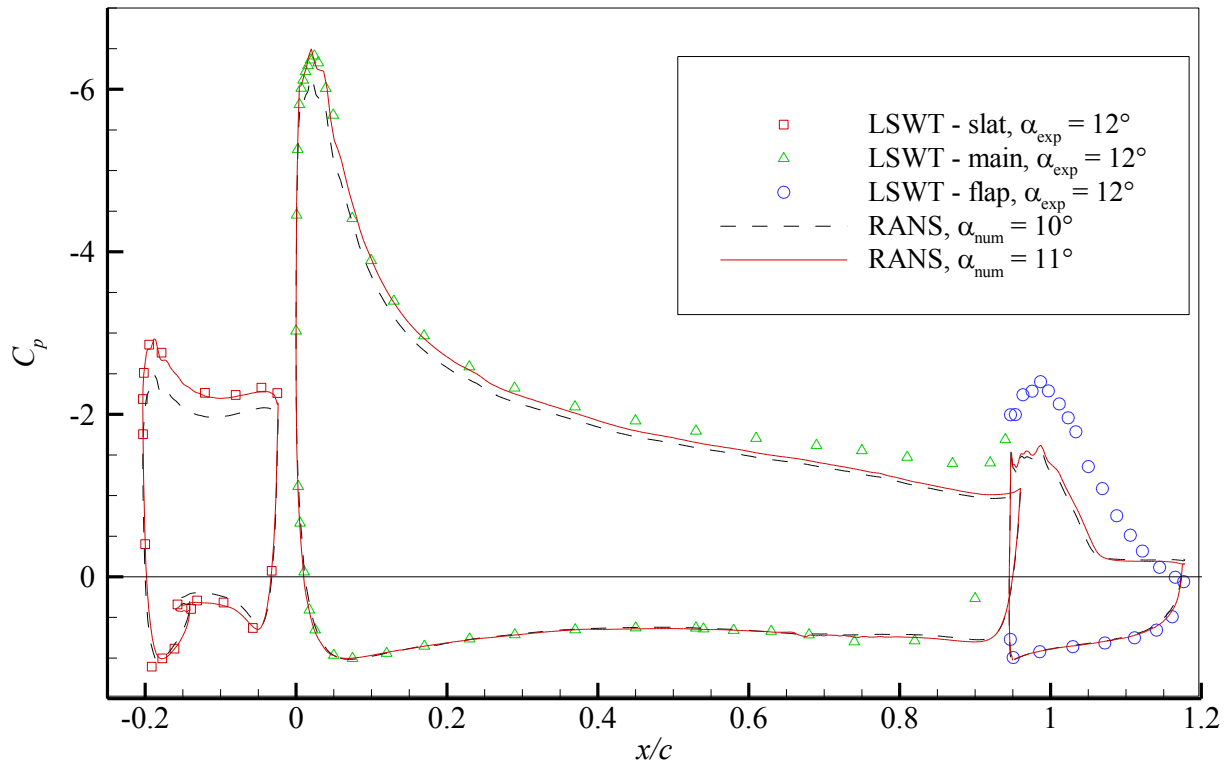


Figure 4-9: Pressure coefficient on the surfaces of the RA16SC1 airfoil. Experimental results of DLR; own RANS simulation results for  $\alpha_{num} = 10^\circ$  and  $\alpha_{num} = 11^\circ$ ,  $U_\infty = 54\text{m/s}$ ,  $Re_\infty = 1.8 \cdot 10^6$ .

The pressure distribution shapes and suction peaks produced by the simulation for the slat and main wing adequately match their experimental equivalents. Large differences appear on the upper surface of the flap, with the experimental values constantly rising towards the trailing edge of the flap. This suggests that there is only minimal flow separation. This shape is not reproduced by the RANS simulations. Here, a pressure plateau over the trailing half of the flap length indicates a large flow separation.

The total velocity distribution around the airfoil also required validation. Figure 4-10a displays the comparative results for the DLR's PIV measurements, Figure 4-10b, the  $\alpha_{num} = 11^\circ$  angle RANS simulation.

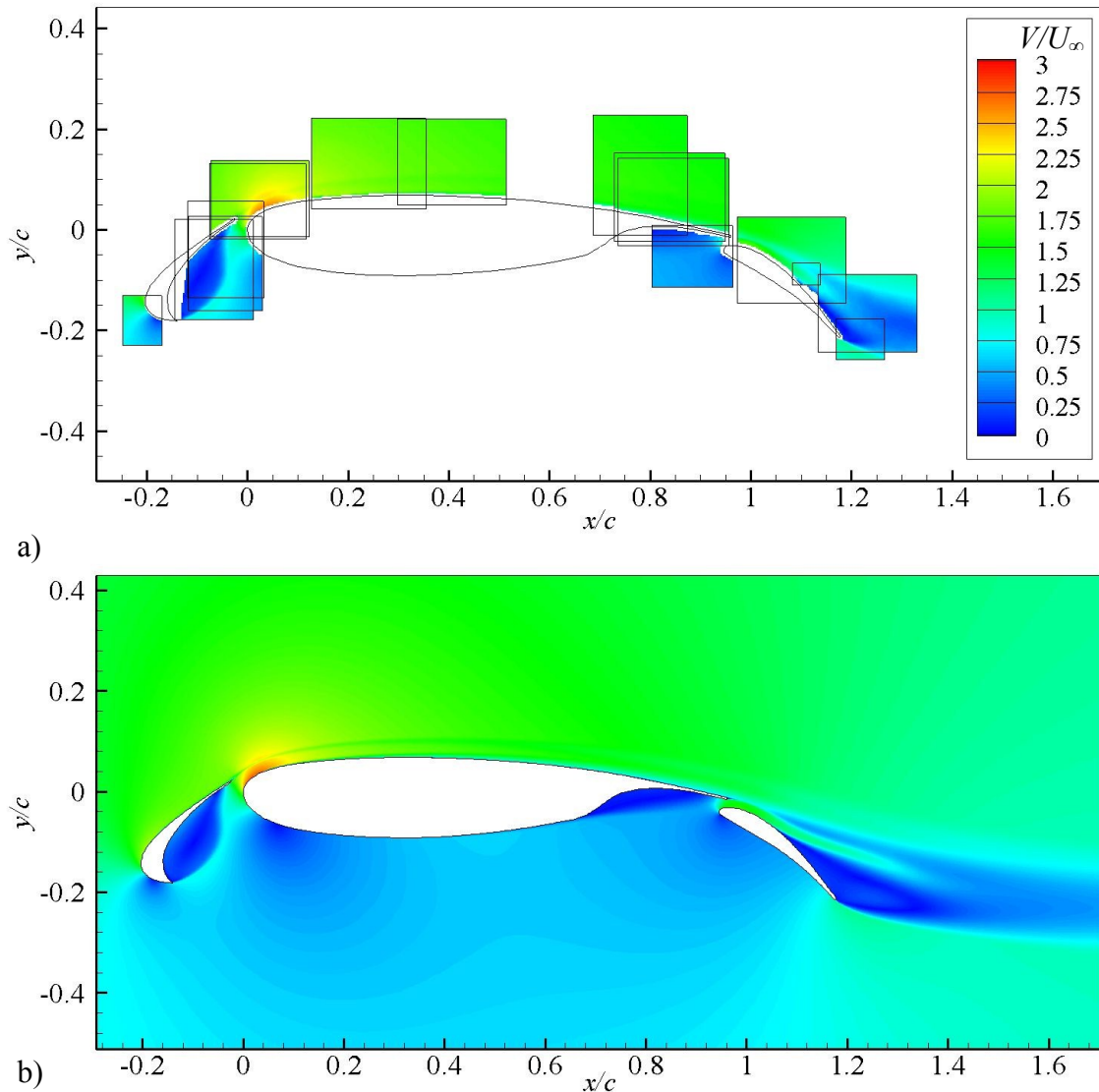


Figure 4-10: Velocity distribution around RA16SC1 airfoil,  $U_\infty = 54\text{m/s}$ ,  $Re_\infty = 1.8 \cdot 10^6$ . a) PIV measurements by DLR; b) own  $\alpha_{num} = 11^\circ$  RANS simulation.

In most areas the velocity distribution around the airfoil and the respective flow features are adequately reproduced by the simulations. Predictably, the largest differences arise on the top of the flap, where the flow topology is highly unstable. In the RANS simulation there is a clear large flow separation zone starting at about a third of the flap length. In contrast, the results from DLR's PIV experiments show a flap separation, which is much more moderate and limited to the trailing edge of the flap.

These results show that the RANS numerical method can replicate the necessary high-lift flow-topology with a good level of accuracy. The weakness of this method lies in reproducing the exact position of flow separation on curved surfaces. In terms of high-lift geometry, this weakness impacts mainly on the flow separation on the top surface of the flap.

## 4.8.3 Validation of URANS method

The high convergence of the RANS simulation of the validation case led to a limit cycle oscillation with a deviation in lift force of only  $\Delta C_L \approx 0.3\%$ . Despite this good result, a URANS simulation was also conducted to validate the results produced by this method. Again an angle of attack of  $\alpha_{num} = 11^\circ$  was chosen. It turned out, that no distinct oscillation appeared in the URANS simulation results. Instead, they showed a steady solution. Figure 4-11 compares this solution with both the RANS simulation and the experimental DLR results by showing the pressure distributions over the three wing element surfaces.

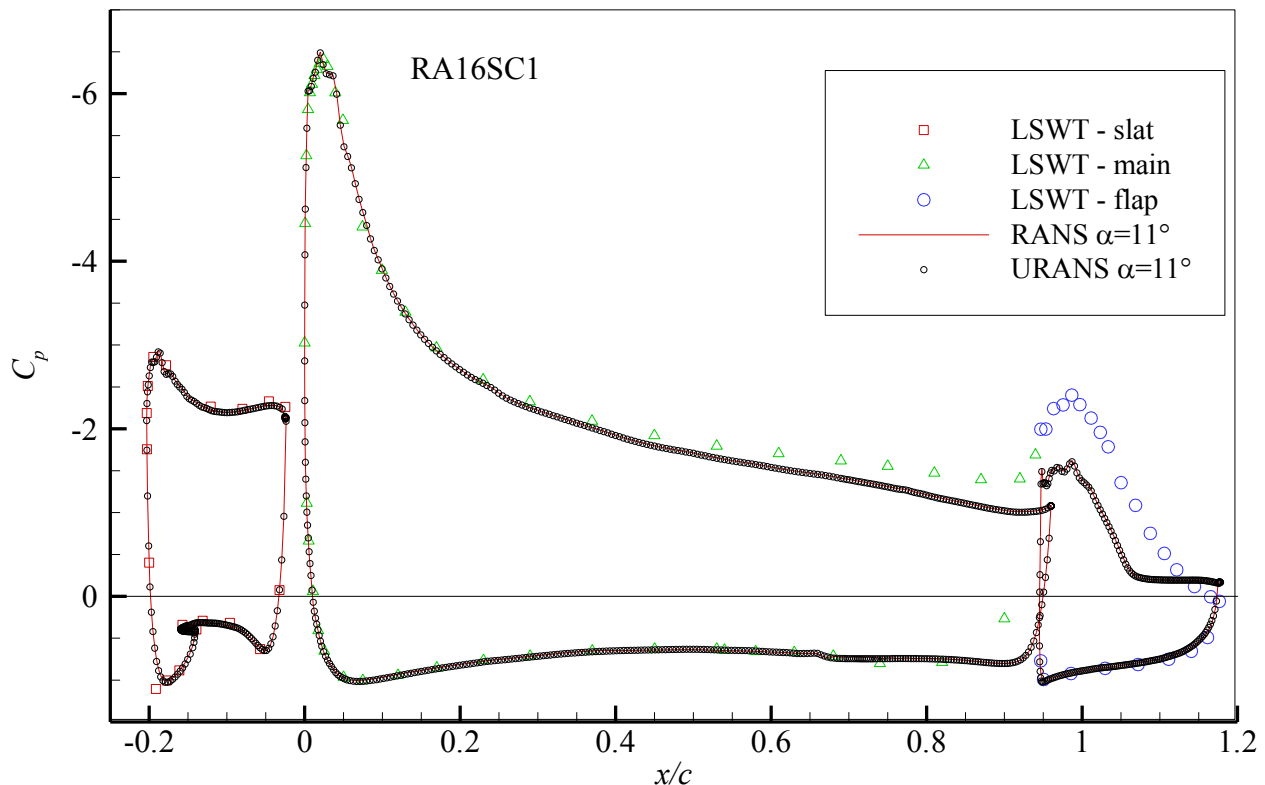


Figure 4-11: Pressure coefficient on the surfaces of the RA16SC1 airfoil. Experimental results of DLR, own RANS and URANS simulation results at  $\alpha_{num} = 11^\circ$ ,  $U_\infty = 54\text{m/s}$ ,  $Re_\infty = 1.8 \cdot 10^6$ .

There is almost no difference between the mean RANS and URANS simulation results leading, for example, to a mean lift coefficient for the URANS simulations which is only 0.19% lower than the mean lift coefficient derived from the RANS simulations. In addition, the local flow features are resolved in exactly same way, as is apparent in the pressure distribution comparison in Figure 4-11.

## 4.8.4 Validation of SAS method

The SAS method should reproduce the detailed turbulent structures of the flow in the highly turbulent regions. This cannot be validated by DLR experiments as no time-resolved data are available. Instead, the SAS results are compared qualitatively with

Deck's RA16SC1-case Zonal LES (ZLES) simulations [52]. One means to visualize turbulent flow structures is to show the iso-surfaces of the Q-criterion (4.7). This is done for the slat flow in Figure 4-12a. Figure 4-12b compares these results with Deck's.

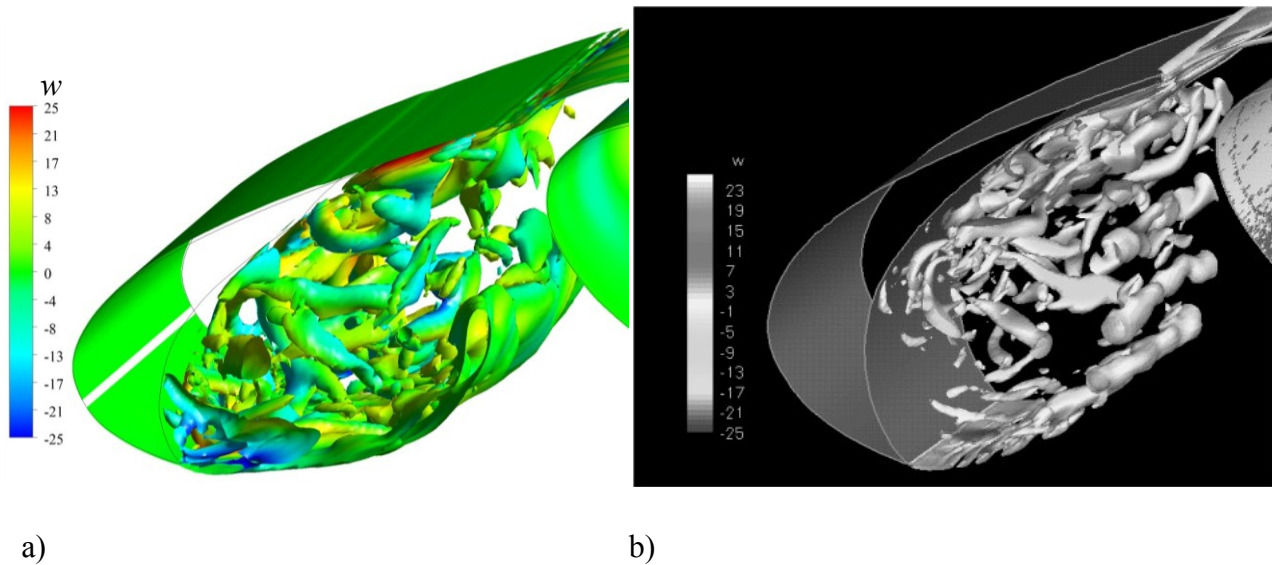


Figure 4-12: Isosurfaces of the Q-criterion for the RA16SC1 simulation, slat area,  $U_\infty = 54\text{m/s}$ ,  $Re_\infty = 1.8 \cdot 10^6$ . a) SAS method,  $Q = 3.3 \cdot 10^6 \text{ s}^{-2}$ ; b) Zonal LES by Deck [52].

Figure 4-13 shows this comparison for the flap flow.

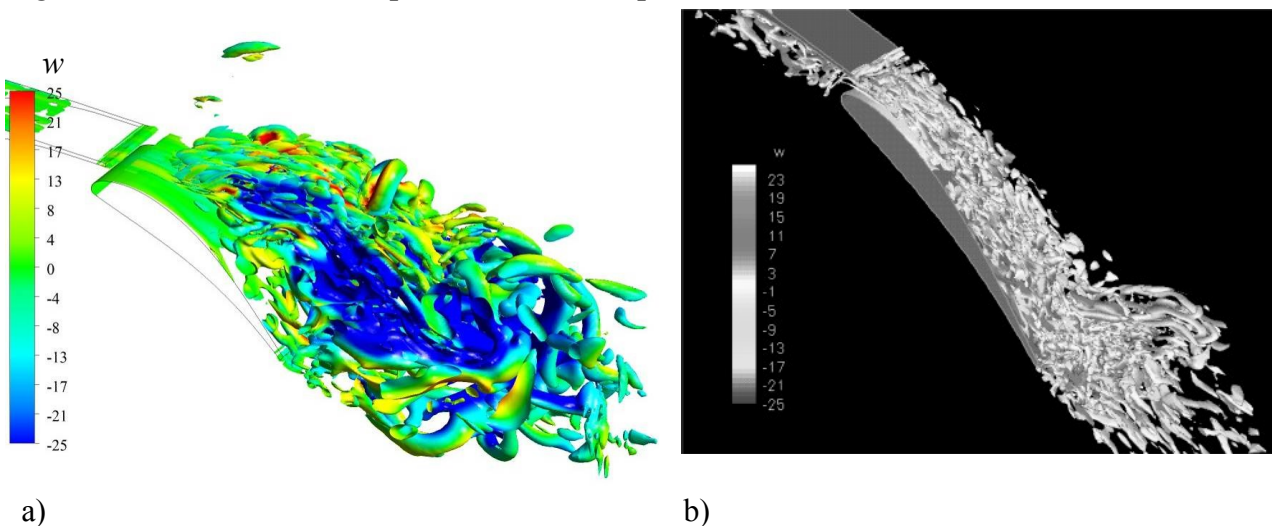


Figure 4-13: Isosurfaces of the Q-criterion for the RA16SC1 simulation, flap area,  $U_\infty = 54\text{m/s}$ ,  $Re_\infty = 1.8 \cdot 10^6$ . a) SAS method  $Q = 3.3 \cdot 10^6 \text{ s}^{-2}$ ; b) Zonal LES by Deck [52].

The SAS results are very similar to Deck's ZLES results in the slat cove. The vortices stay close to the flap surface in the ZLES case, whereas they lift from the flap for the SAS simulations. This indicates that in the SAS simulation the flap flow is separated much further upstream. In both cases, small vortex structures of similar size appear, but the largest structures are even larger for the SAS case. The structures in both cases survive for

similar running length values behind the flap end. All in all the vortical flow structure is comparable for both simulations.

#### 4.8.5 Grid Convergence Study

Grid convergence is an important process in verifying that discrete numerical solutions provide valid representations of the governing partial differential equations describing the phenomenon under investigation. A grid convergence study was conducted to validate a second order convergence focusing on lift, drag, and pitching moment coefficients for the 2D Baseline Research Mesh at  $\alpha = 10^\circ$ . It used the production mesh (PM) as well as a coarsened mesh (CM) and a refined mesh (FM). One requirement for a meaningful grid convergence study is uniform grid refinement. This means the grid family must be parametrically equivalent where a coarser mesh is a subset of the next denser mesh. For the present investigation, this was realized with the limitation that the near wall mesh point distribution was adapted to approximately maintain the  $y^+$ -values of the cells nearest the wall, and that there be no coarsening of the outer mesh for CM compared to PM. The global blocking structure remained unchanged. The properties of the three meshes are grouped in Table 4-4.

Table 4-4: Mesh parameters for mesh convergence study.

Mesh Designation	Cell number	$y^+$ -values
2D Production Mesh (PM)	117984	$y^+ \leq 1$
2D Coarse Mesh (CM)	68634	$y^+ \leq 1$
2D Fine Mesh (FM)	215064	$y^+ \leq 1$

By conducting RANS simulations with each of the three meshes, it emerged that the solutions did not converge satisfactorily. When investigating the flow field in the symmetry plane at timestep  $n = 250$  with the PM mesh shown in Figure 4-14, it became clear that the reason for this poor convergence was the instability of the flow in the area of the top surface of the flap and rear wing in the RANS simulation.

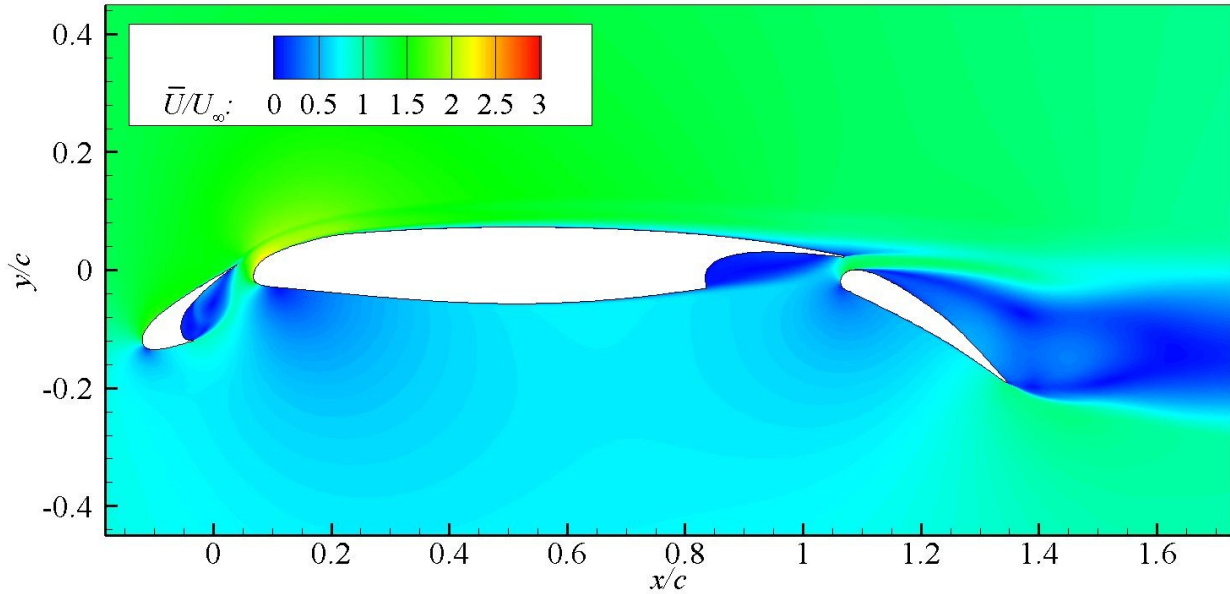


Figure 4-14: Absolute mean velocity distribution  $\bar{U}/U_\infty$  in symmetry plane,  $U_\infty = 50$  m/s,  $Re_\infty = 1 \cdot 10^6$ .

To address this problem, additional URANS simulations were conducted. The simulations were run in the URANS mode for sufficient simulation durations, so that a periodic solution state could be attained. This done, statistical averaging was performed over the reasonable simulation time of  $n \approx 4000$  iterations, which is equivalent to  $\Delta t \approx 80$  ms or about 32 periodic cycles. This provided the arithmetic mean aerodynamic coefficients of lift, drag, and pitching moment presented in Table 4-5.

Table 4-5: Mesh parameters for mesh convergence study.

Mesh Designation	$C_L$	$C_D$	$C_M$
2D Production Mesh (PM)	2.838	0.1907	-1.387
2D Coarsened Mesh (CM)	2.815	0.1904	-1.375
2D Refined Mesh (FM)	2.862	0.1918	-1.398

As mentioned above, each element of the overset grid family used in this study was parametrically equivalent to one another, with all grids converging on the same level. These requirements allow for a meaningful application of Richardson extrapolation, assuming the method's second order spatial accuracy. The coefficients were plotted against grid point number  $n$  raised to the power of -1, which is proportional to the squared 2D meshes' cell edge length  $h^2$ . This is shown in Figure 4-15.

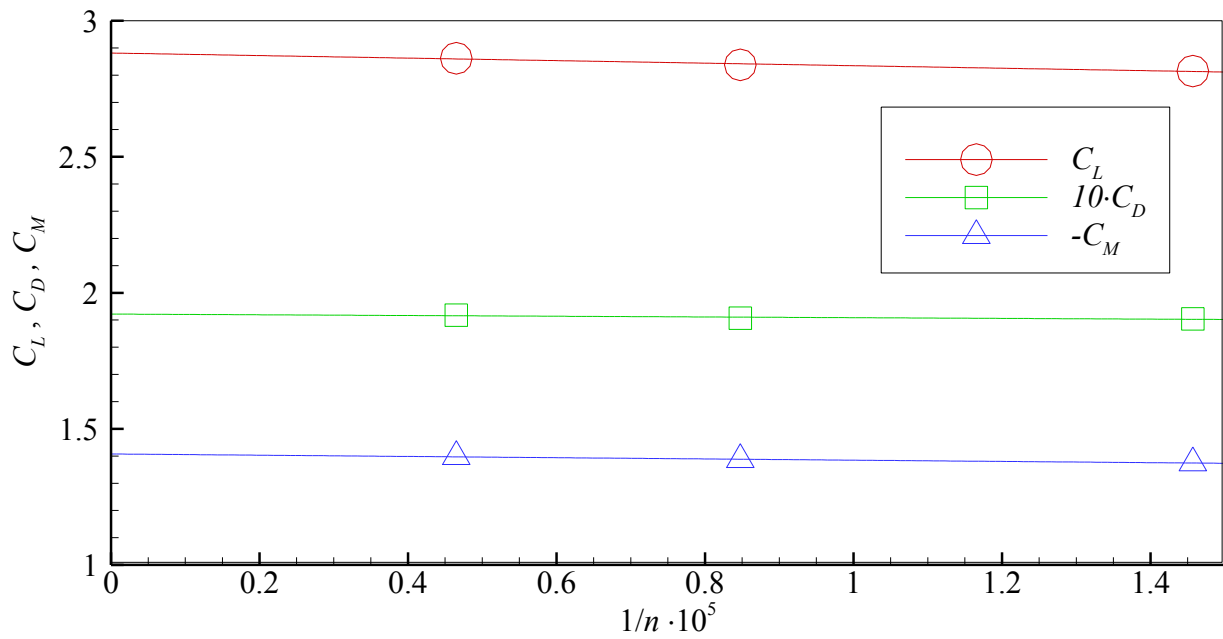


Figure 4-15: Grid convergence study for lift, drag, and pitching moment coefficients.

The first order regression lines are also plotted in Figure 4-15. When the grid refinement trend forms a straight line, asymptotic grid convergence is assumed to have been achieved. All datasets exhibit adequately linear trends, meaning grid convergence has been achieved and PM can be used for the investigation's simulations. In addition, the coefficient values arrived at theoretically using an infinitely fine mesh can be metered at zero abscissa.



# 5. EVALUATION OF DEVICE PERFORMANCE

The performance of the investigated devices is evaluated in this chapter. This evaluation is focused on the devices' task to enable steep approaches of Commercial Transport Aircraft (CTA). The force measurements, conducted in several wind tunnel campaigns, serve exclusively as basis for the evaluation of the flight mechanical performance. Before these evaluations are examined, the accuracy of the underlying measurements is discussed in section 5.1. The data is examined with a view to determine what effect the different devices have on the steep approach performance, the lateral control and the aerodynamic stability (sections 5.2 to 5.4). After that, other non-flight mechanical evaluation fields of minor priority in this project are discussed shortly in section 5.5. From the high number of evaluation fields, it becomes clear, that the design of devices for a commercial aircraft capable to conduct steep approaches must be regarded as a multi-disciplinary design optimization problem. The chapter is concluded by a synthesis in section 5.6. An excerpt of the results was already published in Refs. [97] and [98].

## 5.1 Statistical Evaluation of the Force Measurement Uncertainty

The uncertainty is made up of two components - bias and precision [45]. Both are assessed below.

### 5.1.1 Bias

The absolute bias error is of subordinate importance for this investigation, because all results are referred to a Baseline (BL). To rule out the trend bias error, where a systematic change of the measurement values in only one direction happens over measurement time, two long duration measurements, one of the BL and one of the configuration with Conventional Spoiler (CS) deployed at  $\delta_s = 30^\circ$ , each consisting of one hundred serial measurements were conducted. The value of the angle of attack was chosen to be  $\alpha = 5^\circ$  for the baseline case and  $\alpha = 20^\circ$  for the spoiler case. The lift coefficient over measurement time shows in each case a horizontal characteristic, which rules out a trend bias error for these measurements (Figure 5-1) and this conclusion persists for all other measurements, as the measurement technique is not changed compared to these long duration measurements. All the other coefficients behave analogously, so that they suffer again no trend bias.

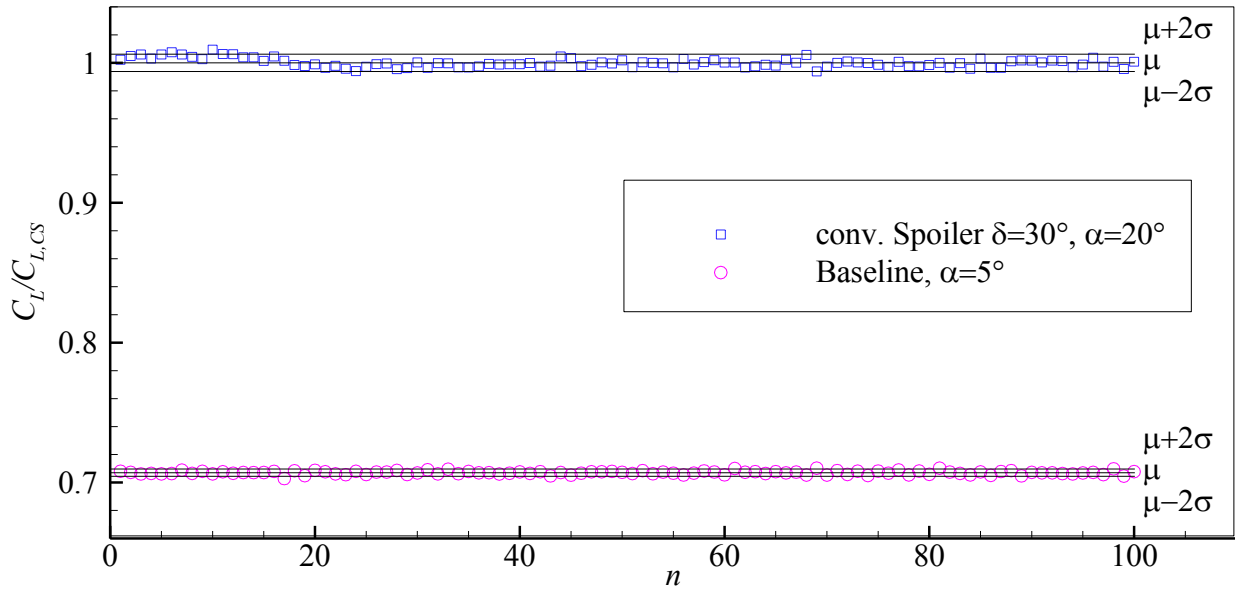


Figure 5-1: Time series of lift coefficients for  $n = 100$  repeated measurements with constant configuration baseline at  $\alpha = 5^\circ$  and Conventional Spoiler with  $\delta_S = 30^\circ$  at  $\alpha = 20^\circ$ .

### 5.1.2 Precision

Precision, also called repeatability, can be quantified by the standard deviation  $\sigma$  of a data series  $y$ :

$$\sigma = \sqrt{\frac{\sum_{i=1}^n (y_i - \bar{y})^2}{(n-1)}} \quad (5.1)$$

The measurement data is assumed to be normally distributed. Thus, the sample mean  $\mu$  and standard error  $\sigma$  can be used to calculate approximate confidence intervals for the mean. The 95%-confidence intervals, which correspond to values of  $\mu \pm 2\sigma$ , are included in Figure 5-1 for the two long duration measurements. There is quite a big difference between the two confidence intervals. The reason for this is that at  $\alpha = 20^\circ$  global stall begins to occur, and thus, not only measurement precision plays a role, but also the highly unsteady physical stall phenomena are overlapping the measurement precision.

For the drag and lift, as well as rolling and pitching moment coefficient measurements, the repeatability standard deviations are estimated with all configurations as basis to be  $\Delta C_D = \pm 0.003$ ,  $\Delta C_L = \pm 0.02$ ,  $\Delta C_l = \pm 0.008$ , and  $\Delta C_m = \pm 0.005$  respectively for  $C_L \leq 0.9 \cdot C_{L,max}$ . This leads to the respective uncertainties of  $U_{C_D} = 0.006$ ,  $U_{C_L} = 0.04$ ,  $U_{C_l} = 0.016$ , and  $U_{C_m} = 0.01$  at a 95% confidence level with the assumption of normally distributed signals. These error bands include measurement resolution, point-to-point repeatability, and geometric uncertainties. That is slight variations in angle settings for repeated runs of one configuration. Given this repeatability of the measurements, relative

trends in aerodynamic coefficients between the investigated configurations can be clearly discerned.

### 5.1.3 Bias between the Campaigns

The beginning of global stall is highly sensible for small changes in geometry and flow conditions. That leads to a limited bias between the campaigns, expressing in varying stall angles of attacks  $\alpha_{max}$  and associated aerodynamic coefficients for the same configurations and different wind tunnel campaigns. However, the relative variation of the coefficients caused by the geometrical variation relative to the Baseline can be assessed with appropriate accuracy. For this reason, the Baseline configuration was repeatedly measured for each campaign. All results discussed in the following relate to the BL-configuration coefficients of the associated campaign. Thus, statistically significant conclusions can be derived.

### 5.1.4 Accuracy Checks During Measurement Campaigns

As already mentioned in subsection 3.6.1, apart from the long duration measurements to assess the statistics, all measurements were conducted twice to ensure a sufficient repeatability. It was also checked that the data does not contain runaway values. In addition, systematic errors caused by apparatus, methods, or experimenter have to be avoided. These systematic errors cannot be controlled by statistics [3], [165]. Instead, this has to be achieved by a precise and thorough way of working.

### 5.1.5 Hysteresis Loop in Polars

A hysteresis loop phenomenon was detected during the first  $\alpha$ -polar measurements. When conducting force measurements for  $\alpha$ -polars sweeping  $\alpha$  from moderate negative values to post stall values and back to moderate negative values this hysteresis phenomenon is observed for a restricted  $\alpha$ -interval. It manifests in a roughly constant difference in the forces and moments on the backward  $\alpha$ -sweep compared to the forward  $\alpha$ -sweep. The interval comprises the  $\alpha$ -region in the high pre-stall domain to angles of attack in the post stall domain. Amongst others, the lift is reduced in this region on the backward  $\alpha$ -sweep compared to the forward  $\alpha$ -sweep. The phenomenon is illustrated with the help of a  $C_L$ - $\alpha$ -polar in Figure 5-2.

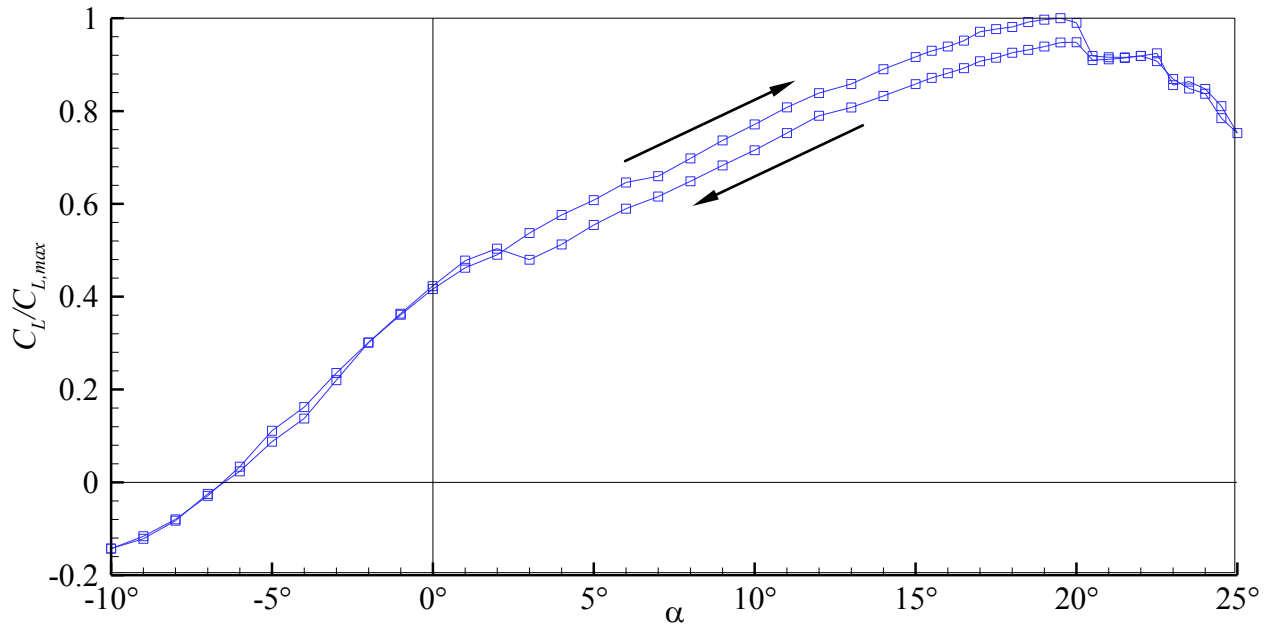


Figure 5-2:  $C_L$ - $\alpha$ -polar for forward and backward  $\alpha$ -sweep.

This kind of phenomenon was already observed in similar campaigns with comparable wind tunnel models by others, for example in Ref. [17]. There, the phenomenon was identified to be typical for low speed low turbulence wind tunnel tests and is more precisely a laminar separation bubble. In this process, sudden stall occurs on the flap surface due to the bursting of a bubble in its nose region. Once bursting occurs, the hysteresis loop in the  $C_L$ - $\alpha$ -polar is observed. To eliminate the corruption of the measurement data by this phenomenon, for all measurements contributing to this work  $\alpha$ -sweeps started at the same lowermost  $\alpha$ .

### 5.1.6 Reynolds Number Effects

To assess Reynolds number effects on the results, three Reynolds numbers based on the wing mean aerodynamic chord ( $c = 0.308$  m) were tested for the BL case. All other balance-measurement results, discussed later in this work, were determined by measurements at the highest possible Reynolds number  $Re \approx 1 \cdot 10^6$ . To alter the  $Re$ -number, the wind tunnel inflow velocity is varied to  $U_\infty = 25$  m/s,  $U_\infty = 40$  m/s, and  $U_\infty = 50$  m/s, leading to inflow  $Re$ -numbers of  $Re_\infty \approx 5 \cdot 10^5$ ,  $Re_\infty \approx 8 \cdot 10^5$  and  $Re_\infty \approx 1 \cdot 10^6$ . This is assumed a valid approach for  $Re$ -number variation for subsonic wind tunnel tests, where compressible effects can be neglected. Figure 5-3 shows the lift over drag polar to assess the effects.

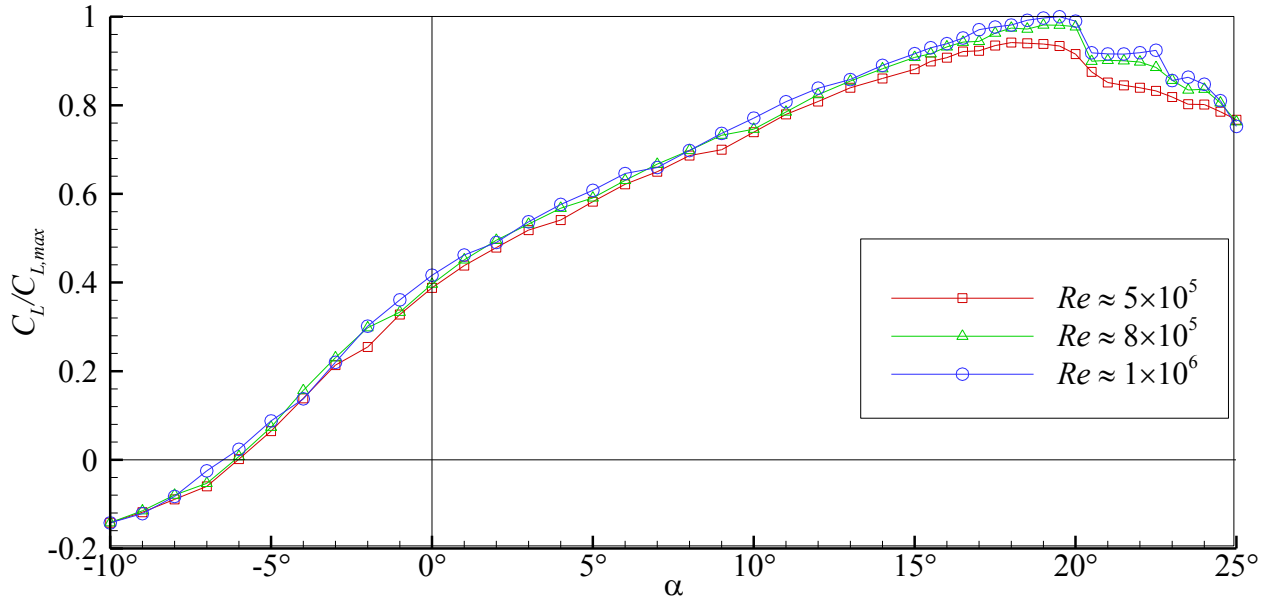


Figure 5-3: Lift over drag polar for Baseline,  $Re_\infty \approx 5 \cdot 10^5$ ,  $Re_\infty \approx 8 \cdot 10^5$  and  $Re_\infty \approx 1 \cdot 10^6$ .

There is some minor effect of the  $Re$ -number on the aerodynamic coefficients. It emanates from the data that the highest  $Re$ -number is close to the critical  $Re$ -number, as the aerodynamic coefficients show a converging behavior from the intermediate to the highest  $Re$ -number, resulting in only small differences in the coefficients between the intermediate and the highest  $Re$ -number measurements compared to the difference between the lowest and the intermediate  $Re$ -number measurements.

## 5.2 Evaluation of Devices Regarding Steep Approach Performance

The effect of the investigated devices on the parameters relevant for the steep approach is discussed in the following. To show the effect of the different air-brake devices regarding the three aerodynamic coefficients associated to longitudinal motion,  $C_L$ ,  $C_D$ , and  $C_M$ , derived in subsection 3.7.1, the polars of  $C_D$  over  $C_L$  as well as  $C_M$  over  $C_L$  are contrasted first. From these aerodynamic coefficients of the longitudinal motion, we can then determine the steep approach parameters derived in subsection 2.4.2. This is the descent velocity  $V_S$  and the descent angle  $\gamma$ . Both parameters are depicted over the approach velocity  $V_{app}$  and in each case with reference to the respective BL, leading to the crucial parameters change in approach-velocity  $V_{app}/V_{app,ref} - 1$ , change in descent-velocity  $V_S/V_{S,ref} - 1$ , and change in descent-angle  $\gamma/\gamma_{ref} - 1$ .

It has to be emphasized that the conclusions from the conducted analysis in the strict sense are only valid for the used model configuration, because the effectiveness of the investigated devices is affected to some extent by the particular high-lift devices. But the setting of these high-lift devices was kept constant for all further tests. Therefore, generalized conclusions about the trends in the effectiveness of the devices can be drawn.

### 5.2.1 Aerodynamic Force and Moment Coefficient Polars

In this subsection,  $C_L$  over  $C_D$  as well as  $C_M$  over  $C_L$  polars are shown per device to illustrate the effect of the parameters for each device. Furthermore, a comparison of the different devices is conducted for selected parameter values. The data points are in each case plotted for all set  $\alpha$  up to  $\alpha_{max}$  and one further data point in the stall regime. The coefficients are plotted relative to the reference value, namely the respective coefficient of BL at MVAP, defined in subsection 2.4.2. The two most important data evaluated from the  $C_L$  over  $C_D$  polar is the deficit in  $C_{L,max}$  per air-brake configuration and the additional drag created by the respective air brake in the region, where approaches are feasible. As explained in Eq. (7), this is the case for  $C_L \leq 0.66 \cdot C_{L,max}$ .

In Figure 5-4, the polars are shown for the Conventional Spoiler (CS) with different deflections from  $\delta_s = 0^\circ$  to  $\delta_s = 60^\circ$ . In Figure 5-4a, the sequence of the curves is monotonous for an increase in spoiler deflection to higher drag coefficients and lower maximum lift coefficients. The pitching moment characteristics in Figure 5-4b is split into two parts: For low lift coefficients around  $C_L \approx 0$  the curves are about parallel with a small variation in the moment coefficients, while for high lift coefficients, most relevant for approach, the curves are still about parallel but the difference in the moments is much larger. Over the whole range of lift coefficients the moment increases monotonously towards a nose up behavior for an increase in spoiler deflection angles.

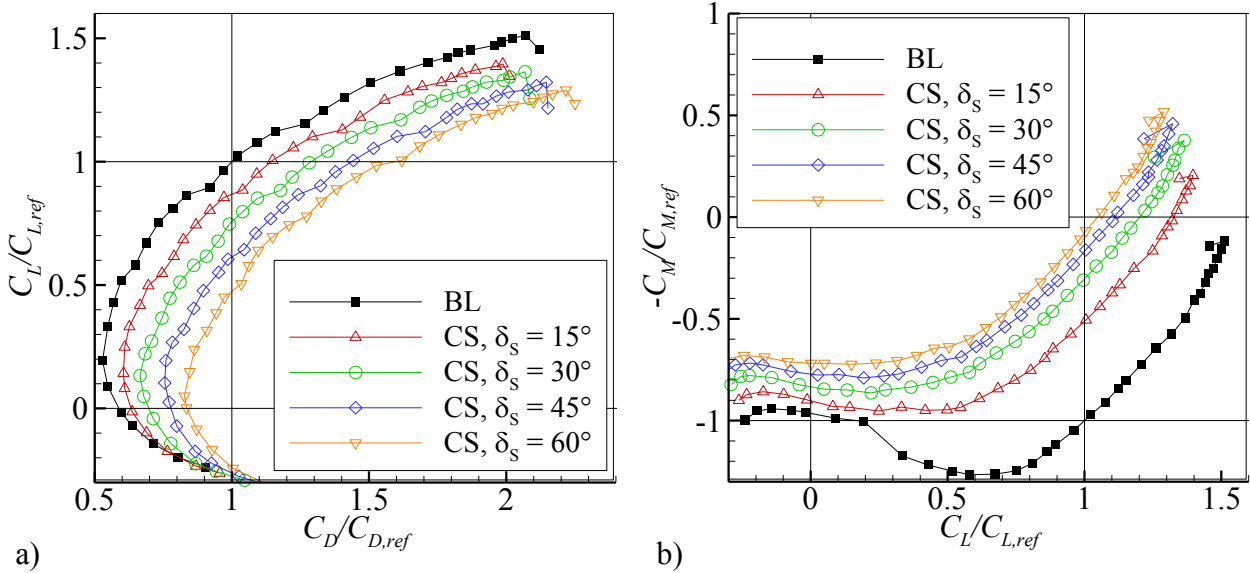


Figure 5-4: Polars for BL and CS; a)  $C_L$  over  $C_D$ , b)  $C_M$  over  $C_L$

Next, we have a look at the characteristics of the Adverse Spoiler (AS) configurations in Figure 5-5. Again, there is a monotonous increase in drag coefficient for higher spoiler deflection angles. However, this increase is not as pronounced as for the conventional spoiler. For high  $C_L$ -values, there is even no difference observable between the curves with different deflections of the AS. There are even data points, where the  $\delta_s = 30^\circ$ -curve

intersects the  $\delta_s = 15^\circ$ -curve. Also, there is no clear trend of an decrease of  $C_{L,max}$  for an increase in  $\delta_s$ : All AS-curves have a significantly lower  $C_{L,max}$  compared to the Baseline, but stay at about the same level for an increase in  $\delta_s$ . Similar to the CS-configurations' behavior the pitching moment coefficient curves in Figure 5-5b are split into two regions: For low  $C_L$ -values around  $C_L \approx 0$ , the curves are very close together with  $C_M$  increasing only slightly towards a nose up behavior for higher  $\delta_s$ -values with the difference between the values for  $\delta_s = 15^\circ$  and BL being about zero. This behavior stays the same for higher  $C_L$ -values, but this time the difference between Baseline and the AS-cases is significantly larger. Finally, the difference in  $C_M$  between the different  $\delta_s$ -curves diminishes for higher  $C_L$ -values and more or less disappears at  $C_L = C_{L,max}$ , where all AS-configurations show a nose up behavior.

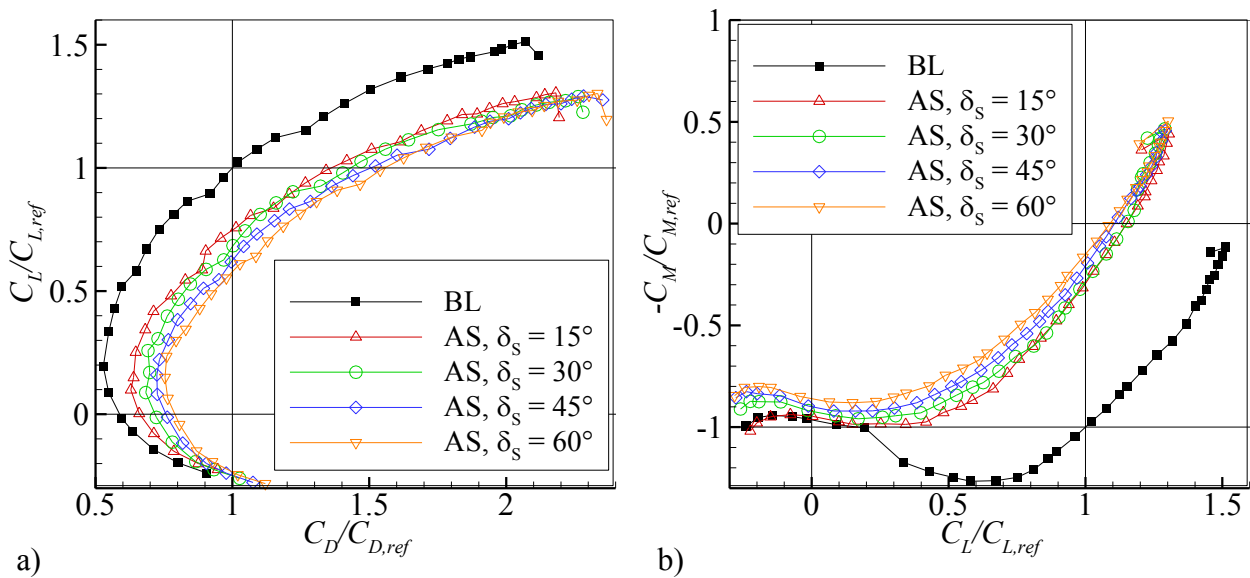


Figure 5-5: Polars for BL and AS; a)  $C_L$  over  $C_D$ , b)  $C_M$  over  $C_L$ .

Next, the results for the cases with the Advanced Adverse Spoiler (AAS) with different deflection angles are shown in Figure 5-6. Similar to the results with CS and AS, the increase in  $C_D$  is monotonous for an increase in  $\delta_s$ . However, there is a slight decline in  $C_{L,max}$  for an increase in  $\delta_s$ , which is in contrast to the AS-results. Looking at the  $C_M$ -characteristics, this is very similar to the conventional spoiler for low lift coefficients with a clear gap between the  $C_M$ -curves of BL and the AAS-cases, which is increasing towards a nose up behavior with an increase in  $\delta_s$ . For higher  $C_L$ -values, the characteristics is closer to the AS-case with a narrowing of the gaps between the curves.

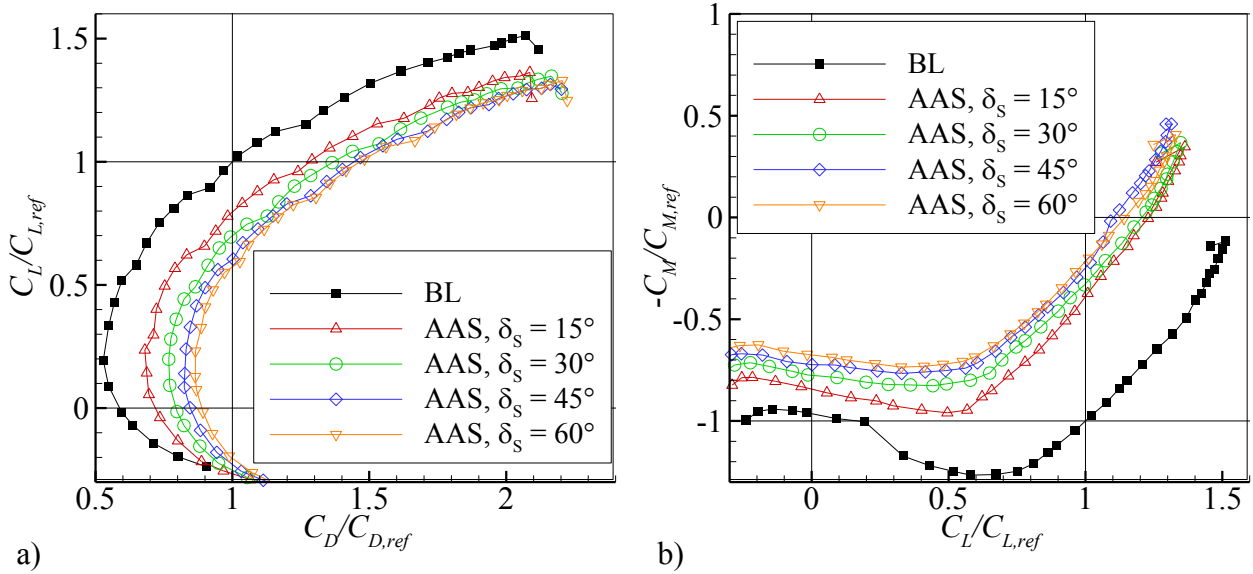


Figure 5-6: Polars for BL and AAS; a)  $C_L$  over  $C_D$ , b)  $C_M$  over  $C_L$ .

In Figure 5-7, the lift over drag polar and pitching moment polar are plotted for CS, AS, and AAS each with the same spoiler deflection value of  $\delta_s = 30^\circ$ , as well as BL to allow for a direct comparison of the different devices with one exemplarily deflection value of the spoilers. From these plots, one recognizes that the sequence of the curves does not stay the same over the complete angle of attack range. While drag is higher for both AS and AAS than for CS in the most relevant region around  $C_L/C_{L,ref}$  the maximum lift coefficient is higher for CS and AAS compared to AS. The pitching moment characteristics in Figure 5-7b show again different characteristics for the different curves, with AS showing the highest increase in  $C_M$  for high  $C_L$ -values towards a nose up behavior and AAS the highest increase for low  $C_L$ -values.

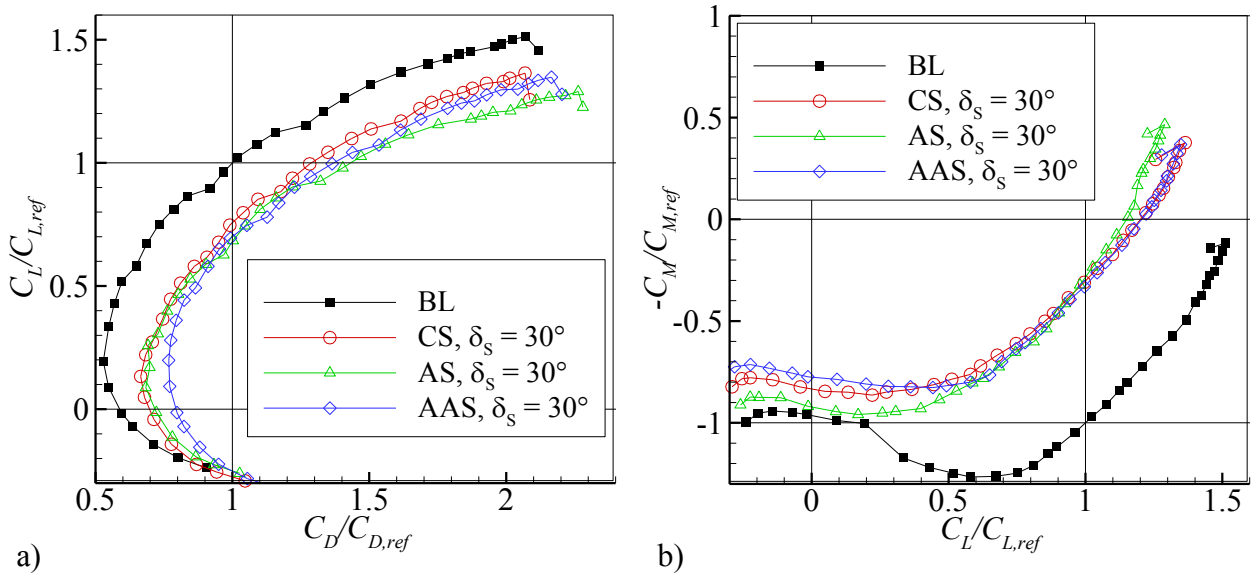


Figure 5-7: Polars for BL, CS, AS, and AAS; a)  $C_L$  over  $C_D$ , b)  $C_M$  over  $C_L$ .

For the two investigated multifunctional aileron devices, Deceleron (DC) and Split Aileron (SA), the first following depicted configurations allow for a comparison of the two devices with zero mean deflection  $\delta_A = 0^\circ$  and a fixed absolute differential deflection  $\delta_A = |90^\circ|$  in Figure 5-8. These are exemplarily configurations used to realize a pure deceleration of the airplane, when used symmetrically for both wings. The drag increase is higher for DC and SA with  $\delta_A = +90^\circ$  compared to SA with  $\delta_A = -90^\circ$ , the  $C_{L,max}$ -values are very similar for all three configurations and all are only marginally smaller compared to the BL. The differences in  $C_M$  are more distinct and the behavior is not monotonously over the angle of attack range: For the low  $C_L$ -range, DC produces the highest  $C_M$ -values, whereas for high  $C_L$  it is SA with  $\delta_A = +90^\circ$ .

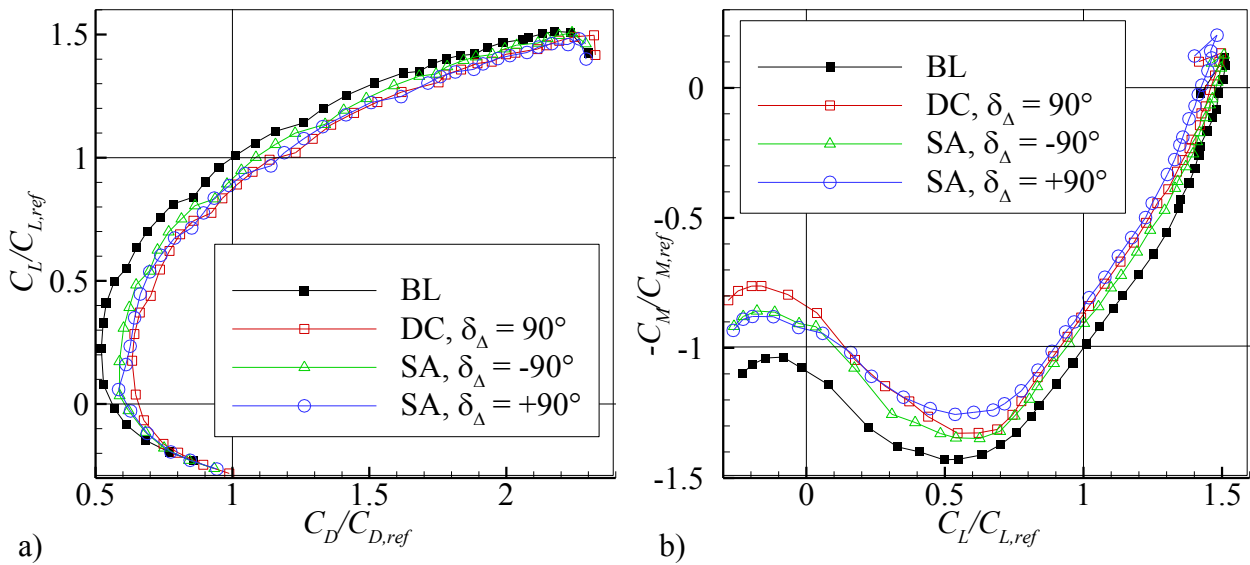


Figure 5-8: Polars for DC and SA with zero mean deflection angle  $\delta_A = 0^\circ$  and fixed absolute differential deflection angle of  $\delta_A = |90^\circ|$ ; a)  $C_L$  over  $C_D$ , b)  $C_M$  over  $C_L$ .

Figure 5-9 shows both aerodynamic coefficient polars for DC with different differential deflection angles of  $\delta_A = 20^\circ$ ;  $\delta_A = 60^\circ$ ; and  $\delta_A = 90^\circ$ .  $C_{L,max}$  stays approximately the same for all differential deflection angles  $\delta_A$  as for the BL and the drag is for the complete range of the  $\alpha$ -sweep monotonously higher correlating to the differential deflection angle  $\delta_A$ . The pitching moment coefficient increases also monotonously for an increase in differential deflection angle for the complete angle of attack range.

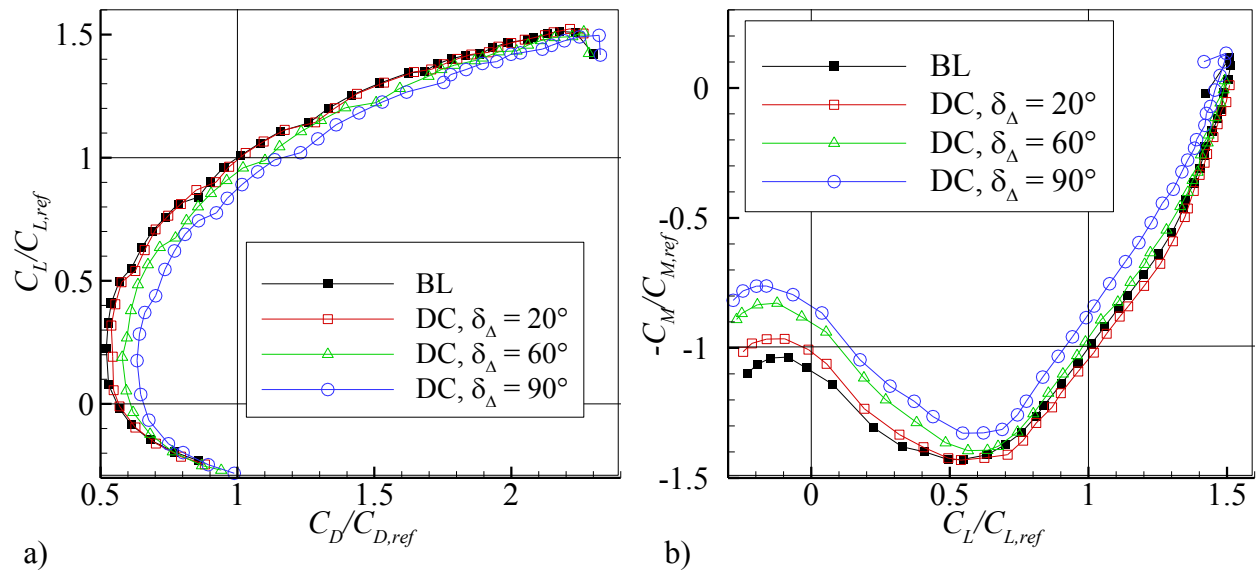


Figure 5-9: Polars for DC with zero mean deflection angle  $\delta_A = 0^\circ$  and differential deflection angles of  $\delta_\Delta = 20^\circ$ ,  $\delta_\Delta = 60^\circ$ , and  $\delta_\Delta = 90^\circ$ ; a)  $C_L$  over  $C_D$ , b)  $C_M$  over  $C_L$ .

The same type of results is shown in Figure 5-10 for SA with representative differential deflection angles ranging from  $\delta_\Delta = -120^\circ$  to  $\delta_\Delta = 120^\circ$ . Similar to the DC,  $C_{L,max}$  is approximately independent from the differential deflection angle  $\delta_\Delta$ . While the drag coefficient  $C_D$  is monotonously increasing by an increase in  $|\delta_\Delta|$ , the drag coefficient increase is higher for positive values of  $\delta_\Delta$  compared to negative ones. The pitching moment is again increased towards a nose up behavior by any differential deflection of SA. This increase is monotonous for an increase in  $|\delta_\Delta|$ . It is similar for positive and negative differential deflection angles for very low lift coefficients, while it is different for higher values, but there is no clear tendency relating to the parameter  $|\delta_\Delta|$ .

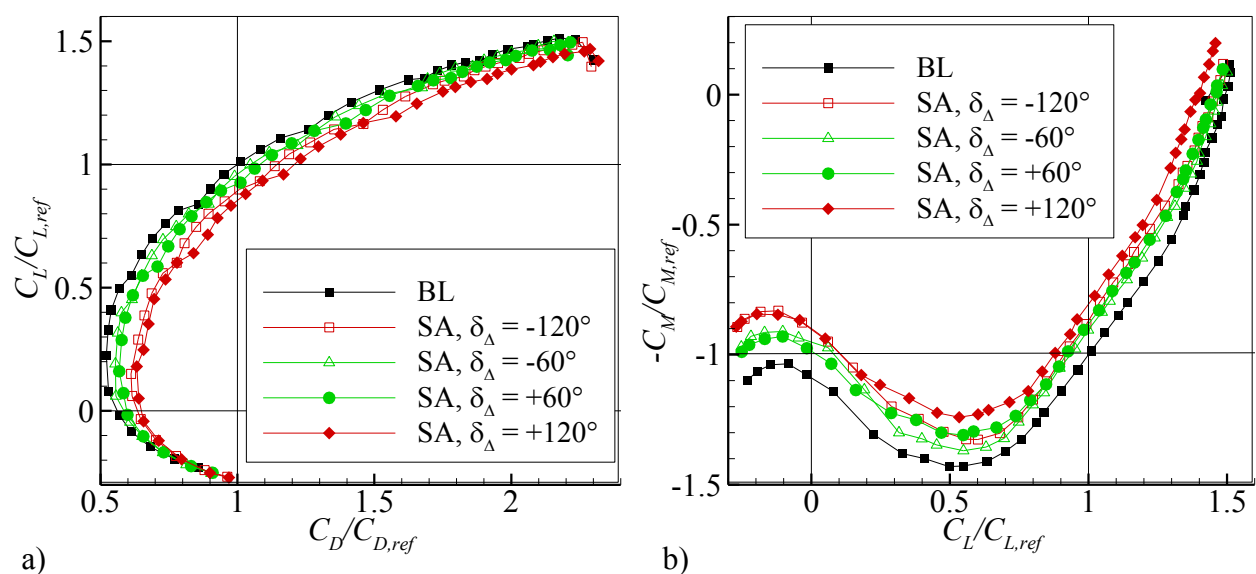


Figure 5-10: Polars for SA with zero mean deflection angle  $\delta_A = 0^\circ$  and differential deflection angles of  $\delta_\Delta = -120^\circ$ ,  $\delta_\Delta = -60^\circ$ ,  $\delta_\Delta = +60^\circ$ , and  $\delta_\Delta = +120^\circ$ ; a)  $C_L$  over  $C_D$ , b)  $C_M$  over  $C_L$ .

When using the aileron devices to simultaneously decelerate and use them for lateral control, the configurations are relevant particularly with  $\delta_A \neq 0^\circ$ . The devices are in this case deflected in antimetric fashion for both wings. Figure 5-11 shows the  $C_L$  over  $C_D$  and  $C_M$  over  $C_L$  polars for DC with  $\delta_A = -30^\circ$ ,  $\delta_A = 0^\circ$ , and  $\delta_A = +30^\circ$ . While the behavior of  $C_L$  over  $C_D$  with  $\delta_A = +60^\circ$  and  $\delta_A = +30^\circ$  is similar to the BL for the lower half of the  $\alpha$ -sweep, it becomes more similar to the DC-configuration with  $\delta_A = +60^\circ$  and  $\delta_A = 0^\circ$  for the higher values  $C_L/C_{Lref} > 1.2$  with the significant difference that  $C_{L,max}$  is somewhat larger than even the BL.  $C_M$  over  $C_L$  is for this case congruent with the BL for the less relevant domains of low  $C_L/C_{Lref} \approx 0$  and high  $C_L/C_{Lref} > 1.3$ , it is significantly lower towards a nose down behavior in between. The DC-configuration with  $\delta_A = +60^\circ$  and  $\delta_A = +30^\circ$  results in a  $C_L$  over  $C_D$ -curve, which is shifted to the lower right compared to BL and in a  $C_M$  over  $C_L$ -curve, which is shifted about uniformly upward towards a nose up behavior compared to the BL.

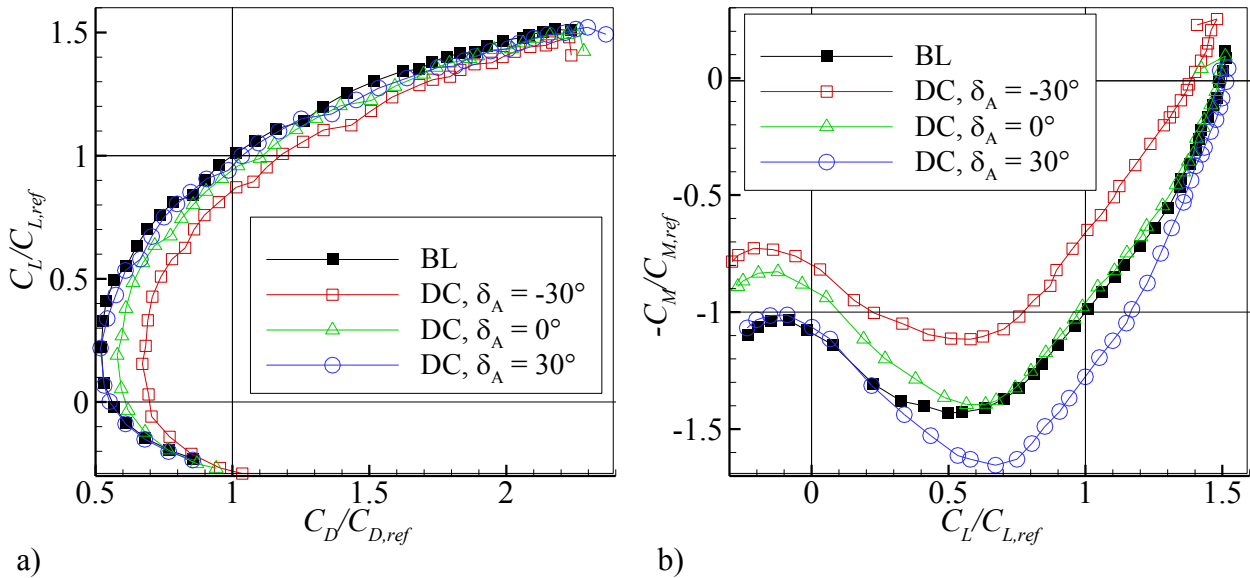


Figure 5-11: Polars of DC with  $\delta_A = +60^\circ$  for different mean deflection angles;  $\delta_A = -30^\circ$ ,  $\delta_A = 0^\circ$ ,  $\delta_A = +30^\circ$ ; a)  $C_L$  over  $C_D$ , b)  $C_M$  over  $C_L$ .

Figure 5-12a shows the lift over drag polar and Figure 5-12b the pitching moment over lift polar of SA with  $\delta_A = -30^\circ$ ,  $\delta_A = 0^\circ$ , and  $\delta_A = +30^\circ$  each with  $\delta_A = -60^\circ$ . The same polars with the same mean aileron deflections are shown in Figure 5-12c and Figure 5-12d, but in this case with  $\delta_A = +60^\circ$ .

For both differential deflections  $\delta_A = -60^\circ$  and  $\delta_A = +60^\circ$ , and a mean deflection of  $\delta_A = +30^\circ$ , the lift over drag curves stay very similar to BL (Figure 5-13a and Figure 5-13c). Other than on the lift over drag characteristics, there is a clear effect on the pitching moment over lift characteristics for both differentially deflected configurations with  $\delta_A = +30^\circ$ : The pitching moment is reduced for most of the  $C_L$ -range, but not for very low  $C_L$ , where the pitching moment is increased compared to the BL.

For the same differential deflections  $\delta_A = -60^\circ$ , and  $\delta_A = +60^\circ$  with a mean deflection of  $\delta_A = -30^\circ$ , there is a clear effect on both the lift over drag as well as the pitching moment over lift characteristic: The increase in the drag coefficient is considerably higher for the complete polar compared to the configuration with no mean deflection, the maximum lift coefficient is also considerably decreased. Pitching moment is increased towards a nose up behavior by the negative mean deflection over the complete angle of attack range.

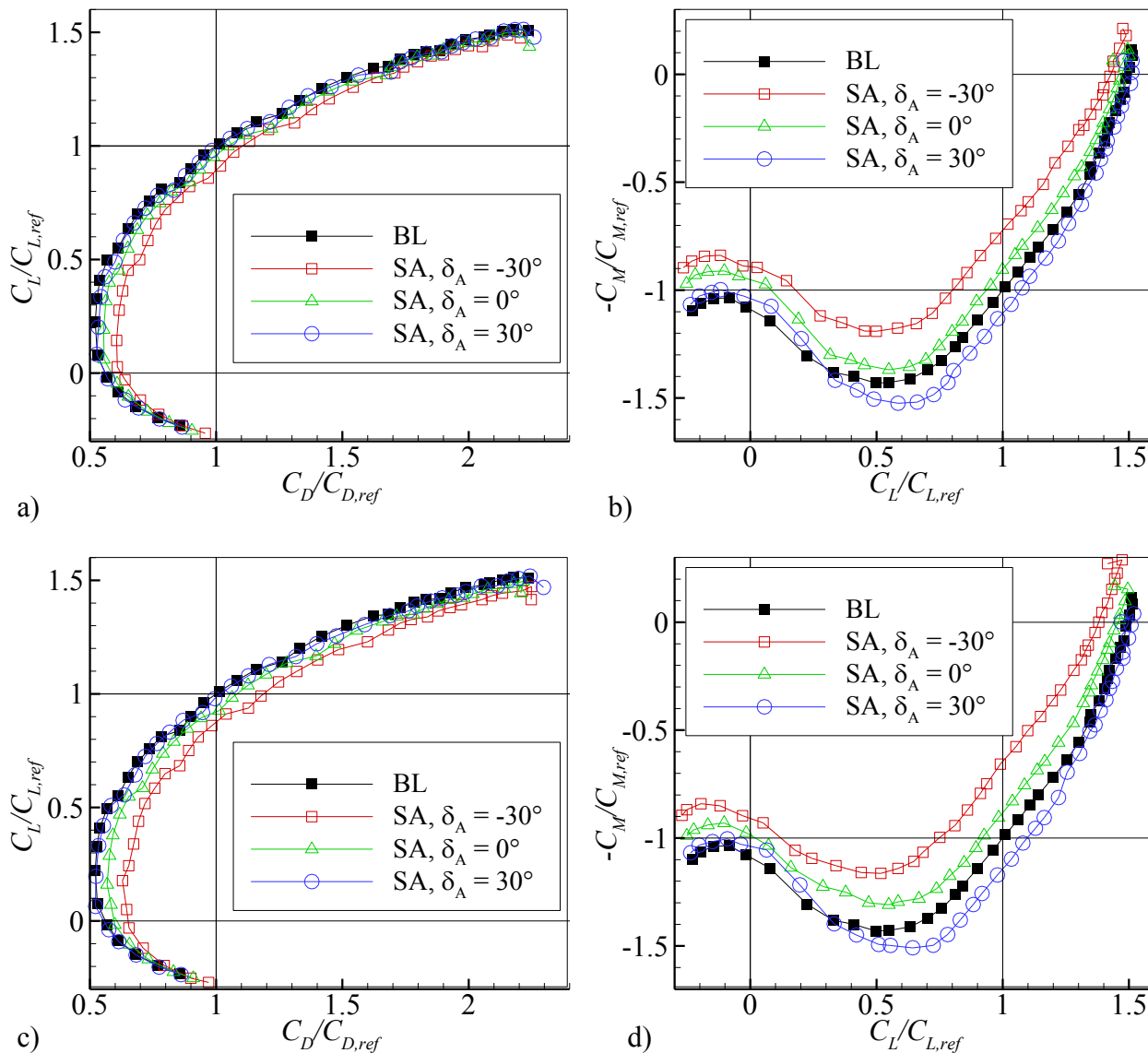


Figure 5-12: Polars of SA  $\delta_A = -60^\circ, +60^\circ$  for different mean deflection angles;  $\delta_A = -30^\circ, \delta_A = +0^\circ, \delta_A = +30^\circ$ ; a)  $\delta_A = -60^\circ$   $C_L$  over  $C_D$ , b)  $\delta_A = -60^\circ$   $C_M$  over  $C_L$ , c)  $\delta_A = +60^\circ$   $C_L$  over  $C_D$ , d)  $\delta_A = +60^\circ$   $C_M$  over  $C_L$ .

To compare the performance of the different devices among each other, the polars of  $C_L$  over  $C_D$  are comparably shown for all spoilers and aileron devices with a fixed deflection of  $\delta_S = 30^\circ$  for the CS, AS and AAS configurations and a fixed absolute differential deflection of  $|\delta_A| = 90^\circ$  for the novel aileron configurations in Figure 5-13. The mean

deflection of all aileron devices is in this case  $\delta_A = 0^\circ$ . The difference in the deflection values of the spoiler cases and the aileron cases is chosen to compare cases with a similar influence on the coefficients. In addition, the BL configuration is shown.

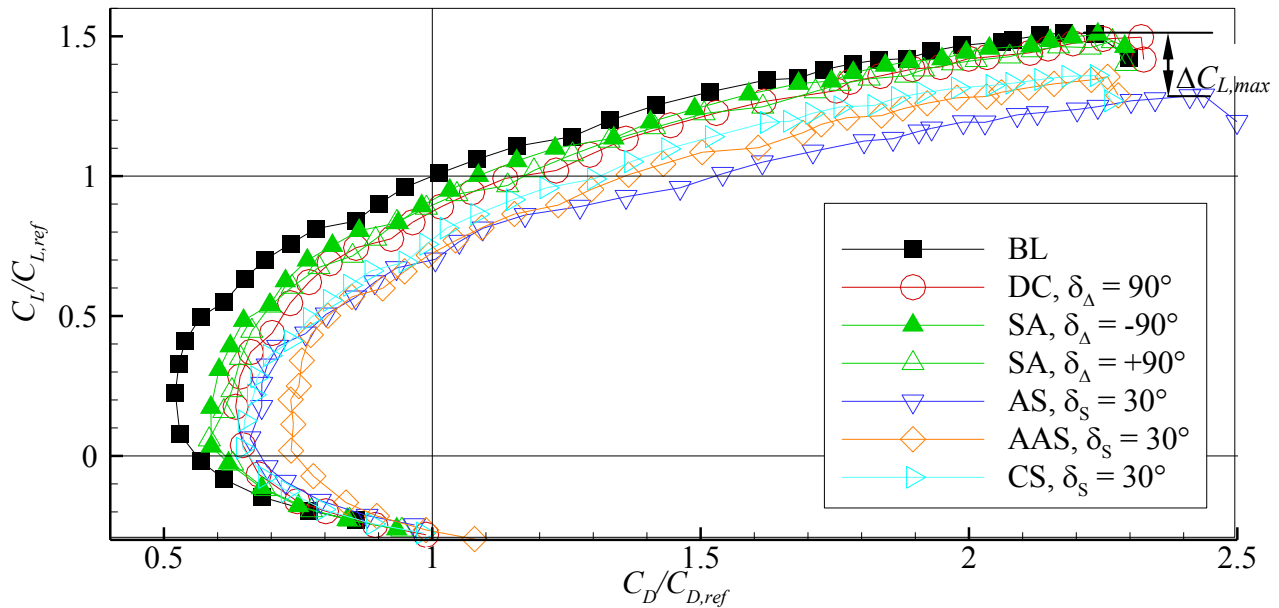


Figure 5-13:  $C_L$  over  $C_D$  for the devices CS, AS, AAS, DC, SA;  $\delta_S = 30^\circ$ ,  $\delta_A = -90^\circ$ ,  $\delta_A = +90^\circ$ . An exemplarily value of  $\Delta C_{L,max}$  is included in the plot for the AS case.

Concerning the deficit in  $C_{L,max}$ , this parameter ranges from approximately zero for both SA-configurations as well as the DC to about 14% for AS,  $\delta_S = 30^\circ$ . The sequence in  $C_D$  of the curves swaps over the complete  $C_L$ -range. For the most relevant area around  $C_L/C_{L,ref} = 1$ , the sequence in rising order of drag is SA with  $\delta_A = -90^\circ$ , SA with  $\delta_A = +90^\circ$  and DC, CS, AAS, and AS. One interesting aspect is thereby, that while there is nearly no difference in  $C_{L,max}$  for the two antimetric SA cases,  $C_D$  shows a quite large difference for  $C_L/C_{L,ref} \approx 1$ . The DC-configuration shows in both aspects comparable characteristics to the SA-configuration with  $\delta_A = +90^\circ$ .

### 5.2.2 Descent Velocity

From the aerodynamic force coefficients of the longitudinal motion follow directly the descent velocity parameter  $V_S/V_{S,ref} - 1$ , as well as the approach velocity parameter  $V_{app}/V_{app,ref} - 1$ , which have been introduced in Eqs. (2.22) and (2.23). They are discussed in this subsection. In the following graphs, the depicted data points represent the feasible range for the approach case, considering the  $V_{st}$ -margin given in Eq. (2.20). Thus, the leftmost data points belong per configuration to the lowest feasible approach velocity  $V_{app,min}$ . The vertical axis of these velocity-polars shows the increment in  $V_S$  caused by the respective air-brake device.

Again, the results are compared for each configuration and the different deflection angles, first. Later the different configurations are analyzed in comparison for fixed deflection angles  $\delta_S$  and differential deflection angles  $\delta_\Delta$ , respectively. The diagram of Figure 5-14 shows the results for CS for all measured  $\delta_S$ -values ranging from  $\delta_S = 5^\circ$  to  $\delta_S = 60^\circ$ , as well as the BL-results.

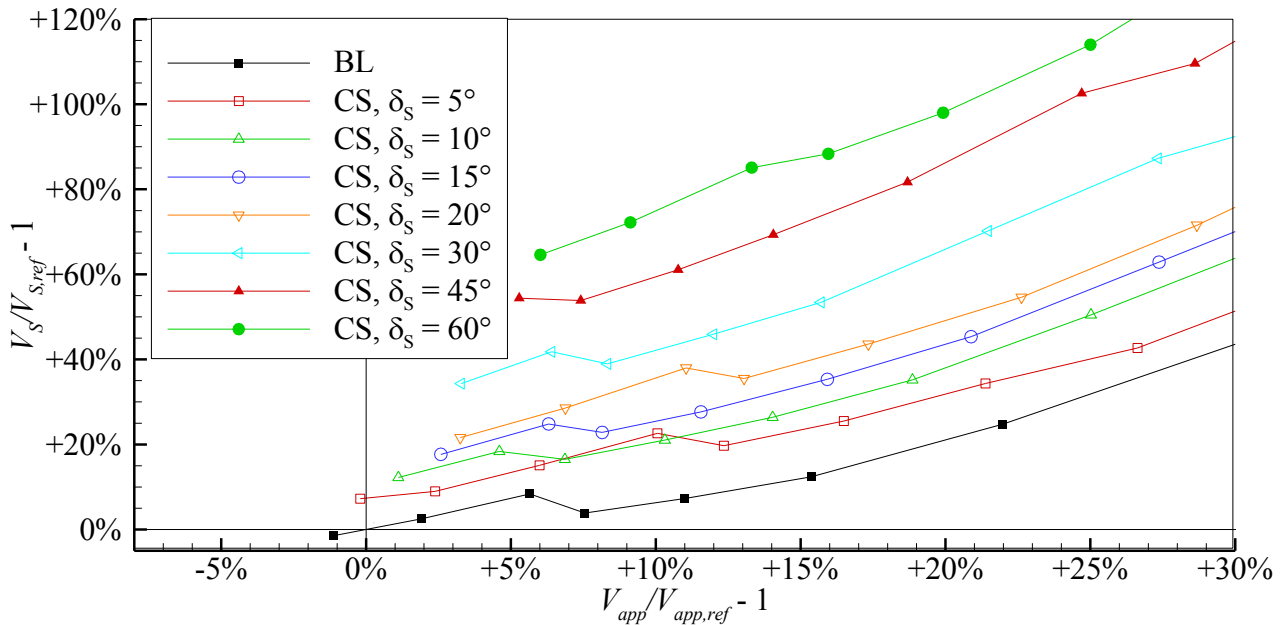


Figure 5-14: Relative descent velocity  $V_S/V_{S,ref} - 1$  over relative approach velocity  $V_{app}/V_{app,ref} - 1$  for BL and CS with various  $\delta_S$  for the range of minimum feasible approach velocities.

Due to the decrease in  $C_{L,max}$  for an increase in  $\delta_S$  the approach velocity is gradually increased for higher  $\delta_S$  with a minimum increase of  $V_{app}/V_{app,ref} - 1 \approx 6\%$  for the highest  $\delta_S = 60^\circ$ . At the same time, the vertical velocity is increased by  $V_S/V_{S,ref} - 1 \approx 65\%$  for the highest spoiler deflection and lowest possible approach velocity.

The same type of graph is shown in Figure 5-15 for the adverse spoiler and the trends are the same, but as a matter of course the values are different: In particular, the approach velocity penalty is considerably higher compared to the conventional spoiler with an increase of about  $V_{app}/V_{app,ref} - 1 \approx 8\%$  for the case with the highest  $\delta_S = 60^\circ$ .

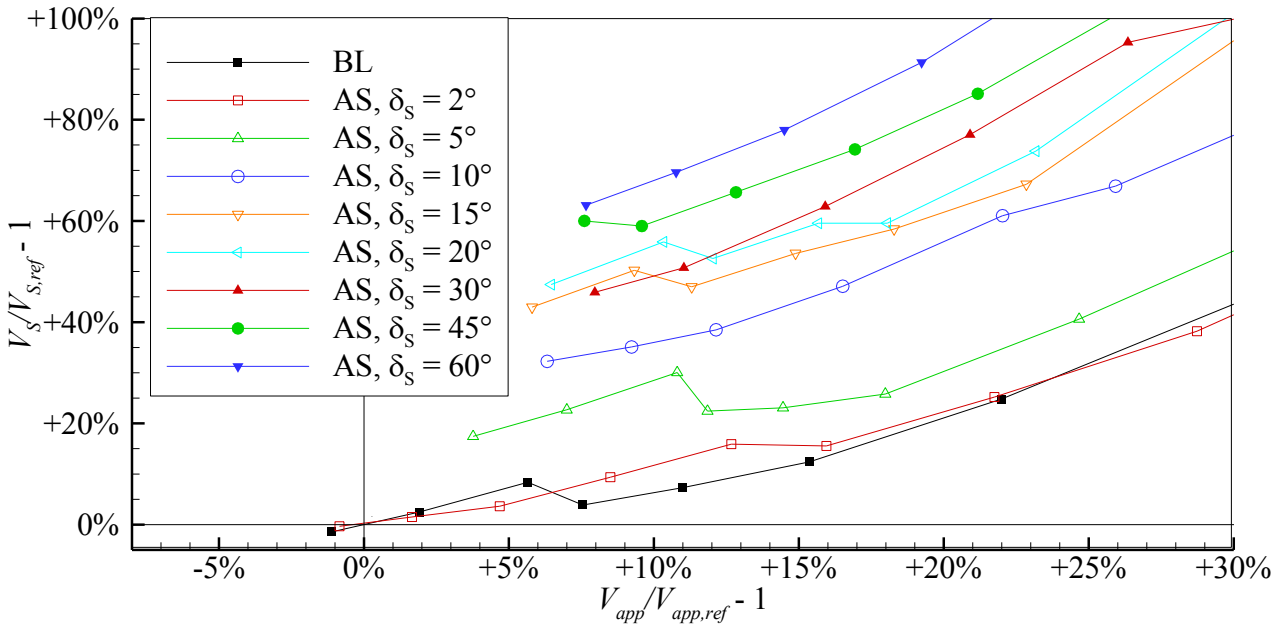


Figure 5-15: Relative descent velocity  $V_S/V_{S,ref} - 1$  over relative approach velocity  $V_{app}/V_{app,ref} - 1$  for BL and AS with various  $\delta_S$  for the range of minimum feasible approach velocities.

Figure 5-16 shows relative vertical velocity over relative approach velocity this time for the AAS and all investigated deflection angles  $\delta_S$ . The sequence of the curves concerning the descent velocity again stays the same according to the deflection angle. One point, which immediately stands out, is that the approach velocity is not consistently increased by an increase in deflection angle, but stays at values around  $V_{app}/V_{app,ref} - 1 \approx 5\%$ .

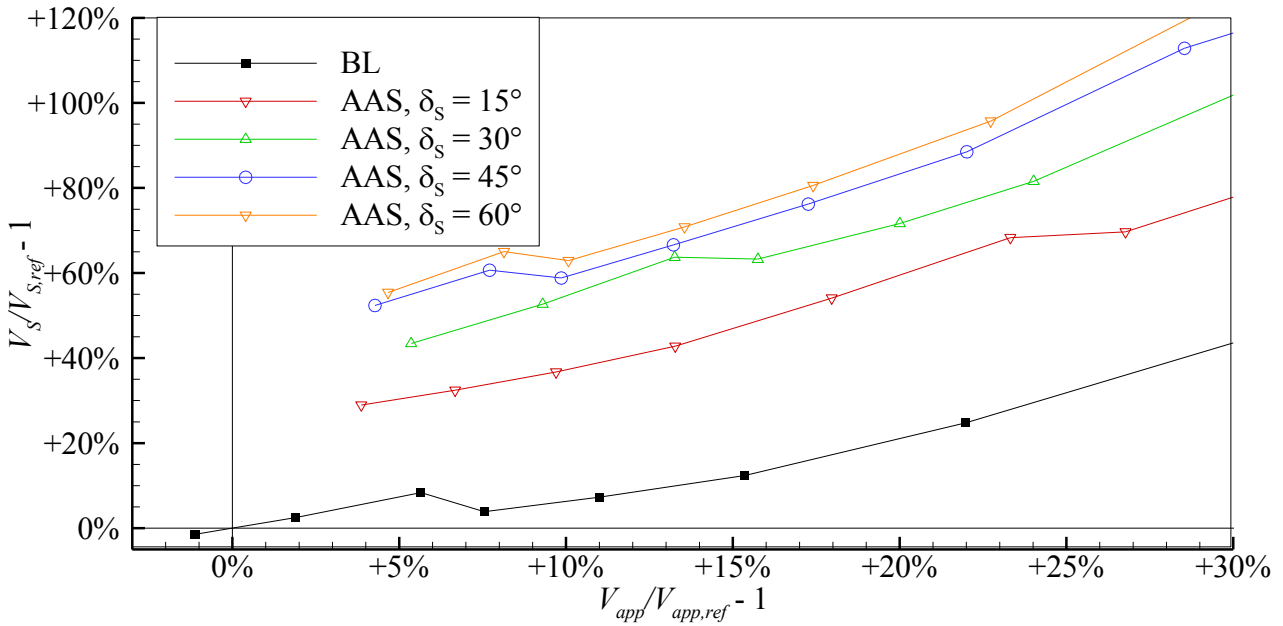


Figure 5-16: Relative descent velocity  $V_S/V_{S,ref} - 1$  over relative approach velocity  $V_{app}/V_{app,ref} - 1$  for BL and AAS with various  $\delta_S$  for the range of minimum feasible approach velocities.

To turn to the multifunctional aileron devices, the influence on the descent and approach velocity of the differential deflection angles  $\delta_\Delta$  for the symmetric DC-cases are comparably shown in Figure 5-17 and for the SA-cases in Figure 5-18. For all deflections of both devices there is no significant increase in the approach velocity, while the increase in  $V_S$  is in both cases monotonous with an increase in deflection angle  $\delta_\Delta$ .

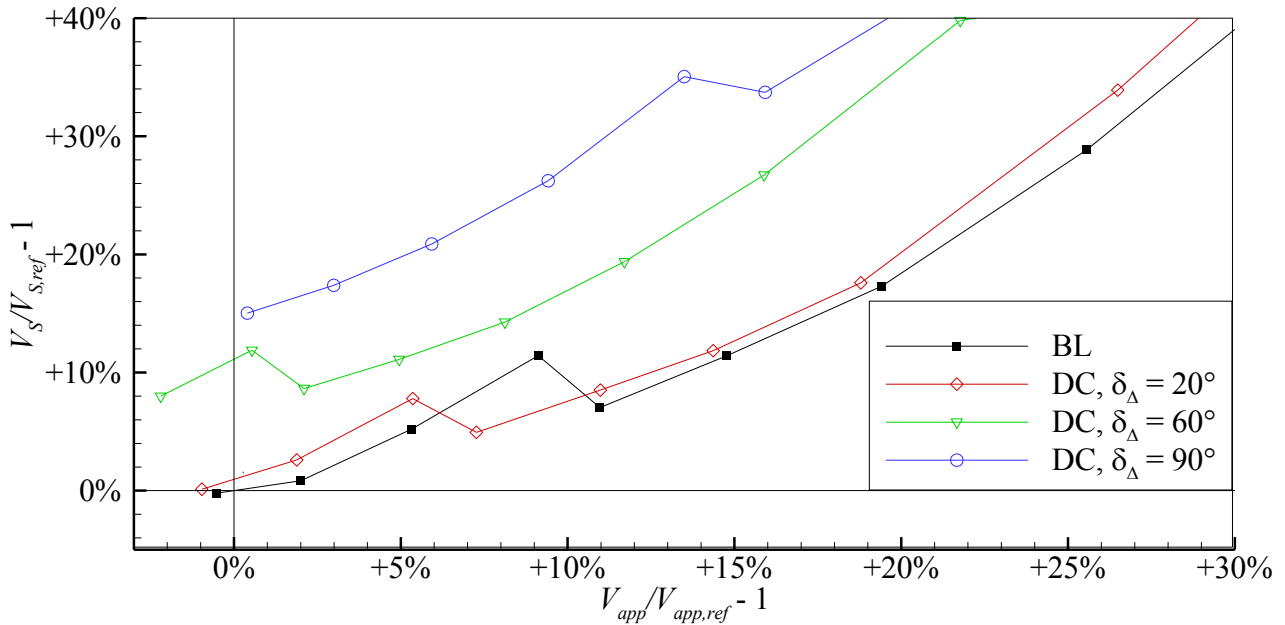


Figure 5-17: Relative descent velocity  $V_S/V_{S,ref} - 1$  over relative approach velocity  $V_{app}/V_{app,ref} - 1$  for BL and DC with various differential deflection angles  $\delta_\Delta$  for the range of minimum feasible approach velocities.

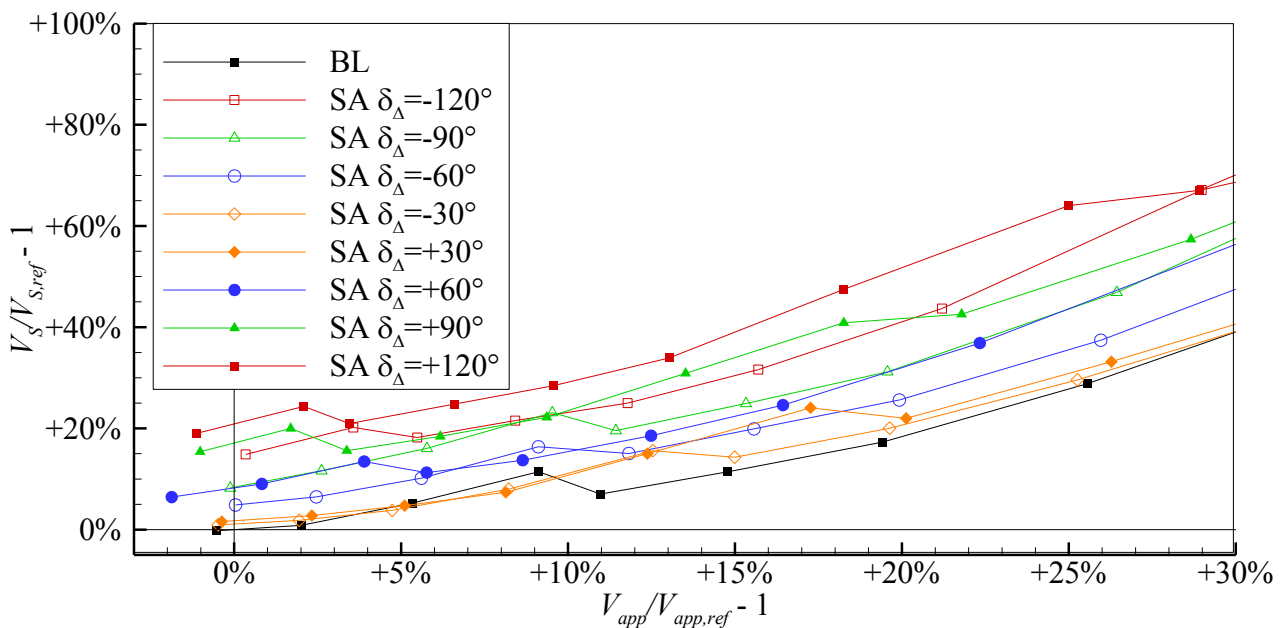


Figure 5-18: Relative descent velocity  $V_S/V_{S,ref} - 1$  over relative approach velocity  $V_{app}/V_{app,ref} - 1$  for BL and SA with various differential deflection angles  $\delta_\Delta$  for the range of minimum feasible approach velocities.

To compare the influence on the descent velocity and approach velocity of the asymmetric novel aileron cases with  $\delta_A \neq 0^\circ$ , Figure 5-19 and Figure 5-20 show graphs, which are analogue to the previous ones, but with various mean aileron deflection angles from  $\delta_A = -30^\circ$  to  $\delta_A = +30^\circ$  for DC and SA, respectively. While the approach velocity is not much influenced by the mean aileron deflection angle  $\delta_A$ , and stays still approximately the same compared to the zero mean deflection angle case, there is a continuous increase in  $V_S$  for  $\delta_A < 0^\circ$ , respectively decrease in  $V_S$  for  $\delta_A > 0^\circ$ . If one bears in mind that the mean aileron deflection angle is changed asymmetrically for both sides of the wing to realize roll control, it becomes readily appearing that in total this effect is approximately cancelled out.

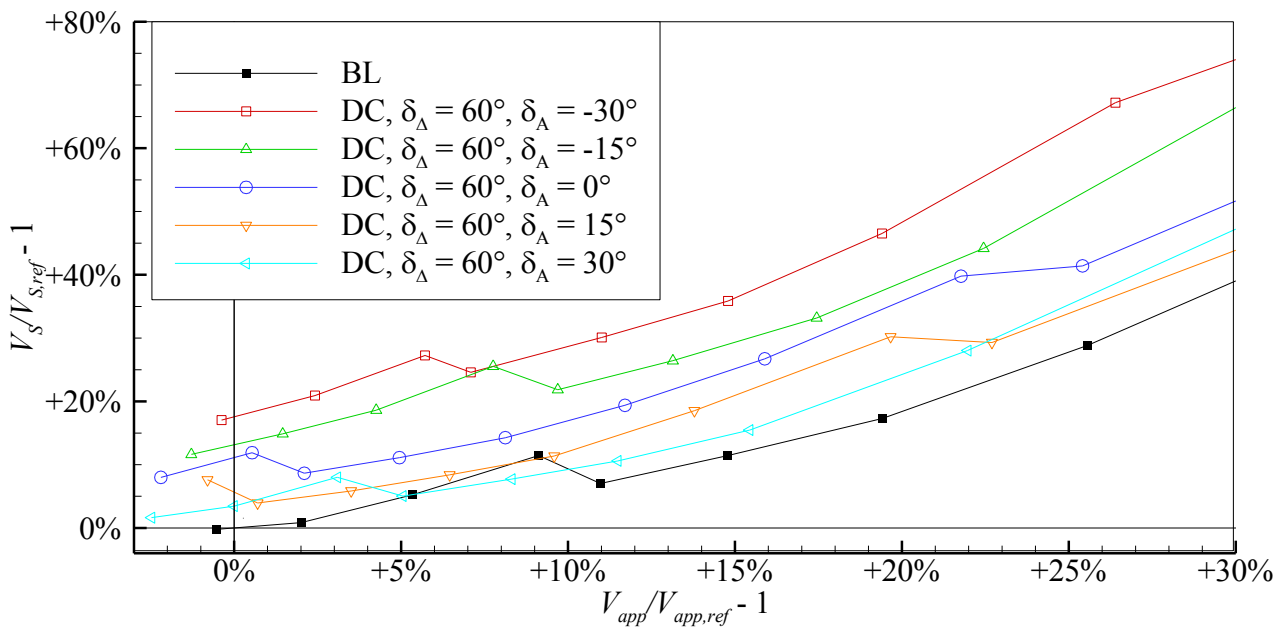


Figure 5-19: Relative descent velocity  $V_S/V_{S,ref} - 1$  over relative approach velocity  $V_{app}/V_{app,ref} - 1$  of BL and DC with  $\delta_A = 60^\circ$ , mean deflection angles  $\delta_A = -30^\circ$ ,  $\delta_A = -15^\circ$ ,  $\delta_A = 0^\circ$ ,  $\delta_A = 15^\circ$ ,  $\delta_A = 30^\circ$  for the range of minimum feasible approach velocities.

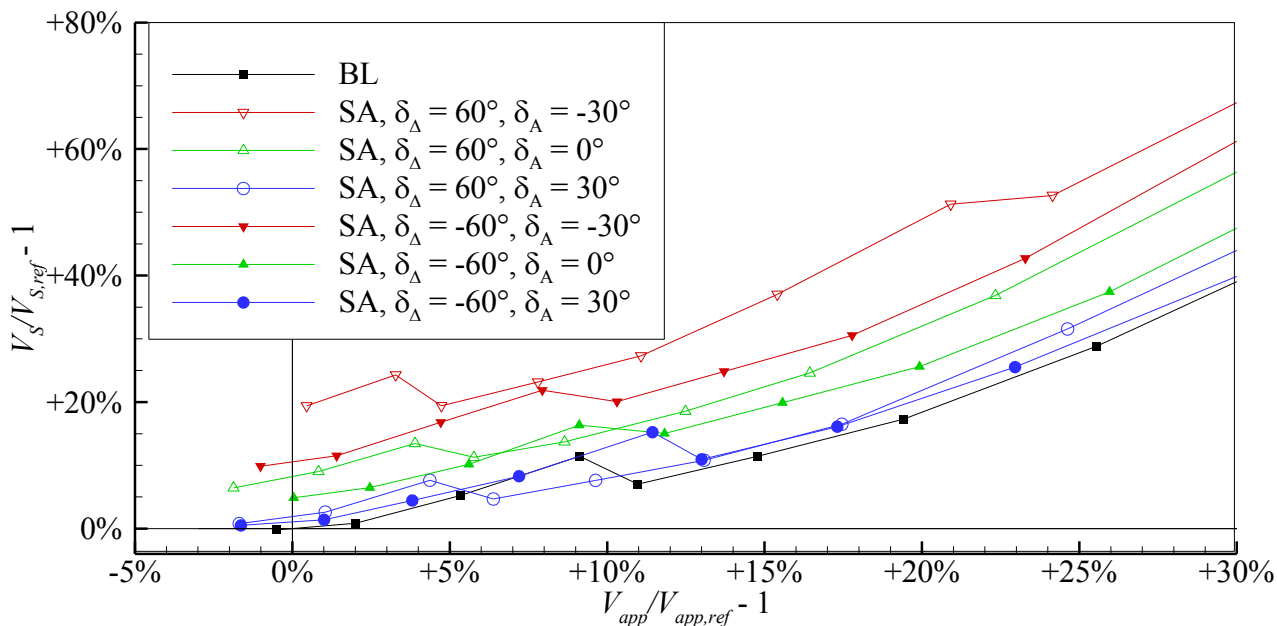


Figure 5-20: Relative descent velocity  $V_S/V_{S,ref} - 1$  over relative approach velocity  $V_{app}/V_{app,ref} - 1$  of BL and SA with  $\delta_\Delta = 60^\circ$  and  $\delta_\Delta = -60^\circ$ , mean deflection angles  $\delta_A = -30^\circ$ ,  $\delta_A = 0^\circ$ ,  $\delta_A = 30^\circ$  for the range of minimum feasible approach velocities.

Finally, the diagram in Figure 5-21 includes the descent and approach velocity parameters of all the devices with  $|\delta_\Delta| = 90^\circ$  and  $\delta_S = 30^\circ$ , respectively.

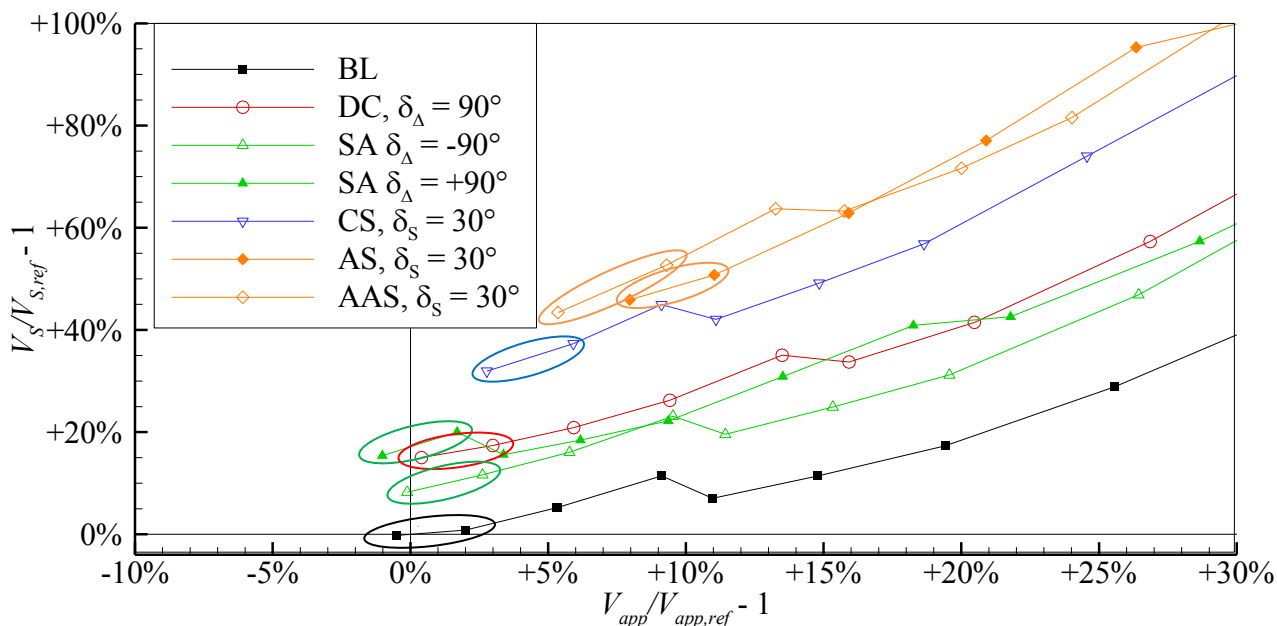


Figure 5-21: Relative descent velocity  $V_S/V_{S,ref} - 1$  over relative approach velocity  $V_{app}/V_{app,ref} - 1$  for the range of minimum feasible approach velocities, comparison of all investigated air-brake types with  $|\delta_\Delta| = 90^\circ$  for the aileron devices and  $\delta_S = 30^\circ$  for the spoiler devices. Data points for  $V_{app} \approx V_{app,min}$  are highlighted by ellipses.

Generally speaking, the sequence of the  $V_S$ -curves stays by trend the same for all air-brake types and deflection angles, though the sequence flips infrequently for some higher

$V_{app}$ -values. The sequence of the aileron configurations at minimum feasible  $V_{app,min}$ -ranges, which are illustrated in Figure 5-21 by ellipses, starts from SA with positive  $\delta_{\Delta}$ , via DC, SA with negative  $\delta_{\Delta}$ , CS, and AAS to AS. These graphs can serve to identify the feasible air-brake types and deflections regarding the maximum descent velocity  $V_S$  limited by the undercarriage and comfort reasons as mentioned in subsection 2.4.2. This limit would then be a horizontal line in the graphs separating the valid configurations below and non-valid ones above.

Concerning minimum approach velocity  $V_{app,min}$ , a completely different behavior is observed for both novel aileron device configurations compared to the spoiler configurations. While there is the tendency of higher  $V_{app,min}$  for higher  $\delta_S$  at CS, AS, and AAS, no such behavior is observed for the aileron devices. Presumably, the reason for this is that the aileron devices do not disturb the flap flow as the spoiler does, so they function almost exclusively as air braking device, rather than as lift dumper. The approach velocity is also limited to values near  $V_{app,ref}$ , where  $V_{app}/V_{app,ref} - 1 = 0$ . This results in a vertical line in the graph, which separates feasible values left of the line from non-feasible values on the right hand side.

To clarify these conclusions, the flight envelope for an exemplarily case is sketched into Figure 5-22. The hatched areas define non-feasible flight attitudes. For this example maximum relative  $V_{app}$  of 105% and maximum relative  $V_S$  of 140% are chosen leaving the rectangular area in the bottom left as feasible flight attitude area. This means for the AAS-configurations that the deflection of the spoiler is only valid up to values of  $\delta_S = 15^\circ$ .

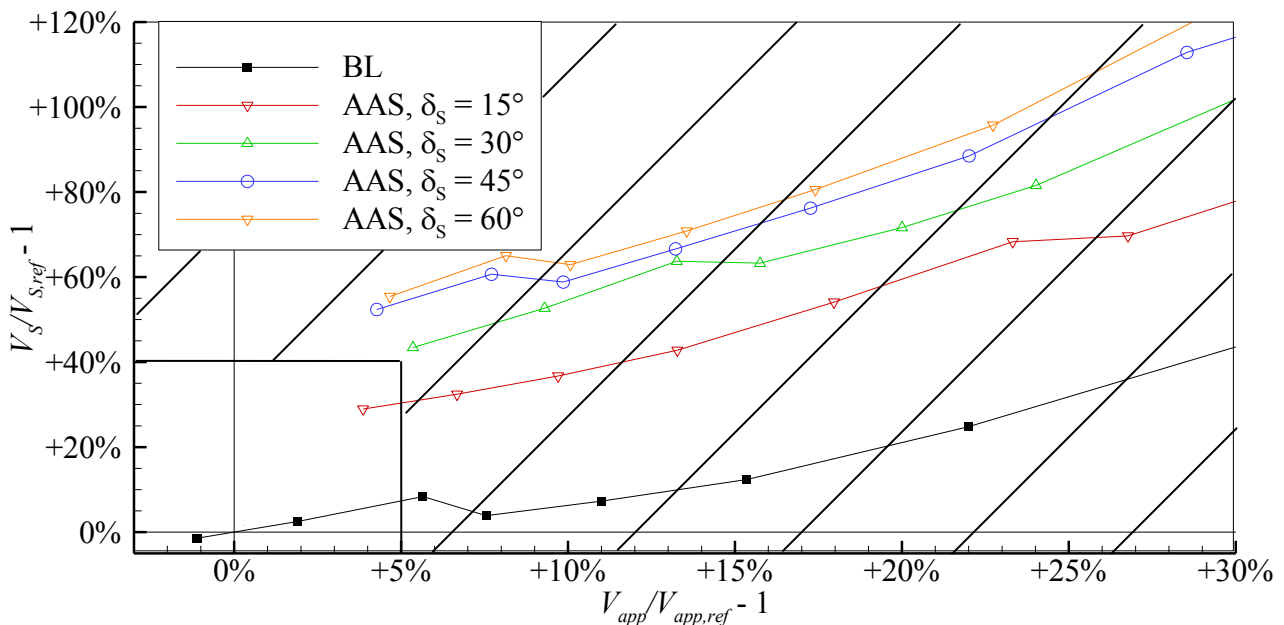


Figure 5-22: Relative descent velocity  $V_S/V_{S,ref} - 1$  over relative approach velocity  $V_{app}/V_{app,ref} - 1$  for the range of minimum feasible approach velocities, example for a flight envelope and reasonable configurations extracted from the graph.

### 5.2.3 Descent Angle

In this subsection the relative change in descent angle  $\gamma/\gamma_{ref} - 1$  over the relative change in approach velocity  $V_{app}/V_{app,ref} - 1$  compared to the BL at MVAP is discussed for the investigated air-brake device configurations. Again, first the influence of the parametric deflection on the results per device is shown, before the different devices are comparatively discussed. To start with the spoiler devices, Figure 5-23 shows the results for CS, Figure 5-24 for AS, and Figure 5-25 for AAS. The results for the aileron devices with symmetric deflection ( $\delta_A = 0^\circ$ ) are then shown for DC in Figure 5-26 and for SA in Figure 5-29. Results for asymmetric aileron configurations ( $\delta_A \neq 0$ ) are presented in Figure 5-28 for DC and in Figure 5-29 for SA. Finally, Figure 5-30 includes the results of  $\gamma$  over  $V_{app}$  for all the investigated devices with one representative spoiler deflection angle of  $\delta_S = 30^\circ$  and one representative differential deflection angle of  $|\delta_A| = 90^\circ$  for the multifunctional aileron devices, respectively.

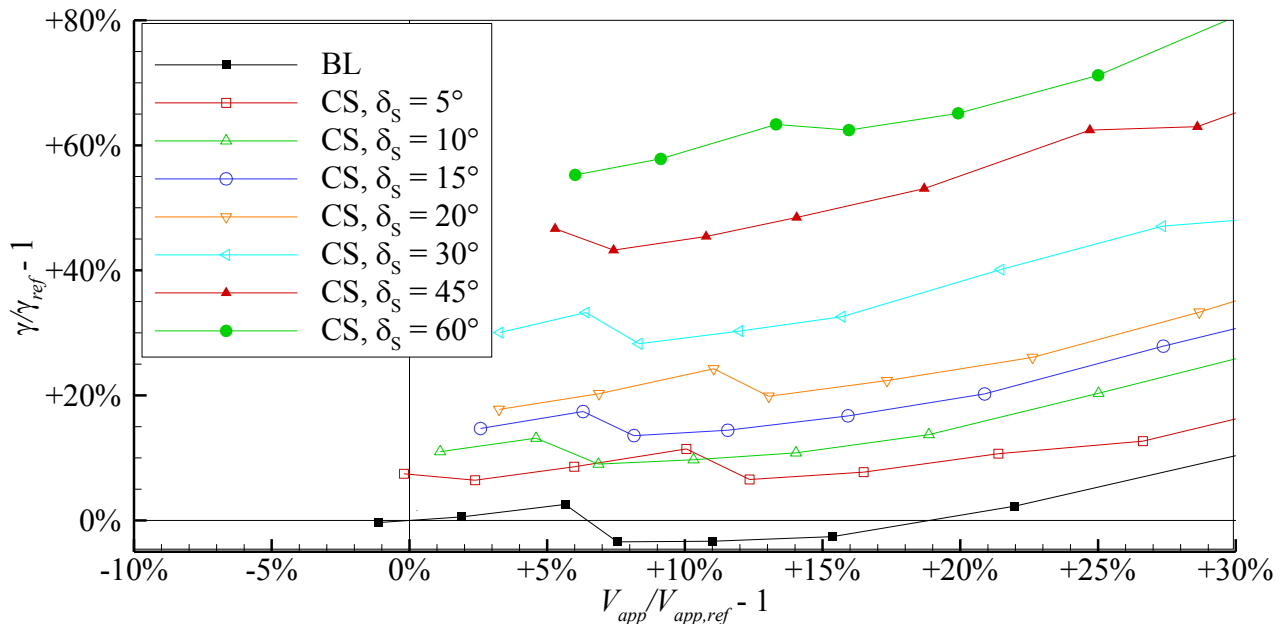


Figure 5-23: Relative descent angle  $\gamma/\gamma_{ref} - 1$  over relative approach velocity  $V_{app}/V_{app,ref} - 1$  for BL and CS with various  $\delta_S$  for the range of minimum feasible approach velocities.

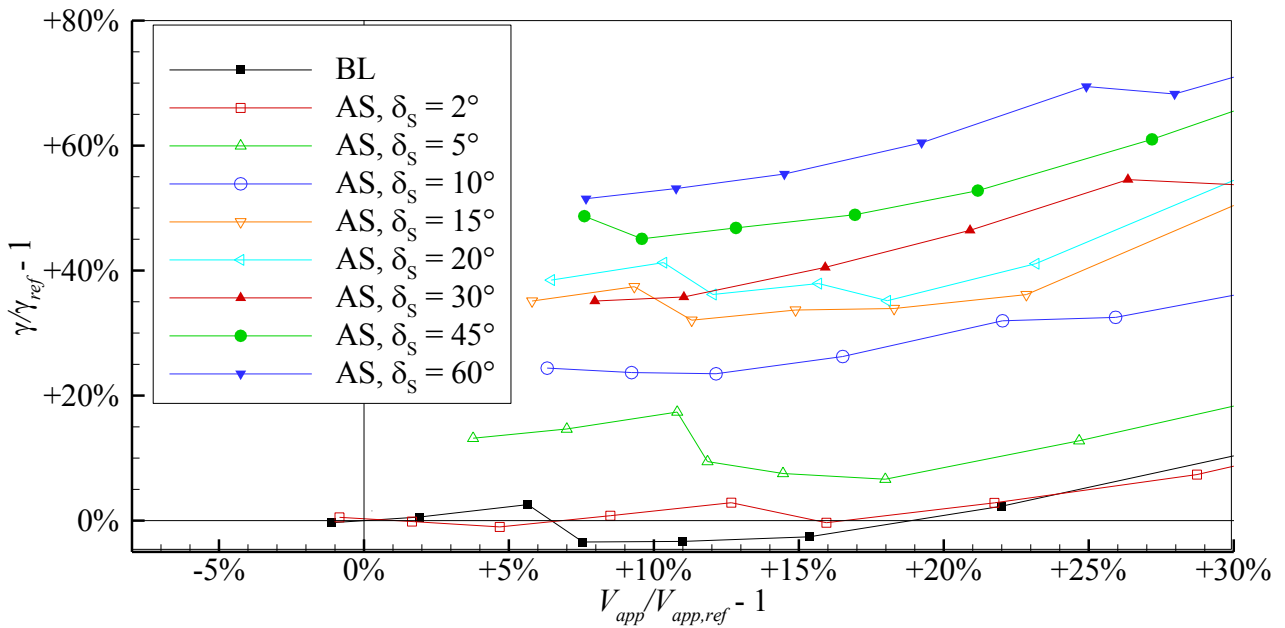


Figure 5-24: Relative descent angle  $\gamma/\gamma_{ref} - 1$  over relative approach velocity  $V_{app}/V_{app,ref} - 1$  for BL and AS with various  $\delta_s$  for the range of minimum feasible approach velocities.

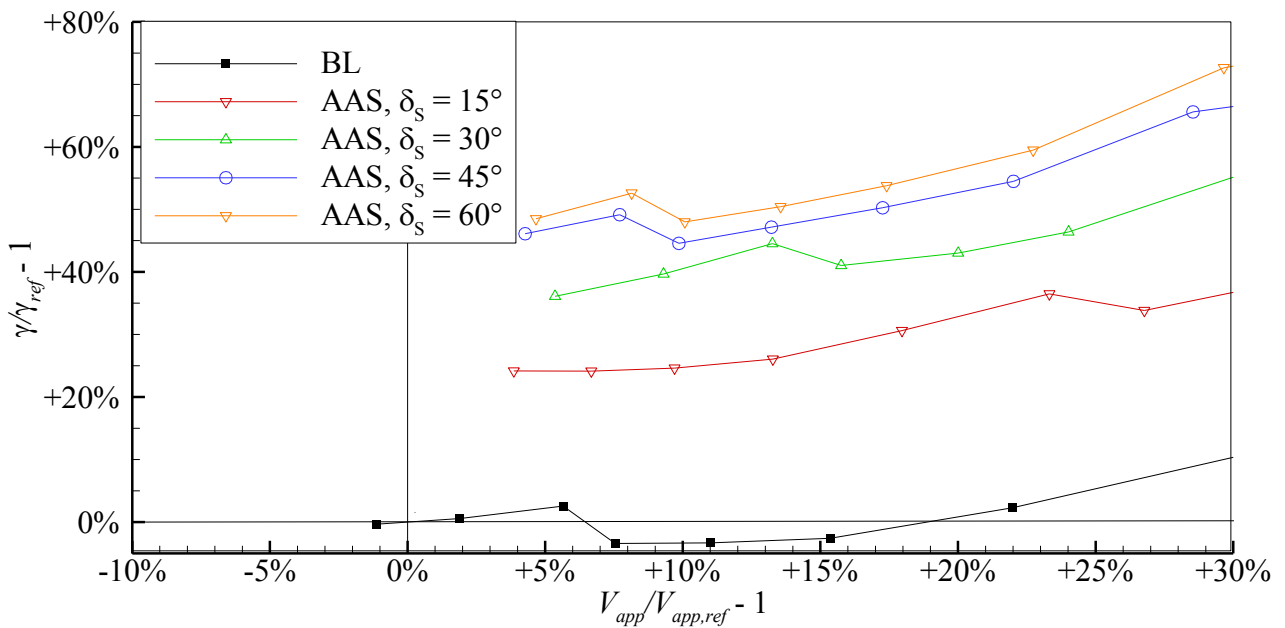


Figure 5-25: Relative descent angle  $\gamma/\gamma_{ref} - 1$  over relative approach velocity  $V_{app}/V_{app,ref} - 1$  for BL and AAS with various  $\delta_s$  for the range of minimum feasible approach velocities.

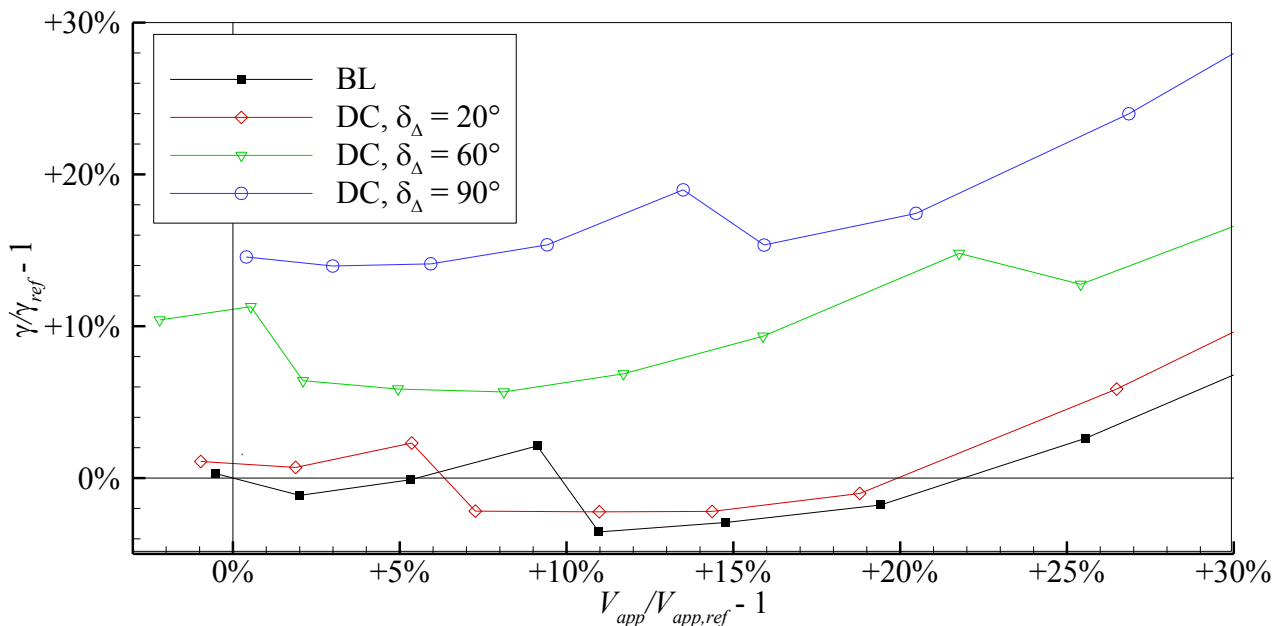


Figure 5-26: Relative descent angle  $\gamma/\gamma_{ref} - 1$  over relative approach velocity  $V_{app}/V_{app,ref} - 1$  for BL and DC with various  $\delta_\Delta$  for the range of minimum feasible approach velocities.

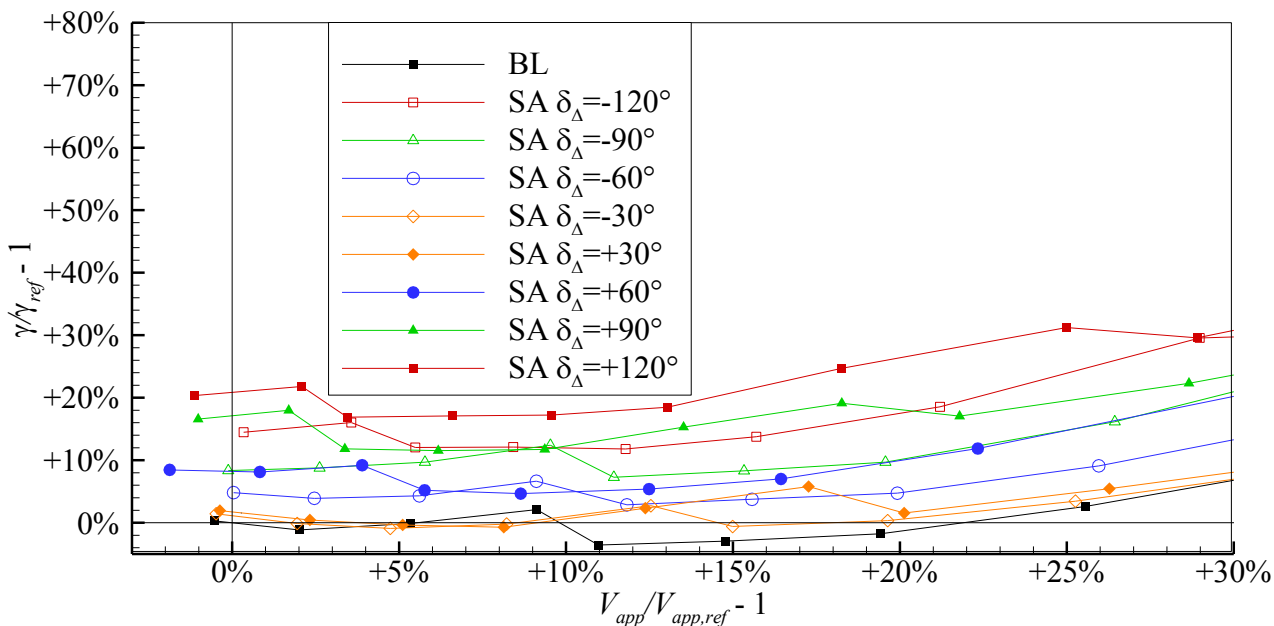


Figure 5-27: Relative descent angle  $\gamma/\gamma_{ref} - 1$  over relative approach velocity  $V_{app}/V_{app,ref} - 1$  for BL and SA with various  $\delta_\Delta$  for the range of minimum feasible approach velocities.

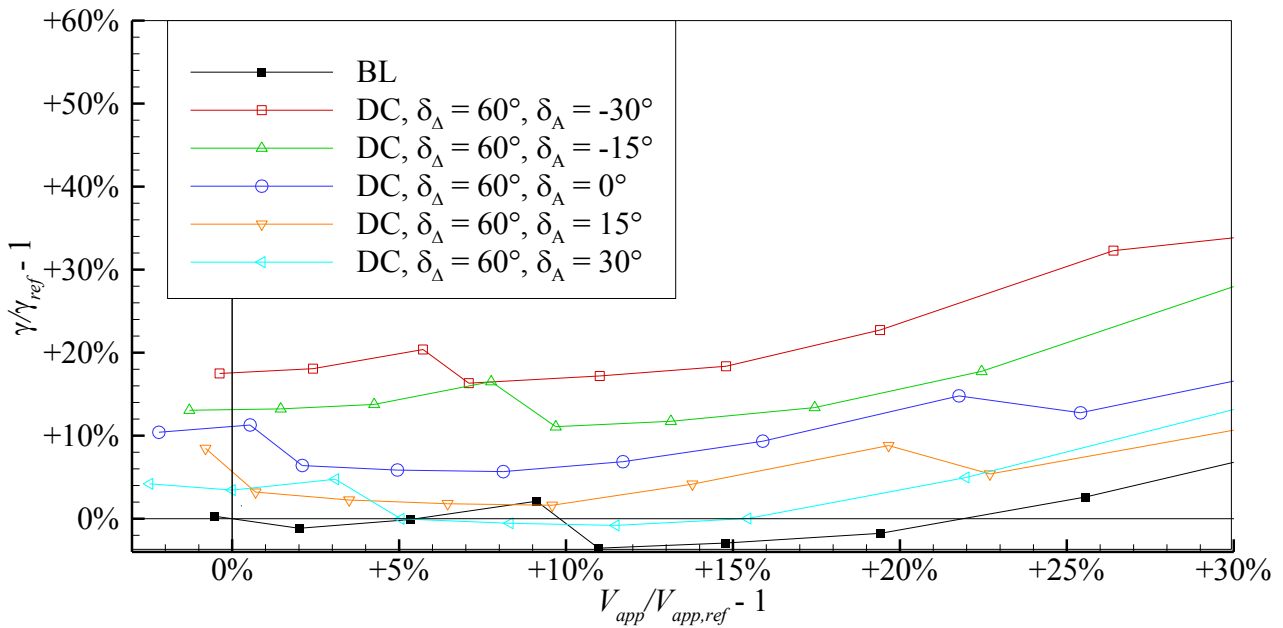


Figure 5-28: Relative descent angle  $\gamma/\gamma_{ref} - 1$  over relative approach velocity  $V_{app}/V_{app,ref} - 1$  for BL and DC with  $\delta_A = 60^\circ$  and various mean deflection angles of  $\delta_A = -30^\circ$ ,  $\delta_A = -15^\circ$ ,  $\delta_A = 0^\circ$ ,  $\delta_A = 15^\circ$ ,  $\delta_A = 30^\circ$  for the range of minimum feasible approach velocities.

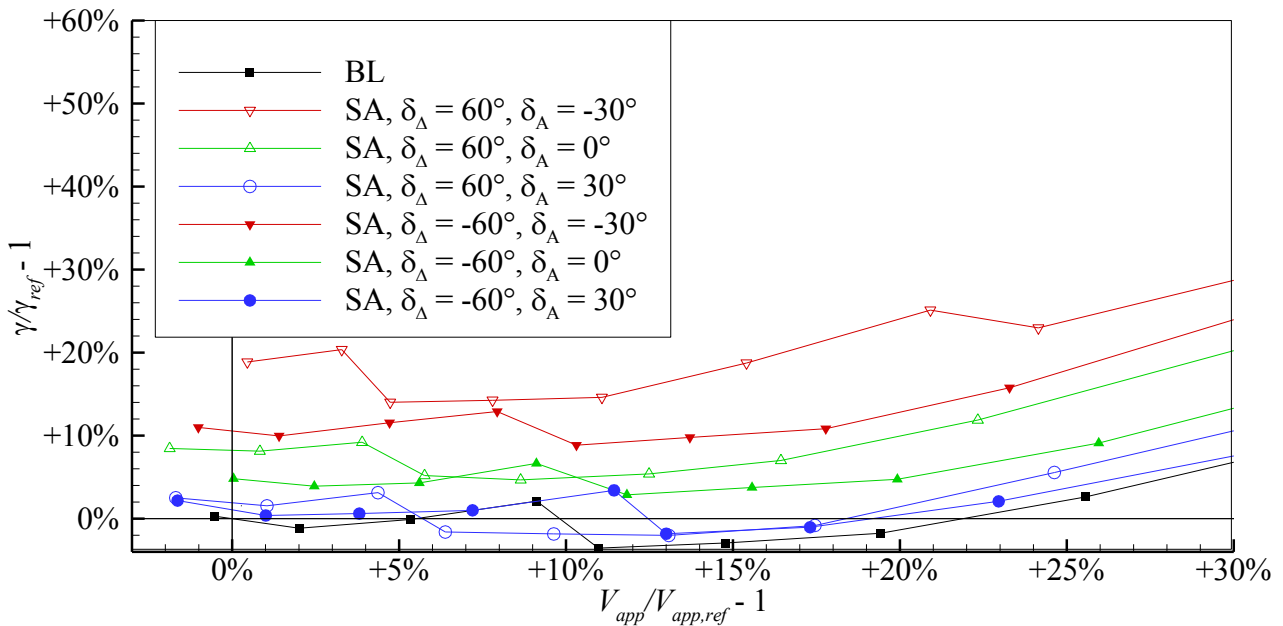


Figure 5-29: Relative descent angle  $\gamma/\gamma_{ref} - 1$  over relative approach velocity  $V_{app}/V_{app,ref} - 1$  for BL and SA with  $\delta_A = -60^\circ$  and  $\delta_A = +60^\circ$ ; various mean deflection angles of  $\delta_A = -30^\circ$ ,  $\delta_A = 0^\circ$ ,  $\delta_A = 30^\circ$  for the range of minimum feasible approach velocities.

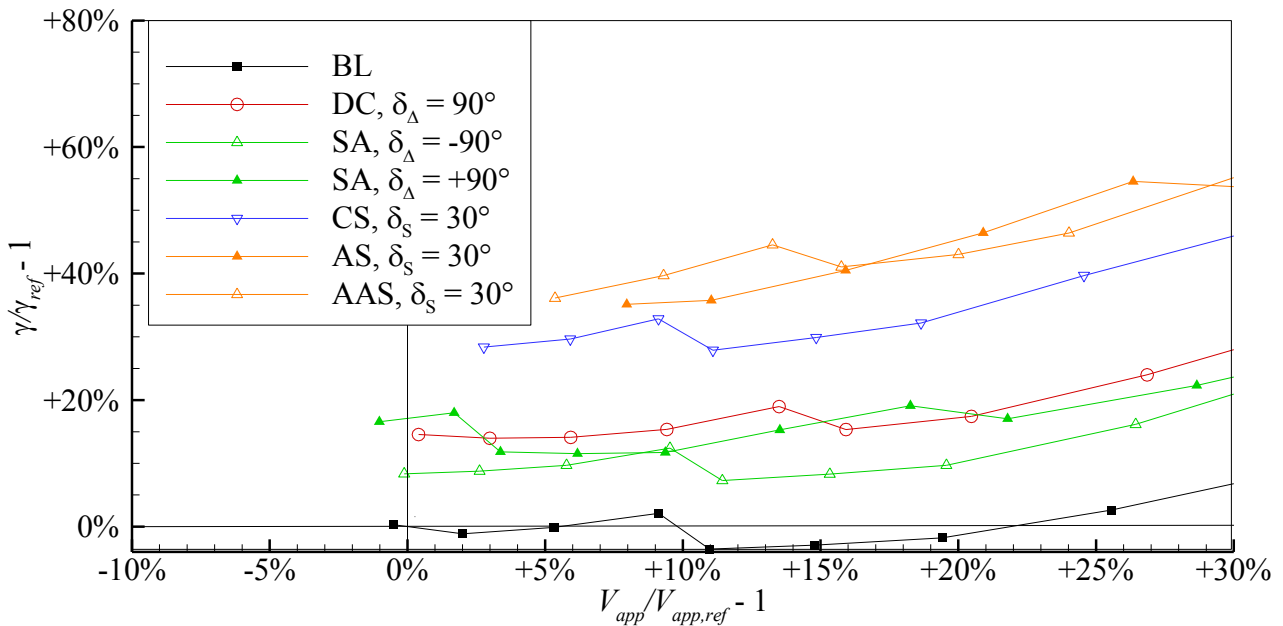


Figure 5-30: Relative descent angle  $\gamma/\gamma_{ref} - 1$  over relative approach velocity  $V_{app}/V_{app,ref} - 1$  for the range of minimum feasible approach velocities: Comparison of all investigated air-brake types at  $|\delta_\Delta| = 90^\circ$  and  $\delta_S = 30^\circ$ .

From these graphs, it appears that all curves of descent angle over approach velocity show a very moderate increase in all cases. This means that the achievable descent angle is not exceptionally sensitive to  $V_{app}$ . However, there is a monotonous coherence between the chosen  $|\delta_\Delta|$ , respectively  $\delta_S$ , and the achievable increase in  $\gamma$  for each device. To compare the results of all configurations, the dependency of change in descent angle on change in minimum feasible  $V_{app,min}$  is displayed for all investigated air-brake types in Figure 5-31a. A linear regression leads to the curves depicted in this graph. The curves' slope  $\partial(\gamma/\gamma_{ref} - 1)/\partial\delta_\Delta$  can be defined as the effectiveness of the air-brake deflection to conduct a steep approach. The effectiveness of DC and SA with positive  $\delta_\Delta$  turns out to be similar, whereas the effectiveness of SA with negative  $\delta_\Delta$  is clearly lower. CS has a considerably higher effectiveness compared to both novel aileron devices. The reason for this is the following: The spoiler not only affects the proximate flow, but also the flow around the flap, which is strongly dependent on the vent size between the trailing edge of the spoiler and the leading edge of the flap. Thus, not only the lift of the wing segment associated with the spoiler decreases, but also the lift produced by the flap is potentially impacted considerably. In contrast to the Conventional Spoiler, both Adverse Spoiler and Advanced Adverse Spoiler show clearly a non-linear effectiveness behavior with a deterioration for high deflection angles in Figure 5-31a, where the maximum increase in approach angle is similar for both configurations as well as for the conventional spoiler.

Figure 5-31b establishes the connection between the deflection values of spoiler  $\delta_S$  and the differential deflection of the multifunctional aileron devices  $\delta_\Delta$ , respectively, and the increase in minimum approach velocity  $V_{app,min}$ . While all aileron devices stay at or

even below the minimum approach velocity of the Baseline with no clear sequence, there is a clear difference in the behavior of the increase in minimum approach velocity for the different investigated spoilers: The increase in  $V_{app,min}$  shows an approximately linear behavior for CS, but a clearly non-linear behavior for AS and AAS with a deterioration in  $V_{app,min}$  at values, which are considerably higher for AS compared to AAS and CS.

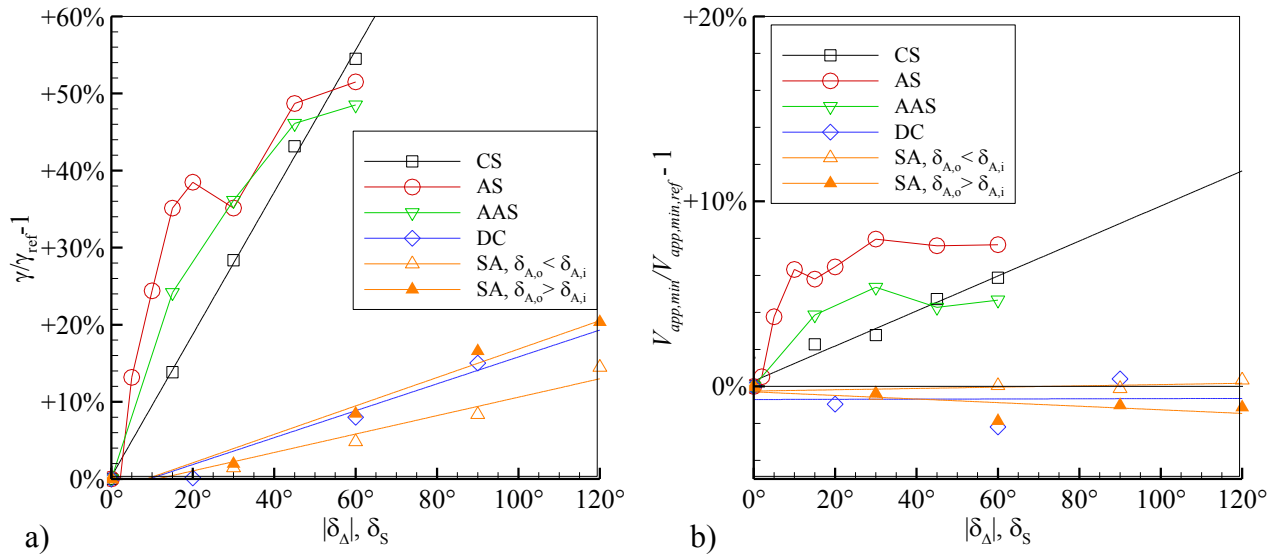


Figure 5-31: a) Relative descent angles  $\gamma/\gamma_{ref} - 1$  of the investigated air-brake configurations over  $|\delta_A|, \delta_S$  at  $V_{app,min}$ . b) Relative approach velocity  $V_{app,min}/V_{app,min,ref} - 1$  of the investigated air-brake configurations over  $|\delta_A|, \delta_S$ .

### 5.2.4 Nonlinear Interference Effects for Combined Usage of Spoiler Devices and Aileron Devices

For linear effects the superposition of the individual trends of a spoiler device and an aileron device is feasible to calculate the combined effect. By comparing the summed up individual effects with the measured effect of the combination the non-linearity of the combination of spoiler and aileron devices becomes clear. This non-linearity is based on interference effects, which are self-evident as both devices are in vicinity to each other. To characterize these interference effects, measurements with combined deflection of aileron and spoiler devices were conducted for selected deflection parameter values. In this subsection, the magnitude of the interference effects should be characterized to touch on this subject. Figure 5-33 shows the results for the change in descent angle over change in approach velocity for a combined deflection of CS with  $\delta_S = 30^\circ$  and DC with  $\delta_A = 0^\circ$  and  $\delta_A = 60^\circ$ , as well as the correspondent cases of solely AS, and solely DC respectively. Additionally, a linear superposition of the AS and DC was conducted and is shown in the graph.

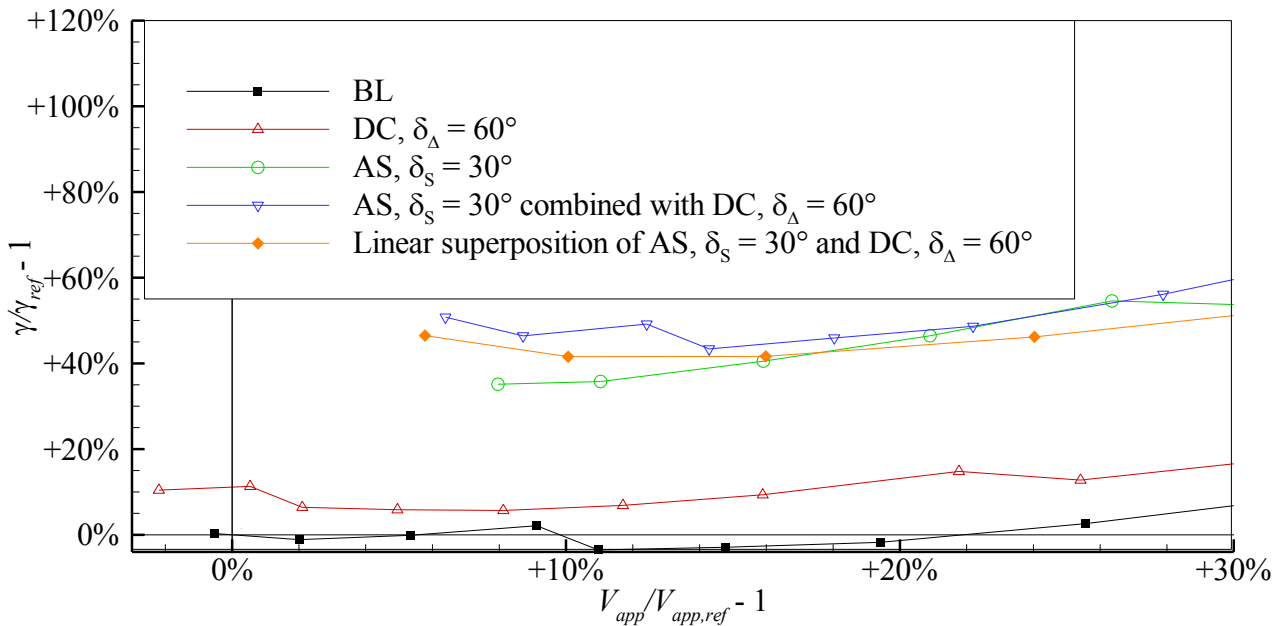


Figure 5-32: Achievable descent angle  $\gamma/\gamma_{ref} - 1$  over approach velocity  $V_{app}/V_{app,ref} - 1$ . Comparison of discrete deployment of DC and AS with combined deployment and linear superposition.

The difference in the results between the combined deployment of DC and AS and the linear superposition of the single deployment of DC and AS is quite small. However, there is a clear tendency of a lower descent angle increase for the superimposed results compared to the combined measurement results over the relevant angle of attack range. This suggests that in this exemplarily case the descent effectiveness is slightly increased by the non-linear interference effects, which appear when the DC device and the AS device are deployed simultaneously.

### 5.3 Evaluation of Aileron Devices Regarding Lateral Control

When using aileron based devices as a means to enhance the steep approach capability of an aircraft, the roll control, which is in the case of the multifunctional aileron devices primarily accomplished by the same devices, must be maintained. In addition, the investigated aileron devices provide the opportunity to provide additional yaw control authority. The reason for this is that the novel aileron can potentially be deflected independently from its roll control function. Both lateral control functions are assessed by the so-called roll control effectiveness and yaw control effectiveness (3.7.3). Regarding the rolling moment it has to be shown, that the roll control effectiveness of the original aileron is retained to ensure that the original maneuverability is not cut back compared to the original high-lift approach configuration. To classify the roll control effectiveness values, the conventional spoiler is included in the lateral control survey.

### 5.3.1 Roll Control Effectiveness

Since the conventional aileron's main purpose is to provide roll control this purpose has to be fulfilled in the same manner by the investigated multifunctional aileron devices. To evaluate the effectiveness providing sufficient roll control the force data was also evaluated with regard to the lateral motion (3.7.2). In this context it is to emphasize again, that the conclusions made here are based on a half-model measurement and can thereby only be used under the assumption of zero angle of yaw.

It is assumed that lateral maneuvering happens at a constant lift coefficient. This assumption leads to changing angles of attack  $\alpha$ , when the control surfaces are deflected. The change in  $\alpha$  providing a specific lift coefficient  $C_{L,app}$ , which is a representative lift coefficient for approach, are shown for different deflections of CS, both multifunctional aileron devices SA and DC, as well as the original aileron (A) in Figure 5-33.

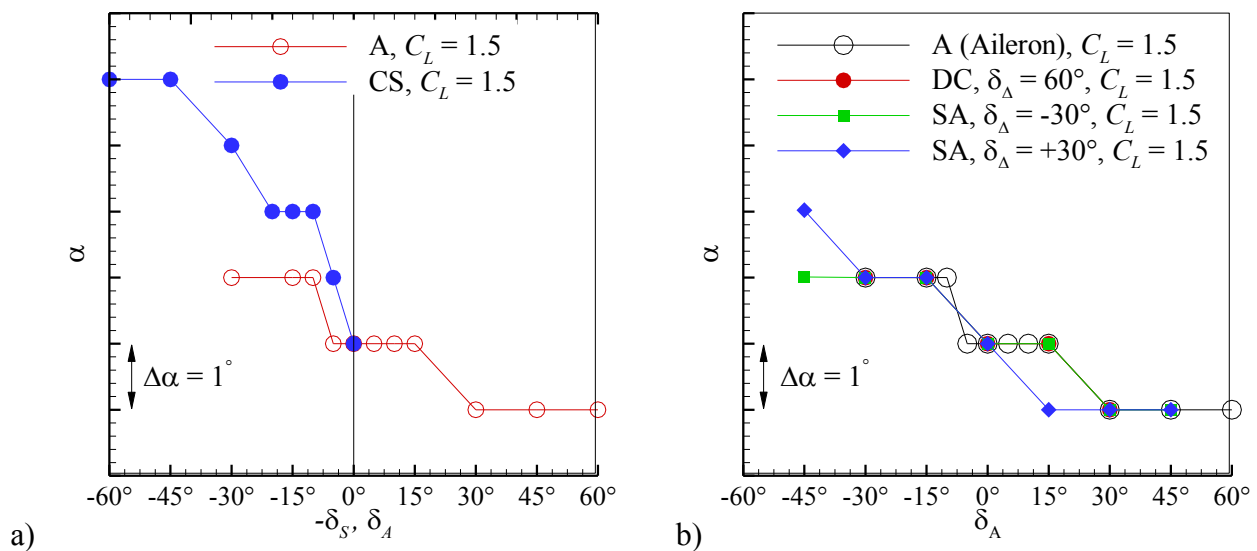


Figure 5-33: Angle of attack  $\alpha$  over control surface deflection angle  $\delta_A$ ,  $\delta_S$  for a constant lift coefficient  $C_L = 1.5$ . a) Configurations A and CS. b) Configurations A, DC, and SA.

Figure 5-34a to Figure 5-34c show the rolling moment coefficient over mean deflection angle  $\delta_A$  for the ailerons, and over spoiler deflection angle  $\delta_S$  for CS. Herein, the lift coefficient is kept constant at  $C_L = 1.5$ .

For all the original and multifunctional aileron-configurations the data behaves approximately linear for small  $\delta_A$ , but decidedly non-linear for higher  $\delta_A$ . The spoiler-data provides a non-linearity included from small  $\delta_S$  on. In all cases, the non-linearity expresses itself in a flattening of the curve and hence a loss in roll control effectiveness for high deflections. To discuss the roll control effectiveness for small deflections of the devices, the rolling moment coefficient  $C_l$  as function of deflection angle  $\delta_A$ ,  $\delta_S$  is divided into an interval I, characterized by a quasi-linear behavior nearby  $\delta_{A,S} = 0^\circ$  and an interval II, with

non-linear characteristics. The ranges of the intervals I are given in Table 5-1. For these intervals I linear regressions were conducted according to subsection 3.7.4. The quality  $R^2$  of the regression is also listed in Table 5-1.

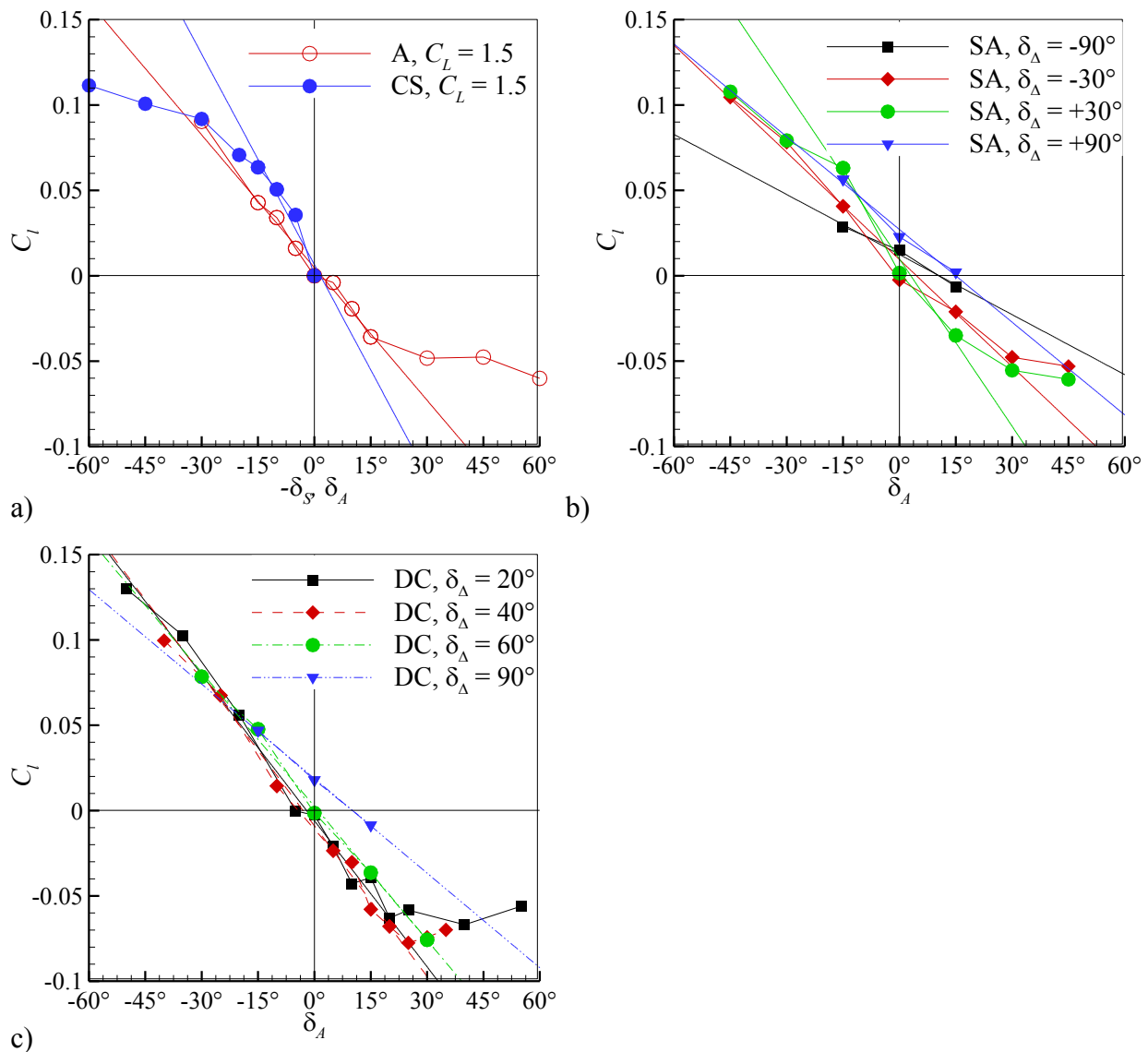


Figure 5-34: Relations of  $C_l$  over  $\delta_A$ ,  $\delta_S$ . Exemplarily plotted for some deflection configuration of the investigated devices at fixed  $C_L = 1.5$ . a) Configurations A and CS. b) Configurations SA. c) Configurations DC.

With  $R^2 > 0.97$  for all performed regressions, except for the CS data, where  $R^2 > 0.935$ , the linear regression type is considered to be representative for the roll control behavior in interval I. The exception of CS is due to spoiler data, which does not linearize very well as the spoiler flow field is characterized by a large portion of separated flow. The linear curve fits are of the form  $C_l = C_{l0} + \partial C_l / \partial \delta_{A,S} \cdot \delta_{A,S}$  and plotted as lines in Figure 5-34a to Figure 5-34c. The coefficients, which describe the linear behavior, are  $C_{l0}$  and  $C_{l\delta_{A,S}} = \partial C_l / \partial \delta_{A,S}$  and can also be found in Table 5-1.  $C_{l0}$ -values describe the offset in rolling moment for zero deflection of the device, whereas more importantly,  $C_{l\delta_{A,S}}$ -values describe the roll control

effectiveness of the control surfaces. When comparing  $|C_{l\delta_{A,S}}|$  of the different devices the conventional spoiler emerges as the most effective one with a value 26% higher than the second largest value and 59% higher than the conventional aileron. The reason for this is again that the spoiler also affects the flap flow. When comparing the effectiveness of an aileron with a spoiler, it must also be kept in mind, that the aileron can be deflected asymmetrically on both wings leading to an approximately doubled effectiveness. This can compensate the lower effectiveness of a single wing's aileron deflection.

Table 5-1: Linear interval identification, coefficients of linear regression and quality of linear regression;  $C_L = 1.5$  for all configurations.

Configuration	$\delta$ -range of interval I	$C_{l_0}$	$C_{l\delta_{A,S}}$	Quality of regression $R^2$
Conventional Aileron	$-15^\circ \div +15^\circ$	$4.841 \cdot 10^{-3}$	$-2.590 \cdot 10^{-3}$	0.987003
Conventional Spoiler	$0^\circ \div +15^\circ$	$6.604 \cdot 10^{-3}$	$4.111 \cdot 10^{-3}$	0.935326
Split Aileron, $\delta_A = -90^\circ$	$-15^\circ \div +15^\circ$	$1.239 \cdot 10^{-2}$	$-1.173 \cdot 10^{-3}$	0.986251
Split Aileron, $\delta_A = -60^\circ$	$-30^\circ \div +30^\circ$	$1.540 \cdot 10^{-2}$	$-1.525 \cdot 10^{-3}$	0.998200
Split Aileron, $\delta_A = -30^\circ$	$-30^\circ \div +30^\circ$	$9.489 \cdot 10^{-3}$	$-2.093 \cdot 10^{-3}$	0.979139
Split Aileron, $\delta_A = +30^\circ$	$-15^\circ \div +15^\circ$	$9.870 \cdot 10^{-3}$	$-3.270 \cdot 10^{-3}$	0.978852
Split Aileron, $\delta_A = +60^\circ$	$-30^\circ \div +30^\circ$	$1.823 \cdot 10^{-2}$	$-1.558 \cdot 10^{-3}$	0.995422
Split Aileron, $\delta_A = +90^\circ$	$-15^\circ \div +15^\circ$	$2.710 \cdot 10^{-2}$	$-1.811 \cdot 10^{-3}$	0.981202
Deceleron, $\delta_A = 20^\circ$	$-20^\circ \div +20^\circ$	$-5.903 \cdot 10^{-3}$	$-2.855 \cdot 10^{-3}$	0.970683
Deceleron, $\delta_A = 40^\circ$	$-25^\circ \div +20^\circ$	$-8.914 \cdot 10^{-3}$	$-2.945 \cdot 10^{-3}$	0.989412
Deceleron, $\delta_A = 60^\circ$	$-30^\circ \div +30^\circ$	$2.512 \cdot 10^{-3}$	$-2.615 \cdot 10^{-3}$	0.996289
Deceleron, $\delta_A = 90^\circ$	$-15^\circ \div +15^\circ$	$1.873 \cdot 10^{-2}$	$-1.847 \cdot 10^{-3}$	0.999355

In Figure 5-35a, the roll control effectiveness of the different systems is plotted against the differential deflection angle  $\delta_A$  to show, whether the roll control effectiveness  $C_{l\delta_{A,S}}$  of the systems remains maintained when utilized as air brake. While DC even has a larger roll control effectiveness than A for moderate  $\delta_A$  with even an increase in the effectiveness between  $\delta_A = 20^\circ$  and  $\delta_A = 40^\circ$ ,  $C_{l\delta_{A,S}}$  decreases for higher  $\delta_A > 40^\circ$  monotonously. For SA with  $\delta_{A,o} > \delta_{A,i}$ ,  $C_{l\delta_{A,S}}$  starts at higher values for  $C_{l\delta_{A,S}}$  compared to A at  $\delta_A = 30^\circ$ , declines then rapidly for  $\delta_A = 60^\circ$ , and recovers slightly for  $\delta_A = 90^\circ$ . SA with  $\delta_{A,o} < \delta_{A,i}$  shows yet another behavior: The roll control effectiveness starts with low values even for a moderate  $\delta_A = 30^\circ$  and decreases monotonously for an increase in  $\delta_A$ . The reason for the generally observable decline in roll control effectiveness for high differential deflection angles is the

following: For high  $\delta_A$ -values there is hardly any mean deflection angle  $\delta_A$ , for which the flow is attached to the low-pressure side of the aileron. The aileron is stalled which results in only moderate aerodynamic lift force. A  $\delta_A$ -variation has little influence on this stall, leading to no big difference in the lift produced for different  $\delta_A$  and, thus, low roll effectiveness.

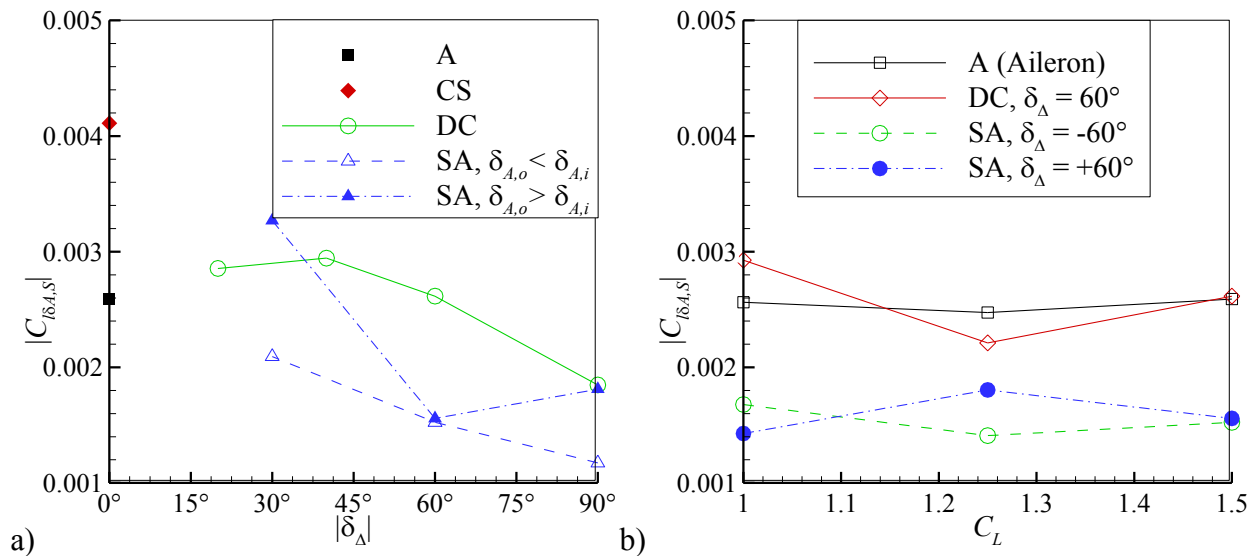


Figure 5-35: a) Relations of  $|C_{l_{\delta_A, s}}|$  over  $\delta_A$ . Plotted for all investigated aileron devices and CS at fixed  $C_L = 1.5$ . b) Relations of  $|C_{l_{\delta_A, s}}|$  over  $C_L$ . Plotted for CA, DC, SA configurations at  $C_L = 1$ ,  $C_L = 1.25$ , and  $C_L = 1.5$ .

Finally, it has to be demonstrated, whether the roll control effectiveness is maintained for different levels of  $C_L$ . Thus, the linear regressions are also conducted for representative configurations with  $|\delta_A| = 60^\circ$  at three representative levels of  $C_L = 1$ , 1.25, and 1.5.  $|C_{l_{\delta_A, s}}|$  is plotted against  $C_L$  for these cases in Figure 5-35b.  $|C_{l_{\delta_A, s}}|$  of the conventional aileron is nearly unchanged for the different  $C_L$ -levels, whereas there is a difference of approximately 30% in the values of DC and SA for the different  $C_L$ -levels. The progress of the local flow separation at the device for an increase in  $|\delta_A|$  is supposed to be the reason for that.

### 5.3.2 Yaw Control Effectiveness

To briefly assess the yaw control effectiveness of SA and DC, Figure 5-36a shows the results for  $C_n$  over  $\delta_A$  for all investigated SA configurations and Figure 5-36b shows it for all investigated DC configurations. The curves cover a range of mean aileron deflection of  $\delta_A = -30^\circ$  to  $+30^\circ$ . A quadratic regression analysis has been performed and the curves are included in the graphs to show the global tendency of the yaw control effectiveness. This is not the case for SA with  $\delta_A = -15^\circ$ , as well as DC with  $\delta_A = 0^\circ$ , because the regression analysis quality was not satisfying for these curves. The number of data points is very

different for the different cases, so that the value of the regression curves is very limited. However, some interesting facts can be inferred from this qualitative analysis: The trends in the curves are all showing an increase in yawing moment for an increase in  $|\delta_A|$ . Minor discrepancies are only found for very small differential deflection angles of SA with  $\delta_A = 0^\circ$ . For the SA-configurations it becomes clear that for all mean deflection values the achievable yawing moment is significantly higher for positive values of  $\delta_A$  compared to the same absolute values of negative sign. Another outcome is that the yawing moment is significantly higher for negative mean deflection angles compared to positive ones. This is also the case for DC, at which due to kinematic constraints the mean angle is limited in negative direction to a value of  $\delta_A = -15^\circ$ .

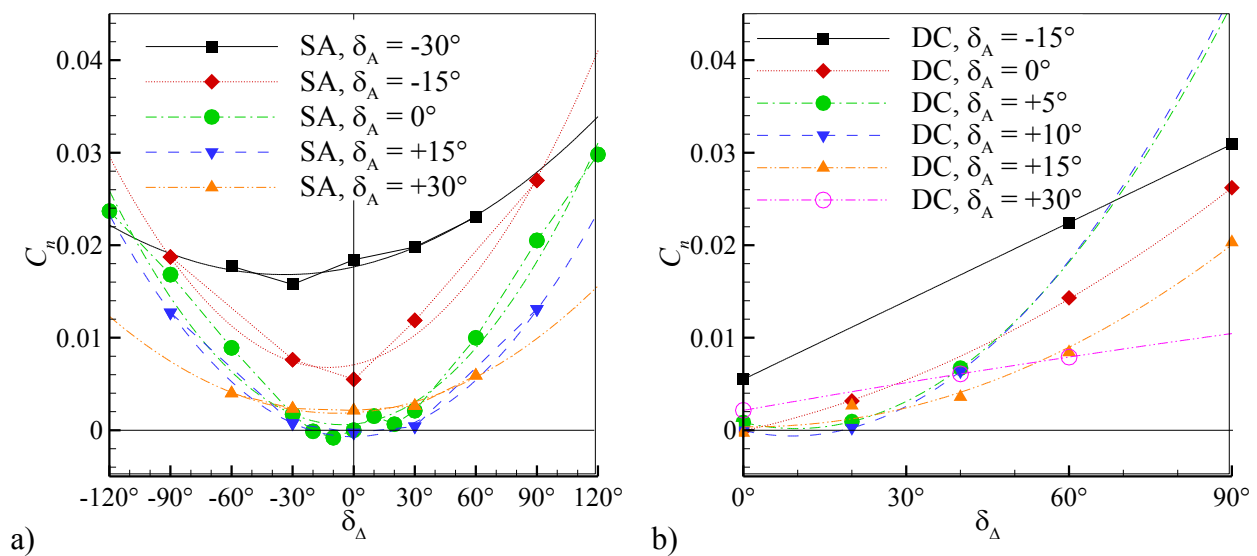


Figure 5-36: Relations of  $C_n$  over  $\delta_A$ , exemplarily plotted for some deflection configurations of the investigated devices at fixed  $C_L = 1.5$ . a) Configurations SA. b) Configurations DC.

## 5.4 Effect of Devices on the Static Longitudinal Stability

The condition for static longitudinal stability was introduced in subsection 2.4.3. It is depending on the pitching moment over lift coefficient characteristics  $dC_M/dC_L$ . The pitching moment behavior of the investigated configurations was already discussed. To make a statement about the influence of the devices on the static longitudinal stability in comparison, Figure 5-37 shows the pitching moment over lift coefficient for all investigated configurations with one representative deflection, as well as for the Baseline (BL).

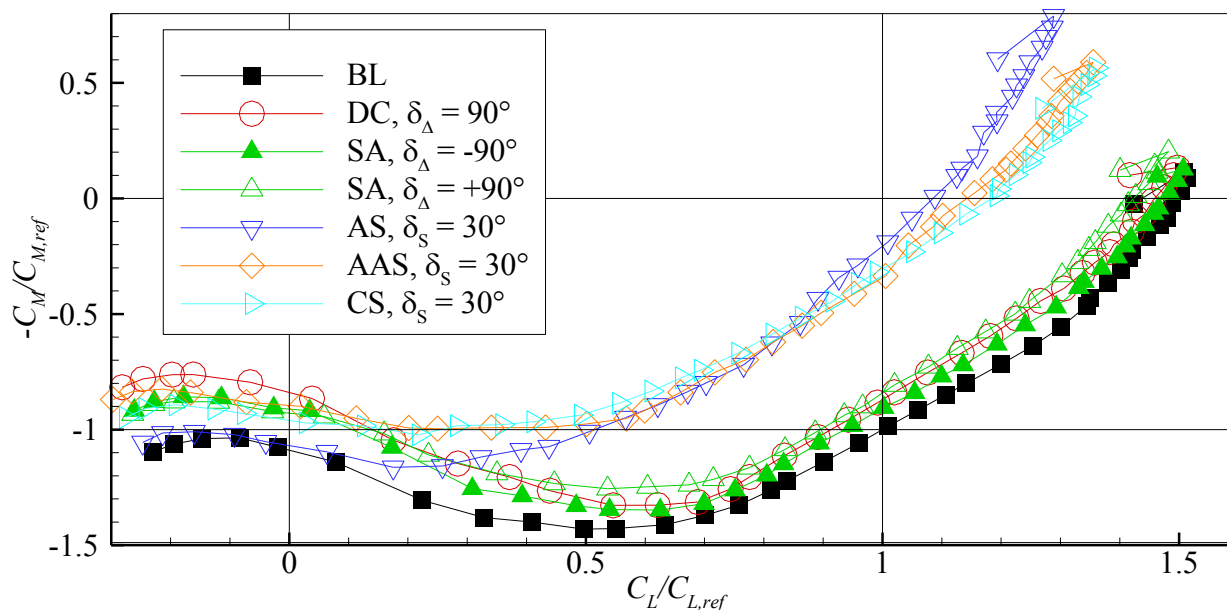


Figure 5-37:  $C_M$  over  $C_L$  for the devices CS, AS, AAS, DC, SA;  $\delta_s = 30^\circ$ ,  $\delta_\Delta = -90^\circ$ ,  $\delta_\Delta = +90^\circ$ .

While the influence on the pitching moment coefficient is quite small and similar for all cases for low  $C_L$ , there is a different behavior in this aspect for all multifunctional aileron devices compared to the spoilers for higher  $C_L$ . Even the sequence of the curves is inverted. Indeed, the pitching moment coefficient is increased towards a nose up behavior for all investigated cases. At the same time, the difference in  $C_M$  is much higher for all investigated spoiler devices AS, AAS, and CS compared to SA and DC in the most relevant region at  $C_L/C_{Lref} \approx 1$ . This tendency has to be kept in mind, regarding total drag for the case, if one is considering trim drag.

In contrast to that, the influence of the investigated air-brake devices on longitudinal stability is negligible as  $dC_M/dC_L$  is nearly unchanged for all configurations in the relevant region around  $C_L/C_{Lref} \approx 1$ . Only AS shows a slightly steeper trend in the  $C_M$  over  $C_L$  curve and thus leads potentially to a higher static longitudinal stability.

## 5.5 Other Evaluation Fields

A complete evaluation of new devices for CTA to enable conducting steep approaches would also have to include various fields beyond aerodynamics and flight mechanics discussed until here. To address all fields would go beyond the scope of this thesis. If thinking about further fields one would surely include among others the following ones, for which some aspects are outlined: Manufacturing, actuation, and structural mechanics.

### *Manufacturing*

Nowadays, ailerons and spoilers are mostly produced out of Carbon-Fiber Reinforced Plastics. This material has a very high stiffness and strength compared to the more conventional aluminum, mostly used on today's CTA-structures. The geometry of the

Conventional Spoiler (CS), the Adverse Spoiler (AS) and the Advanced Adverse Spoiler (AAS) is very similar with the exception that the lower side of the Adverse Spoiler has to be smooth, whereas the lower sides of CS and AAS do not have this requirement. This is due to the fact that flow passes through the gap between AS and main wing. However, it should not be necessary to have a higher surface quality on the lower AS side compared to the upper side, so that similar manufacturing methods are valid for all three spoiler types. Unlike CS, AS, and SA, AAS and DC have to be thinner due to the splitting of the geometry in upper and lower parts. This reduction in material thickness has to be kept in mind, so that the material and with that the manufacturing method is valid to support the loads on the surfaces.

#### *Actuation Design*

The development and design of the high-lift drive systems to actuate the high-lift devices is a complex process. Additionally, all flight control systems, including the high-lift drive system, have to be fault-tolerant and fulfill high requirements regarding the reliability [135]. These requirements also lead to high costs, if a high-lift device with a complex actuation is chosen for a CTA design. This again argues against complex high lift systems in general.

From an actuation point of view the AS and AAS devices are no more complex than the conventional spoiler as only a one dimensional rotational movement has to be actuated. By contrast, the DC system and SA system are more complex in their actuation. The actuation of the DC needs a second rotational actuation integrated into the aileron. This means also, that this actuation system has to be limited in size. The SA needs two separate actuation systems for the two aileron parts. This means a doubling of the number of actuation systems of the aileron.

#### *Weight*

Considering the Breguet range equation, the key design drivers of CTA design are aerodynamic efficiency, specific fuel consumption, and structural mass [26]. Therefore, a minimization of the structural mass has always to be aimed when designing a CTA and its subsystems, including the control devices.

If we start from the assumption of similar materials used for the new devices compared to the conventional ones, then only the mass difference due to differences in mechanical loads are relevant. Due to the fact that the mounting of the AS is not possible along the stronger front side of the device as it is the case for a CS device, the loads are considered higher and thus the system should be heavier. It is not possible to quantify this without performing a detailed structural analysis, but the tendency is quite obvious. To a lower extent this is also the case for the AAS but this time it is at least possible to induce the loads along the complete span of the trailing edge through the sealing of the main wing gap. On the other hand, the AAS has to be thinner due to the split, and therefore needs a

reinforcement compared to the AS. This effect is also relevant for the DC, which has in a best-case scenario just halve the thickness of the conventional aileron due to the splitting.

## 5.6 Synthesis

Experimental investigations have been conducted to study the effect of two multifunctional aileron devices and two innovative spoiler devices, as well as a conventional spoiler on the aerodynamic coefficients of longitudinal and lateral motion with the aim to use them as air brakes for steep approaches. For that purpose, a wind tunnel half model in full approach setting is successively fitted with the devices, which ought to be investigated. Each of the devices is tested with various deflection angles. For each configuration, the angle of attack is varied in order to obtain polars of the desired aerodynamic coefficients. For each campaign, the Baseline configuration with no air-brake devices installed was remeasured at the beginning to eliminate uncertainties connected to the reassembly of the model in the wind tunnel. As final result, the effectiveness of each configuration to increase the descent angle, while keeping the approach velocity low for steep approach purposes is evaluated. The limits of the maximum descent velocity are also discussed and compared for the different configurations. As the aileron of a CTA has the main purpose to provide roll control, the roll control effectiveness of both novel ailerons is evaluated and compared to the effectiveness of the conventional aileron and the conventional spoiler. Additionally, other minor evaluation topics are raised shortly: Yaw control effectiveness, effect of devices on longitudinal stability, manufacturing, actuation, and weight.

Concerning the applicability of the investigated configurations for conducting steep approach, one can sum up the most important findings by a graph, which presents the change in minimum approach velocity relative to the Baseline's minimum approach velocity and the corresponding change in descent angle (Figure 5-38).

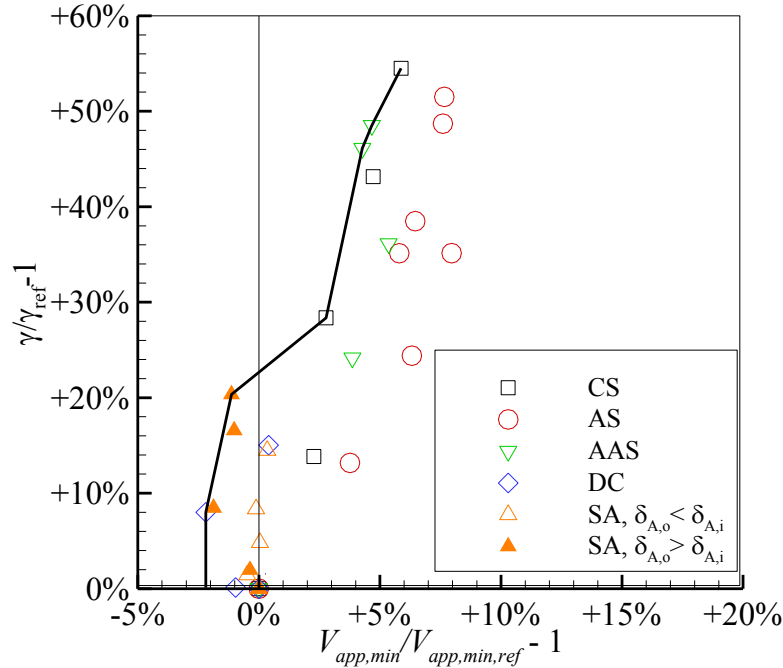


Figure 5-38: Relative descent angles  $\gamma/\gamma_{ref} - 1$  over relative  $V_{app,min}/V_{app,min,ref} - 1$  for all investigated air-brake configurations with Pareto frontier.

Included in the graph is the Pareto frontier, which exposes the optimal configurations for either a given minimum approach velocity or a given required value of increase in descent angle. The Pareto frontier passes through configurations of all devices except AS, depending on the value combination of approach velocity and descent angle: For low descent angles the DC-configuration with  $\delta_A = 60^\circ$  and for slightly higher ones the SA-configuration with  $\delta_A = 60^\circ$  turns out to be superior. This is followed by the CS-configuration with  $\delta_S = 30^\circ$ , two AAS-configurations with  $\delta_S = 45^\circ$  and  $\delta_S = 60^\circ$ , and the CS-configuration with  $\delta_S = 60^\circ$ . This is due to the fact, that concerning minimum approach velocity  $V_{app,min}$ , a completely different behavior is observed for the multifunctional aileron configurations compared to the spoilers. While there is a clear dependency of higher minimum  $V_{app,min}$  for an increase in  $\delta_S$  for the CS, and a leap in  $V_{app,min}$  for AS and AAS with low  $\delta_S$ , which stays approximately constant for higher  $\delta_S$ , no such behavior is observed for the investigated aileron devices, DC and SA. Instead, minimum  $V_{app}$  stays nearly constant for the aileron devices compared to BL, and is even lower than for BL in some cases.

The tendency of increased descent angle  $\gamma$  for higher differential deflection angles  $\delta_A$  is monotonous for both investigated aileron devices. Two of these configurations have a similar effectiveness: The Deceleron and the Split Aileron with a larger inner deflection angle compared to the outer deflection angle  $\delta_{A,o} < \delta_{A,i}$ . The other Split Aileron configuration with a smaller inner deflection angle compared to the outer deflection angle  $\delta_{A,o} > \delta_{A,i}$  trails the other two configurations concerning this matter. When comparing the results for the ailerons to the ones for the spoilers, it appears that the effectiveness to

increase  $\gamma$  is substantially higher for all three spoiler devices compared to both multifunctional aileron devices. To sum up the results for the spoilers, it can be concluded, that both novel spoilers AS and AAS have a higher increase in descent angle than the CS for the lower investigated deflection angles up to  $\delta_s = 45^\circ$  with AS being in average slightly more effective than AAS. This advantage is deteriorate progressively for higher  $\delta_s$  leading to a slight disadvantage in descent angle change compared to CS for the highest investigated deflection of  $\delta_s = 60^\circ$ , which does not show such a deterioration. With respect to the other main steep-approach parameter, the increase in approach velocity is significantly lower for the AAS compared to the AS, but trails the CS in this aspect.

Regarding roll control, the analysis reveals that the roll control effectiveness values for the aileron devices are in the same magnitude as for the conventional aileron for low differential deflection angles, but decrease significantly for higher investigated differential deflection angles.

# 6. FLOW TOPOLOGY ANALYSIS

The aerodynamic coefficients, which were just discussed and account for the steep approach performance of the individual devices are related to the individual local flow topology created by the investigated devices. Thus, it is of importance to analyze the flow topology to understand the corresponding flow mechanisms. After this analysis is performed and the flow topology is understood, one has the ability to benefit from this and try to design improved devices.

Two different methods serve to analyze the flow topology in this work: On the one hand, there are CFD simulations, which give values of the flow parameters in the complete flow domain. However, the domain complexity for the numerical investigations was reduced to 2D and 2.5D, respectively, to reduce the computational effort (see section 4.2). All the details of the conducted CFD simulations and their constraints were introduced and discussed in chapter 4. On the other hand, there is tuft flow visualization, which is applied in the wind tunnel tests and thereby uses the complete complex 3D geometry. This technique was introduced in subsection 3.2.2 and is restricted to evaluate the near-surface flow only qualitatively.

The investigated configurations comprise the Baseline configuration (BL) without any air-brake devices, as well as three configurations with spoiler devices: Conventional Spoiler (CS), Adverse Spoiler (AS), and Advanced Adverse Spoiler (AAS). The flow topology associated with a three-element high-lift airfoil similar to BL was already discussed based on a literature review in subsection 2.3.5. Thus, the discussion of the flow topology for the BL focuses on how our specific research configuration compares to the general case and, more importantly, serves as a basis for the subsequent assessment of the flow topology of the configurations with the different spoilers.

## 6.1 Flow Topology Analysis by CFD Simulations

Referring to the 2D CFD-simulations, it turned out that all investigated configurations contain highly unsteady flow features. For this reason, RANS simulations do not converge to a satisfying degree in any case. Instead, URANS simulations need to be conducted, exclusively, and are used to analyze both the unsteady features of the flow as well as the mean flow, gathered by statistically averaging the results over sufficiently long simulation duration. The 2.5D simulations with the SAS turbulence model (SAS) serve to get insight into the detailed 3D turbulent flow structures, which are not resolved by the 2D URANS simulation method. Due to the high computational effort, which is necessary for the SAS-simulations, the number of configurations investigated by this method had to be very

limited, whereas a parameter variation of the main parameters, namely angle of attack  $\alpha$  and deflection angle  $\delta_s$ , was carried out for the 2D URANS simulations. However, the abundance of cases is reduced to representative ones for the detailed discussion in this chapter.

In the following subsections, the URANS-results for selected  $\alpha$ - and  $\delta_s$ -values are discussed in detail in one subsection per spoiler configuration. Afterwards, the URANS results for all the spoiler configurations with fixed angle of attack of  $\alpha = 10^\circ$  and spoiler deflection of  $\delta_s = 30^\circ$  are comparatively discussed concerning the global unsteady features by conducting FFTs. Finally, the SAS simulation results are presented.

The Strouhal number  $St$ , introduced in subsection 2.3.1, is calculated in the following discussion for different unsteady flow phenomena. To illustrate the characteristic length scales used for this purpose, Figure 6-1 shows a sketch of the periodic vortex shedding areas at the spoiler and flap of the CS-case. In the sketch, the characteristic length scales resulting from the lengths of the flap  $c_{Fl,proj}$  and spoiler plus flap  $c_{Fl,Sp,proj}$ , in both cases projected perpendicularly to the inflow direction, are included. The length scales relevant for other flow phenomena result analogously by projecting the geometric dimensions perpendicularly to the inflow direction.

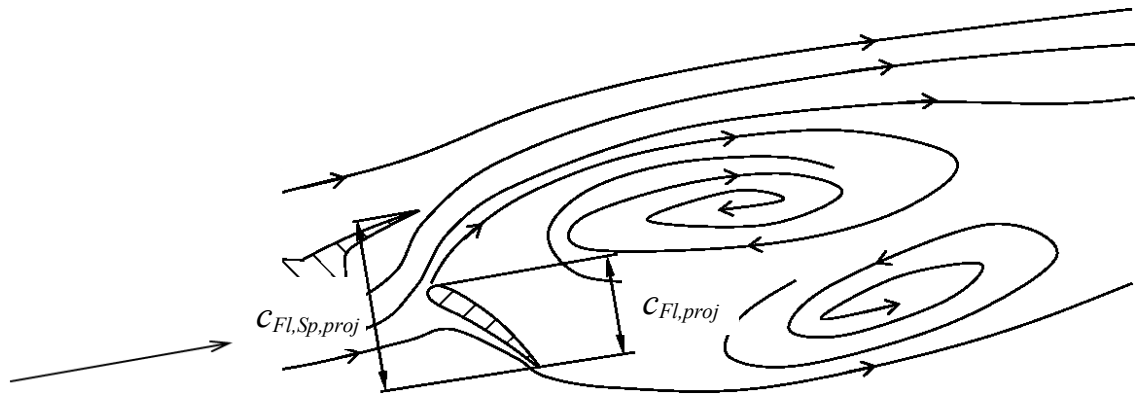


Figure 6-1: Sketch of periodic vortex shedding areas and the associated characteristic length scales for the CS-case.

### 6.1.1 Flow Topology of Baseline Case

The following discussion of the BL simulations is aimed to show at first that the gathered results are valid with reference to results found in literature (subsection 2.3.5) for comparable three-element high-lift airfoil geometries and secondly to discuss the flow-field associated to the actual BL-case in more detail. In analogy to Figure 2-16, the average pressure coefficient distribution over the surfaces from the URANS simulations is displayed in Figure 6-2 for BL with  $\alpha = 0^\circ$ ,  $\alpha = 10^\circ$ , and  $\alpha = 15^\circ$ .

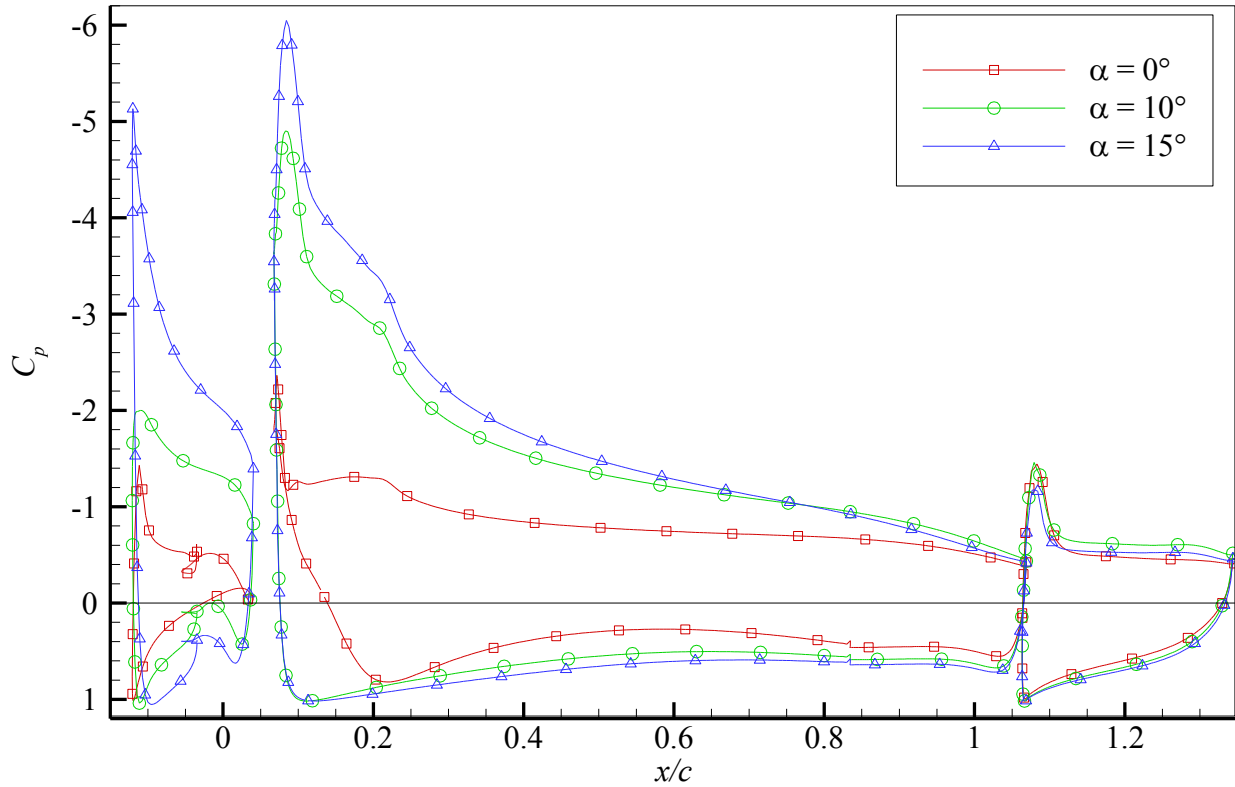


Figure 6-2: Average surface pressure coefficient distributions. URANS result of BL-case at  $\alpha = 0^\circ$ ,  $\alpha = 10^\circ$ , and  $\alpha = 15^\circ$ ,  $U_\infty = 50$  m/s,  $Re_\infty = 1 \cdot 10^6$ .

All features discussed in subsection 2.3.5 for the general three-element high-lift airfoil case appear again in the results with  $\alpha = 10^\circ$  and  $\alpha = 15^\circ$ , which are representative angles of attack for the approach: In the nose region of each of the three elements a suction peak forms on the top side. Each is followed by a steep pressure rise. The suction peaks at slat and main wing increase, when  $\alpha$  is increased. In difference to the general case discussed in subsection 2.3.5, the pressure rise on the flap is not distinct downstream to the trailing edge, but instead a plateau forms shortly after the suction peak. This indicates an extensive flow separation on the top side of the flap for the BL-cases. This also explains the fact that the suction peak is stagnating from  $\alpha = 10^\circ$  to  $15^\circ$ , as the flap is already stalled at  $\alpha = 10^\circ$ . For  $\alpha = 0^\circ$ , the pressure on top and bottom side of slat is reversed, leading to a suction peak on the lower side. On the main wing, nearly no suction peak is formed, and on the flap, the pressure distribution is very similar to the cases at higher  $\alpha$ . The distribution in the symmetry plane of the mean total velocity related to the inflow velocity is shown in Figure 6-3 for the case with  $\alpha = 10^\circ$ .

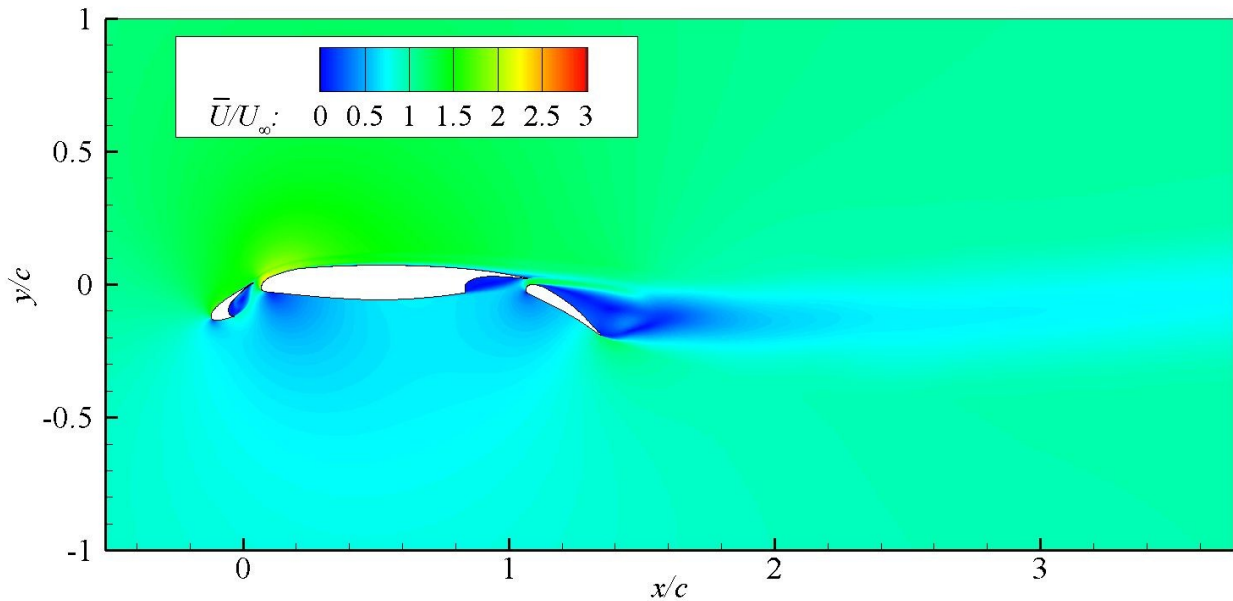


Figure 6-3: Distribution of mean total velocity in symmetry plane. URANS result of BL-case at  $\alpha = 10^\circ$ ,  $U_\infty = 50$  m/s,  $Re_\infty = 1 \cdot 10^6$ .

Herein, the separating streamline can be clearly identified by the sharp color difference between the flow separation area in the slat cove in blue and the flow, which is accelerated from below the slat through the gap between slat trailing edge and the main wing leading curvature in green. This is also the case for the main wing flap cavity, where a clear color difference in the velocity contour plot gives the separating line between the flow separation area in the cavity and the flow, which is accelerated through the flap gap. This jet flow created by the flap gap is even clearly recognizable behind the gap downstream as far as approximately the length of the flap. Again, the velocity contour plot reveals the wake of the wing with a reduced velocity compared to the inflow velocity, which stays observable far downstream.

Areas of reversed flow velocity  $u < 0$  m/s (Figure 6-4) are located for  $\alpha = 10^\circ$  in the slat cove, the main wing flap cavity and at the flow separation zone on nearly the complete top side of the flap. This zone emanating from the flap flow separation extends downstream to about three quarters of the flap chord length behind the flap's trailing edge.

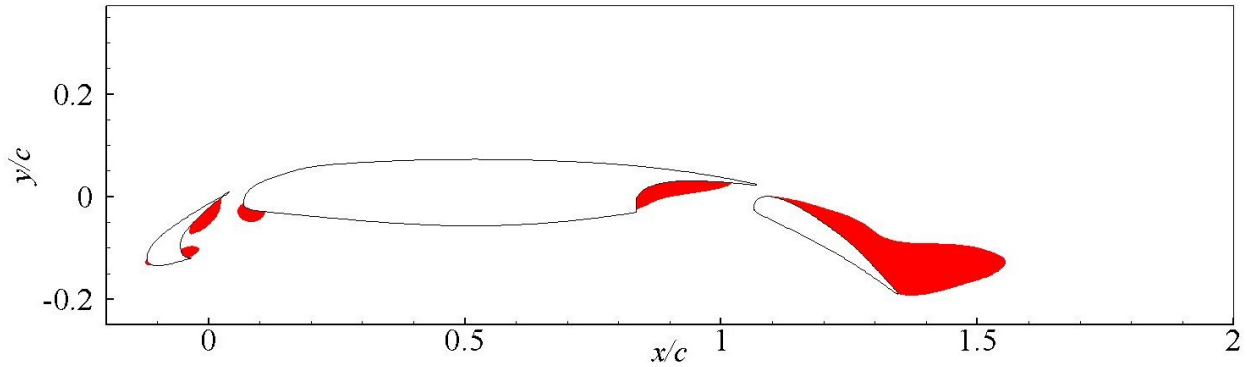


Figure 6-4: Areas of reverse velocity in symmetry plane. Averaged URANS result of BL-case at  $\alpha = 10^\circ$ ,  $U_\infty = 50$  m/s,  $Re_\infty = 1 \cdot 10^6$ .

The distribution of the pressure loss coefficient  $K_L$ , displayed as contour plot in Figure 6-5, reveals the regions in the flow field where a high distortion and thus a high aerodynamic loss occurs. Areas, where  $K_L < 0.003$  are blanked to emphasize the high loss regions. These are located in the flow separation region of slat cove and main wing flap cavity and where the separation occurs on the top side of the flap. Also, a thin wake with high distortion forms from the trailing edge of the slat, which progresses up to the main wing's trailing edge, but does not merge with the boundary layers high distortion band of the main wing. This again forms a distortion band behind the main wing's trailing edge, which merges with the distortion area originating from the flap separation and finally forms a wide distortion region behind main wing and flap.

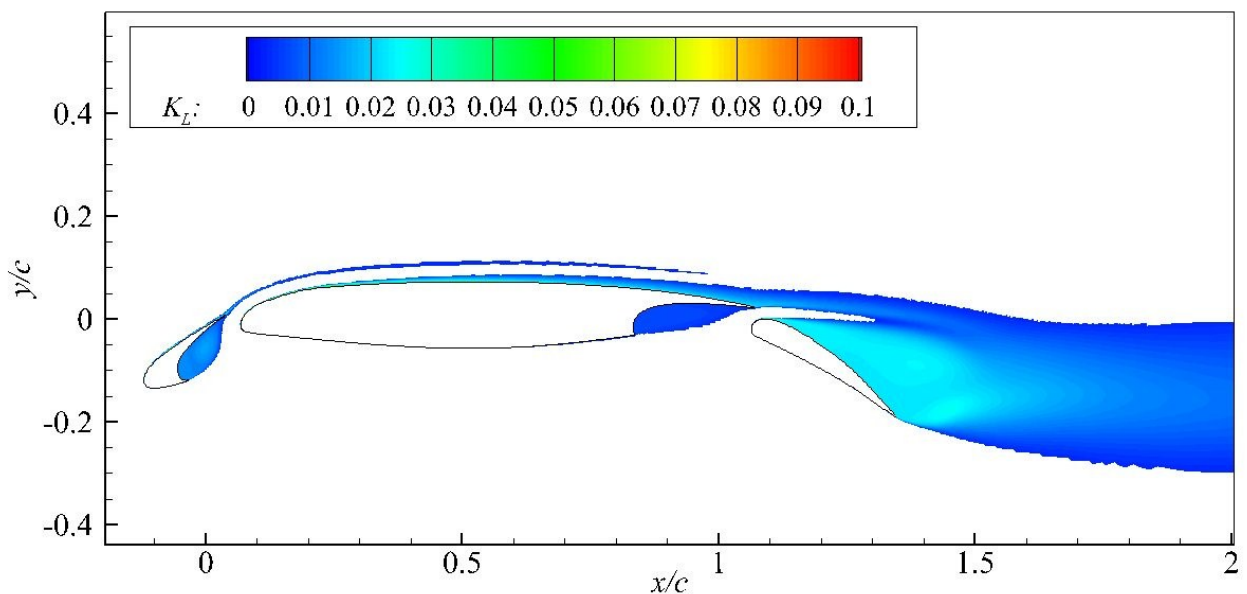


Figure 6-5: Distribution of mean total pressure loss coefficient  $K_L$  in symmetry plane. URANS result of BL-case at  $\alpha = 10^\circ$ ,  $U_\infty = 50$  m/s,  $Re_\infty = 1 \cdot 10^6$ .

Having a look at the transient results from the URANS simulations, one recognizes that the main unsteady flow region in this BL-case is the flow associated to the flap, namely the

flow above the flap and in the wake: The streamwise position of the flow separation on the upper flap side is harmonically oscillating and thereby generating a vortex street behind the airfoil. For  $\alpha = 10^\circ$ , the structure of this flow instability with a frequency of  $f = 391\text{Hz}$  and subsequently a Strouhal number of  $St = 0.3$  based on the streamwise projected flap chord  $c_{Fl,proj}$  becomes apparent, when having a look at the total velocity distribution for two points in simulation time  $t_1$ , and  $t_2$ . These represent two opposing states in the oscillation cycle of the flow. This is illustrated in Figure 6-6 by the total velocity distribution  $U/U_\infty$  in the symmetry plane for  $t_1$  and  $t_2$ .

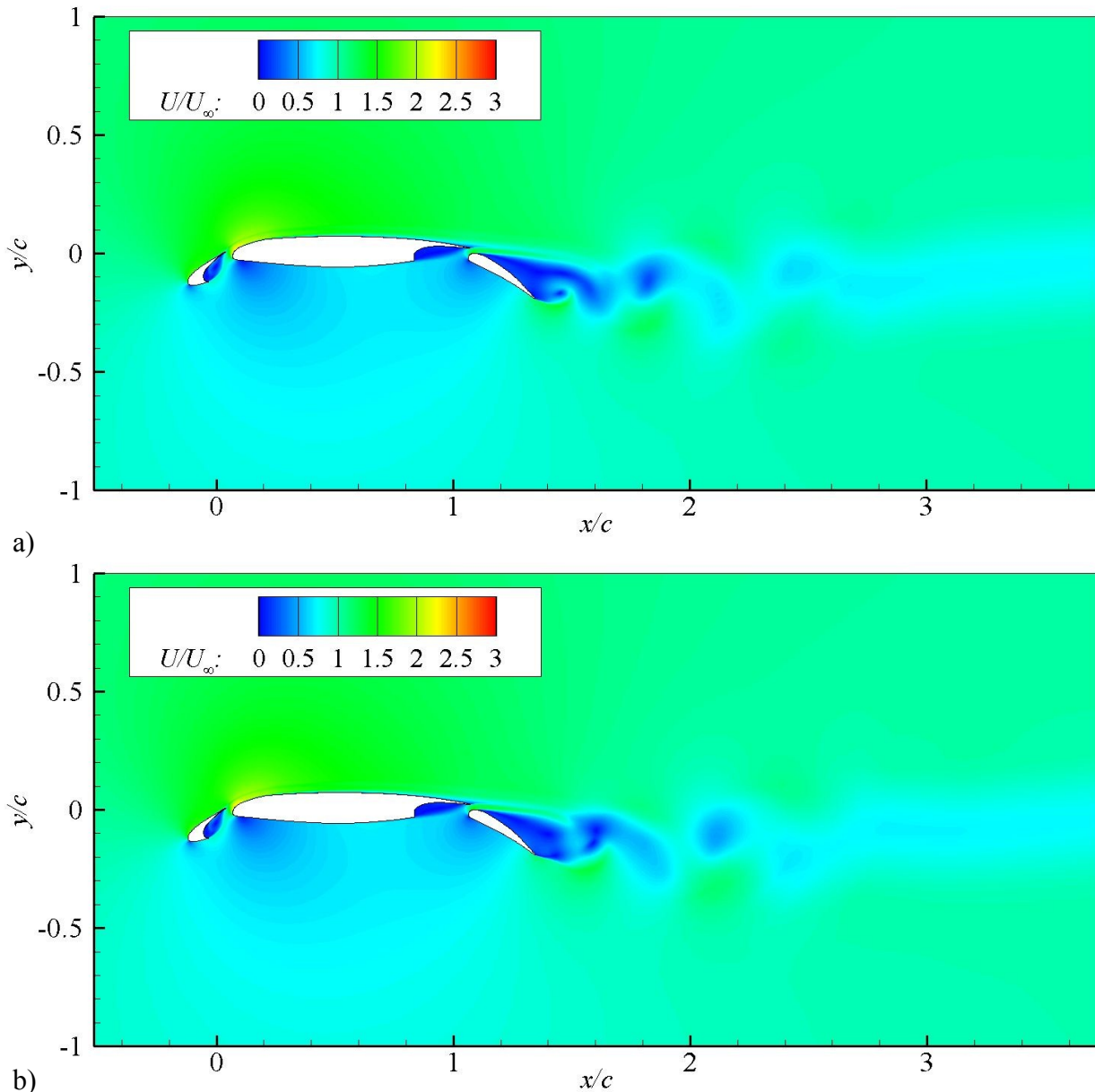


Figure 6-6: Distribution of total velocity in symmetry plane. URANS result of BL-case at  $\alpha = 10^\circ$ ,  $U_\infty = 50\text{ m/s}$ ,  $Re_\infty = 1 \cdot 10^6$ . a)  $t_1 = 134,7\text{ms}$ ; b)  $t_2 = 136\text{ms}$ .

Periodic structures trail the flap in an upper and a lower wake-path. The length scale of these structures is comparable to the flap length. They are generated by an alternating

shedding of vortical structures originating from the leading and the trailing edge of the flap. The strength of these structures is decaying rapidly in downstream direction. This decay process is not triggered by the coarsening of the mesh, because the mesh is kept refined up to about two and half flap chord lengths behind the trailing edge of the flap. But the decaying process occurs already in this refined spatial domain. Apparently, behind the refined domain the decay process is accelerated. For this reason, only one pair of the unsteady structure is visible behind the refined mesh domain.

### 6.1.2 Flow Topology of High Lift Airfoil with Spoiler

To discuss the flow field associated with the conventional spoiler configuration (CS), the focus is in the following on the simulations with one representative value of angle of attack and deployment angle:  $\alpha = 10^\circ$  and  $\delta_s = 30^\circ$ . The contour plot of the velocity distribution in Figure 6-7 unveils the associated flow structures. To start with the features in close proximity to the spoiler, the flow separation of the main wing cavity is redirected upwards co-acting with the spoiler movement. This flow separation is not increased in size compared to the BL-case with the same angle of attack (Figure 6-3), but is still limited to the proximity of the spoiler. The jet flow through the flap gap is widened considerably, redirected upwards and thus degraded in terms of delaying the flap separation. This is considered the main reason for the movement of the flap separation point to the nose of the flap compared to the corresponding BL-case. By this, the separation bubble on the top side of the flap is increased considerably. On the top of the main wing, the flow separates about one spoiler length upstream of the spoiler kink, forming a flow separation from the separation point to the trailing edge of the spoiler. Even the flow in the slat cove is altered considerably compared to the BL-case: The flow separation region in the slat cove is enlarged and more convex compared to the corresponding BL-case.

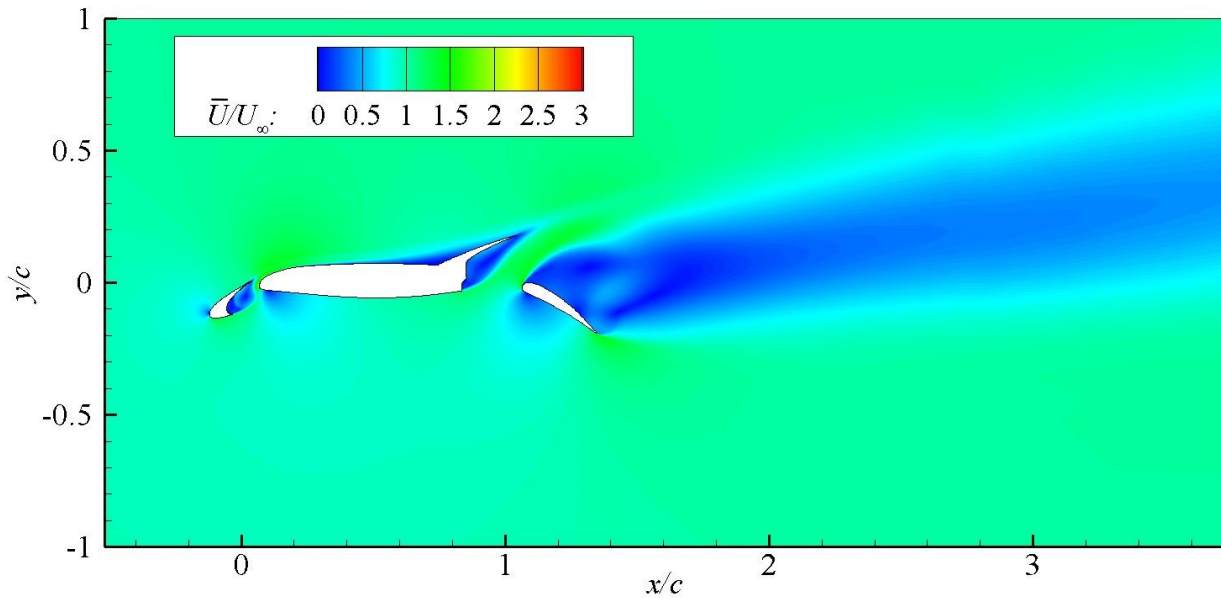


Figure 6-7: Distribution of mean total velocity in symmetry plane. Averaged URANS result of CS-case with  $\delta_S = 30^\circ$  at  $\alpha = 10^\circ$ ,  $U_\infty = 50$  m/s,  $Re_\infty = 1 \cdot 10^6$ .

The plot of the total pressure loss coefficient in Figure 6-8, where  $K_L < 0.003$  is again blanked to emphasize the high-loss regions, clarifies that the main distortion of the flow for the conventional spoiler is produced by the flap, but not so much by the spoiler. Near the spoiler only a relatively small region of distorted flow is observable compared to the large green spot, which trails the flap. The spoiler has a pronounced indirect effect on the separation of the flap, which becomes clear when comparing the size and strength of the zone of flow separation on the flap in Figure 6-7 with the same phenomenon for the BL-case (Figure 6-5). Another well recognizable difference is that the total pressure loss band, which originates at the slat's trailing edge merges in this configuration with the main wing's, respectively spoiler's upper surface total pressure loss zone, originating from the boundary layer. This combined band merges with the lower surface band originating from the front edge of the flap-cavity of the main-wing and, finally, this combined band merges with the large disturbance area originating from the separation of the flow on top of the flap.

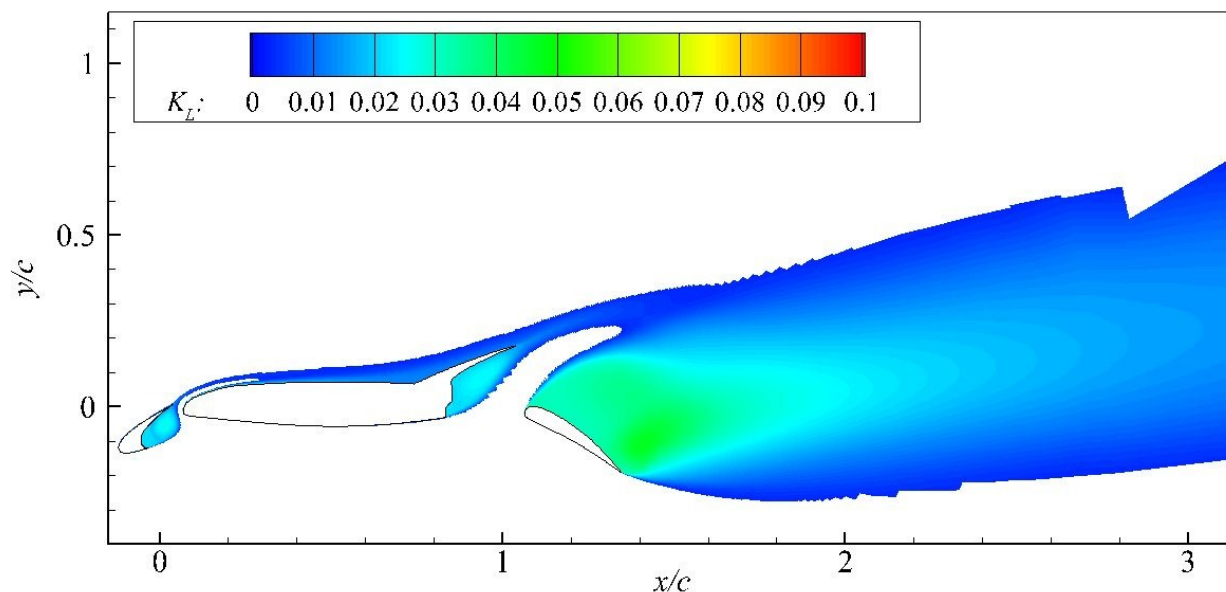


Figure 6-8: Distribution of mean total pressure loss in symmetry plane. Averaged URANS result of CS-case with  $\delta_S = 30^\circ$  at  $\alpha = 10^\circ$ ,  $U_\infty = 50$  m/s,  $Re_\infty = 1 \cdot 10^6$ .

Figure 6-9 shows the distribution of the total velocity at two points in simulation time  $t_1$  and  $t_2$ , of the same simulation. These represent two opposing states in the main oscillation cycle of the flow with a frequency of  $f = 171$  Hz,  $k = 0.562$ .

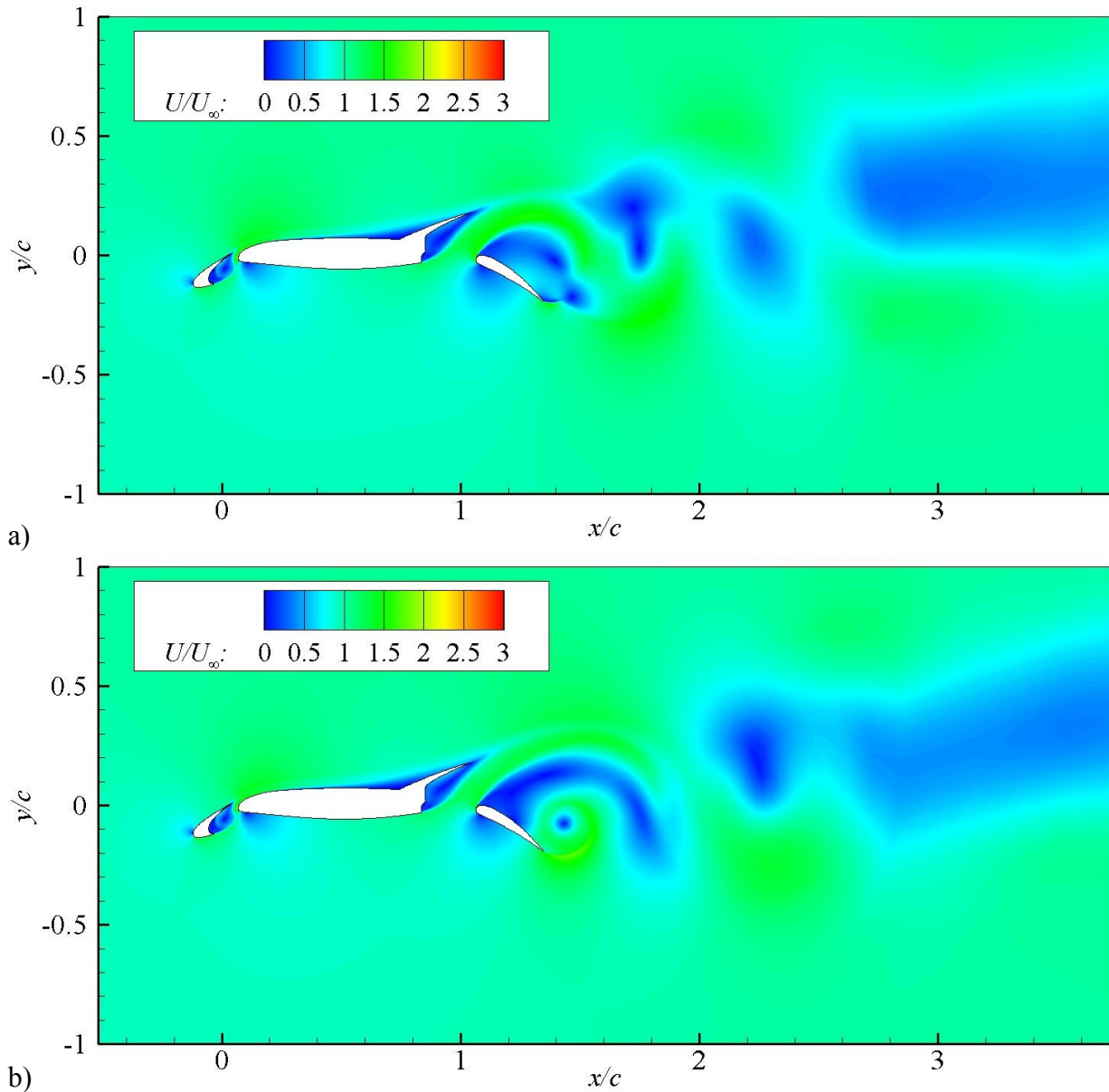


Figure 6-9: Distribution of total velocity in symmetry plane. URANS results of CS-case with  $\delta_S = 30^\circ$  at  $\alpha = 10^\circ$ ,  $U_\infty = 50\text{ m/s}$ ,  $Re_\infty = 1 \cdot 10^6$ . a)  $t_1 = 130\text{ms}$ ; b)  $t_2 = 132.9\text{ms}$ .

In general, the time-resolved flow structures are in this case more complex in comparison to the BL-case. However, the resolved unsteadiness is again limited to the wake flow and the flow on top of the flap. The main mechanism for the flow instability is the alternating separation and partly reattachment of the flow on the aft part of the flap. Through this mechanism, large flow structures trail alternately the wing. These structures have a length scale similar to the distance from the trailing edge of the spoiler to the trailing edge of the flap in direction perpendicular to the flow  $C_{Fl,Sp,proj}$ .

### 6.1.3 Flow Topology of High Lift Airfoil with Adverse Spoiler

To discuss the flow topology of the AS-configuration with  $\delta_S = 30^\circ$ , the mean flow in the symmetry plane of the URANS simulations is visualized by a contour plot with false color of the total velocity in Figure 6-10.

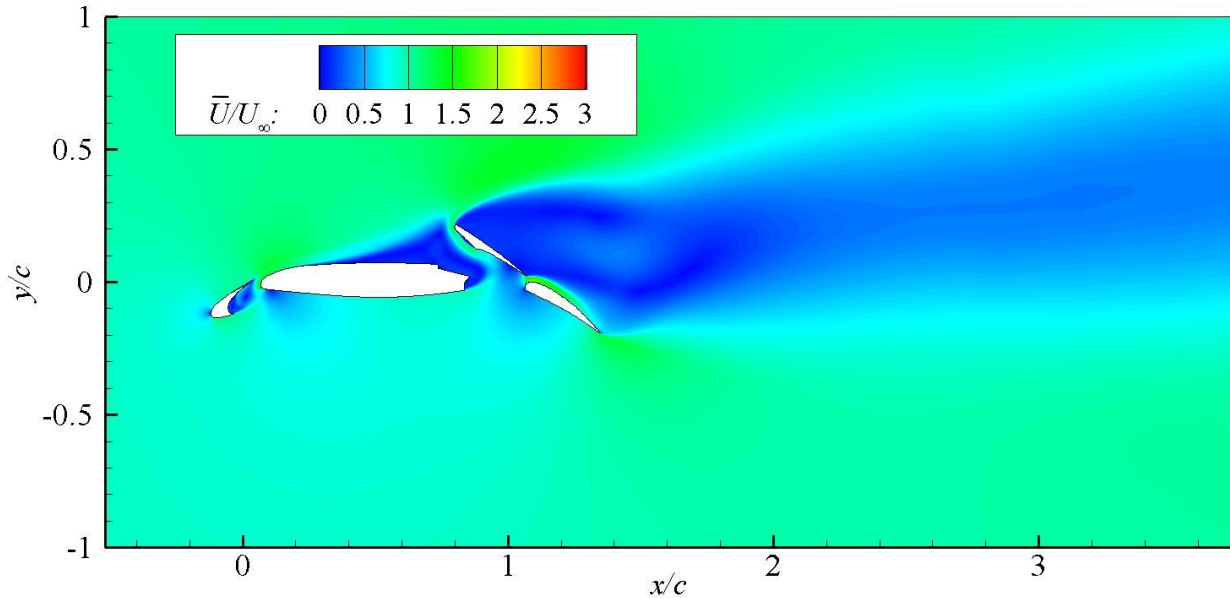


Figure 6-10: Distribution of mean total velocity in symmetry plane. Averaged URANS result of AS-case with  $\delta_S = 30^\circ$  at  $\alpha = 10^\circ$ ,  $U_\infty = 50$  m/s,  $Re_\infty = 1 \cdot 10^6$ .

The flow field is overall not similar to the CS-case discussed just before this. There are similarities for the bottom side of the main wing and the proximity of the slat including the slat cove. Again similar, the flow separates from the main wing top side, but differently the separation starts upstream compared to the position in the discussed CS-case and the size of the flow separation is considerably larger. This flow separation is connected to the flow separation, which develops in the main wing cavity, to form a combined flow separation. The combined flow separation is bounded by a jet flow path, which originates below the main wing and is turned upwards and backwards to follow the spoiler's lower, respectively front side. The jet shows a velocity, which is similar to the inflow velocity and thus resulting in a low static pressure on the lower side of the spoiler, leading to a local negative lift. Continuing downstream, above the spoiler this portion of the flow streams backwards adjoining the separation zone downstream of the spoiler, which extends from the Adverse Spoiler device's leading to trailing edges. In contrast to the CS-case, the flow separation associated to the Adverse Spoiler device stretches far behind the wing. Another fraction of the flow originating below the main wing feeds the flow through the flap gap. This highly energized flow causes that the boundary layer on the top side of the flap does not separate like in the CS-case with  $\delta_S = 30^\circ$ . Instead, the flow is attached entirely downstream to the trailing edge of the flap, at least this is true for the mean result. This fact causes the expectation to increase the lift produced by the flap compared to the conventional spoiler

configuration. However, it has been shown in section 5.2 by the help of the results from the wind tunnel experiment that there is no increase in global  $C_L$  detectable. This applies also for angles of attack near  $\alpha_{max}$ . To evaluate the situation of the flow topology for angles of attack near  $\alpha_{max}$ , the mean flow in the symmetry plane is visualized by a contour plot at  $\alpha = 20^\circ$  in Figure 6-11.

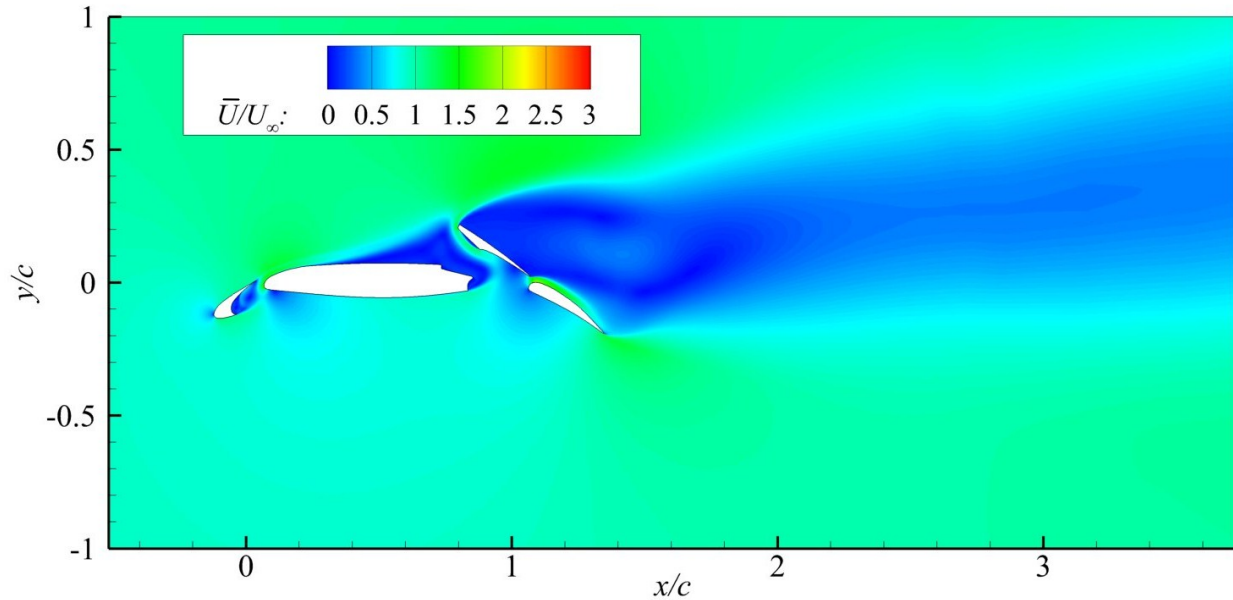


Figure 6-11: Distribution of mean total velocity in symmetry plane. Averaged URANS result of AS-case with  $\delta_S = 30^\circ$  at  $\alpha = 20^\circ$ ,  $U_\infty = 50$  m/s,  $Re_\infty = 1 \cdot 10^6$ .

The mean flow is again not separating from the top side of the flap in this case. Thus, by this method it is not explainable, why the lift at high angles of attack collapses compared to the BL, as discovered in chapter 5.

Coming back to the discussion of the results with  $\alpha = 10^\circ$ , the high drag produced by the adverse spoiler expresses itself by a large zone of total pressure loss created behind the wing. This zone extends from the trailing edge of the flap up to considerably above the leading edge of the spoiler. This is illustrated in Figure 6-12. The highest pressure loss coefficient values of  $K_L \approx 0.05$  (green) appear in the immediate wake of flap and spoiler and extends to about 3 times the flap length behind the flap trailing edge. This core zone is limited by a lower total pressure loss zone (blue), which extends far further downstream.

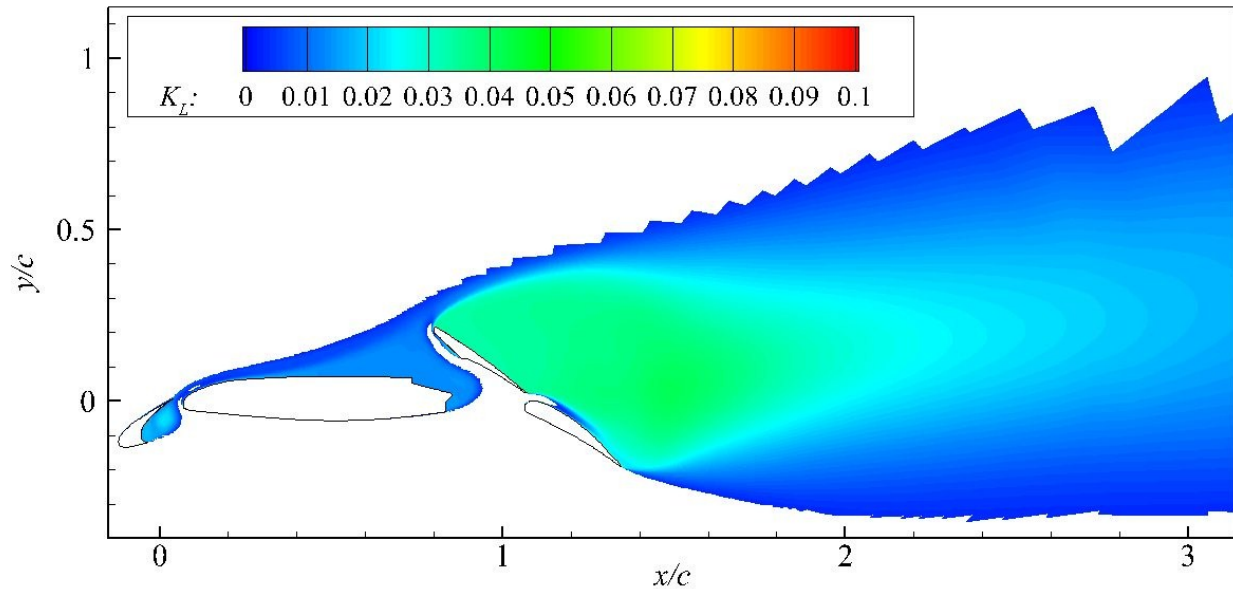


Figure 6-12: Distribution of mean total pressure loss in symmetry plane. Averaged URANS result of AS-case with  $\delta_s = 30^\circ$  at  $\alpha = 10^\circ$ ,  $U_\infty = 50$  m/s,  $Re_\infty = 1 \cdot 10^6$ .

Next, two points in simulation time  $t_1$ , and  $t_2$  are taken, which represent two opposing states in the main oscillation cycle of the flow, for this case at  $\alpha = 10^\circ$  with a frequency of  $f = 122$  Hz,  $k = 0.401$  in Figure 6-13. The areas, in which the flow instability becomes manifest, are again the wake of spoiler and flap, and the flow on the top side of the flap. Like in the case of the conventional spoiler, the flow structures in the wake are much more complex compared to BL with  $\alpha = 10^\circ$ . Large flow structures with a size comparable to the flap length trail alternately the wing, which lead to the lowest frequency peak at  $k = 0.401$  (Figure 6-18). Smaller structures form in the near wake of flap and spoiler, as well as on the top side of the flap due to an alternating flap separation and reattachment. This unstable flap boundary layer condition, which could not be identified by the mean results discussed earlier, can surely cause a decrease in the lift coefficient. In any case it becomes obvious, that the flap separation is very sensitive to small differences in the simulation method and accuracy of the geometrical representation. One reason for this is that the two-dimensional URANS simulations neglect the effects at the lateral edges of the spoiler, existing in the wind tunnel as well as in the actual airplane, completely.

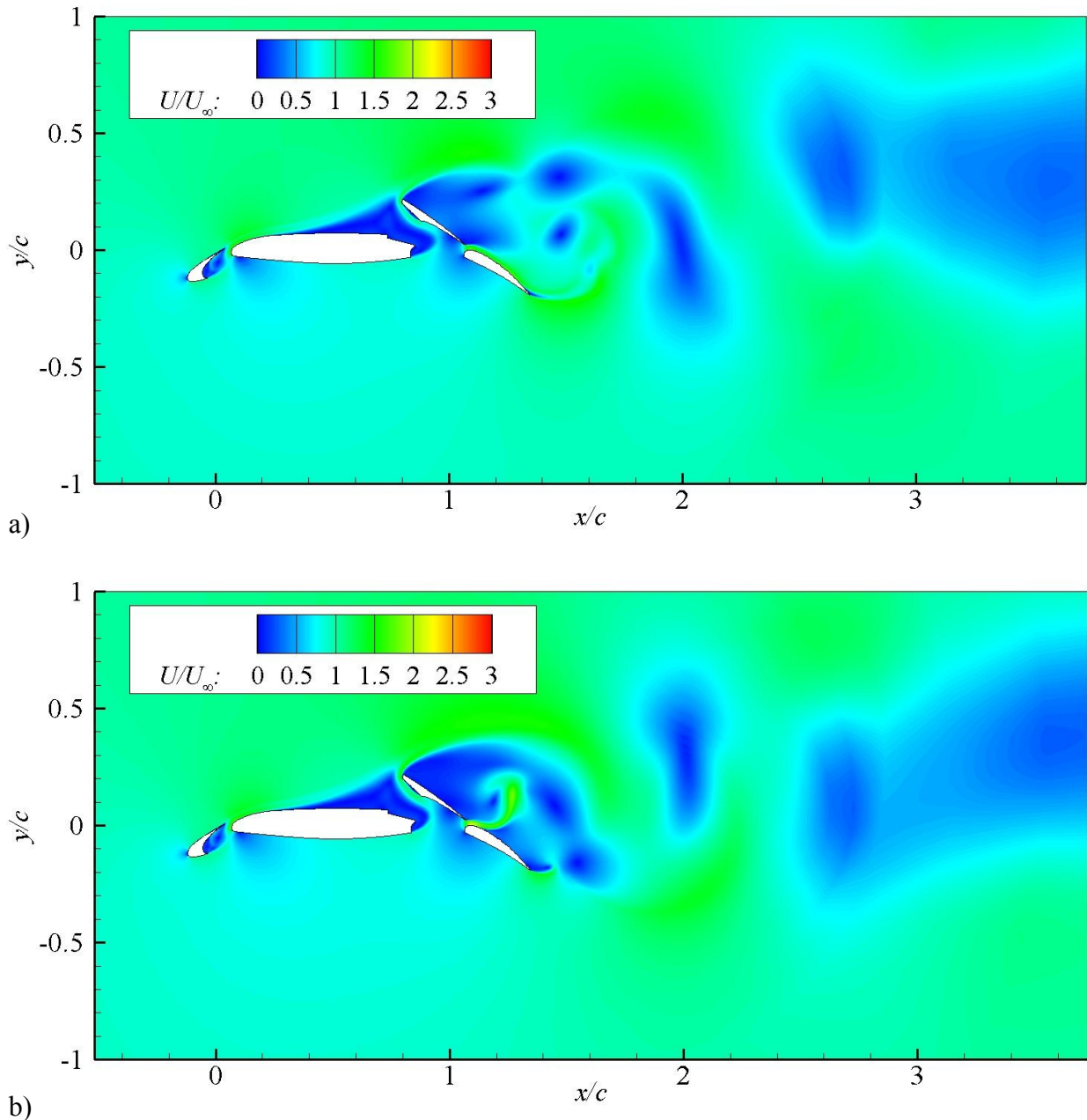


Figure 6-13: Distribution of total velocity in symmetry plane. URANS results of AS-case with  $\delta_S = 30^\circ$  at  $\alpha = 10^\circ$ . a)  $t_1 = 224.96\text{ms}$ ; b)  $t_2 = 228.96\text{ms}$ ,  $U_\infty = 50\text{ m/s}$ ,  $Re_\infty = 1 \cdot 10^6$ .

#### 6.1.4 Flow Topology of High Lift Airfoil with Advanced Adverse Spoiler

When having a look at the mean velocity distribution of the Advanced Adverse Spoiler (AAS) with  $\delta_S = 30^\circ$  at  $\alpha = 10^\circ$  in Figure 6-14, it emerges that it is very similar to the AS with  $\delta_S = 30^\circ$  at  $\alpha = 10^\circ$ . The main difference is the absence of the jet flow coming from below the main wing running through the gap upwards along the spoiler. This flow is blocked by the thin sealing separating the flow below the wing from the flow above the wing. Instead, a coherent flow separation develops, which encloses the region between the spoiler the sealing, as well as about half of the upper main wing surface.

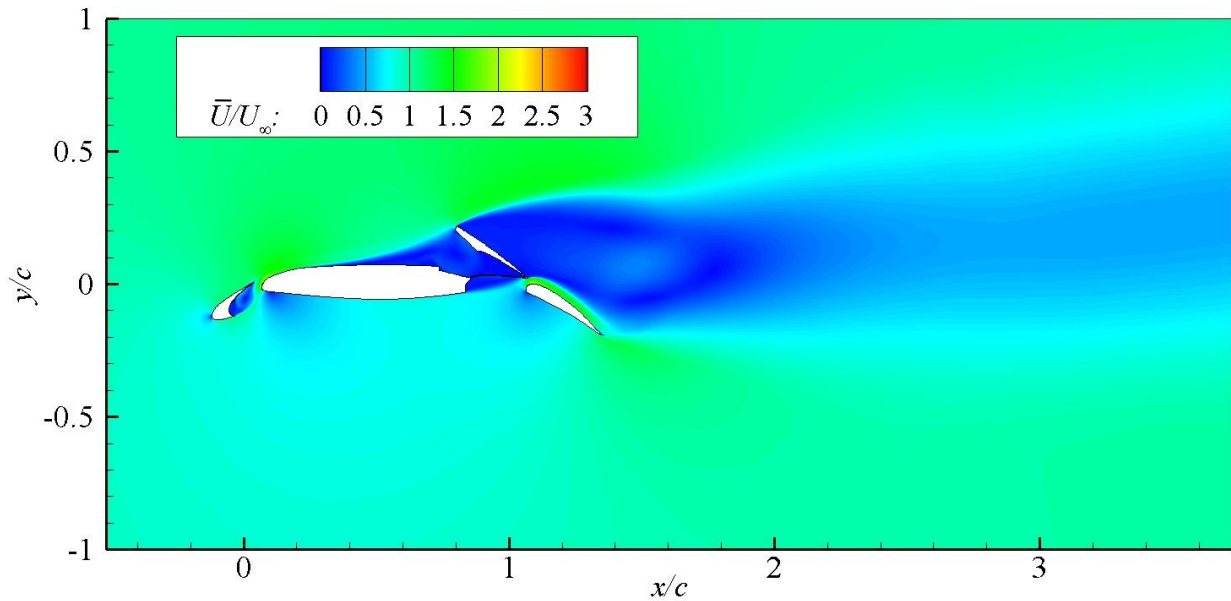


Figure 6-14: Distribution of mean total velocity in symmetry plane. Averaged URANS result of AAS-case with  $\delta_s = 30^\circ$  at  $\alpha = 10^\circ$ ,  $U_\infty = 50$  m/s,  $Re_\infty = 1 \cdot 10^6$ .

To evaluate the flow topology at a high angle of attack near stall, Figure 6-15 shows again the distribution of the mean total velocity of AAS, but this time with  $\alpha = 20^\circ$ . Generally, the changes in the flow topology remain limited.

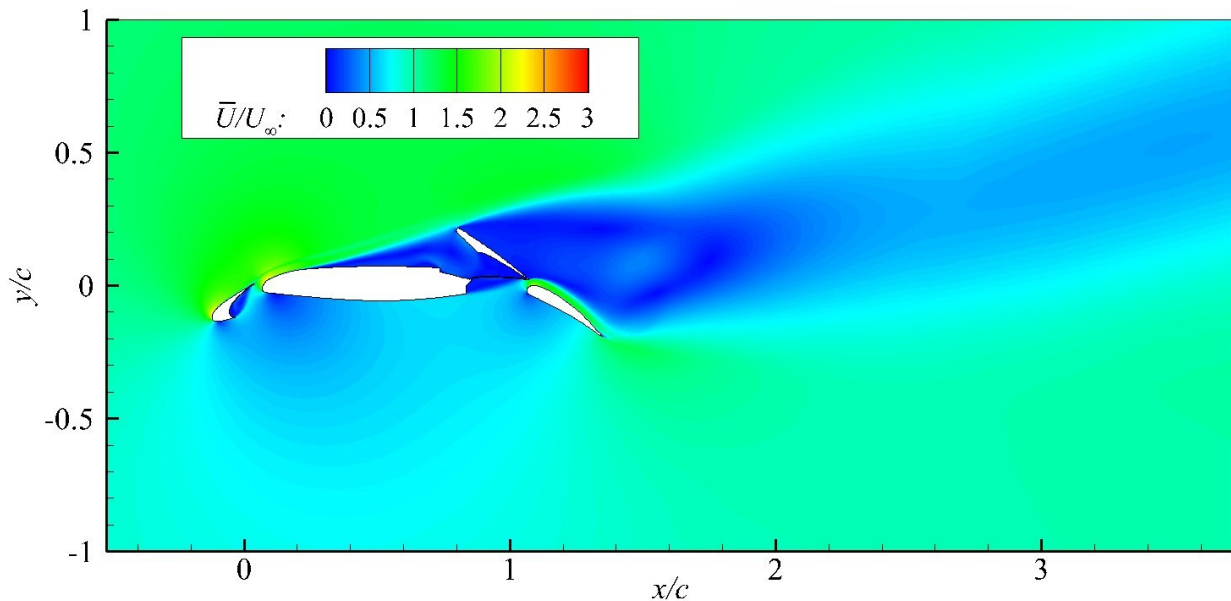


Figure 6-15: Distribution of mean total velocity in symmetry plane. Averaged URANS result of AAS-case with  $\delta_s = 30^\circ$  at  $\alpha = 20^\circ$ ,  $U_\infty = 50$  m/s,  $Re_\infty = 1 \cdot 10^6$ .

Most importantly, the flap flow stays attached. The flow separation region between spoiler and main wing is enlarged in upstream direction to a minor extent. The flow separation in the wake of the spoiler is reshaped by a minor extent and stays approximately the same size. Moreover, the slat cove flow separation is also reshaped in that way that it becomes

less convex. Larger differences show up for the total pressure loss in the symmetry plane, which is displayed in Figure 6-16.

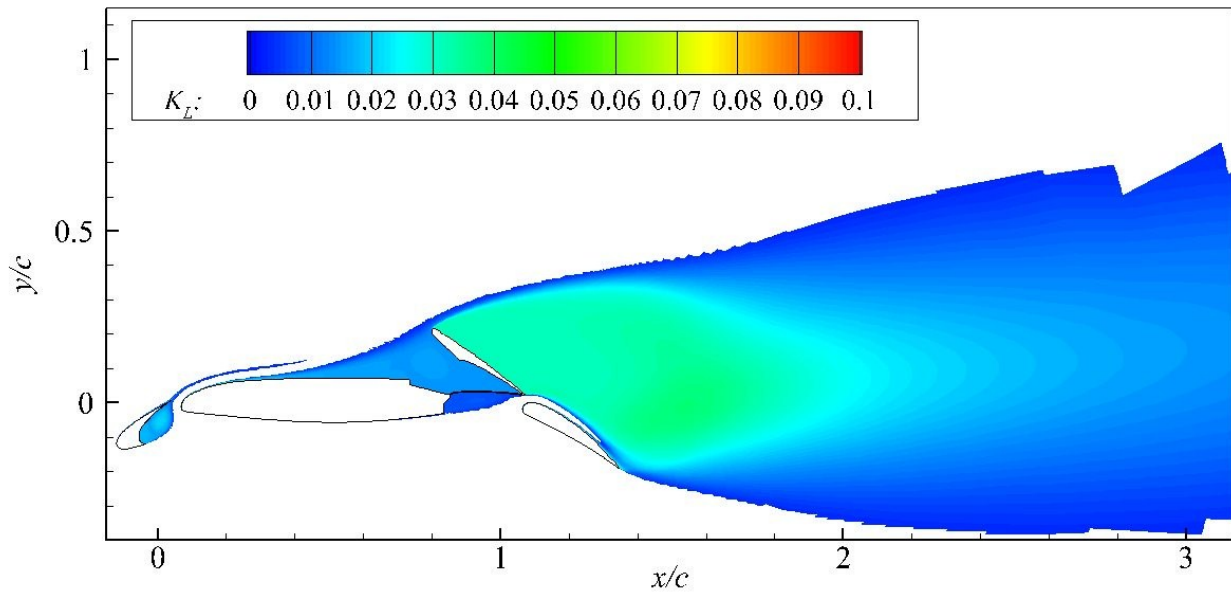


Figure 6-16: Distribution of mean total pressure loss in symmetry plane. Averaged URANS result of AAS-case with  $\delta_S = 30^\circ$  at  $\alpha = 10^\circ$ ,  $U_\infty = 50$  m/s,  $Re_\infty = 1 \cdot 10^6$ .

In contrast to the total pressure loss distribution of CS with  $\delta_S = 30^\circ$  and AS with  $\delta_S = 30^\circ$ , the slat trailing shear layer does not merge with the main wing's boundary layer shear layer. This suggests that the relatively small change in spoiler geometry has a large effect even on the upstream flow topology. A broad band of high pressure loss trails the wing from trailing edge of the flap up to above the spoiler leading edge.

The transient velocity distribution in the symmetry plane at two points in simulation time  $t_1$ , and  $t_2$ , which once again represent two opposing states in the main oscillation cycle of the flow with a frequency of  $f = 134$  Hz,  $k = 0.440$ , are presented in Figure 6-17.

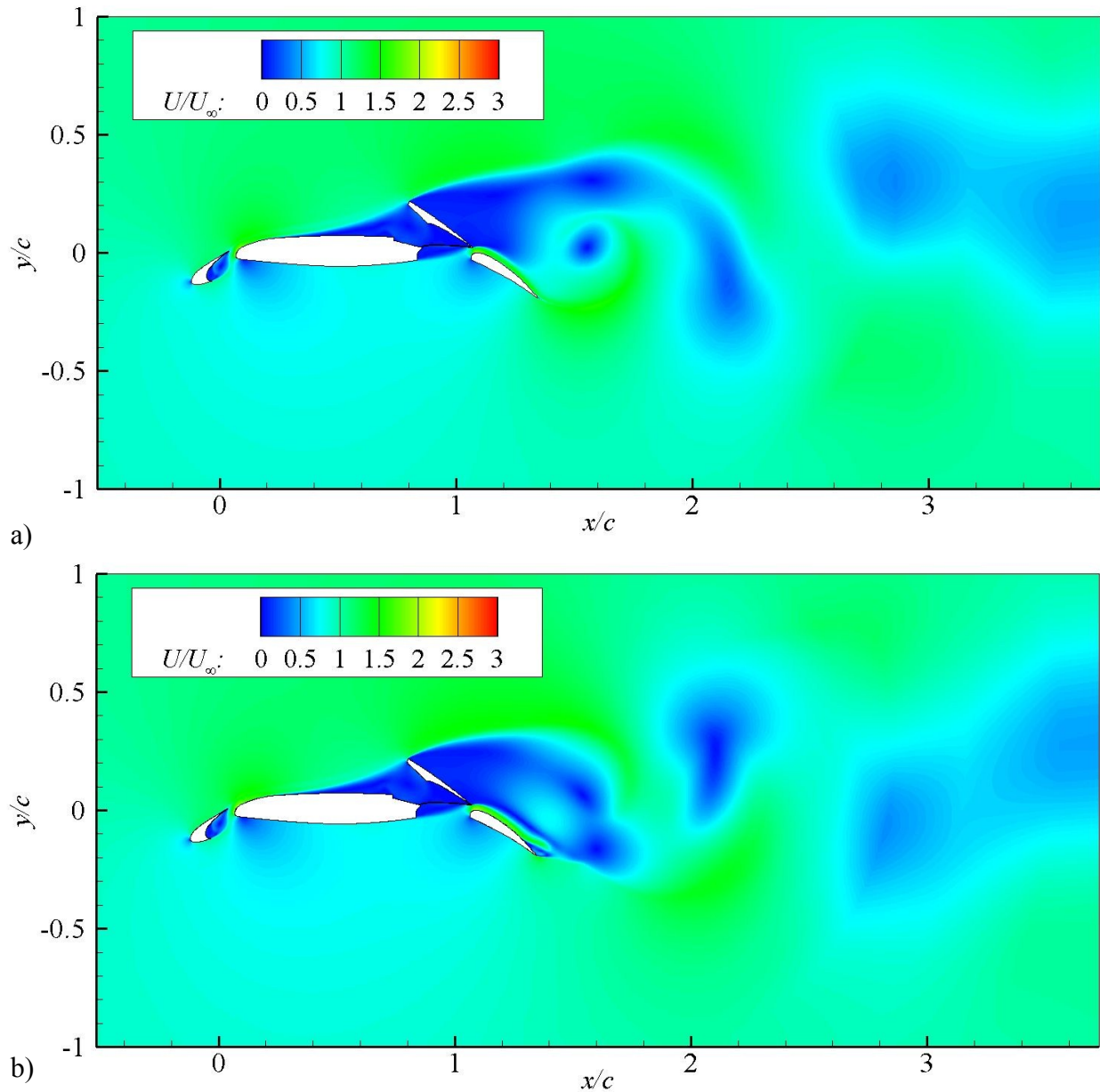


Figure 6-17: Distribution of total velocity in symmetry plane. URANS results of AAS-case with  $\delta_S = 30^\circ$  at  $\alpha = 10^\circ$ ,  $U_\infty = 50$  m/s,  $Re_\infty = 1 \cdot 10^6$ . a)  $t_1 = 151.7$  ms; b)  $t_2 = 155.52$  ms.

The trailing wake structure is comparable to the AS-case with again dominating structures with a scale comparable to the flap length. However, in significant contrast to the AS-case, the flow stays now almost completely attached on the flap. Only a small portion at the trailing edge part of the boundary layer on the top side of the flap is separated for only one of both situations at  $t_2 = 155.52$  ms. This main difference makes a decisive contribution towards the increase in lift compared to the AS-case at the same angle of attack and device deflection conditions.

### 6.1.5 Analysis of the Unsteadiness in the 2D URANS Simulations

To analyze and compare the periodical behavior of the flow for the different configurations in the frequency domain, a Fast Fourier Transformation (FFT) of the unsteady lift coefficient results of the 2D URANS simulations was conducted. For that purpose, the mean lift coefficient is subtracted from the unsteady lift coefficient to reduce the analysis to the fluctuation part  $C'_L$ . A sufficient number of 4096 unsteady simulation results over time serve as basis for the FFTs. Figure 6-18 shows the resulting spectra. The amplitude values of  $C'_L$  are herein plotted versus the reduced frequency ( $k = f \cdot l / U_\infty$ ) for cases BL, CS with  $\delta_s = 30^\circ$ , AS with  $\delta_s = 30^\circ$ , and AAS with  $\delta_s = 30^\circ$ . The reduced frequency is gathered by using the inflow velocity  $U_\infty$  as well as the mean aerodynamic cord length  $c$  as basis. The deflection parameters of the high lift elements are chosen to correspond to the wind tunnel model (Table 3-7).

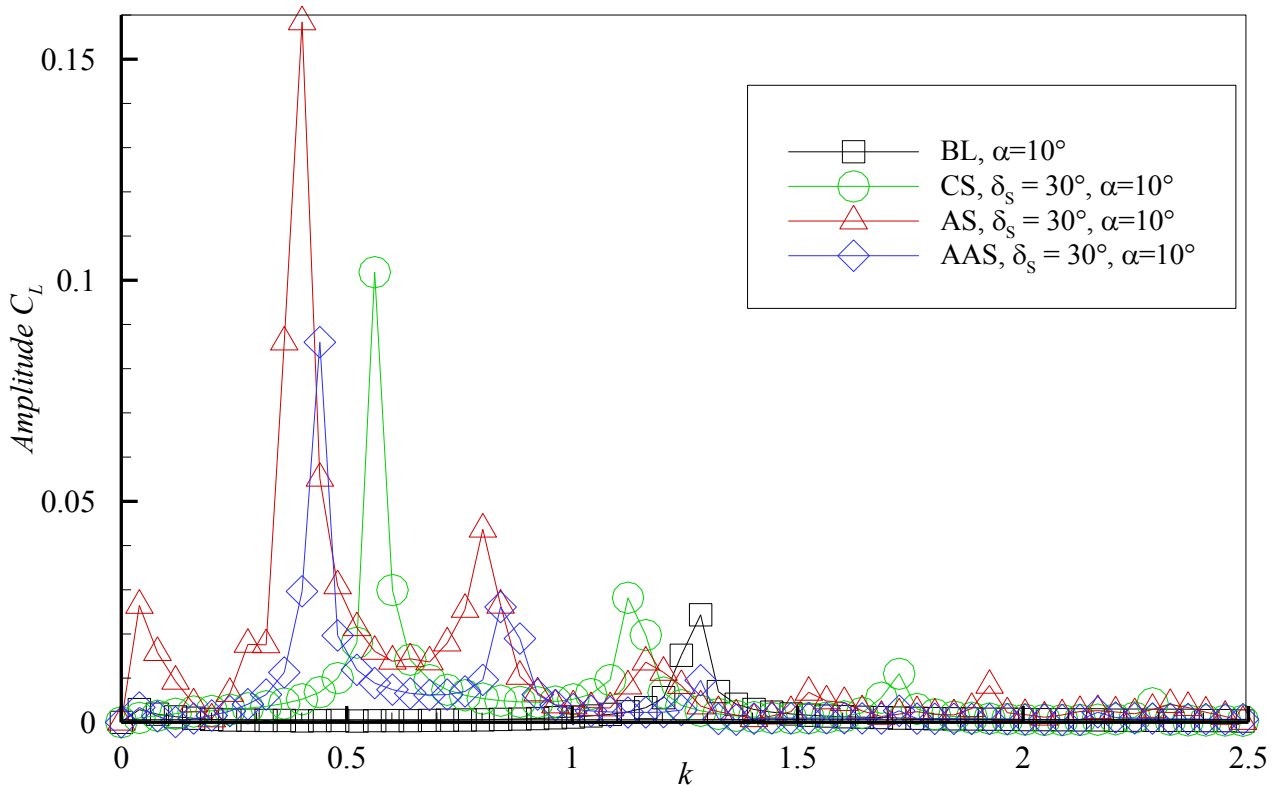


Figure 6-18: Lift coefficient spectra gathered by FFT. URANS results of configurations BL, CS with  $\delta_s = 30^\circ$ , AS with  $\delta_s = 30^\circ$ , and AAS with  $\delta_s = 30^\circ$ , each at  $\alpha = 10^\circ$ ,  $U_\infty = 50$  m/s,  $Re_\infty = 1 \cdot 10^6$ .

The BL-case is dominated by only one unsteady flow phenomenon with a reduced frequency of  $k = 1.285$ . This indicates the not as complex unsteady flow behavior compared to the other cases. The underlying phenomenon is based on a periodical flow, where vortices are shedding alternately at the leading and trailing edge of the flap. This was already shown by the help of time-resolved velocity plots in subsection 6.1.1. When

calculating the Strouhal number  $Sr$  based on the freestream velocity and streamwise projected flap chord  $c_{Fl,proj} = 38.4$  mm (Figure 6-1), one gets  $Sr = 0.3$ . The difference to the  $Sr$ -number range  $Sr \approx 0.16$  to  $Sr \approx 0.2$ , which appears for cylinders (Figure 2-21) and should be comparable to the shedding vortex structure at the flap, suggests that the length scale and freestream velocity used for the calculation of  $Sr$  are not representative for the flow phenomenon. One explanation for this is a higher local velocity, which is accelerated compared to the freestream velocity, when it passes through the flap gap and below the flap.

On the other hand, all the other cases are dominated by more than one phenomenon with different frequencies and associated amplitudes attributed to each. In all cases, peaks appear in the FFT results at frequencies close to the frequency of the flap flow detachment of BL  $k = 1.285$ . It suggests itself that the attributed phenomena are similar to the flap detachment process of BL. The amplitudes in  $C_L$  of the associated phenomenon is similar to BL in the CS with  $\delta_S = 30^\circ$  case, but in both cases, AS with  $\delta_S = 30^\circ$  and AAS with  $\delta_S = 30^\circ$ , the amplitudes are reduced by at least half the value. This gives the hint that the flap flow detachment is suppressed by both the AS with  $\delta_S = 30^\circ$  and the AAS with  $\delta_S = 30^\circ$  geometries. As already mentioned, all three spoiler-cases have more peaks in the FFT graphs each with higher amplitudes than the one associated to the flap-flow detachment. For the CS-case with  $\delta_S = 30^\circ$ , there is one significant peak at  $k = 0.562$  and two minor peaks at  $k = 1.725$  and  $k = 2.287$ . The low frequency of the strongest peak indicates that the underlying flow phenomenon is associated with the flow fluctuation due to a larger geometry, namely the spoiler and flap combined. The Strouhal number based on the associated streamwise projected geometry becomes  $Sr = 0.268$ . Peaks at similar frequencies in the FFT spectrum for AS with  $\delta_S = 30^\circ$  and AAS with  $\delta_S = 30^\circ$  indicate that there is also an unsteady flow phenomenon involved for these cases, which is due to the wake of the combined spoiler and flap geometries. In both cases, the streamwise projected length scale is equal, respectively slightly larger compared to the CS-case with  $\delta_S = 30^\circ$ . This leads to a Strouhal number for AS with  $\delta_S = 30^\circ$  and AAS with  $\delta_S = 30^\circ$  of  $Sr_{AS,\delta_S=30^\circ} = 0.199$  and  $Sr_{AAS,\delta_S=30^\circ} = 0.219$ . In both novel spoiler cases a second peak appears in the spectrum at a frequency, which is double the frequency of the just before discussed dominating unsteady phenomenon. This indicates that there are flow phenomena, which are harmonic components to the one, which is associated with the wake of the combined spoiler and flap.

#### 6.1.6 Synthesis of URANS-Simulations

In this section, the results from the URANS-simulations with  $\alpha = 10^\circ$  are recapitulated and juxtaposed to the corresponding experimental force measurement results for the sake of comparison. Table 6-1 shows the differences in  $C_D$  and  $C_L$  relative to the BL for CS, AS, and AAS each with  $\delta_S = 30^\circ$  gained from the URANS simulations as well as from the wind

tunnel measurements. For the simulation results, the coefficient fractions related to slat, main wing including spoiler, and flap are additionally evaluated.

Table 6-1: Aerodynamic force coefficient trends relative to BL.

		$\Delta C_D$	$\Delta C_L$	$\Delta C_{L,Slat}$	$\Delta C_{L,Main+Spoiler}$	$\Delta C_{L,Flap}$
CS	URANS	+0.350	-2.134	-0.441	-1.859	+0.166
	Wind Tunnel	+0.003	-0.248			
AS	URANS	+0.643	-1.344	-0.344	-1.195	+0.194
	Wind Tunnel	+0.027	-0.273			
AAS	URANS	+0.503	-1.031	-0.273	-0.986	+0.228
	Wind Tunnel	+0.019	-0.247			

When comparing force coefficients from the wind tunnel measurements with the 2D simulations results, one has to keep in mind that only about 10% of the wingspan of the wind tunnel model is directly affected by the spoiler. Thus, the effect on the aerodynamic coefficients based on the complete wing area should be about one magnitude lower than for the case, when only the airfoil section affected by the spoiler is considered, which is the case for the 2D URANS simulations.

The trends by algebraic sign in  $\Delta C_D$  and  $\Delta C_L$  are similar for the experimental and the numerical results in all cases, whereas the sequence of the cases is only consistent in  $\Delta C_D$ , but not in  $\Delta C_L$ . Most additional drag is produced by AS, followed by AAS with the least additional drag produced by CS. For  $\Delta C_L$ , the wind tunnel results show the least reduction for AAS and similar values for CS and a higher reduction for AS. But here, the numerical simulation gives a sequence in negative direction from AAS, to AS to CS. When having a look at the fractions of  $\Delta C_L$  associated to slat, main wing including spoiler and flap, the first thing, which attracts someone's attention is the fact that all spoilers lead to a positive  $\Delta C_{L,Flap}$ . As expected, due to the result in a completely attached flap flow, AS and AAS lead to a higher  $\Delta C_{L,Flap}$  compared to CS. An even larger effect on the component-lift coefficient is observable for the slat. All spoilers lead to a decrease in slat lift. The same is true for the share of the main wing including spoiler: Due to the flow separation on the main wing for all spoiler cases, the lift created by the main wing is vastly reduced for all three cases. The novel spoilers counteract this effect leading to an approximately half as high decrease in  $C_{L,Main+Spoiler}$  compared to CS. In this regard, AAS produces even more lift than AS.

Table 6-2 gives numbers for three main parameters of BL, CS, AS, and AAS, which were discussed before. These are extension of the wake, defined by the maximum vertical extent of the zone with  $K_L > 0.02$ , the position of the mean flow separation on the main wing, and the position of the mean flow separation on the flap. There is no mean flow

separation on the main wing of BL and there is no mean flow separation of the flap for AS and AAS. The wake size is considerably increased by all spoilers, but even larger for AS and AAS compared to CS. This is consistent with the level of increase in  $C_D$  for the different spoilers. The separation on the main wing is located further behind for CS compared to AS and AAS, where the location is similar in both cases. Concerning the flap flow separation, it is moved towards the leading edge for the CS-case compared to BL.

Table 6-2: Maximum vertical extent of wake ( $K_L > 0.02$ ) and separation positions on main wing and flap ( $\bar{u} < 0$  at the wall) for the investigated spoiler cases.

		$\Delta z_{Wake}/c$	$\Delta x_{SepMain}/c$	$\Delta x_{SepFlap}/c_{Flap}$
BL	URANS	0.247	N/A	0.117
CS	URANS	0.366	0.651	0.010
AS	URANS	0.592	0.348	N/A
AAS	URANS	0.540	0.387	N/A

### 6.1.7 Flow Topology Analysis Based on SAS Simulation Results

For one selected set of parameters per investigated spoiler configuration as well as the Baseline-case (BL), SAS simulations were performed. In particular, the angle of attack is for all investigated cases constant at  $\alpha = 10^\circ$ , the deflection of the Conventional Spoiler (CS), the Adverse Spoiler (AS), and of the Advanced Adverse Spoiler (AAS) is consistently  $\delta_s = 30^\circ$ . The numerical conditions, under which the simulations were performed, were introduced in section 4.6 and the method was validated in subsection 4.8.4. The main advantage of the 2.5D SAS method in comparison to the 2D URANS method is that the three dimensional vortex structures are resolved instead of modeled. Thus, we focus in this section on the unsteady flow features: The turbulent structures are exhibited most suitably by iso-values of the Q-criterion introduced in section 4.7. The presented iso-surfaces are colored by the ratio of the eddy viscosity to the molecular viscosity  $\nu_t/\nu$ . Furthermore, false color plots of the unsteady total velocity  $U/U_\infty$  in longitudinal cuts through the flow field at different points in simulation time  $t$  serve, similarly to the discussion of the 2D URANS results, to illustrate the unsteady phenomena.

Figure 6-21 shows for the BL-case the velocity distribution at two points in simulation time,  $t_1$  in Figure 6-21a and  $t_2$  in Figure 6-21b. Similar to the URANS-simulations, the major unsteady region observable from these pictures is located in the wake of the main wing, respectively above the flap. Unsteady structures are alternately shed from the top surface of the flap. This is similar to the structures of the typical single-mode vortex separation, already seen before for the URANS-results. These structures have a size which is comparable to the flap length. However, additionally to these large vortex-structures, for the SAS-simulation, there is a cascade of smaller structures embedded in the

dominant structures. Similar to the validation-case discussed in subsection 4.8.4, the second area, where the flow is highly unsteady, is the slat cove. Here, small structures are embedded in the flow separation of the slat cove. However, the shape of the boundaries of the flow separation remains approximately unchanged over time.

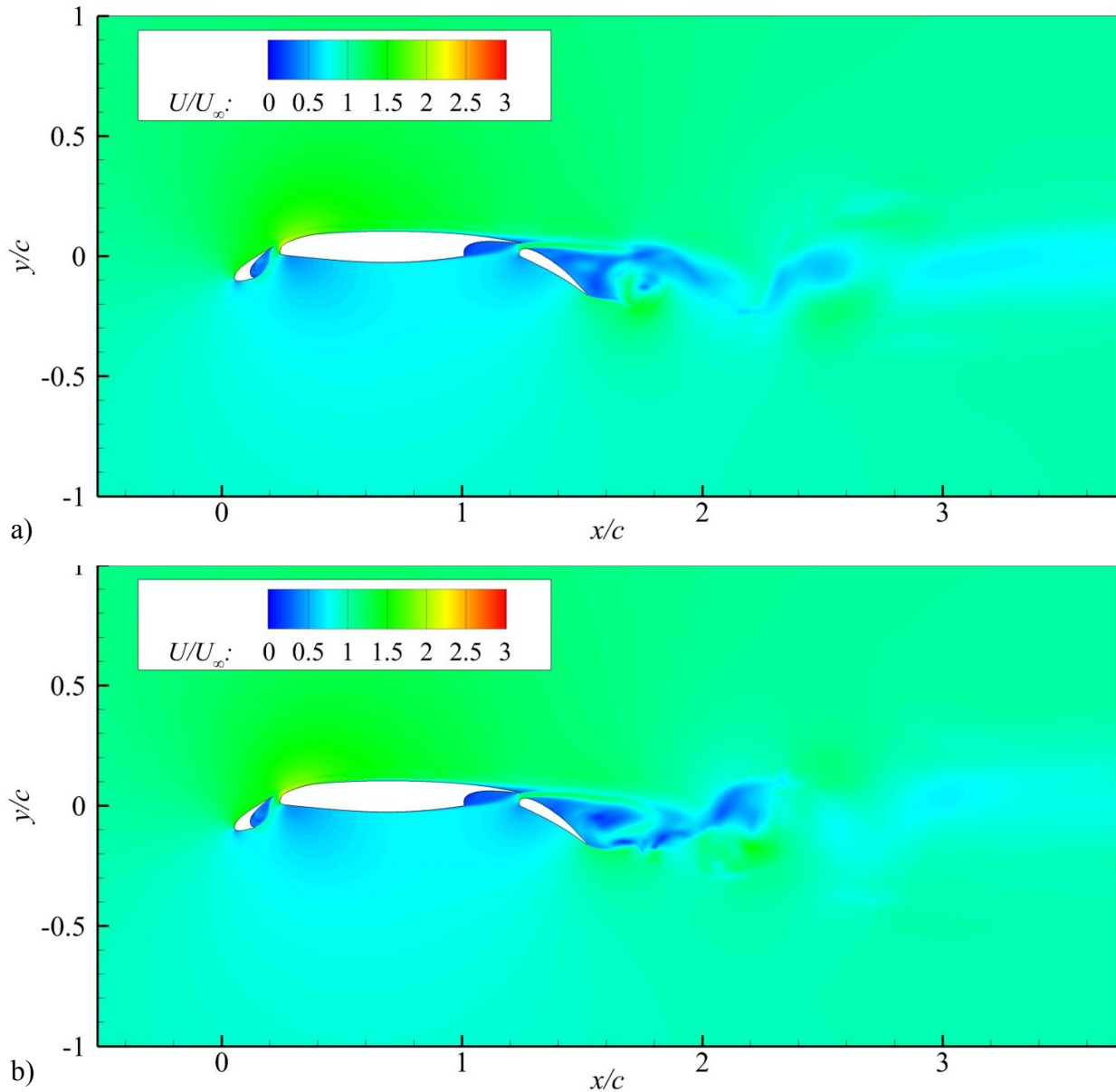


Figure 6-19: Distribution of total velocity in symmetry plane. SAS results of BL-case at  $\alpha = 10^\circ$ ,  $U_\infty = 50$  m/s,  $Re_\infty = 1 \cdot 10^6$ . a)  $t_1 = 37.5$  ms; b)  $t_2 = 43.26$  ms.

Figure 6-20 shows the turbulent structures around the Baseline high lift airfoil in even more detail: They are illustrated by iso-surfaces of the Q-criterion with a value of  $Q = 1.2 \cdot 10^7$  s<sup>-2</sup>. The iso-surfaces are colored by the ratio of the eddy viscosity to the molecular viscosity  $\nu_t/\nu$ . The two areas, where unsteady flow is dominating, slat cove and flap wake, become clear by vortex-tubes, which feature a broad range of magnitudes and do not have a clear preferred orientation. They are even winding around each other. The

diameter of the smallest vortex-tubes in the wake of the flap has the magnitude of the flap gap, whereas the magnitude of the vortex tubes in the slat cove is considerably smaller.

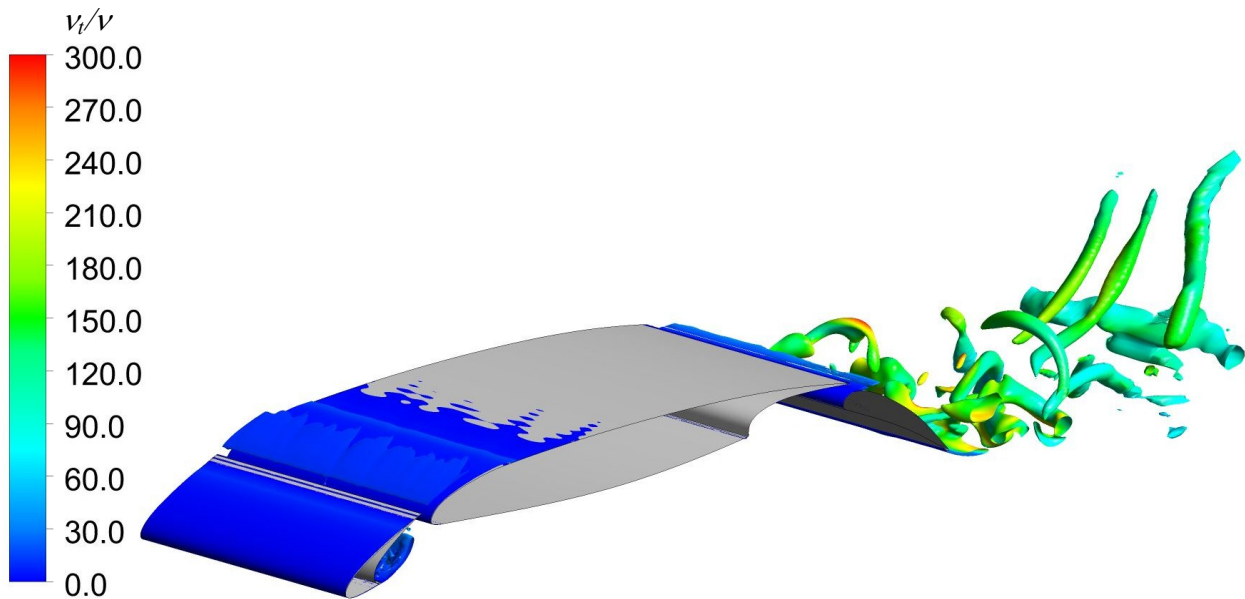


Figure 6-20: Turbulent structures around the BL-airfoil, visualized by ISO surfaces of Q-criterion  $Q = 1.2 \cdot 10^7 \text{ s}^{-2}$  colored by the ratio of the eddy viscosity to the molecular viscosity,  $t = 43.26 \text{ ms}$ ,  $U_\infty = 50 \text{ m/s}$ ,  $Re_\infty = 1 \cdot 10^6$ .

Turning to the CS-configuration with  $\delta_s = 30^\circ$ , the diagrams in Figure 6-21 show the distribution of the total velocity in longitudinal cuts for two points in simulation time  $t_1$  and  $t_2$ . Again, unsteady flow phenomena are observable for the slat cove and the wake of the flap, but this time also on top of the main wing and spoiler unsteady flow structures appear. Here, the structures come into view at the border of the flow separation and are limited in size to the thickness of the flow separation on top of the main wing. The flow structures in the wake of the flap and spoiler are similar to the ones, which appeared in the URANS-results. They are superposed by a cascade of smaller unsteady flow-structures.

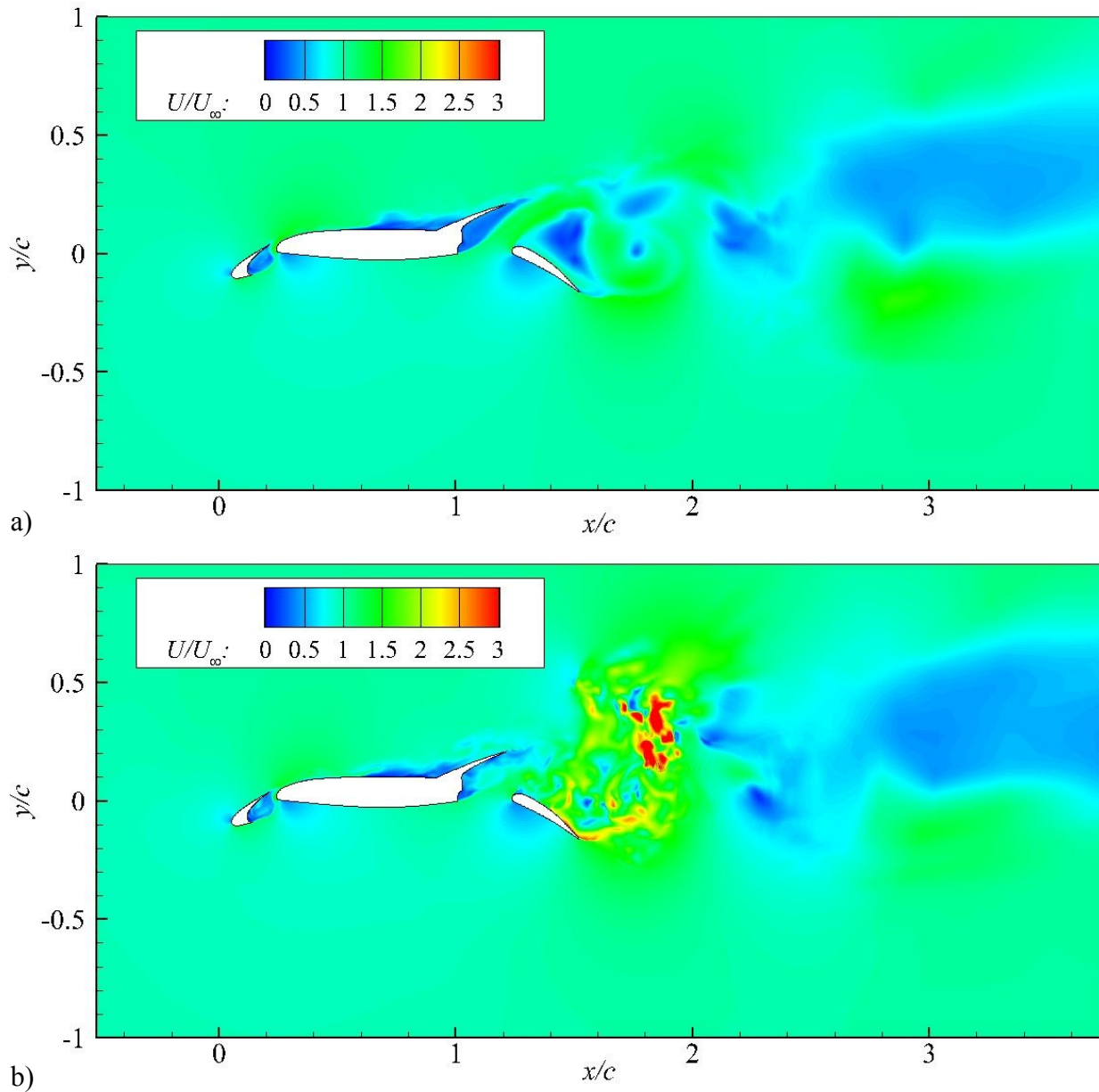


Figure 6-21: Distribution of total velocity in symmetry plane. SAS results of CS-case with  $\delta_S = 30^\circ$  at  $\alpha = 10^\circ$ ,  $U_\infty = 50$  m/s,  $Re_\infty = 1 \cdot 10^6$ . a)  $t_1 = 19.79$  ms; b)  $t_2 = 27.35$  ms.

Figure 6-22 shows the turbulent structures by the help of iso-surfaces of the Q-criterion for the CS-case with  $\delta_S = 30^\circ$ . From this illustration, it is observable that the top of the main wing and spoiler is reseeded with small-scale vortex structures, which originate from the slat gap and are mainly orientated in freestream direction. The density of these vortex tubes decreases at about a fifth of the main wing's length and increases again considerably in front of the spoiler, where the flow on the main wing's top side separates. The preferential direction becomes less distinctive in downstream direction and converts into both freestream-wise and spanwise directed vortex tubes in the wake of the spoiler and flap. Furthermore, the structures have a much larger scale in the wake compared to the structures in the slat cove, as well as the ones on top of the main wing and spoiler.

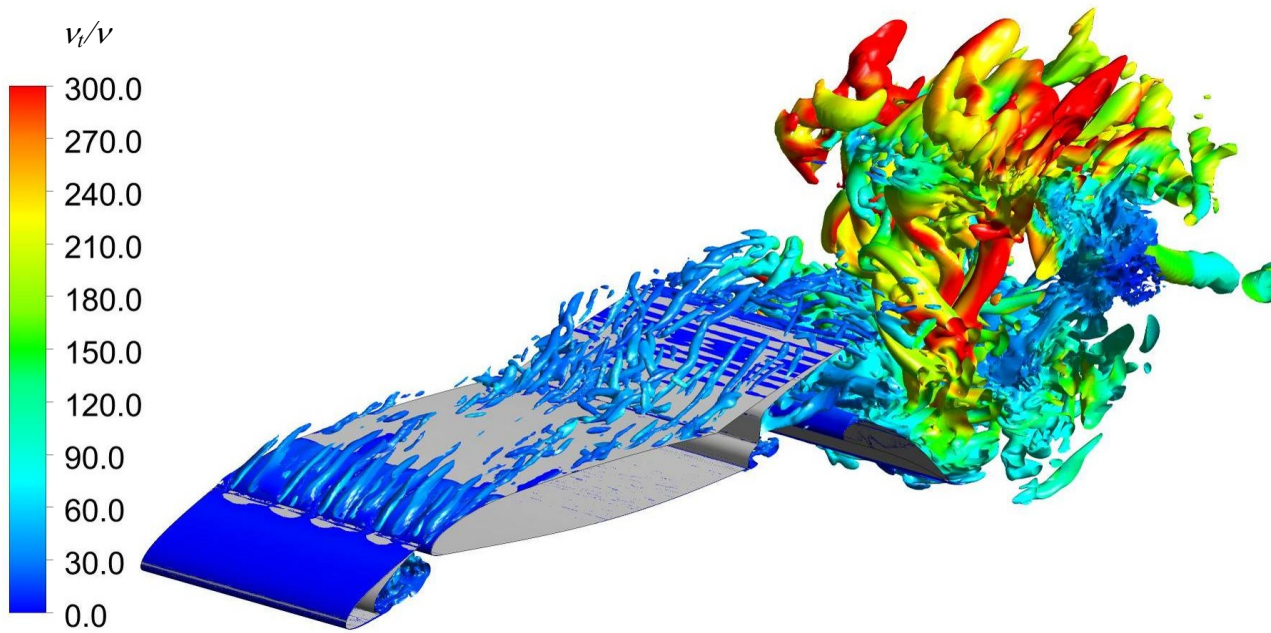


Figure 6-22: Turbulent structures around the CS-airfoil with  $\delta_s = 30^\circ$  at  $\alpha = 10^\circ$ , visualized by ISO surfaces of Q-criterion  $Q = 1.2 \cdot 10^7 \text{ s}^{-2}$  colored by the ratio of the eddy viscosity to the molecular viscosity,  $t = 27.35 \text{ ms}$ ,  $U_\infty = 50 \text{ m/s}$ ,  $Re_\infty = 1 \cdot 10^6$ .

When having a look at the instantaneous total velocity distribution at two points in time for the AS-case in Figure 6-23, it becomes obvious that turbulent structures extend in this case on nearly the complete top side of the main airfoil. However, there is no connection of the turbulent structures in the slat cove and the structures created at the top side of the main wing. Instead these structures start to arise, where the flow separation occurs on the top side of the main wing. These structures are then progressively amplified downstream in a billowing process, which is recognizable by the curved edge of the blue part in the flow velocity illustration in Figure 6-23. This amplifying turbulent structures is sharply underlined by the illustration of the Q-criterion iso-surface in Figure 6-24, where the number of vortex tubes is increasing downstream and the diameter of the tubes is also increased. In contrast to these structures with an axis in longitudinal direction, mainly two dimensional eddies, with the axis directed in lateral direction are observable in the gap between the main wing and flap. The density of eddy-structures is increased vastly in the wake of the spoiler and the flap. Here, very small scale structures are mixed up with larger structures with a diameter as large as the flap chord length. The larger structures are mainly directed in lateral direction,

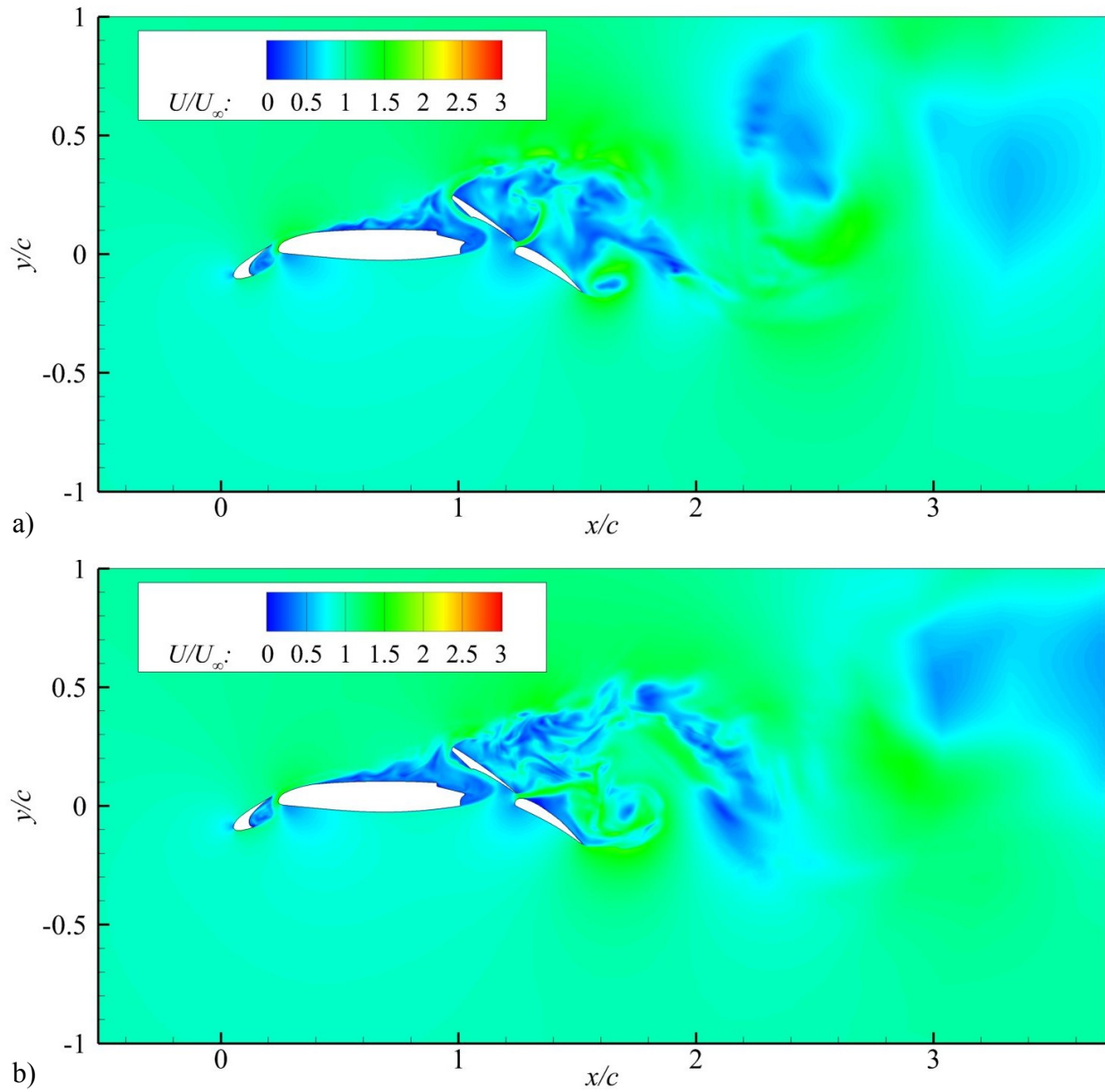


Figure 6-23: Distribution of total velocity in symmetry plane. SAS results of AS-case with  $\delta_s = 30^\circ$  at  $\alpha = 10^\circ$ ,  $U_\infty = 50$  m/s,  $Re_\infty = 1 \cdot 10^6$ . a)  $t_1 = 24.33$  ms; b)  $t_2 = 27$  ms.

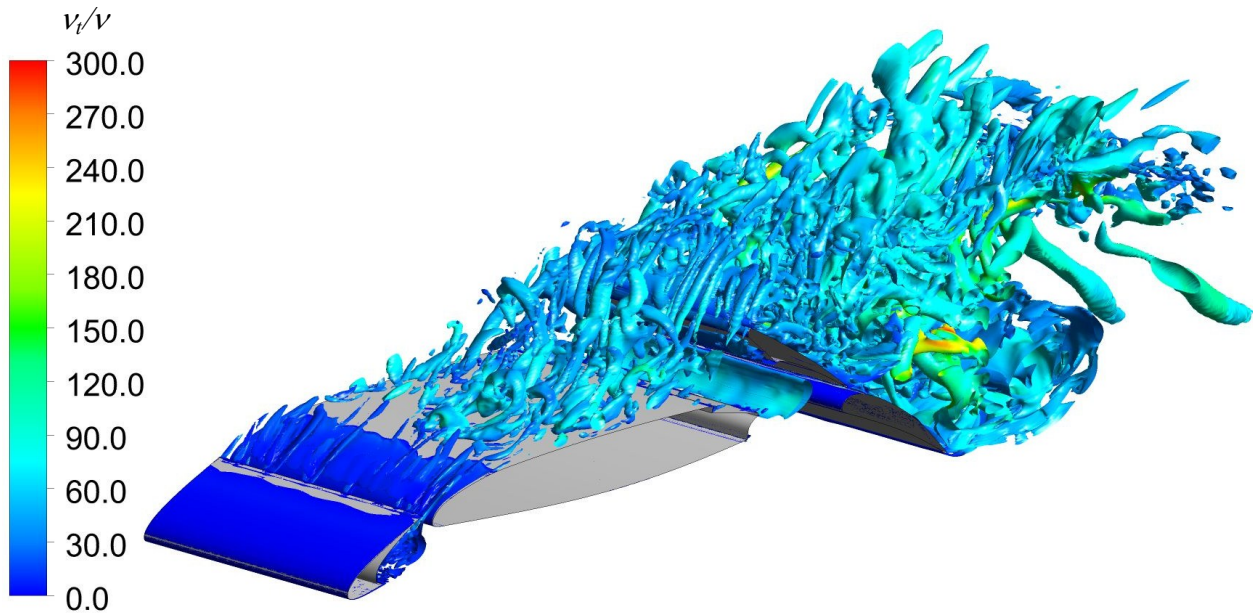


Figure 6-24: Turbulent structures around the AS-airfoil with  $\delta_s = 30^\circ$  at  $\alpha = 10^\circ$ , visualized by ISO surfaces of Q-criterion  $Q = 1.2 \cdot 10^7 \text{ s}^{-2}$  colored by the ratio of the eddy viscosity to the molecular viscosity,  $t = 27 \text{ ms}$ ,  $U_\infty = 50 \text{ m/s}$ ,  $Re_\infty = 1 \cdot 10^6$ .

The last case to be discussed is AAS with  $\delta_s = 30^\circ$ . Again, the instantaneous velocity distribution at two points in simulation time is illustrated in Figure 6-25 and the iso-surfaces of the Q-criterion in Figure 6-26. These results give a very similar picture for the vortex topology of the AAS-case and the AS-case. Thus, the following discussion is limited to the differences of AAS compared to AS: Obviously, the laterally orientated vortical structures in the gap between main wing and the trailing edge of the spoiler, which were observed for the AS, are suppressed by the sealing. Instead, no vortical structures are observable for the cavity at the bottom trailing edge of the main wing. Also, there are very few vortical structures created between the trailing edge of the spoiler and the flap. This continues on the top side of the flap, where much less vortical structures are generated compared to the AS-case. Having a look at the region between the sealing and the spoiler there is a high density of small three-dimensional eddies observable. These are connected to the eddies, which are created on the top side of the main wing and mainly point toward the leading edge of the spoiler.

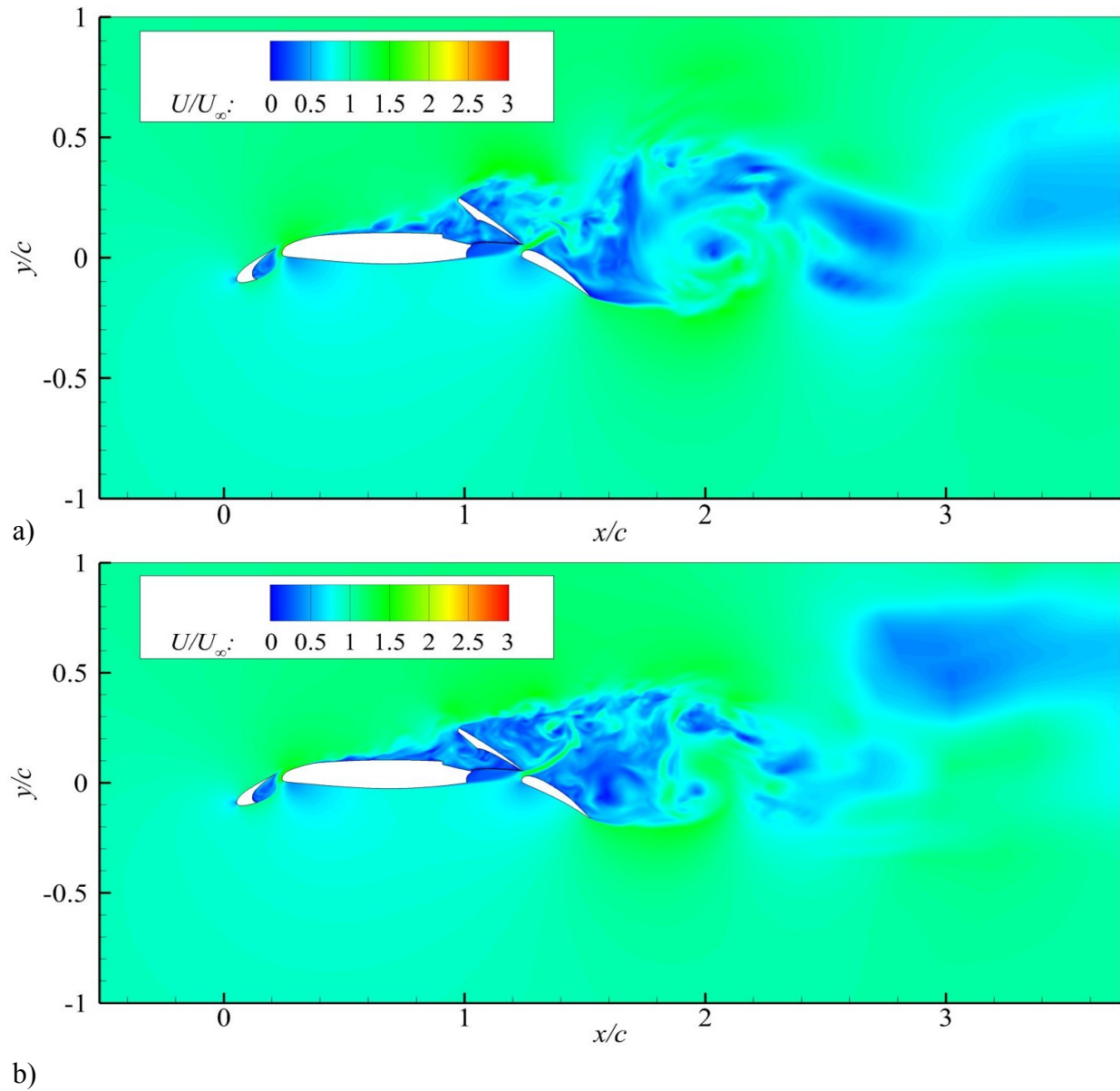


Figure 6-25: Distribution of total velocity in symmetry plane. SAS results of AAS-case with  $\delta_s = 30^\circ$  at  $\alpha = 10^\circ$ ,  $U_\infty = 50$  m/s,  $Re_\infty = 1 \cdot 10^6$ . a)  $t_1 = 43.2$  ms; b)  $t_2 = 50.8$  ms.

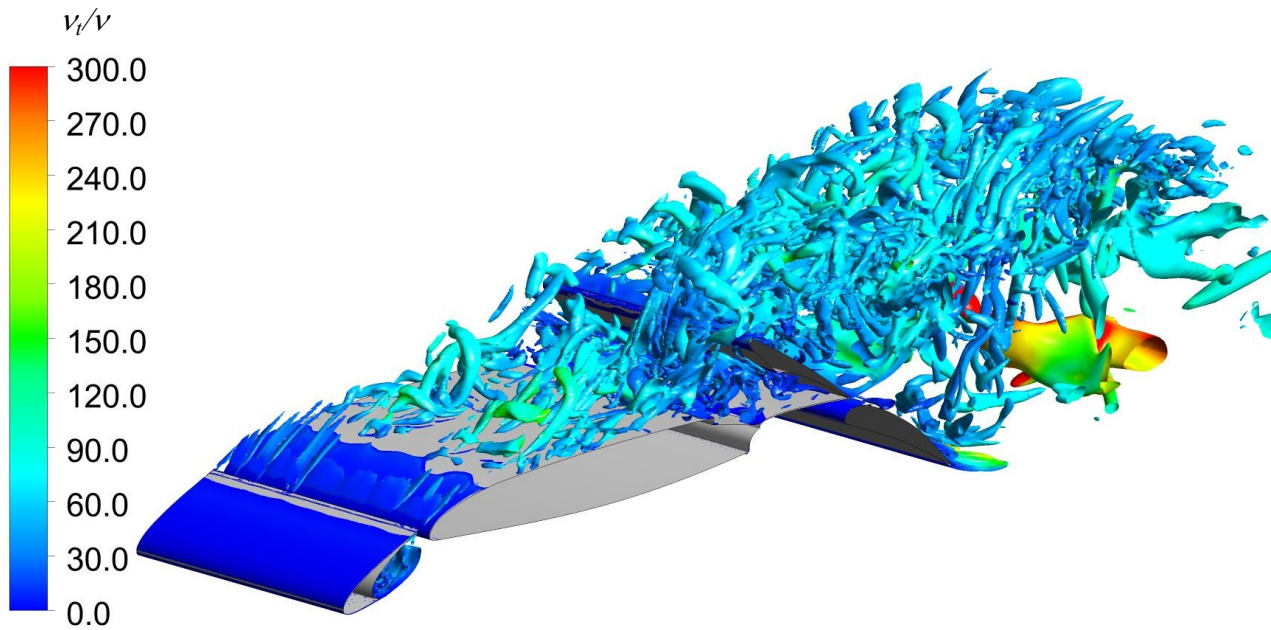


Figure 6-26: Turbulent structures around the AAS-airfoil with  $\delta_S = 30^\circ$  at  $\alpha = 10^\circ$ , visualized by ISO surfaces of Q-criterion  $Q = 1.2 \cdot 10^7 \text{ s}^{-2}$  colored by the ratio of the eddy viscosity to the molecular viscosity,  $t = 50.8 \text{ ms}$ ,  $U_\infty = 50 \text{ m/s}$ ,  $Re_\infty = 1 \cdot 10^6$ .

## 6.2 Flow Topology Identification by Tuft Flow Analysis

As introduced in subsection 3.2.2, tuft flow visualization by short tufts affixed to the model serves to characterize the flow in the vicinity of the wind tunnel model surfaces. By this means, the flow topology can be characterized associated with the investigated air-brake devices and their parameters. The device-configurations, investigated by affixed tufts, comprise BL and the spoiler configurations CS, AS and AAS each with  $\delta_S = 30^\circ$ . The flow topology associated to the aileron devices, DC and SA, is examined only by the simpler tuft stick method (3.2.2). The test parameters are constrained to representative values, which reveal the effects of the devices for specific flight attitudes, primarily for  $\alpha = 0^\circ$ , the MVAP (minimal velocity approach point, subsection 2.4.2) and cases in the proximity of  $\alpha = \alpha_{max}$ .

Figure 6-27 includes the pictures taken for configurations BL and CS with  $\delta_S = 30^\circ$  each at  $\alpha = 0^\circ$ . For the BL-case (Figure 6-27a), the flow is globally attached. Nearly all tufts are aligned straight backwards in inflow-direction and keep still. The only exceptions from this behavior are the tufts on the aileron and the ones on the flap in proximity to the flap kink. These feature a minor lateral oscillation. Figure 6-27b shows the condition for the CS-case. The inner half of the wing highlights the very same behavior as the BL-case. This is also true for the outboard part of the wing ranging from 85% span to the wing tip, the slat, and the main wing part upstream of the spoiler. In contrast, both the flow ahead of the spoiler and the flap flow directly behind the spoiler are affected. The tuft direction

indicates that the flow on the main wing and the spoiler apart from the spoiler lateral center line moves in lateral direction due to the blockage effect of the spoiler. This leads to a local flow component directed outwards outboard of the spoiler lateral center line and a component directed inwards inboard of the spoiler lateral center line. A much larger effect can be seen on the flap: Here, the tufts are directed opposite to the inflow direction and wagging. The wagging is reflected by a blur appearance of the tufts in the picture. This behavior indicates a flow separation on the flap, which is locally limited to the part directly behind the spoiler.

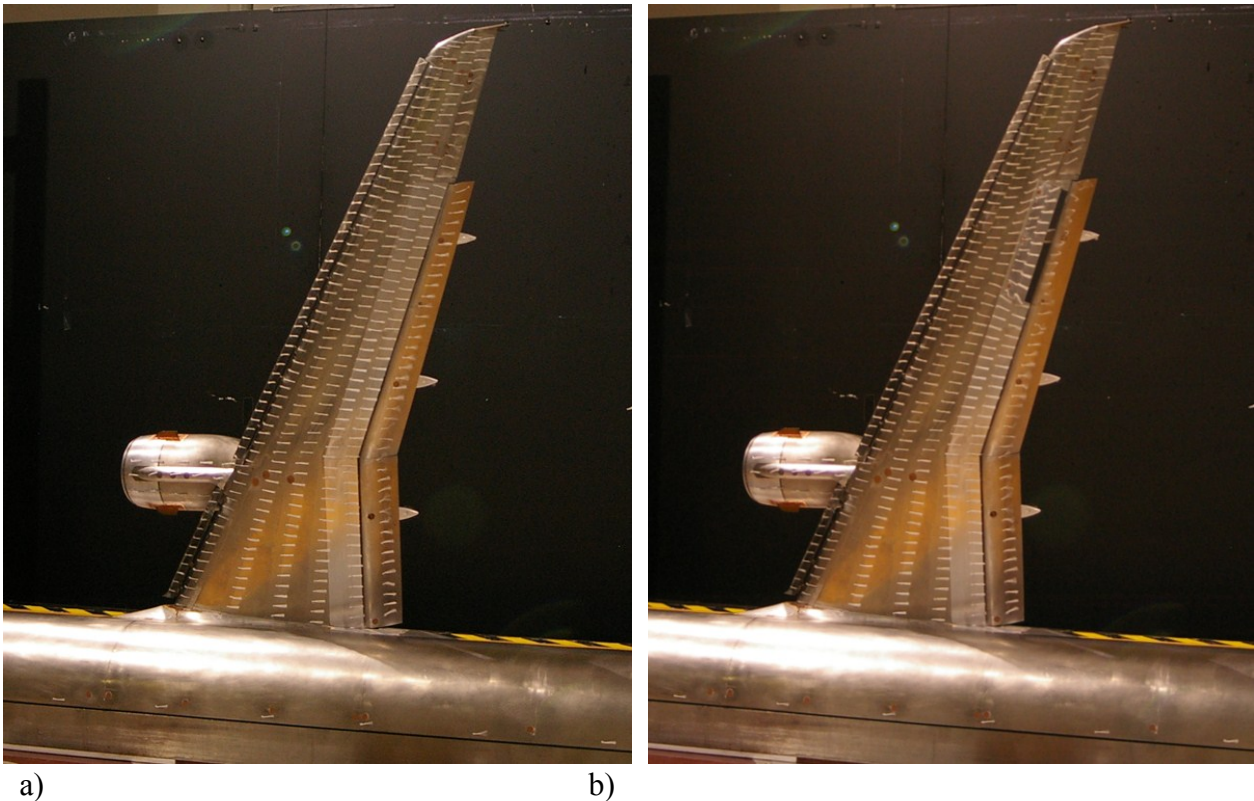


Figure 6-27: Overall view for cases BL (a) and CS with  $\delta_s = 30^\circ$  (b) at  $\alpha = 0^\circ$ .

In Figure 6-28, the tuft analysis results are compared for the AS with  $\delta_s = 30^\circ$  and AAS with  $\delta_s = 30^\circ$  cases again at an angle of attack of  $\alpha = 0^\circ$ .

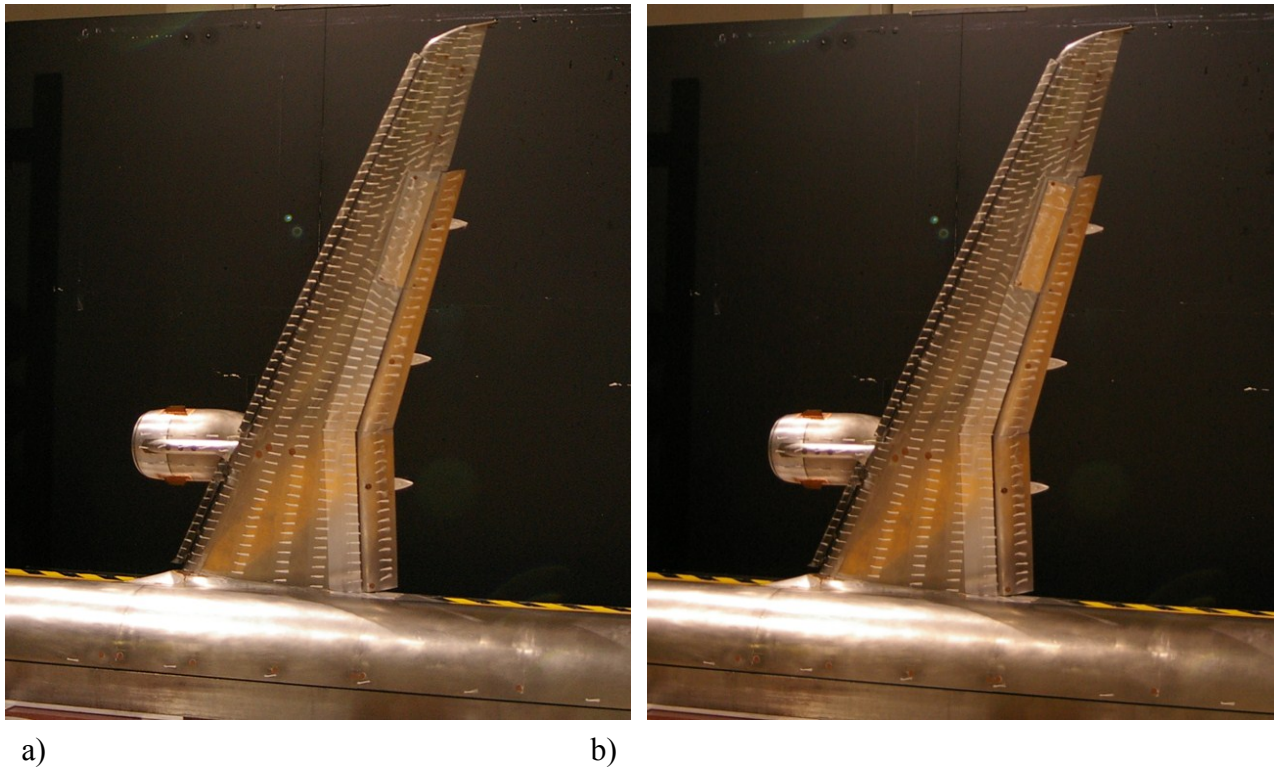


Figure 6-28: Overall view for cases AS with  $\delta_s = 30^\circ$  (a) and AAS with  $\delta_s = 30^\circ$  (b) at  $\alpha = 0^\circ$ .

Both cases, the main wing and slat, show a quite similar behavior to the conventional spoiler case. The flow, which streams to the spoiler, moves out in lateral direction due to the blockage effect of the spoiler. This is again indicated by laterally inclined tufts. All the tufts on the spoiler are in both cases directed against the inflow direction and waggling, indicating the flow separation on the leeward side of the spoiler. Finally, the flow on the flap keeps attached in both cases on nearly the complete flap. There is only a marginal indication in both cases for a starting separation for the part of the flap, which is located immediately downstream of the spoiler. This indication is expressed by a slight waggling of the tufts there.

Figure 6-29 and Figure 6-30 show the tuft flow pictures for the MVAP-case. This case represents the maximum feasible approach angles of attack, which ranges from  $\alpha = 6.6^\circ$  to  $\alpha = 8.4^\circ$  for the four cases of interest, namely BL, CS, AS, and AAS. All four pictures look very similar to the corresponding four pictures at  $\alpha = 0^\circ$  presented in Figure 6-27 and Figure 6-28. Thus, all the observable phenomena are considered nearly unchanged by the increase in  $\alpha$  in this range. The indication of unsteady but not clearly separated flow on the flap downstream of the Adverse Spoiler and Advanced Adverse Spoiler is in agreement to the findings from the unsteady 2D simulations presented in subsections 6.1.3 and 6.1.4. There, the flap boundary layer ranged between an attached and a separated state, even though the separation was much more distinct for the AS-case compared to the AAS-case in the simulation.

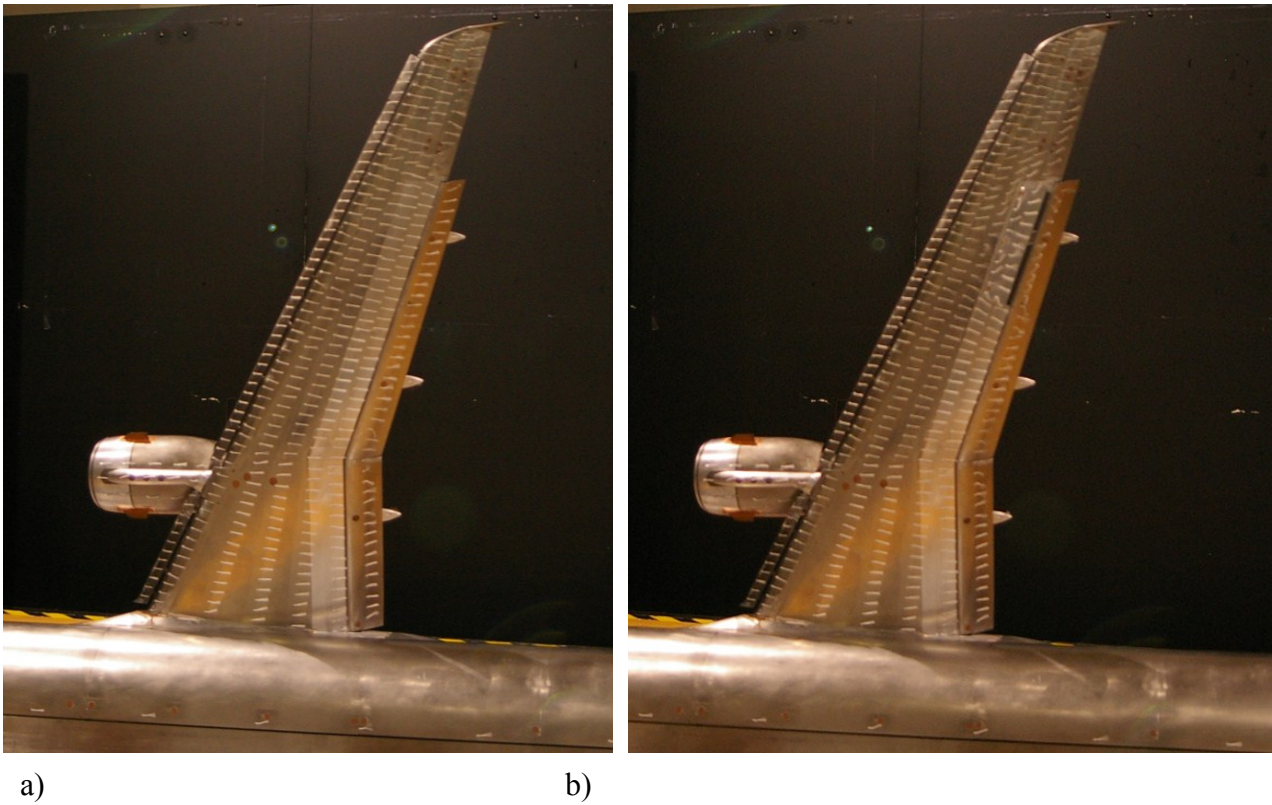


Figure 6-29: Overall view for cases BL (a) and CS with  $\delta_S = 30^\circ$  (b) at MVAP.

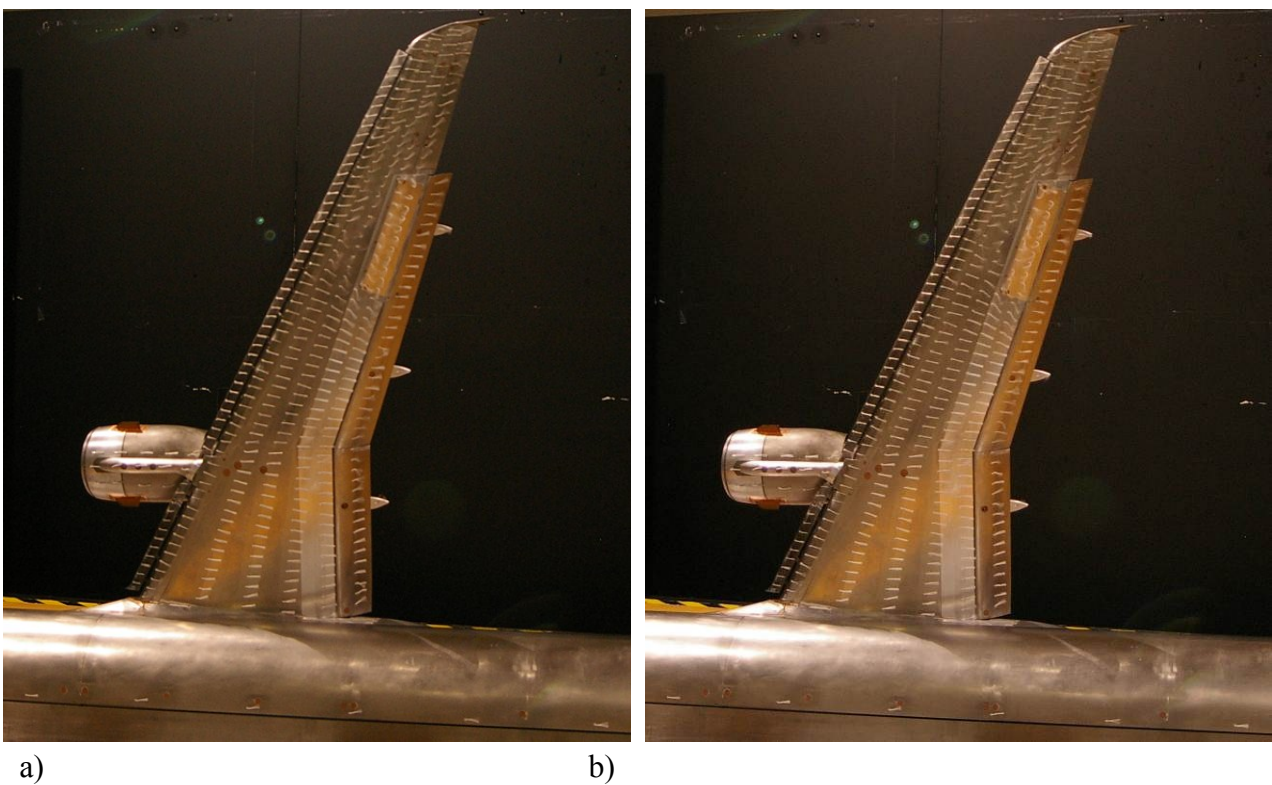
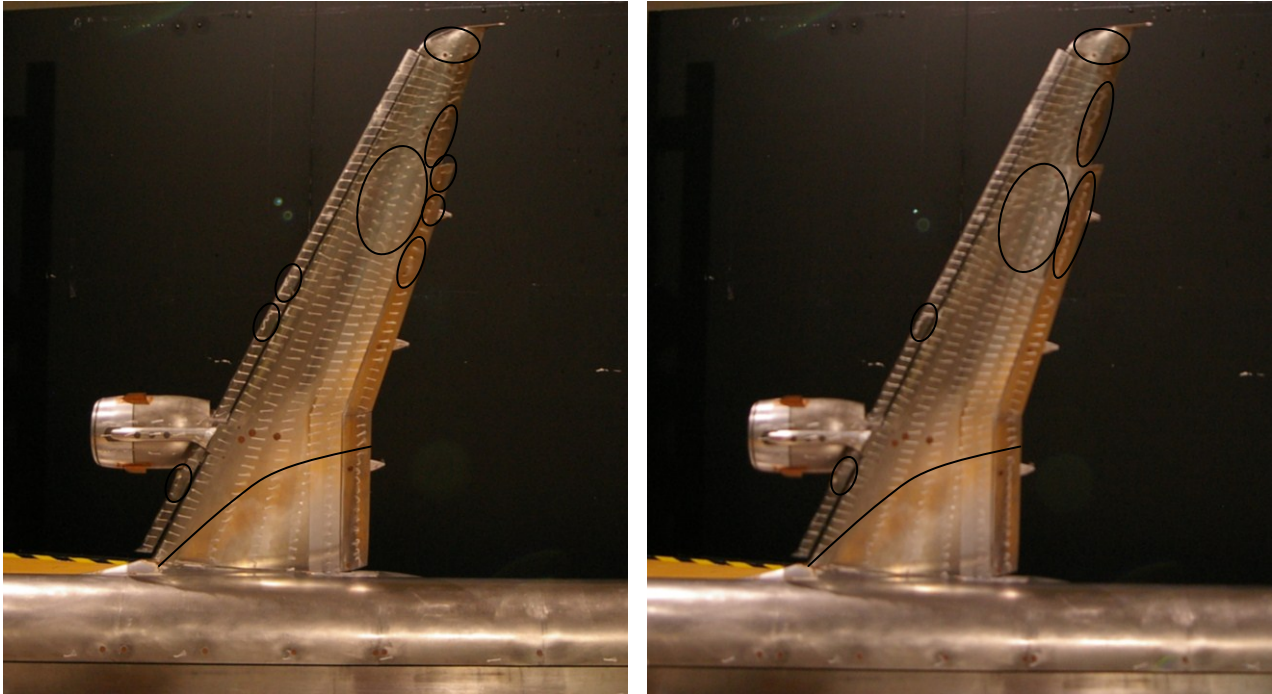


Figure 6-30: Overall view for cases AS with  $\delta_S = 30^\circ$  (a) and AAS with  $\delta_S = 30^\circ$  (b) at MVAP.

Finally, the pictures in Figure 6-31 and Figure 6-32 show the situation of the flow near to the surface at  $\alpha = 22^\circ$ , which represents an angle of attack near  $\alpha_{max}$  and thus the onset of

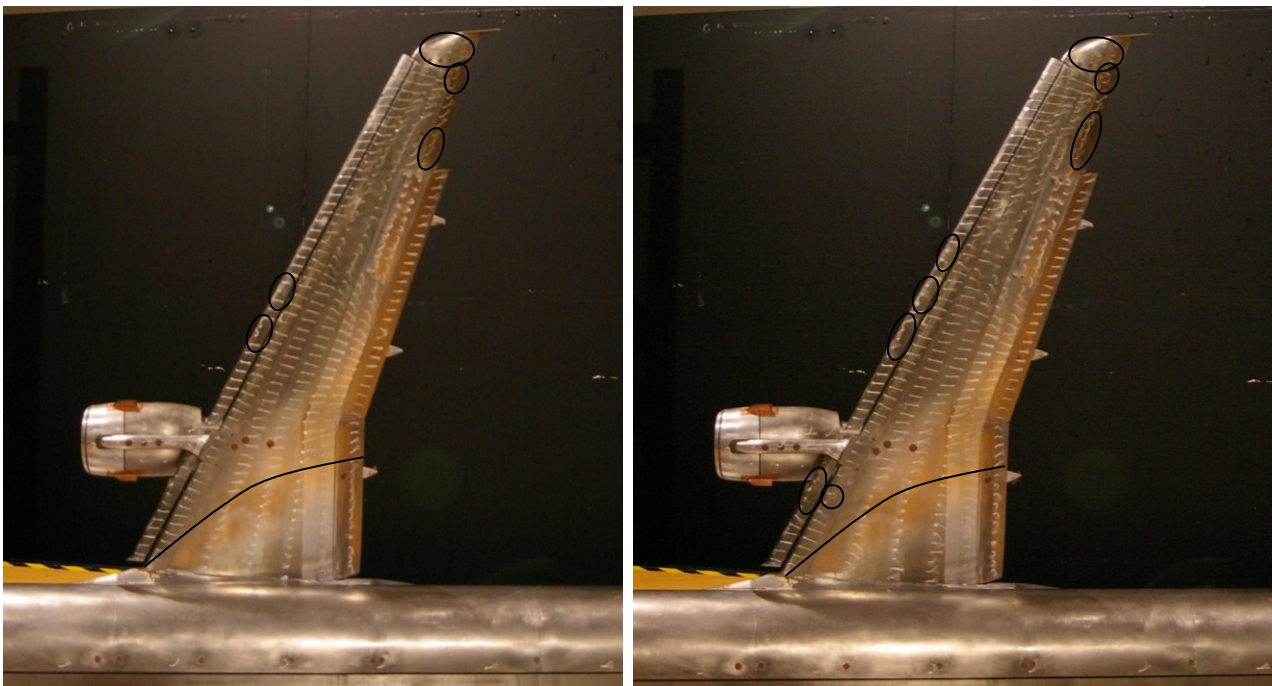
the global stall. In these pictures, the borders of the separation zone are marked by black lines. Generally, when increasing the angle of attack, an inboard separation propagates from the trailing to leading edge on the wing while the separation area becomes enlarged in spanwise direction.



a)

b)

Figure 6-31: View for cases BL (a) and CS,  $\delta_S = 30^\circ$  (b) in the stall angle range at  $\alpha = 22^\circ$ .



a)

b)

Figure 6-32: Overall view for cases AS with  $\delta_S = 30^\circ$  (a) and AAS with  $\delta_S = 30^\circ$  (b) in the stall angle range at  $\alpha = 22^\circ$ .

In Figure 6-32a, the tufts for the BL-case show the onset of stall by a flow separation area on the top side of the main wing in the inboard area. The first end of this flow separation band is located at the leading edge of the wing root and the band becomes wider downstream to comprise the inner wing from the fuselage to about a quarter the span at the trailing edge. Flow separation is also detectable on the flap from the inner edge to about a quarter of the wingspan. This stall onset area is consistent with the desired inboard position of starting flow separation to maintain aileron effectiveness (subsection 2.3.6). Flow separation also occurs at the very tip of the wing outboard of the slat. This is due to the absence of the slat upstream from the very outboard wing. To a lower extent, there is also an onset of flow separation on the part of the wing at about three-quarters of wingspan, the immediately downstream-located top side of the flap and the inner part of the aileron, which expresses itself by a wagging of the tufts and by only selectively backward pointed tufts. Most of the upper side flow of the slats stays attached for this angle of attack. Only at three small portions of the slat top side flow separation can be detected. One of these areas is located inboard close to the nacelle in lateral direction. This separation arises due to the upstream location of the nacelle. The cause for the other two small separation zones on the slat, which are located at about half wingspan, cannot be revealed by this method.

The situation of the top side flow near the wing surface for the CS-configuration with  $\delta_S = 30^\circ$  is illustrated by a picture of the tuft-equipped model in Figure 6-32b. The situation is quite similar to the BL- case. The inboard separation band has about the same size. Again, most of the slat top side flow is attached, although the three separation areas have now converted into two. This occurs by an absence of the most outboard-located separation zone. The inboard separation on the slat stays the same in size and position. Larger differences are observable for the area near the spoiler. This is due to a complete flow separation on the aileron's top side, as well as on the flap's top side reaching the complete span of the spoiler exactly downstream from the spoiler.

Finally, in Figure 6-32 the situation is illustrated by pictures of the models configured for the cases AS with  $\delta_S = 30^\circ$  and AAS with  $\delta_S = 30^\circ$ . Again, the situation of flow separation areas on the slat is similar to the BL. In the AS-case with  $\delta_S = 30^\circ$ , there are again three areas of separation at the same positions as in the BL-case. In the AAS-case with  $\delta_S = 30^\circ$ , the inboard separation on the slat is broader, the two outboard separation zones again exist and there is a fourth separation on the slat a bit further outboard. Contrary to the CS-case, the flow on the top side of the flap is not separated, albeit the tufts are in both cases wagging a bit, which show that the flow on the top side of the flap has the unstable status, shortly before flow separation occurs.

### 6.3 Flow Topology Synthesis

To form a synthesis from the extensive investigations of the flow topology resulting from the Baseline as well as the three different spoiler configurations for an angle of attack

representative for approach, schematic flow topology sketches were created. These show all major features identified by the numerical as well as the experimental investigation methods. Thereby, the experimental findings from the tuft analysis serves to describe the 3D effects near the model surfaces, while the 2D and 2.5D results from the numerical simulations give an insight into the flow field away from the model surface. However, the results from the numerical simulations hold approximately only for the symmetry plane at the mid spoiler position. Figure 6-33 shows the flow-topology of the Baseline-case.

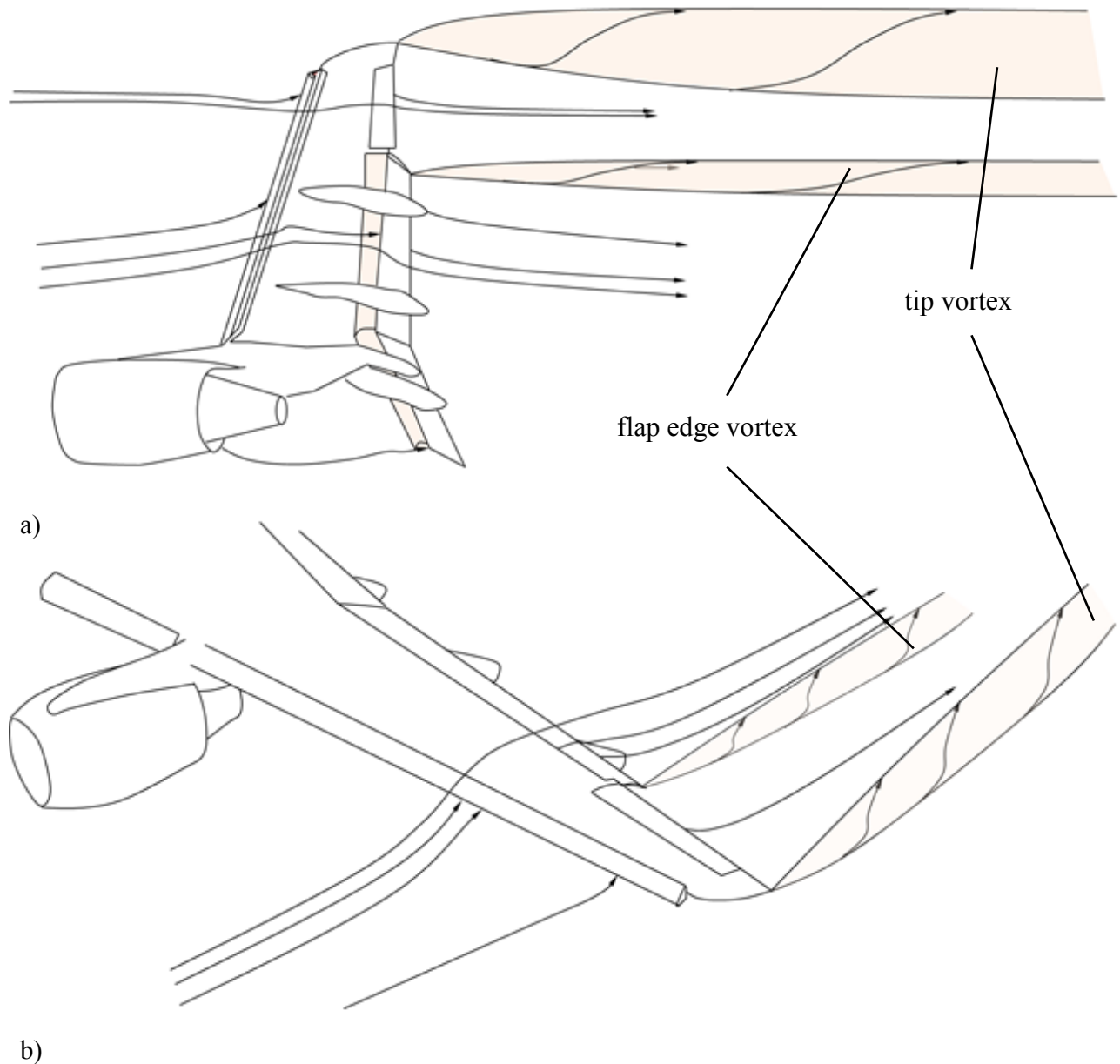


Figure 6-33: Flow topology sketch of the approach situation for the Baseline. a) View from below; b) view from above.

Figure 6-33a shows a low angle shot and Figure 6-33b the top view. In the view from below, tip vortex, flap edge vortex, slat cove separation and main wing cavity separation are illustrated. The top view shows again the tip and flap edge vortices. Additionally,

streamlines serve to visualize the flow topology in both views. Figure 6-34 shows the same two perspectives for the CS-case.

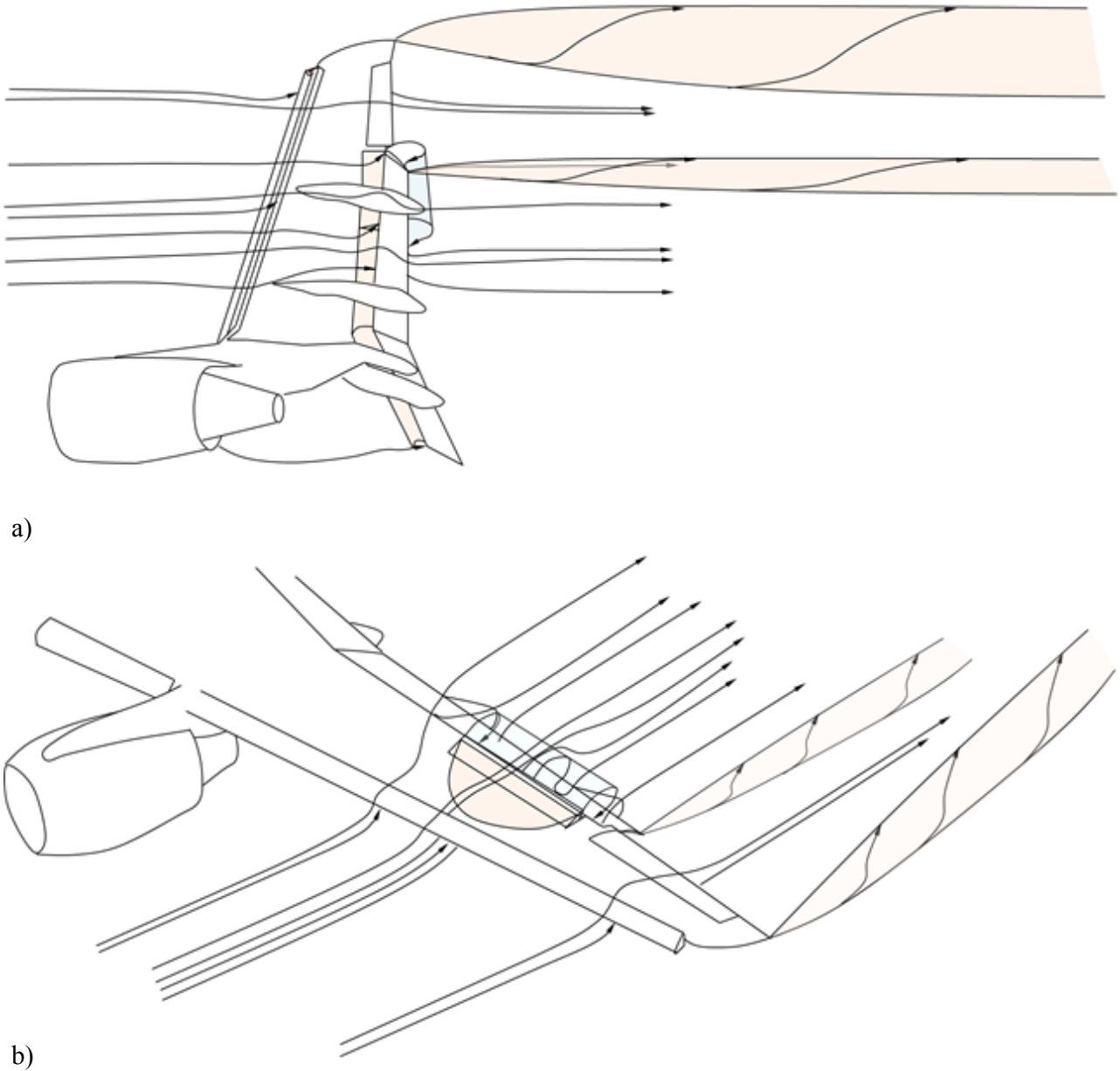


Figure 6-34: Flow topology sketch of the approach situation with deployed Conventional Spoiler. a) View from below; b) view from above.

The vortex flow phenomena at the wing tip and flap edge and the flow separation in the slat cove and the main wing cavity are not influenced significantly by the conventional spoiler. The new phenomena illustrated in the sketches are the flow on the wing, which deflects in lateral direction in front of the spoiler, the flow separation area in front of the spoiler on the main wing (top view in light orange), and the large-scale separation roller on the flap downstream of the spoiler (top and bottom view in light blue).

The situation for the AS-configuration is shown in Figure 6-35. Again, the same two perspectives are given. Similarly to the CS-case, there is a flow separation zone on the top

side of the main wing upstream of the spoiler (top view in light blue), but this time this separation zone does not range downstream to the front end of the spoiler. Instead, there are streamlines, which pass below the wing and then through the flap in the main wing to the top side. These stream lines then pass close above the separation at the leading edge of the Adverse Spoiler. This separation zone is illustrated by a large roller behind the spoiler (light purple). There is no separation on the top side of the flap though. The flow to the flap comes from below the wing.

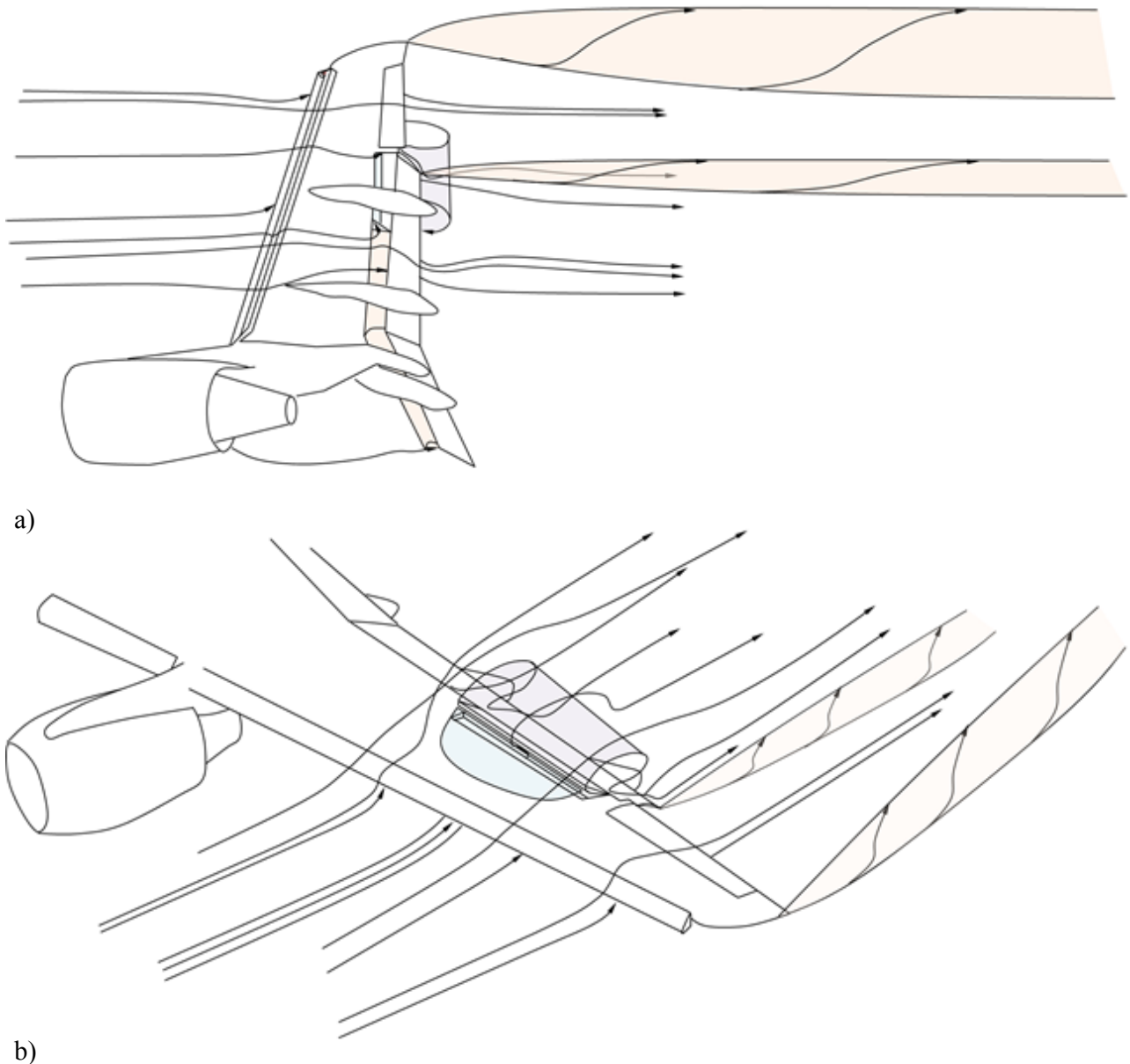


Figure 6-35: Flow topology sketch of the approach situation with deployed Adverse Spoiler. a) View from below; b) view from above.

Finally, Figure 6-36 shows the situation for the AAS-configuration. The main difference to the AS-configuration is that the flow is not passing from below the main wing through the gap between Adverse Spoiler and main wing, which is no more present for the AAS due to

the sealing. A flow separation roller is again present at the leeward side of the spoiler (light purple), but this time the streamlines, which pass close above the separation line at the leading edge of the spoiler, pass over the main wing upstream of the AAS.

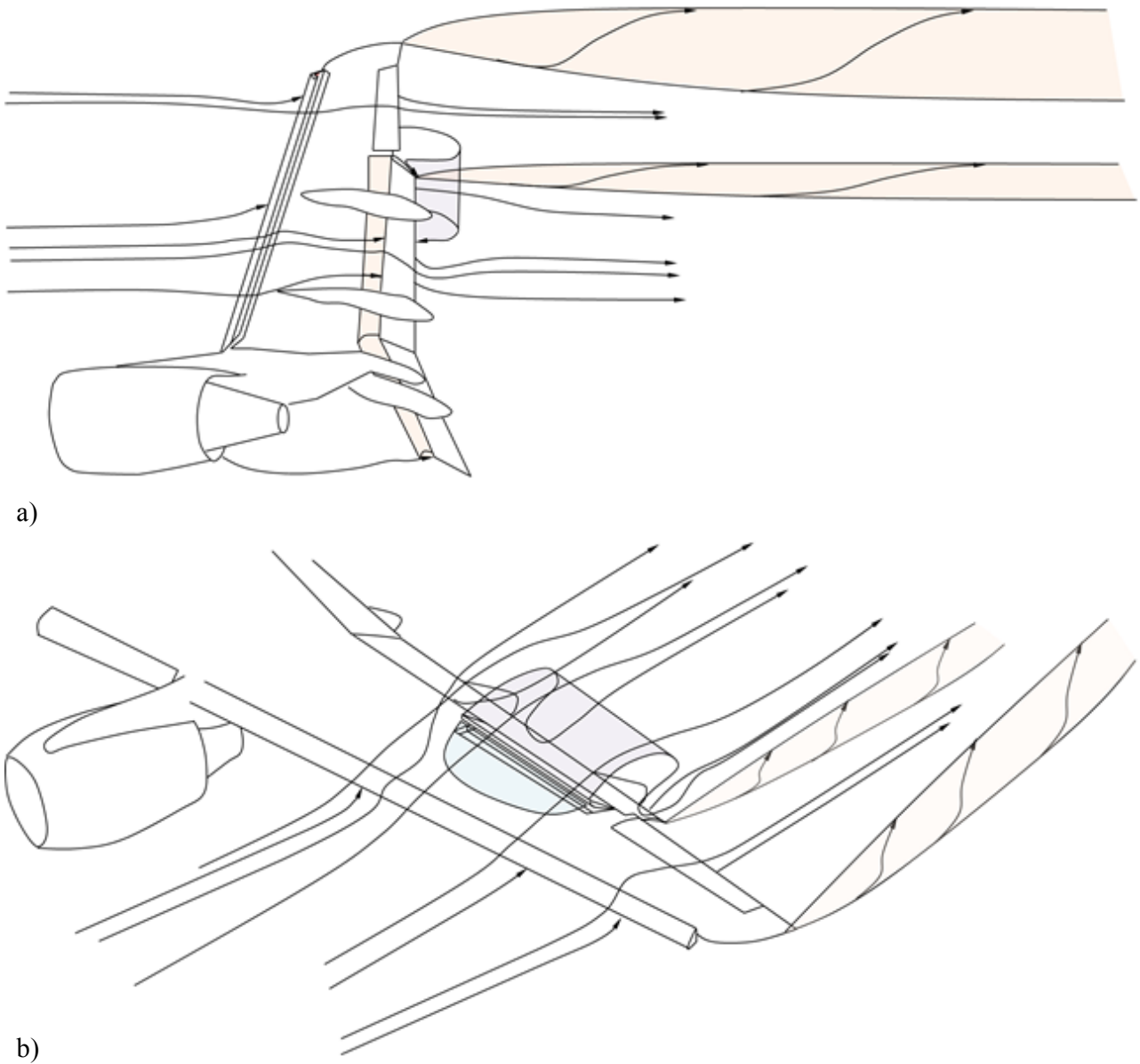


Figure 6-36: Flow topology sketch of the approach situation with deployed Advanced Adverse Spoiler. a) View from below; b) view from above.

# 7. INVESTIGATION OF THE NEAR WAKE

Earlier research projects on the investigation of the wake of CTA mainly focused on the investigation and possibilities to manipulate the wake downstream of the CTA, which potentially interacts with following aircraft [28], [9]. Nevertheless, there have also been studies on the optimization of the interaction of the wing mounted air-brake system and the HTP. For example, in the European project AWIATOR, a wing based spoiler with a gap between the top side of the wing and the lower edge of the spoiler was investigated to limit the interaction between the wing's wake and the HTP, thereby reducing HTP-buffet and improve the descent rate for operational procedures [38].

Analogous to the last-mentioned investigations, the aim of the wake-investigations in this work is to evaluate the effect of the investigated spoiler devices on the flow field starting from the trailing edge of the wing extending to the back end of the aircraft. Thereby, a better understanding of the aerodynamic wake phenomena induced by deployment of the investigated device is to be achieved. In addition, it is possible to estimate, whether the flow field can cause HTP-buffet with its corresponding negative aeroelastic effects. For predicting the actual buffet loads, a random gust response analysis, or PSD analysis, could be used in the future as basis to perform the buffet predictions [140].

The configuration, regarding the investigated device used as air brake, is varied in this work's wake investigations, whereas the deployment angle of the devices is held constant at  $\delta_S = 30^\circ$ . The configurations comprise the Baseline-configuration (BL), the configuration with Conventional Spoiler (CS), the configuration with Adverse Spoiler (AS) and the configuration with Advanced Adverse Spoiler (AAS). The velocity-distribution as well as turbulence intensities are obtained from measurements by the PIV-method. These results are discussed in sections 7.1 and 7.2. Power spectral densities as function of reduced frequency are gathered by HWA-measurements. These are conducted for only some selected positions, which include points in an array straight in the wake of the devices, as well as at positions representing the location, where a HTP would be installed for the real CTA. The background of both measurement methods was already introduced in subsections 3.2.3 and 3.2.4. The set-up of the parameters can be found in subsection 3.6.2 and the post-processing-methods are described in subsection 3.7.5.

As already mentioned in subsection 3.2.3, it is not possible to obtain the velocity field of the complete wake of the wing by the used PIV-system at once, but only sequentially for rectangular sectors due to the window size of the PIV-system. Thus, the laser sheet and the cameras of the PIV-system are traversed to get 10 to 20 overlapping

sectors in lateral and vertical direction and thereby covering a large wake area reaching from  $y^* \approx 0.25$  to  $y^* \approx 1.1$ . The vertical position of each sector is chosen to include all the major wake phenomena. The PIV-results have not been interpolated. This occasionally leads to comparatively harsh value intersection from a measurement sector to the next.

## 7.1 Mean Flow Topology

The results from the PIV-measurements are averaged over each measurement cycle period to obtain the mean flow. Figure 7-1a and Figure 7-1b show the velocity field in cross flow plane  $x_1$  ( $x_1/b = 0.12$ ) for the BL-configuration and the CS-configuration with  $\delta_S = 30^\circ$ .

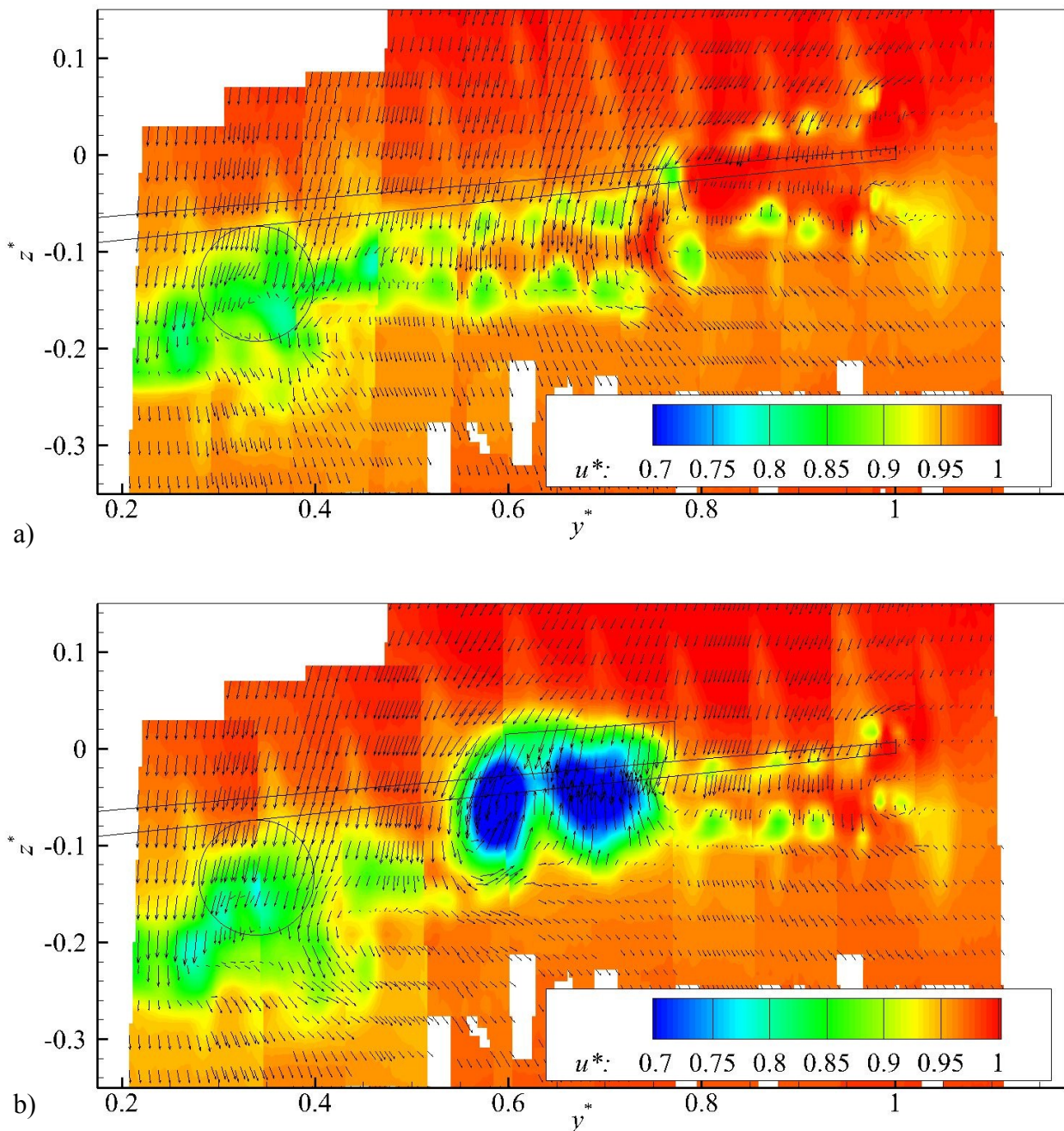


Figure 7-1: Velocity distribution in plane  $x_1$  ( $x_1/b = 0.12$ ). a) BL; b) CS with  $\delta_S = 30^\circ$ .

Figure 7-2a and Figure 7-2b show the velocity distribution for the AS-configuration with  $\delta_S = 30^\circ$  and AAS-configuration with  $\delta_S = 30^\circ$ , respectively. The cross flow velocity components  $v$  and  $w$  are depicted by vector arrows, whose length is proportional to the cross flow velocity  $V_g$ . The axial velocity  $u^*$  is depicted by false color. In each figure, the periodically repeating vertical streaks in the false color pictures are a sign of minor measurement artifacts. The silhouette of the half-model's wing, engine nacelle and spoiler is sketched into the pictures to facilitate the attribution of detected flow phenomena to geometrical details of the model.

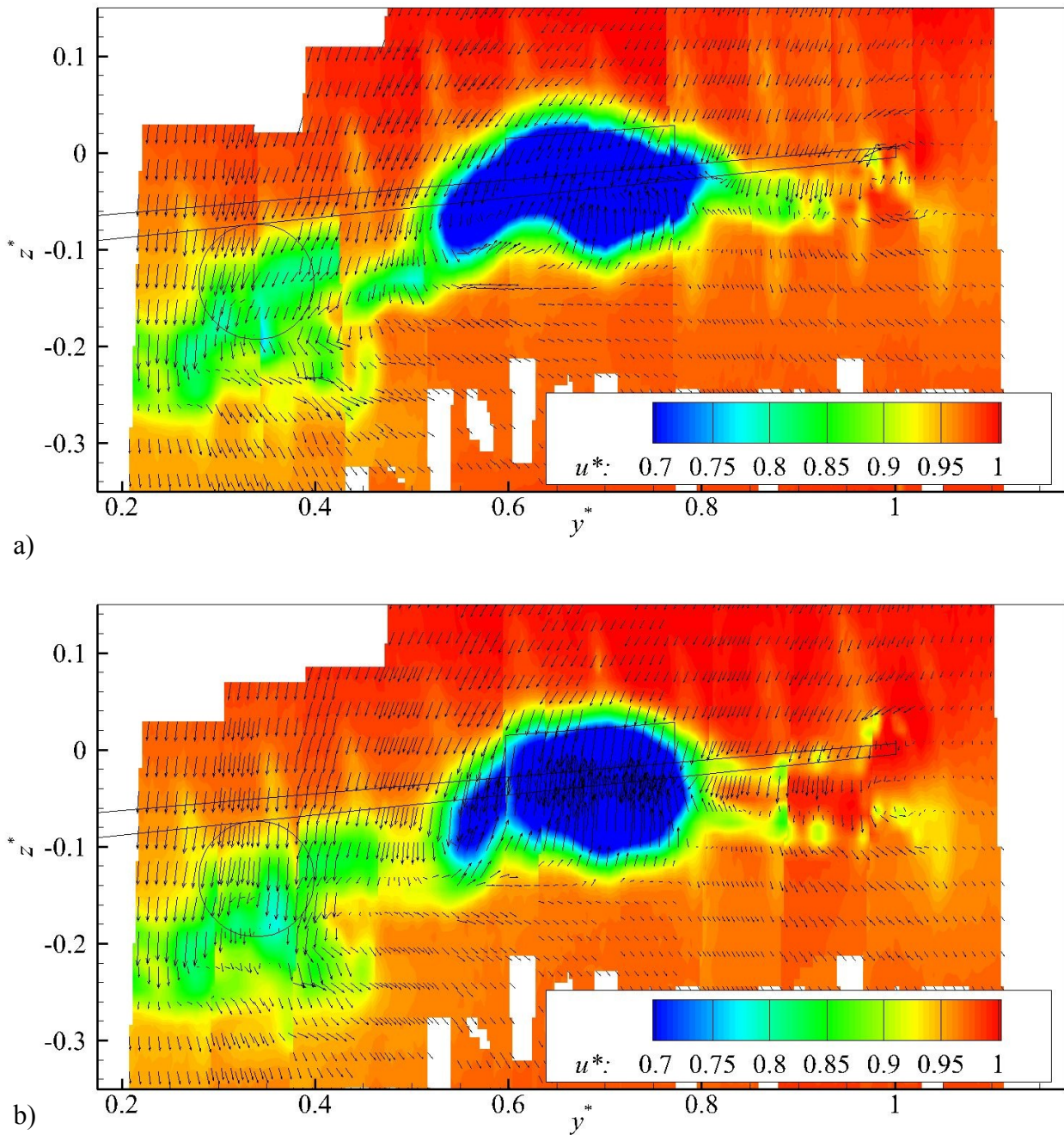


Figure 7-2: Velocity distribution in plane  $x_1$  ( $x_1/b = 0.12$ ). a) AS with  $\delta_S = 30^\circ$ ; b) AAS with  $\delta_S = 30^\circ$ .

Analyzing the distribution of the axial velocity  $u^*$  of the BL-configuration, one can identify the main area of velocity deficit which is concentrated inboard between  $y^* = 0.25$  and  $y^* = 0.5$ . This is due to the inboard flap and the nacelle positioned upstream of this area. Ranging between  $y^* = 0.5$  and  $y^* \approx 0.8$ ,  $u^*$ -deficit spots are ordered in two horizontal streaks at  $z^* \approx -0.15$  and  $z^* \approx -0.08$ , constituted by the free shear layer of the wing. It is assumed that this wake structure with two streaks is not exactly representing the actual flow field, but other influences distorting the measurement are rather the reason for this doubled structure, where a single structure would be expected. Further outboard, the streaks are not so clear anymore and no more ordered in clear lines, but still observable ranging outboard to  $y^* \approx 1$ . The distribution of the velocity-components in the plane shows the downwash generated by the wing in the complete wake-plane superimposed by vortical structures. These wake vortices arise at the trailing edge of the wing, where a gradient in the spanwise aerodynamic load distribution is present.

Compared to the velocity distribution of the BL-configuration, the CS-configuration with  $\delta_S = 30^\circ$  shows clear differences between  $y^* \approx 0.4$  and  $y^* \approx 0.75$ . Within this interval, two widespread and high-amplitude velocity-deficit spots are present. These spots are connected only by a narrow intersection and originate from the deployed spoiler. This wake region behind the spoiler is even more pronounced for both the AS-configuration with  $\delta_S = 30^\circ$  and the AAS-configuration with  $\delta_S = 30^\circ$  (Figure 7-2a and Figure 7-2b). For the AS-configuration with  $\delta_S = 30^\circ$ , the structure with a substantial axial velocity deficit ( $u^* < 0.75$ ) is much wider and at the same time no more separated into two spots, but concentrated in one spot with a kidney-like shape. The lateral extension of this velocity-deficit spot has nearly the same size for the AAS-configuration with  $\delta_S = 30^\circ$ , but it has more of an elliptic shape.

In Figure 7-3a and Figure 7-3b, the distribution of the mean velocity in cross flow plane x2 ( $x_2/b = 0.92$ ) is depicted for the BL-case and the CS-case with  $\delta_S = 30^\circ$ . Figure 7-4a and Figure 7-4b complement the graphs of the mean velocity distribution, depicting the results in plane x2 for the AS-configuration with  $\delta_S = 30^\circ$  and the AAS-configuration with  $\delta_S = 30^\circ$ .

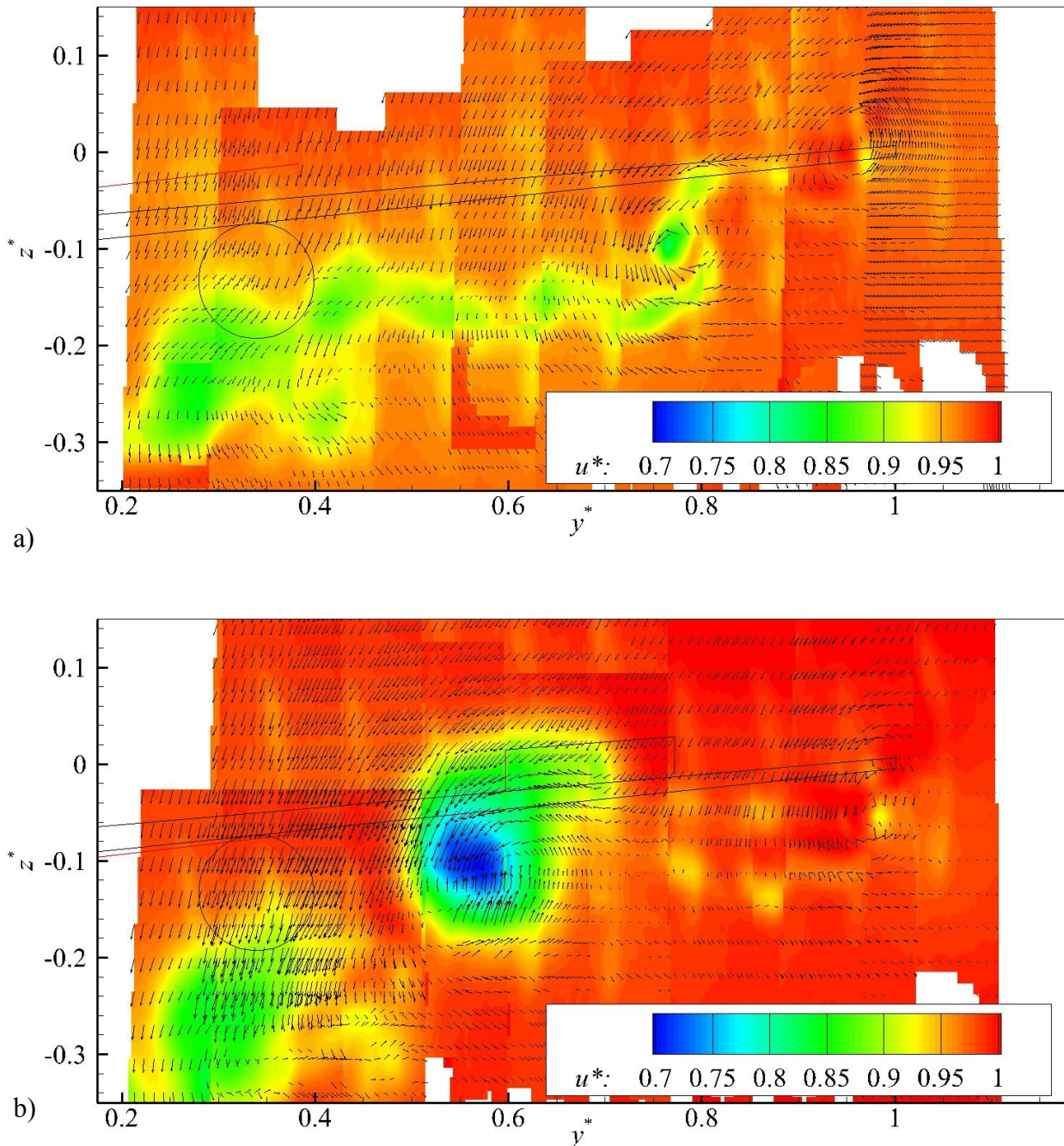


Figure 7-3: Velocity-distribution in plane  $x_2$  ( $x_2/b = 0.92$ ). a) BL; b) CS with  $\delta_s = 30^\circ$ .

In the downstream plane  $x_2$ , the flow topology develops for the BL-configuration in a way that the two outboard lines of deficit spots in axial velocity merge into one line. This line is no more as much discontinued as in  $x_1$ . Furthermore, the vertical offset of the inboard deficit line  $y^* < 0.8$  to the outboard one is increased, which is due to the roll up of the wake around the vortex, which is formed at the outer edge of the flap. The wake of the nacelle develops in a way that the axial velocity deficit is diminished to values of  $U^* > 0.8$ .

For the CS-configuration with  $\delta_s = 30^\circ$  (Figure 7-3b), the velocity deficit is reduced similarly to the BL-configuration in the wake structure originating from the inboard flap and the nacelle. The flow structure attributed to the spoiler-wake, which was two-part in

$x_1$ , is now concentrated in one velocity deficit spot. The velocity vectors in the plane show that the flow is rotating around this vortex-spot. The center of the spot has moved inboards compared to  $x_1$  to  $y^* \approx 0.55$ . The areas of a deficit in axial velocity between the nacelle-spot and the spoiler-spot have nearly disappeared compared to  $x_1$ , the same is true for the areas outboard of the spoiler-spot.

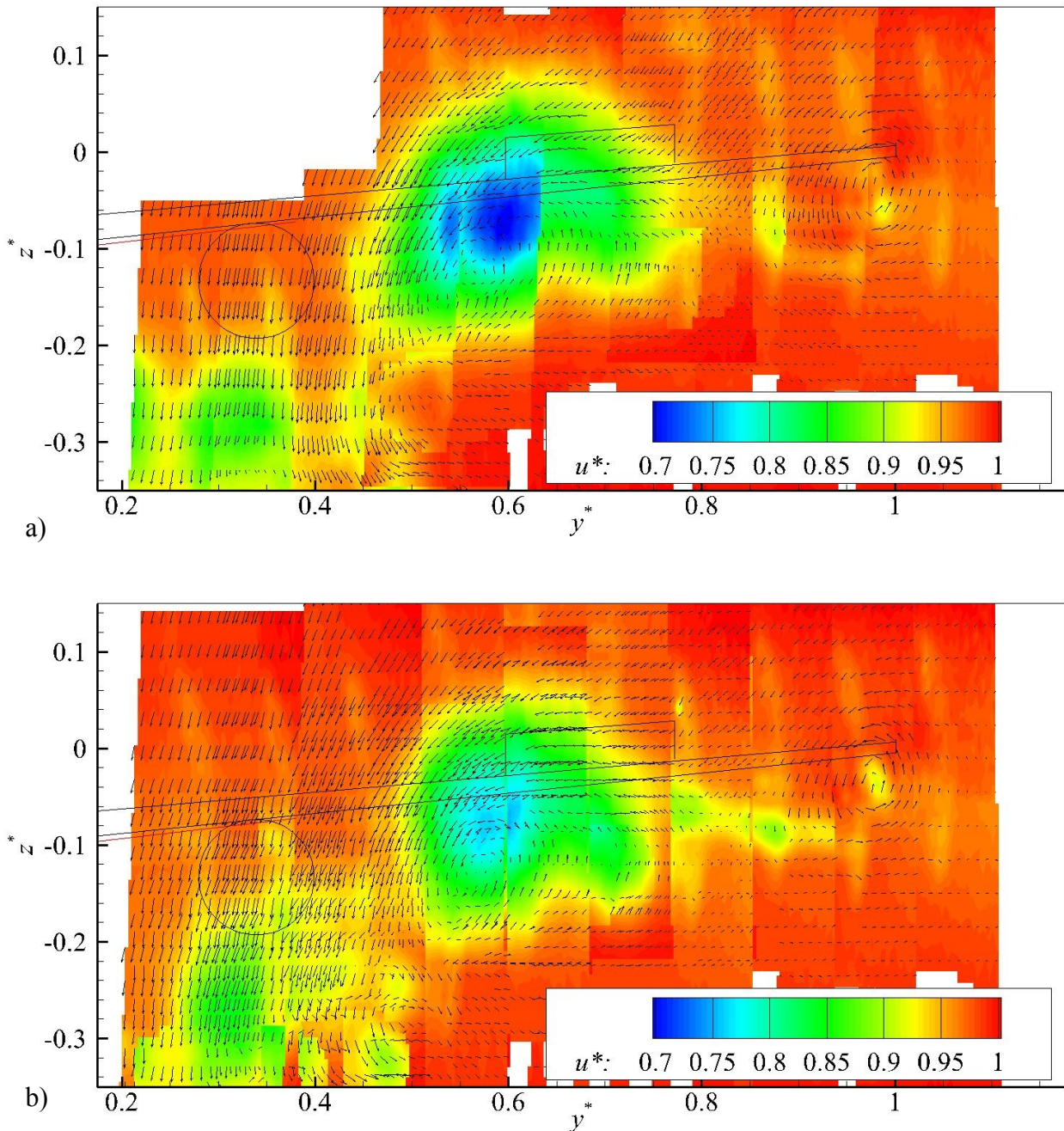


Figure 7-4: Velocity distribution in plane  $x_2$  ( $x_2/b = 0.92$ ). a) AS with  $\delta_S = 30^\circ$ ; b) AAS with  $\delta_S = 30^\circ$ .

When having a look at the results in plane  $x_2$  of the AS- and AAS-configurations, a development can be detected for the wake of the nacelle similar to the one at BL and CS. This is not the case for the wake area, which emanates from the spoiler-device, where the

axial velocity deficit stays considerably higher for the AS-configuration in x2, compared to the AAS-configuration. Also, the area with medium to high axial velocity-deficit ( $U^* < 0.9$ ) is considerably larger for the AS-configuration, compared to the AAS-configuration.

## 7.2 Vertical Turbulence Distribution

The vertical turbulence intensity  $Tu_z$  is the mainly accountable component of the turbulent flow in the wake of the wing for a potential excitation of the HTP. Its spatial distribution provides information whether an area of high  $Tu_z$  is colliding with the HTP or not, respectively the safety clearance between areas of high  $Tu_z$  and the HTP. This gives valuable information on the risk of HTP buffet.

The turbulence intensity data is gathered by the PIV measurements. As introduced in subsection 3.2.3, the used PIV system is no actual time-resolving system. However, by recording a sufficient number of samples, one can gather datasets, which can be statistically analyzed. In the following, contour plots of the vertical turbulence intensity distribution are presented. Most of these  $Tu_z$ -plots show some scatter of regularly located spots in the low turbulence areas. These statistical artifact errors are due to a too low number of sample points. Nevertheless, the shapes of the high intensity turbulence areas are clearly observable. In the following plots, the low turbulence areas with  $Tu_z < 0.02$  are blanked. Figure 7-5a shows the vertical turbulence intensity distributions in plane x1 for BL, Figure 7-5b for CS with  $\delta_s = 30^\circ$ , Figure 7-6a for AS with  $\delta_s = 30^\circ$ , and Figure 7-6b for AAS with  $\delta_s = 30^\circ$ . The small circles filled with white color in these pictures represent the positions, where HWA was used to gather time-resolved velocity results.

For all configurations, one distinct high  $Tu_z$ -structure is observable inboard in plane x1, which is related to the nacelle, which is located upstream. The three spoiler-configurations feature a second high  $Tu_z$ -structure related to the respective devices. For this second structure, significantly larger areas of high  $Tu_z$  are found for both unconventional spoiler configurations AS and AAS compared to CS. The spoiler-related high turbulence area of AS and AAS is expanded in both vertical and lateral dimensions compared to the corresponding area of CS. This is different for plane x2.

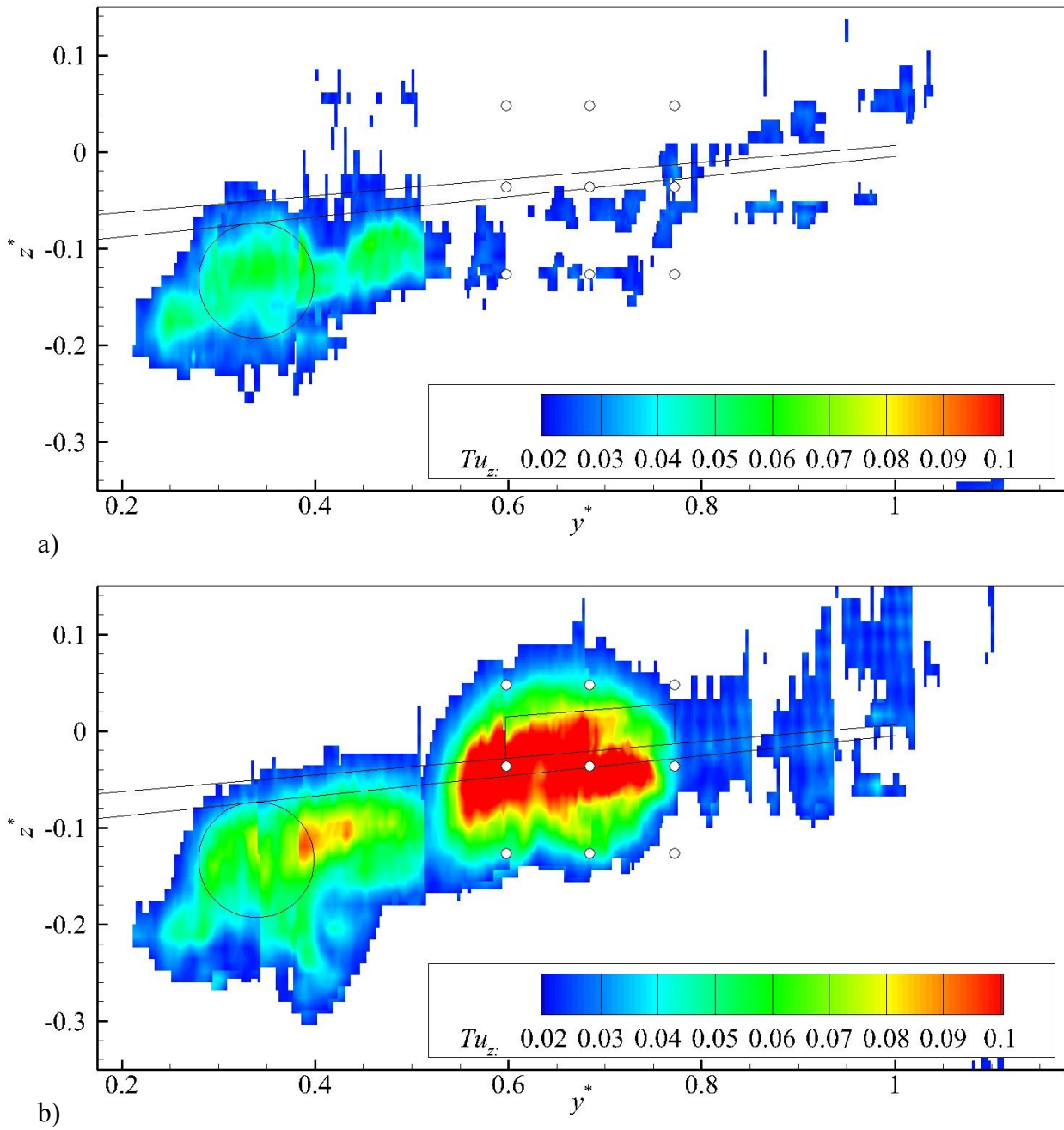


Figure 7-5: Vertical turbulence intensity distribution in plane  $x_1$  ( $x_1/b = 0.12$ ). a) BL; b) CS with  $\delta_s = 30^\circ$ .

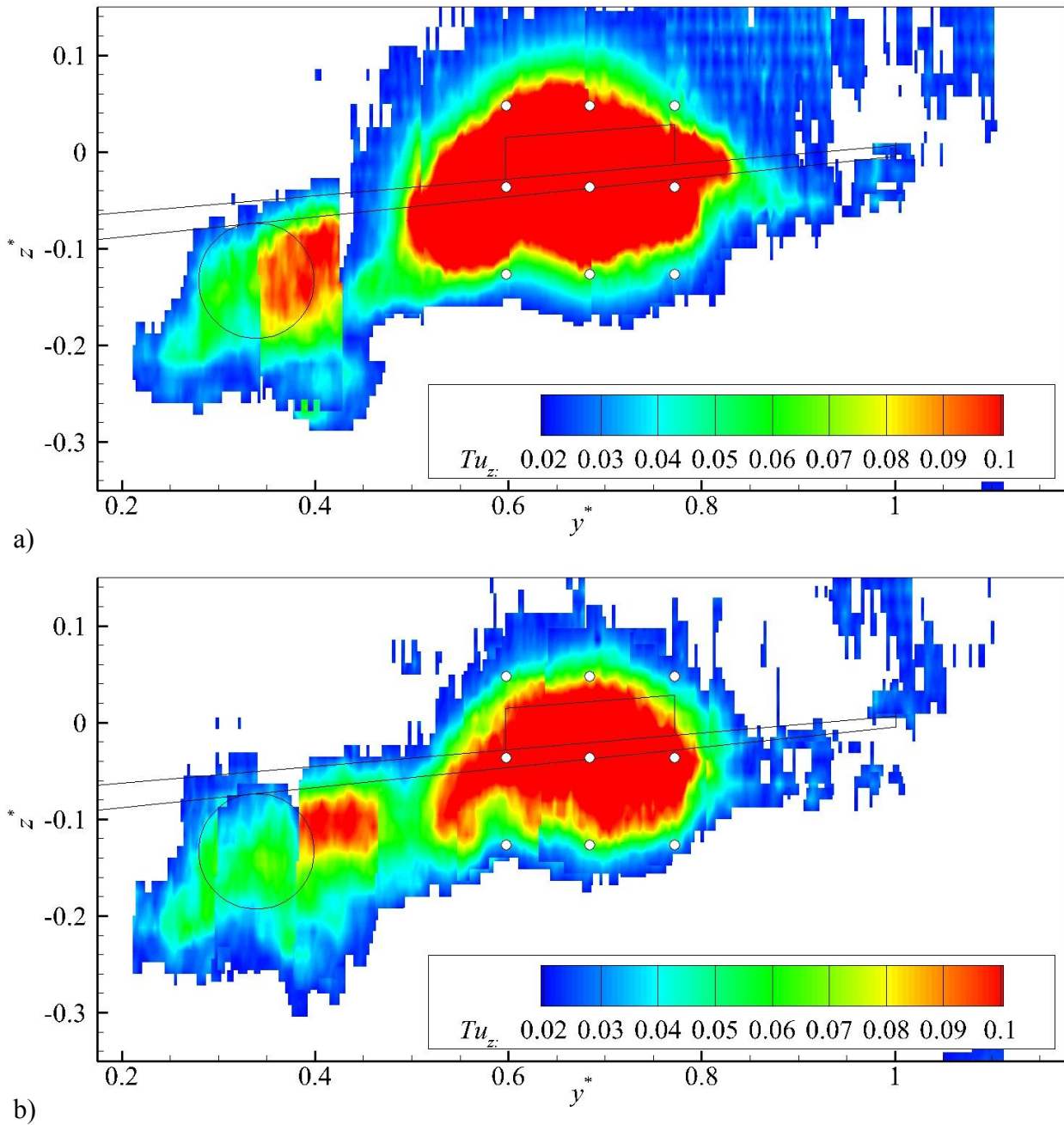


Figure 7-6: Vertical turbulence intensity distribution in plane  $x_1$  ( $x_1/b = 0.12$ ). a) AS with  $\delta_S = 30^\circ$ ; b) AAS with  $\delta_S = 30^\circ$ .

Figure 7-7 and Figure 7-8 show the distributions in the further downstream located plane  $x_2$ , which represents the position where the HTP's leading edge is located. In these pictures the area, where the HTP would be located is depicted by a red line. The measurement point of the HWA, which is most relevant to evaluate the risk for HTP buffet, namely the tip of the HTP, is marked with a red arrow. The results for this measurement position are discussed in section 7.3, exclusively.

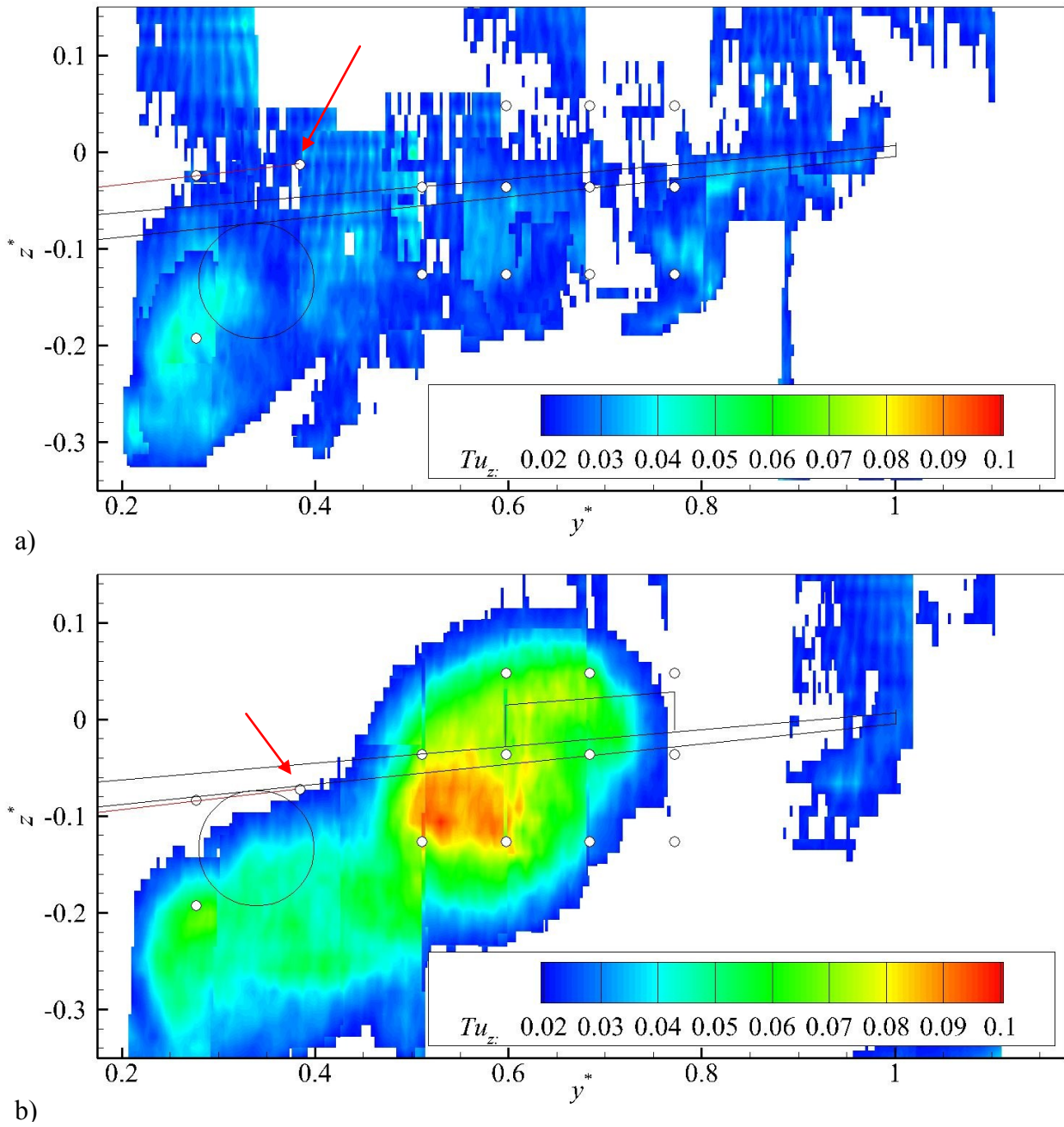


Figure 7-7: Vertical turbulence intensity distribution in plane  $x_2$  ( $x_2/b = 0.92$ ). a) BL; b) CS with  $\delta_\gamma = 30^\circ$ .

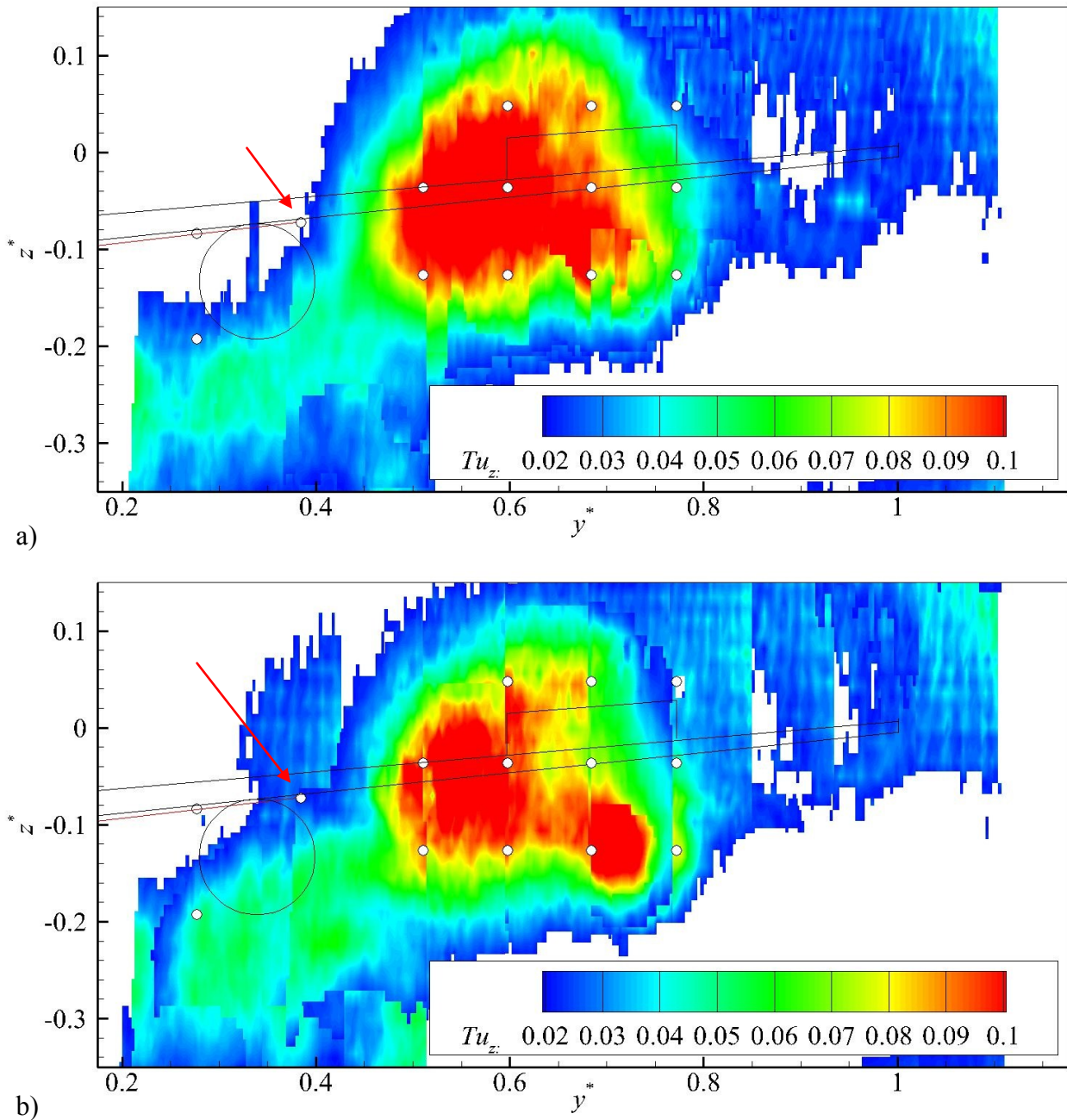


Figure 7-8: Vertical turbulence intensity distribution in plane x2 ( $x_2/b = 0.92$ ). a) AS with  $\delta_S = 30^\circ$ ; b) AAS with  $\delta_S = 30^\circ$ .

In plane x2, the  $Tu_z$ -areas related to the spoiler are, similarly to the results in x1, significantly larger for both unconventional spoiler configurations AS and AAS compared to CS. Other than in x1, in x2 the lateral extensions of these high turbulence areas are comparable to the lateral extension of the areas of the CS-configuration. However, the very same areas are vertically more elongated for AS and AAS compared to CS and have a different shape.

For all three spoiler cases, the area of high turbulence intensity,  $Tu_z \geq 0.1$ , is limited to lateral positions, which are outboard of the HTP's tip and thus the corresponding region of high turbulence intensity does not directly impinge on the HTP. This leads to the

conclusion that none of the three spoiler configurations poses a high danger relating HTP buffet for the investigated zero side slip flow conditions. There is only marginal difference in the potential for HTP buffet for the three different configurations. To further strengthen this conclusion the HWA data are discussed in the following section.

### 7.3 Spectral Analysis of Vertical Turbulence

The white color filled circles in the previous figures, which show the turbulence intensity distribution gathered by PIV (Figure 7-5 et seqq.) represent the positions, where HWA-measurements were carried out in the cross-flow planes. These positions were chosen to resolve the immediate wake region of the spoiler in plane  $x_1$  and  $x_2$ , as well as positions along the span of the HTP in plane  $x_2$ . One of the positions along the span of the HTP represents the tip of the HTP and is designated as TIP. It is marked by red arrows in Figure 7-7 and Figure 7-8. The other positions are located inboard from this position. It should be noted that the vertical positions of the measurement points along the HTP's span vary per configuration due to the fact that  $\alpha$  is adjusted for each configuration to maintain a constant lift coefficient of  $C_L = 1.5$ .

The wake produced by the air-brake devices potentially exhibits narrow-band concentrations or peaks of turbulent kinetic energy at characteristic frequencies attributed to the air-brake vortex shedding. This energy peak is commonly referred to as a "buffet peak". To identify such buffet peaks, a Fast Fourier Transformation (FFT) of the HWA data was carried out to obtain the power spectral density  $S$  as function of reduced frequency  $k = f \cdot c / U_\infty$ . The vertical component of the velocity fluctuation's power spectral density  $S_{w'}$  is the most significant component, when evaluating the influence of the wake generated by the device-deployment on strong excitation of structural HTP modes. For this reason, the following discussion focuses on this component, exclusively.

Figure 7-9 shows the results for the fluctuations of the vertical velocity  $w'$  at the measurement point TIP, which is located at the HTP's tip; Figure 7-9a for BL, Figure 7-9b for CS with  $\delta_S = 30^\circ$ , Figure 7-9c for AS with  $\delta_S = 30^\circ$ , and Figure 7-9d for AAS with  $\delta_S = 30^\circ$ . For the BL-case,  $S_{w'}$  is smaller than  $10^{-3}$  for all frequencies except a moderate peak at  $k = 2.5 \cdot 10^{-1}$  with a magnitude of  $S_{w'} = 2 \cdot 10^{-3}$ . All three spoiler cases show no significant peak at a specific frequency in the power spectral density analysis, but feature a broadband and moderate  $S_{w'}$ -distribution in the range from  $k = 1 \cdot 10^{-2}$  to  $k = 5$ . The maximum  $S_{w'}$  is thereby  $S_{w'} = 4 \cdot 10^{-3}$  for AAS with  $\delta_S = 30^\circ$ ,  $S_{w'} = 7 \cdot 10^{-3}$  for AS with  $\delta_S = 30^\circ$ , and  $S_{w'} = 1 \cdot 10^{-2}$  for CS with  $\delta_S = 30^\circ$ . For higher frequencies  $k \geq 2.5 \cdot 10^{-1}$ ,  $S_{w'}$  degrades monotonously in each case.

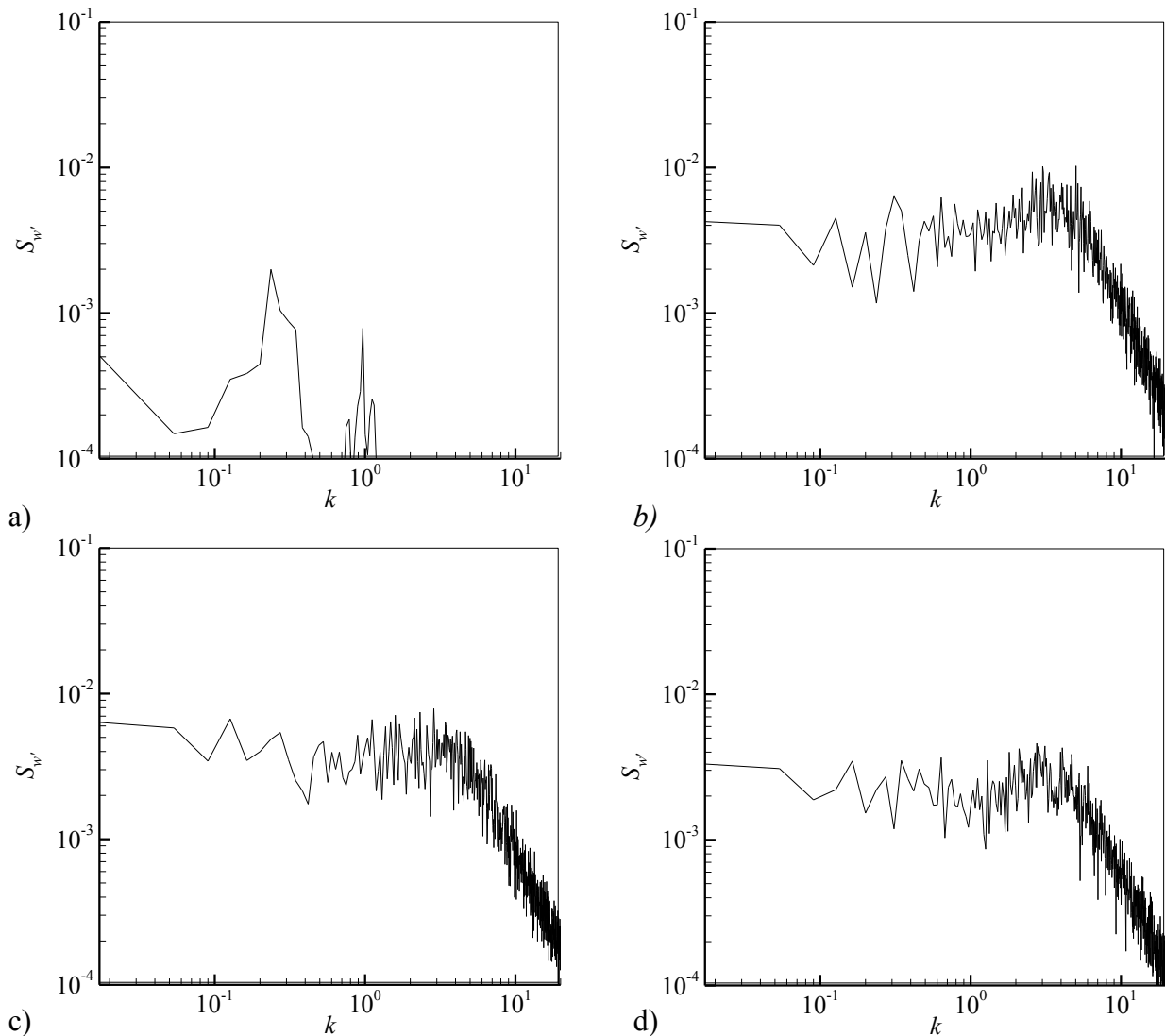


Figure 7-9: Spectral power density over reduced frequency distribution for measurement point TIP. a) BL; b) CS with  $\delta_S = 30^\circ$ ; c) AS with  $\delta_S = 30^\circ$ ; d) AAS with  $\delta_S = 30^\circ$ .

## 7.4 Synthesis

To sum up the wake investigations, the following conclusions can be drawn: The Conventional Spoiler (CS) as well as the Adverse Spoiler (AS) and Advanced Adverse Spoiler (AAS), each with a constant deployment angle, along with the Baseline (BL) are investigated for an angle of attack, which leads to a constant representative lift coefficient of  $C_L = 1.5$  for each configuration. The velocity distribution in the near wake as well as a statement about the influence of the spoiler type on a HTP-buffet hazard could be evaluated by the usage of the measurement techniques Stereo Particle Velocimetry (PIV), as well as Hot Wire Anemometry (HWA). The differences in the flow field of the model's near wake are comparably discussed. The evaluation of devices regarding buffet of the horizontal tail plane (HTP) is based on the turbulence intensity distribution in the near wake of the wing. This is accomplished on the one hand regarding the turbulence intensity

gathered from PIV-measurements and on the other hand by using the HWA-data to obtain the spectral turbulence distribution at selected points.

Based on these measurements, it can be concluded that all three investigated spoiler-configurations pose no risk of HTP-buffet for the zero side slip condition investigated here. As a matter of course, this also means that the two unconventional spoiler configurations, AS and AAS, hold no more risk of the excitation of structural modes of the HTP and thus HTP buffet compared to the CS-configuration. This is based on the finding, that a HTP would be located inboard of the high turbulence areas identified by the PIV-measurements and originating from the spoilers. This is the case despite the fact that the turbulent wake region is significantly larger for both investigated novel spoilers, AS and AAS, but the enlarged regions extend only in the vertical direction. The HWA-measurements confirm this just once more by showing moderate values of power spectral densities of vertical velocity fluctuations for all frequencies and all spoiler configurations, though higher values than for the BL-configuration. Thereby, the peak values are even lower for both AS- and AAS-configurations compared to the CS-configuration.

## 8. CONCLUSION

This conclusion summarizes the key findings of the inquiry and makes suggestions for possible further investigations.

Steep approach is recognised as a valid means to reduce perceived noise in airport surroundings. Other advantages associated with steep approach include the potential to increase airport landing capacities and the possibility to operate into airports surrounded by large buildings or mountains. Improvements to the aerodynamic performance of a Commercial Transport Aircraft (CTA) through steep approach enabling devices could also aid better lateral flight mechanics performance, reduced landing velocities and thus further reduce noise and decreased landing length. All these reasons justify efforts to scrutinize the aerodynamics of novel high-lift devices that potentially enable CTA to conduct steep approaches.

The configurations under investigation here have been: the Baseline-configuration (BL), namely, a standard landing configuration of a CTA without any air-brake device; a configuration fitted with a Conventional Spoiler (CS); two novel spoiler configurations, (a different novel spoiler on each one, but which cover the same base area as the CS); and two novel aileron device configurations (again, a different novel device on each one, and which replace the conventional aileron). The reason to develop and investigate devices that directly replace present devices is to minimize expenses through the integration of the novel devices in existing configurations. The novel spoilers are designated Adverse Spoiler (AS) and Advanced Adverse Spoiler (AAS); the designations for the novel aileron-devices are Deceleron (DC) and Split Aileron (SA). The aileron devices are multifunctional as they can be used not only as air brakes, but also to provide roll control and yaw control.

The methods underpinning the investigations were experimental and numerical. For the experiments, a detailed half-model of a CTA's high-lift devices in approach setting was used exclusively. This model was fitted successively with wind tunnel model parts of all the devices under investigation. The mounting of each device allowed various deflection-settings to be tested. Angle of attack was also varied in each configuration. Force measurements were carried out in the frame of the wind tunnel measurements to obtain the aerodynamic polars of the global aerodynamic coefficients for each configuration. Based on these measurements, the effect of the devices on the longitudinal aerodynamic coefficients and, consequently, the effectiveness of each configuration in terms of steep approach was evaluated. This evaluation incorporates the capability to increase the descent angle, as well as the capability to minimize the approach and descent velocities. As the main purpose of a CTA aileron is to provide roll control, the effectiveness of the novel

aileron devices' roll control was also evaluated and compared to the effectiveness of the conventional aileron. The effectiveness of the novel ailerons' yaw control was also evaluated so as to show their potential to be used as yaw control devices. The coefficients of the lateral motion at zero angle of yaw used for this evaluation were also gathered by the force measurements.

The experimental investigations reveal that no one of the investigated devices is the clear winner regarding steep approach capability. Actually, it depends on the concrete interval of values regarding the descent angle and approach velocity to be achieved. At the combination of the requests for a low additional descent angle combined with low approach velocities similar to the values for the BL, both the SA and DC are applicable. For higher descent angles, combined with some deficit in minimal approach velocity, the CS- and AAS-configurations are the preferable ones. The first novel device AS, which formed the original basis for this investigation, cannot compete in any range of value combinations of descent velocity and approach velocity deficit. For details of this finding, see the synthesis section 5.6. Regarding roll control, the analysis reveals that for low differential deflection angles, roll control levels for the novel aileron devices are of the same magnitude as the conventional aileron, but decrease significantly for higher differential deflection angles. It can be concluded that some of the novel aerodynamic devices under investigation are better suited for conducting steep approaches compared with conventional spoilers. This is found true for the various investigated requirements, which apply for aerodynamic devices of CTA.

The numerical investigations serve to provide insight into the flow-topology associated with the different devices. Their geometric complexity is reduced by only investigating the two-dimensional airfoil cuts which are located laterally at the middle of the spoiler width. The configurations comprise the BL-configuration as well as the configurations with CS, AS, and AAS. The numerical methods of choice are the Unsteady Reynolds Averaged Navier-Stokes (URANS) method with the SST-turbulence model and the Scale Adaptive Simulation (SAS) method. The former provides a good compromise between an affordable numerical effort and comparatively high accuracy; the latter, which needs a considerably higher computational effort, provides insight into the three-dimensional turbulence structure. To be able to make use of the SAS-method, the two-dimensional-geometry used for the URANS-simulations was extruded in the spanwise direction to become a two-and-half-dimensional geometry. To complement the numerical investigations, tufts were attached to the wind tunnel model used in the experimental campaigns. Photographs of the tufts were taken to make qualitative assessment of the near wall behavior of the flow possible. Combining the numerical investigation and tuft flow analysis made it possible to create sketches of the flow topology of each spoiler device. These are presented in the synthesis section 6.3.

Finally, the wake of the wind tunnel model wing both with and without novel and conventional spoilers was investigated. This provides a general understanding of the flow field in the wake. As unsteadiness in the wake is recognized as posing a potential threat to the HTP by inducing tail buffet phenomena, the results of the wake of the novel spoilers is therefore of additional interest. The experimental techniques of Stereo Particle Image Velocimetry (PIV) and Hot Wire Anemometry (HWA) were used to record the flow in the near wake of the BL-, CS-, AS-, and AAS-configurations. The former combines the distribution data of all three velocity components, thereby allowing for calculation of the mean flow and turbulence intensity of the flow. The latter is used to supplement the PIV-data with velocity measurements of high sample rates at selected positions. Spectral analyses deliver data sets of the power spectral density as a function of reduced frequency related to a particular spoiler-configuration. Two cross-flow planes were chosen for these wake-investigations: One immediately behind the wing, the other representing the leading edge of the horizontal tail plain (HTP), which is not included in the wind tunnel model. For each configuration, the angle of attack is adjusted for the wake investigations to set the lift-coefficient to a constant value of  $C_L = 1.5$ . Results from both measurement methods, PIV and HWA, lead to the principle conclusion that both unconventional spoiler configurations, AS and AAS, provide no more risk on the excitation of the HTP's structural modes, and thus to increasing the HTP buffet level compared to the CS-configuration.

With regard to suggestions for further work in the context of this project, alternatives to the investigated devices are perhaps the most obvious. This could be other passive devices or active systems, such as the actively blown flap. These offer great possibilities to increase the high-lift performance, especially with regard to maximum lift. The challenge facing application of this class of devices is legal certification. With the use of such systems it must be ensured that in case the active system fails, the high lift performance is still maintained in such a way that the aircraft can be operated safely.

The HTP buffet evaluation performed in this work is the beginning of a deeper analysis where the prediction of the actual buffet loads will be done. To predict buffet loads in future, a random gust response analysis, or PSD analysis, could be used as a basis.

The next logical step for future numerical research would be to use a complete and detailed three-dimensional configuration. More sophisticated methods, like the Large Eddy Simulation, could give further insight into the flow topology and, in particular, the turbulent structures associated with the configurations fitted with the conventional and novel devices.



# REFERENCES

- [1] *A. A. Lab. AN-1003 Hot-Wire & Film Anemometry Systems – User’s Manual*, A. A. Lab Systems Ltd., 1999.
- [2] Abbott, Ira H., von Doenhoff, Albert E. “Theory of Wing Sections, Including a Summary of Airfoil Data,” Dover ed., Dover Publications, Mineola, N.Y., 1959.
- [3] Adam, Mario, *Statistische Versuchsplanung und Auswertung (DoE Design of Experiments)*, lecture hand out, Fachhochschule Düsseldorf, faculty Maschinenbau und Verfahrenstechnik, 2004.
- [4] “Advisory Council for Aeronautics Research in Europe: 2008 Addendum to the Strategic Research Agenda Advisory Council for Aeronautics Research in Europe,” European Commission, Luxembourg, November 2008.
- [5] “Airbus A318 powered by CFM56 engines approved for steep approach,” *Airbus Press Release*, 23 November 2007, URL: <http://www.airbus.com/presscentre/pressreleases/press-release-detail/detail/airbus-a318-powered-by-cfm56-engines-approved-for-steep-approach> [cited October 2011].
- [6] “Aircraft Technology and Emissions,” *SBAC Aircraft Technology and Emissions, Aviation and Environment Briefing Paper*, Sustainable Aviation, SBAC, URL: <http://www.sustainableaviation.co.uk/images/stories/key%20documents/aircraft-technology-and-emissions-briefing-paper.pdf> [cited October 2010].
- [7] “Airport Operations,” London City Airport Consultative Committee, URL: <http://www.lcacc.org/operations/operations.html> [cited October 2010].
- [8] “Airports with Noise and Emissions Restrictions,” Boeing Co., URL: <http://www.boeing.com/commercial/noise/list.html> [cited September 2010].
- [9] Allen, Alexander, *Beeinflussung des Nachlaufwirbelsystems von Transportflugzeugen*, Dissertation, Technische Universität München, 2008.
- [10] Ansys Inc., *ANSYS CFX-Solver, Theory Guide*, Rel. 12.0, April 2009.
- [11] Ansys Inc., *Documentation for ANSYS ICEM CFD/AI\*Environment*, Rel. 11.0, 2007.
- [12] Antoine, N. E., Kroo, I. M., “Aircraft Optimization for Minimal Environmental Impact,” *Journal of Aircraft*, Vol. 41, No. 4, 2004, pp. 790 - 797.

- [13] Argüelles, P., Bischoff, M., Busquin, P., Droste, B.A.C., Sir Evans, R., Kröll, W., Lagardère, J-L., Lina, A., Lumsden, J., Ranque, D., Rasmussen, S., Reutlinger, P., Sir Robins, R., Terho, H., Wittlöv, A., "European Aeronautics: A Vision For 2020," European Commission, Luxembourg, January 2001.
- [14] Arnott, A., Neitzke, K. P., Agocs, J., Sammer, G., Schneider, G., Schröder, A., "Detailed Characterisation Using PIV of the Flow Around an Aerofoil in High Lift Configuration," *EUROPIV2 Workshop on Particle Image Velocimetry*, Springer, Berlin, 2003.
- [15] Aumann, P., Barnewitz, H., Schwarten, H., Becker, K., Heinrich, R., Roll, B., Galle, M., Kroll, N., Gerhold, Th., Schwamborn, D., Franke, M., "MEGAFLOW: Parallel complete aircraft CFD," *Parallel Computing Journal*, Vol. 27, 2001, pp. 415 - 440.
- [16] *BAe 146*, BAE Systems, Brochure, PM 047 August 2007.
- [17] Baragona, Marco, Bijl, Hester, van Tooren, Michel "Bubble Bursting and Laminar Separation Unsteadiness on a Multi-Element High Lift Configuration," *Flow, Turbulence and Combustion*, Vol. 71, No. 1-4, 2003, pp. 279 - 296.
- [18] Barth, T. J., Jespersen, D., "The Design and Application of Upwind Schemes on Unstructured Meshes," *27<sup>th</sup> Aerospace Sciences Meeting*, AIAA 89-0366, Reno, NV, 9-12 Jan 1989.
- [19] Becker, Ralf, King, Rudibert, Petz, Ralf, Nitsche, Wolfgang, "Adaptive Closed-Loop Separation Control on a High-Lift Configuration Using Extremum Seeking," *AIAA Journal*, Vol. 45, No. 6, June 2007, pp. 1382 - 1392.
- [20] Benat, J. S., Persol, A. G., *Engineering Applications of Correlation and Spectral Analysis*, John Wiley & Sons, New York, 1980.
- [21] Bertsch, Lothar, Dobrzynski, Werner, Guérin, Sébastien, "Tool Development for Low-Noise Aircraft Design," *Journal of Aircraft*, Vol. 47, No. 2, March – April 2010.
- [22] Bieler, H., Fischer, M., Emunds, R., Sutcliffe, M., "CAA in Industrial Environment: First Analysis of Noise Sources on a 2D High-Lift Profile at Airbus," *11<sup>th</sup> AIAA/CEAS Aeroacoustics Conference (26<sup>th</sup> AIAA Aeroacoustics Conference)*, AIAA-2005-2977, AIAA, Monterey, California, 2005.
- [23] Boeing Commercial Airplanes, "Airport Reference Code and Approach Speeds for Boeing Airplanes," *Airport Technology Report*, 8 February 2007, URL: <http://www.boeing.com/commercial/airports/faqs/arcandapproachspeeds.pdf> [cited October 2010].
- [24] Bohn, A. J., "Edge Noise Attenuation by Porous-Edge Extensions," AIAA Paper 1976-80, January 1976.
- [25] Bray, Bob, "Supersize Wings," *The Ingenia Magazine*, Iss. 31, June 2007.

- [26] Breitsamter, Christian, *Aerodynamik des Flugzeugs I – Profile*, Lecture hand out, Lehrstuhl für Aerodynamik – Technische Universität München, winter term 2009.
- [27] Breitsamter, Christian, *Aerodynamik des Flugzeugs II – Konfigurationen*, Lecture hand out, Lehrstuhl für Aerodynamik – Technische Universität München, summer term 2009, p. 96.
- [28] Breitsamter, Christian, *Nachlaufwirbelsysteme großer Transportflugzeuge - Experimentelle Charakterisierung und Beeinflussung*, Habilitation, Technische Universität München, 2007.
- [29] Breitsamter, Christian, *Strömungsphysik und Modellgesetze*, Lecture hand out, Lehrstuhl für Aerodynamik - Technische Universität München, summer term 2006, pp. 3 - 12.
- [30] Breitsamter, Christian, *Turbulente Strömungsstrukturen an Flugzeugkonfigurationen mit Vorderkantenwirbeln*, Dissertation, Technische Universität München, Herbert Utz Verlag Wissenschaft, 1997.
- [31] “British Airways 2008/09 Annual Report and Account,” URL: [https://batraveltrade.com/cms/global/microsites/ba\\_reports0809/pdfs/BA\\_AR\\_2008\\_09.pdf](https://batraveltrade.com/cms/global/microsites/ba_reports0809/pdfs/BA_AR_2008_09.pdf) [cited October 2010].
- [32] Bruun, H. H., *Hot wire anemometry – Principles and signal analysis*, Oxford University Press Inc., New York, 2002.
- [33] Burnham, D. C., “B-747 Vortex Alleviation Flight Tests: Ground-Based Sensor Measurements,” Report No. DOT-FAA-RD-81-99, February 1982.
- [34] Butler, R. W., “Separation Characteristics and Aerodynamic Load Data for the KM-826P, BLU-27, and 450-GAL Fuel Tank in the Vicinity of the A-10A Aircraft at Subsonic Speeds,” ASD/WPAFB USAF report, AEDC-TR-71-207, October 1971.
- [35] “Certification Specifications for Large Aeroplanes CS-25,” Amendment 10, European Aviation Safety Agency, 23 December 2010, pp. 1-B-10 – 1-B-11.
- [36] “Certification Specifications for Large Aeroplanes CS-25,” Amendment 10, European Aviation Safety Agency, 23 December 2010, p. 1-B-12.
- [37] Chen, Jerry M., Fang, Yuan-Cheng, “Strouhal numbers of inclined flat plates,” *Journal of Wind Engineering and Industrial Aerodynamics*, Vol. 61, 1996, pp. 99 – 112.
- [38] Chieramonte, Jean-Yves, *AWIATOR, WP 1: Far Field Impact, Task 1.2: Airbrake Wake Optimisation*, Final Review, Toulouse, 26/27 June 2007.
- [39] Choudhari, M. M., Lockard, D. P., Macaraeg, M. G., Singer, B. A., Streett, C. L., Neubert, G. R., Stoker, R. W., Underbrink, J. R., Berkman, M. E., Khorrami, M. R., Sadowski, S. S., “Aeroacoustic Experiments in the Langley Low-Turbulence Pressure Tunnel,” NASA TM-2002-211432, February 2002.

- [40] Chow, L. C., Mau, K., Remy, H., "Landing Gears and High Lift Devices Airframe Noise Research," *8<sup>th</sup> AIAA/CEAS Aeroacoustics Conference and Exhibit*, AIAA-2002-2408, AIAA, Breckenridge, Colorado, 17 - 19 June 2002.
- [41] Clancy, L.J., *Aerodynamics*, 1<sup>st</sup> ed., Pitman Publishing Limited, London. 1975, Sub-section 11.19(a).
- [42] Clarke, J. P., Ho, N. H., Ren, L., Brown, J. A., Elmer, K. R., Tong, K. O., Wat, J. W., "Continuous Descent Approach: Design and Flight Test for Louisville International Airport," *Journal of Aircraft*, Vol. 41, No. 5, 2004, pp. 1054 – 1066.
- [43] "CLEAN SKY JTI," Clean Sky Joint Undertaking, URL: <http://www.cleansky.eu> [cited October 2010].
- [44] Cockburn, Barbara, "First commercial Dornier 328 flight lands at London City Airport from Reykjavik," *Flightglobal.com*, 3 August 2007, <http://www.flightglobal.com/articles/2007/08/03/215929/picture-first-commercial-dornier-328-flight-lands-at-london-city-airport-from-reykjavik.html> [cited October 2010].
- [45] Coleman, Hugh W., Steele, W. Glenn, Jr., *Experimentation and Uncertainty Analysis For Engineers*, John Wiley & Sons, Inc, 1<sup>st</sup> Edition, 1989, p. 35.
- [46] Collins, Peter, "FLIGHT TEST: Piaggio Avanti II - Hard to beat," *Flight International*, 1 November 2005, URL: <http://www.flightglobal.com/articles/2005/11/01/202480/hard-to-beat.html> [cited October 2010].
- [47] Crandall, Ronald E., Glenn, John E., US Patent Application for an "Aileron, Flap, and Dive brake," No. 2,612,329, patented on 30 September 1952.
- [48] Croom, D. R., "Low-speed wind-tunnel parametric investigation of flight spoilers as trailing-vortex-alleviation devices on a transport aircraft model," NASA-TP-1419, 1979.
- [49] Croom, D. R., "The development and use of spoilers as vortex attenuators," Document ID: 19780004084, NASA.
- [50] Croom, D. R., Vogler, R. D., Williams, G. M., "Low-speed wind-tunnel investigation of flight spoilers as trailing-vortex-alleviation devices on a medium range wide-body tri-jet airplane model," NASA-TN-D-8360, 1976.
- [51] de Bruin, Anton C., Tuinstra, Marthijn, "Aircraft Noise Simulation Environment, Suitable for Development of Noise Abatement Procedures," *27<sup>th</sup> Congress of the International Council of the Aeronautical Sciences*, edited by I. Grant, ICAS 2010-5.1.1, Nice, France, 19 - 24 September 2010.
- [52] Deck, Sebastien, "Zonal-Detached-Eddy Simulation of the Flow Around a High-Lift Configuration," *AIAA Journal*, Vol. 43, No. 11, November 2005.

- [53] DIN 9300-2:1990-10, *Aerospace; concepts, quantities and symbols for flight dynamics; motions of the aircraft and the atmosphere relative to the earth*, Norm ISO 1151-2, 1990.
- [54] Dobrzynski, W., “Almost 40 Years of Airframe Noise Research: What Did We Achieve?,” *Journal of Aircraft*, Vol. 47, No. 2, March – April 2010, pp. 353 - 367.
- [55] Doyle, Andrew, “Fokker will challenge Avro's jet monopoly at London City,” *Flight International*, 21 June 1995, URL: <http://www.flightglobal.com/articles/1995/06/21/25554/fokker-will-challenge-avros-jet-monopoly-at-london.html> [cited October 2010].
- [56] Earnshaw, P. B., Green, A. R., Hardy, B. C., Jelly, A. H., “A Study of the Use of Half-Models in High-Lift Wind-Tunnel Testing,” AGARD CP-515, Neuilly-sur-Seine, France, September 1993, pp. 20.1 - 20.9.
- [57] Egorov, Y., Menter, F. R., Lechner, R., Cokljat, D., “The Scale-Adaptive Simulation Method for Unsteady Turbulent Flow Predictions. Part 2: Application to Complex Flows,” *Journal on Flow, Turbulence and Combustion*, Vol. 85, No. 1, 2010, pp. 139 - 165.
- [58] “Farnborough 2004 - A318 displays steep approach,” *Flight International*, 27 July 2007, URL: <http://www.flightglobal.com/articles/2004/07/27/185047/farnborough-2004-a318-displays-steep-approach.html> [cited October 2010].
- [59] “Farnborough 2008: Indian carrierborne MiG handover inches closer,” *Flight International*, 14 July 2008, URL: <http://www.flightglobal.com/articles/2008/07/14/225339/farnborough-2008-indian-carrierborne-mig-handover-inches.html> [cited October 2010].
- [60] “Federal Aviation Regulations, Part 25 – Section 119 - Landing Climb: All Engines Operative, Part 25 – Section 121 - Climb: One Engine Inoperative,” Federal Aviation Administration, 9 October 2007.
- [61] “Federal Aviation Regulations - Part 25 – Section 125 – Landing,” Federal Aviation Administration, 9 October 2007.
- [62] “Federal Aviation Regulations - Part 25 – Section 723 - Subpart D-Design and Construction Landing Gear” Federal Aviation Administration, 15 June 2001.
- [63] Filippone, Antonio, “Inverted Jet Spoilers for Aerodynamic Control,” *Journal of Aircraft*, Vol. 46, No. 4, July–August 2009.
- [64] Filippone, Antonio, “Steep-Descent Maneuver of Transport Aircraft,” *Journal of Aircraft*, Vol. 44, No. 5, 2007, pp. 1728 - 1739.
- [65] Fink, M. R., Bailey, D. A., “Model Tests of Airframe Noise Reduction Concepts,” AIAA Paper 1980-0979, June 1980.

- [66] Fisher, David F., Meyer, Robert R. jun., "Flow Visualization Technique for Flight Research," NASA technical memorandum 100455, October 1988, p. 20-5.
- [67] Flaig, A., Hilbig, R., "High-Lift Design for Large Civil Aircraft," *High-Lift System Aerodynamics Conference*, AGARD-CP-515, Neuilly-sur-Seine, France, September 1993, pp. 31-1 – 31-12.
- [68] Flaig, A., Hilbig, R., "High-Lift Design for Large Civil Aircraft," *High-Lift System Aerodynamics Conference*, AGARD-CP-515, Neuilly-sur-Seine, France, September 1993, p. 31-9.
- [69] Flaig, A., Hilbig, R., "High-Lift Design for Large Civil Aircraft," *High-Lift System Aerodynamics Conference*, AGARD-CP-515, Neuilly-sur-Seine, France, September 1993, p. 31-10.
- [70] Flaig, A., Hilbig, R., "High-Lift Design for Large Civil Aircraft," *High-Lift System Aerodynamics Conference*, AGARD-CP-515, Neuilly-sur-Seine, France, September 1993, p. 31-12.
- [71] "Flight Operations Briefing Notes - Approach Techniques, Aircraft Energy Management during Approach," Airbus, URL: <http://www.britflight.com/wingfiles/approach/energymanage.pdf> [cited January 2010].
- [72] Franssen, E. A. M., van Wiechen, C. M. A. G., Nagelkerke, N. J. D., Lebet, E., "Aircraft noise around a large international airport and its impact on general health and medication use," *Journal of Occupational & Environmental Medicine*, Vol. 61, 2004, pp. 405 – 413.
- [73] Fröhlich, Jochen, von Terzi, Dominic, "Hybrid LES/RANS Methods for the Simulation of Turbulent Flows," *Progress in Aerospace Sciences*, Vol. 44, Iss. 5, July 2008, pp. 349 - 377.
- [74] Fronista, G. L., Bradbury, G., "An electromechanical actuator for a transport aircraft spoiler surface," *32nd Intersociety Energy Conversion Engineering Conference*, IECEC-97, Vol. 1, 27 July - 1 August 1997, Honolulu, HI, USA, pp. 694 - 698.
- [75] Fujino, Michimasa, "Design and Development of the HondaJet," *Journal of Aircraft*, Vol. 42, No. 3, May–June 2005, pp. 755 - 764.
- [76] Geister, R., "Flight testing of steep precision approaches based on GBAS," *27<sup>th</sup> Congress of the International Council of the Aeronautical Sciences*, edited by I. Grant, ICAS 2010-11.11.2, Nice, France, 19 - 24 September 2010.
- [77] Gerzanics, Mike, "FLIGHT TEST: C-27J - No small measure," *Flight International*, 24 August 2004, URL: <http://www.flightglobal.com/articles/2004/08/24/186528/no-small-measure.html> [cited October 2010].
- [78] Girvin, Raquel, "Aircraft noise-abatement and mitigation strategies," *Journal of Air Transport Management*, Vol. 15, 2009, pp.14 – 22.

- [79] Gliebe, Philip, "GE Expectations for the NASA Quiet Aircraft Technology Program," *QAT Workshop*, NASA, Dallas, TX, 2000. <http://www.aeronautics.nasa.gov/events/encompat/qat/gliebe/gliebe.ppt> [cited October 2010].
- [80] Goldston, Bill, "Embraer Receives Steep Approach Certification for London Airport," *AvStop.com - Aviation Online Magazine*, 3 February 2010, URL: [http://avstop.com/news\\_feb\\_2010/embraer\\_receives\\_steep\\_approach\\_certification\\_for\\_london\\_airport.htm](http://avstop.com/news_feb_2010/embraer_receives_steep_approach_certification_for_london_airport.htm) [cited October 2010].
- [81] Good, Mark S., Viigen, Paul M., Gitnes, Seth E., Glynn, Michael Thomas, US Patent for "Aircraft Wing Systems for Providing Differential Motion to Deployable Lift Devices," Patent No. 7,494,094, Date of Patent 24 February 2009.
- [82] Grawunder, Moritz, *Anwendung eines Stereo-PIV-Messsystems auf wirbeldominierte Strömungen*, semester thesis, AER-2007/6, Technische Universität München - Lehrstuhl für Aerodynamik, 2007.
- [83] Gray, Peter, "Bigger brother," *Flight International*, 4 February 2003, URL: <http://www.flightglobal.com/articles/2003/02/04/161280/bigger-brother.html> [cited October 2010].
- [84] Gray, Peter, "Stability with style," *Flight International*, 25 January 1995, URL: <http://www.flightglobal.com/articles/1995/01/25/22505/stability-with-style.htm> [cited October 2010].
- [85] Gray, Peter, "Vertical virtuality," *Flight International*, 13 March 1996, URL: <http://www.flightglobal.com/articles/1996/03/13/17653/vertical-virtuality.html> [cited October 2010].
- [86] Griffin, Owen M., "A universal Strouhal number for the 'locking-on' of vortex shedding to the vibrations of bluff cylinders," *Journal of Fluid Mechanics*, Vol. 86, Part 3, 1978, p. 601.
- [87] Grosche, F., "A Body for Location in a Fluid," United Kingdom Patent No. 1541108, June 1975.
- [88] "Growth in Airport Noise Restrictions," Boeing Co., URL: <http://www.boeing.com/commercial/noise/restrictions.pdf>, [cited 09 April 2010].
- [89] Haftmann, B., Debbeler, F.-J., Gielenf, H., "Takeoff Drag Prediction for Airbus A300-600 and A310 Compared with Flight Test Results," *Journal of Aircraft*, Vol. 25, No. 12, 1988, p. 1089.
- [90] Haines, A. B., "The Contribution of Aerodynamics to Advances in Transport Aircraft Design," *Physics in Technology Journal*, Vol. 13, Northern Ireland, 1982.

- [91] Hallock, J. N., Burnham, D. C., “Decay Characteristics of Wake Vortices from Jet Transport Aircraft,” *35<sup>th</sup> Aerospace Sciences Meeting and Exhibit*, AIAA-1997-60, AIAA, Reno, NV, 6 - 9 January 1997.
- [92] Hellsten, Antti, “New Advanced  $k-\omega$  Turbulence Model for High-Lift Aerodynamics,” *AIAA Journal*, Vol. 43, No. 9, September 2005, pp. 1857 - 1869.
- [93] Hileman, J. I., Reynolds, T. G., de la Rosa Blanco, E., Law, T. R., Thomas, S., “Development of Approach Procedures for Silent Aircraft,” *45<sup>th</sup> AIAA Aerospace Sciences Meeting and Exhibit*, AIAA-2007-451, AIAA, Reno, Nevada, 8 – 11 January 2007.
- [94] Hopkins, Harry, “A better pace-setter,” *Flight International*, 8 November 1995, URL: <http://www.flightglobal.com/articles/1995/11/08/21159/a-better-pace-setter.html> [cited October 2010].
- [95] International Organization for Standardization, *Standard Atmosphere*, ISO 2533, 1975.
- [96] Jameson, Antony, “Optimum Transonic Wing Design Using Control Theory,” URL: <http://aero-comlab.stanford.edu/Papers/jameson.gottingen.pdf> [cited October 2010].
- [97] Jung, Ulrich, Breitsamter, Christian, “Aerodynamics of Multifunctional Transport Aircraft Devices,” *28<sup>th</sup> AIAA Applied Aerodynamics Conference*, AIAA-2010-4949, AIAA, 28 June – 1 July 2010, Chicago, USA.
- [98] Jung, Ulrich, Breitsamter, Christian, “Aerodynamics of Transport Aircraft Spoiler Solutions,” *CEAS/KATnet II Conference on Key Aerodynamic Technologies*, Bremen, Germany, 12 - 14 May 2009.
- [99] Jung, Ulrich, Breitsamter, Christian, “Experimental and numerical investigations of commercial transport aircraft aerodynamics during approach,” *International Symposium on Simulation of Wing and Nacelle Stall*, Braunschweig, Germany, 22 – 23 June 2010.
- [100] Jung, Ulrich, Breitsamter, Christian, “Experimentelle Untersuchung des Einflusses der Triebwerksgondelgeometrie auf die Aerodynamik einer Verkehrsflugzeugkonfiguration,” *Deutscher Luft- und Raumfahrtkongress*, DLRK2008-81176, Darmstadt, 23 - 25 September 2008.
- [101] Kaminski-Morrow, David, “Air Berlin 737 simulates satellite approaches to Frankfurt,” *Air Transport Intelligence news*, 6 September 2010, URL: <http://www.flightglobal.com/articles/2010/09/06/347032/air-berlin-737-simulates-satellite-approaches-to-frankfurt.html> [cited October 2010].
- [102] Kaminski-Morrow, David, “Authorities clear ATR 72 for London City operations,” *Air Transport Intelligence news*, 10 February 2009, URL: <http://www.flightglobal.com/articles/2009/02/10/322337/authorities-clear-atr-72-for-london-city-operations.html> [cited October 2010].

- [103] Kaminski-Morrow, David, "Slow approach led Swiss RJ to strike tail at London City," *Air Transport Intelligence news*, 14 August 2008, URL: <http://www.flightglobal.com/articles/2008/08/14/314786/slow-approach-led-swiss-rj-to-strike-tail-at-london.html> [cited October 2010].
- [104] Khare, Abhishek, Baig, Raashid, Ranjan, Rajesh, Shah, Stimit, Pavithran, S., Nikam, Kishor, Moitra, Anutosh, "Computational Simulation of Flow Over a High Lift Trapezoidal Wing," *International Journal of Aerospace Innovations*, Vol. 1, No. 4, December 2009, pp. 189 - 199.
- [105] Kempe, Tobias, *Strömungssimulation für Ingenieurwissenschaften*, lecture hand-out, winter term 2009, chapter 4.
- [106] Kiefner, Bernhard, "HIT - Fortschrittliche Hochauftriebstechnologien und -konzepte," URL: [http://www.dlr.de/pt-lf/Portaldata/50/Resources/dokumente/verbuende-lufo/VUE\\_2007\\_HIT.pdf](http://www.dlr.de/pt-lf/Portaldata/50/Resources/dokumente/verbuende-lufo/VUE_2007_HIT.pdf) [cited October 2010].
- [107] Kingsley-Jones, Max, "As Airbus A350 takes shape, can it avoid the A380's troubles?," *Flight International*, 8 July 2008, URL: <http://www.flightglobal.com/articles/2008/07/08/225120/as-airbus-a350-takes-shape-can-it-avoid-the-a380s.html> [cited October 2010].
- [108] Kirschstein, Stefan, *Identifizierung flugdynamischer Kenngrößen*, Dissertation, Maschinenwesen Faculty, RWTH Aachen, 21 January 2005, p. 69.
- [109] Klement, Péter, *Vergleich verschiedener Turbulenzmodelle zur Berechnung realer Strömungen in Laufrädern*, Herbert Utz Verlag, München, 1999.
- [110] Knopp, Tobias, *Turbulenzmodellierung*, Lecture hand out, Institut für Aerodynamik und Strömungstechnik, Abteilung C<sup>2</sup>A<sup>2</sup>S<sup>2</sup>E, winter term 2008.
- [111] Landman, Drew, Alvarez, Julian, Blackburn, Spiros, Ash, Robert, "Wind Tunnel Testing of the Wright Brothers Model B Airfoil," *Proceedings of the 39<sup>th</sup> Aerospace Sciences Meeting and Exhibit*, AIAA-2001-0310, AIAA, Reno, NV, 8-11 January 2001.
- [112] Lauterbach, A., Ehrenfried, K., Koop, L., "Array Measurements in Wind Tunnels With Open Test Sections," *2<sup>nd</sup> Berlin Beamforming Conference*, BeBeC-2008-09, 19-20 February 2008.
- [113] Learmount, David, "Global airline accident review of 2009," *Flight International*, 11 January 2010, URL: <http://www.flightglobal.com/articles/2010/01/11/336920/global-airline-accident-review-of-2009.html> [cited October 2010].
- [114] Lewis, Paul, "Embraer 170 gets airbrake for steep approaches," *Flight International*, 29 October 2002, URL: <http://www.flightglobal.com/articles/2002/10/29/156759/embraer-170-gets-airbrake-for-steep-approaches.html> [cited October 2010].

- [115] Liu, Sandy, "FAA Operational Evolution Plan (OEP): Version 8 – CDA Core & Ring elements," *Continuous Descent Arrivals (CDA) Workshop #2*, Atlanta, 18 April 2006.
- [116] Lockard, David P., Choudhari, Meelan M., "Noise Radiation from a Leading-Edge Slat," *15<sup>th</sup> AIAA/CEAS Aeroacoustics Conference (30<sup>th</sup> AIAA Aeroacoustics Conference)*, AIAA-2009-3101, AIAA, Miami, Florida, 11 - 13 May 2009.
- [117] Lord Wesley, K., "Aircraft Noise Source Reduction Technology," *Airport Noise Symposium*, Palm Springs, CA, 2 March 2004.
- [118] Mani, M., Willhite, P., Ladd, J., "Performance of one-equation turbulence models in CFD applications," *26<sup>th</sup> Fluid Dynamics Conference*, AIAA-1995-2221, San Diego, CA, 19 - 22 June 1995.
- [119] Menter, F. R., "Two-Equation Eddy-Viscosity Turbulence Models for Engineering Applications," *AIAA Journal*, Vol. 32, No. 8, 1994, pp. 1598 – 1605.
- [120] Menter, F. R., Egorov, Y., "A Scale-Adaptive Simulation Model using Two-Equation Models," *Proceedings of the 43rd AIAA Aerospace Sciences Meeting*, AIAA 2005-1095, Reno, USA, 2005.
- [121] Menter, F. R., Egorov, Y., "The scale-adaptive simulation method for unsteady turbulent flow predictions. Part 1: theory and model description," *Journal on Flow, Turbulence and Combustion*, Vol. 85, No. 1, 2010, pp. 113 - 138.
- [122] Mertol, Bertol Anil, "An Airbrake Design Methodology for Steep Approaches," *15<sup>th</sup> DGLR Symposium of STAB- International Symposium of the German working Committee of Fluid Mechanics*, STAB06-M071, DGLR, Darmstadt, Germany, 2006.
- [123] Mertol, Bertol Anil, WIPO Patent Application for a "Lifting wing with adjustable Spoiler," No. WO/2008/151760, publication date 18 December 2008.
- [124] Merzkirch, Wolfgang, *Flow Visualization*, Academic Press, London, 1987.
- [125] "Messtechnik," *Institute of Aerodynamics - Technische Universität München*, [website], URL: <http://www.aer.mw.tum.de/windkanal/MT.de.php> [cited 01 November 2010]
- [126] Moir, I. R. M., "Measurements on a two-dimensional aerofoil with high-lift devices," AGARD-AR-303 Vol. 2, Hull, Canada, August 1994, p. A2-8.
- [127] Moores, Victoria, "Sukhoi Superjet Russian regional jet to have steep-approach capability for airports such as London City," *Flight International*, 10 October 2006, URL: <http://www.flightglobal.com/articles/2006/10/10/209735/sukhoi-superjet-russian-regional-jet-to-have-steep-approach-capability-for-airports-such-as-london.html> [cited October 2010].

- [128] Moxon, Julian, "New identity," *Flight International*, 14 July 1999, URL: <http://www.flightglobal.com/articles/1999/07/14/53920/new-identity.html> [cited October 2010].
- [129] Murayama, Mitsuhiro, Lei, Zhong, Mukai, Junichi, Yamamoto, Kazuomi, "CFD Validation for High-Lift Devices: Three-Element Airfoil," *Trans. Japan Soc. Aero. S Sci.*, Vol. 49, Iss. 163, 2006, pp. 40 - 48.
- [130] National Aeronautics and Space Administration, "NASA's Quiet Aircraft Technology Program Fact Sheet," FS-2002-09-73-LaRC, 2002, URL: [http://www.nasa.gov/centers/langley/pdf/70882main\\_FS-2002-09-73-LaRC.pdf](http://www.nasa.gov/centers/langley/pdf/70882main_FS-2002-09-73-LaRC.pdf) [cited November 2010].
- [131] Neise, W., Dobrzynski, W., Isermann, U., König, R., Claßen, A. B., Bischoff, G., "Strategien zur Lärminderung an der Quelle unter Einschluss operationeller Möglichkeiten, speziell für den Nachtflug," *Research project report*, FE-No. L-3/2004-50.0307/2004, URL: <http://www.fv-leiserverkehr.de/pdf-dokumenten/BMVBS/Bericht%20BMVBS%20100225.pdf> [cited October 2010].
- [132] Norberg, C., "Flow around rectangular cylinders: Pressure forces and wake frequencies," *Journal of Wind Engineering and Industrial Aerodynamics*, Vol. 49, 1993, pp. 187 – 196.
- [133] Ostrower, Jon, "Green and versatile," *Flight International*, 8 July 2008, URL: <http://www.flightglobal.com/articles/2008/07/08/225112/green-and-versatile.html> [cited October 2010].
- [134] Passchier-Vermeer, W., Passchier, Wim. F., "Noise exposure and public health," *Journal of Environmental health perspectives*, Vol. 108 Suppl. 1, March 2000, pp. 123 - 31.
- [135] Pfennig, Malte, Thielecke, Frank, "Implementation of a Modelica Library for Simulation of High-Lift Drive Systems," *Proceedings Modelica 2008*, Bielefeld, Germany, 3 - 4 March 2008.
- [136] Phelan, Michael, "Airbus adapts A320 for Florence," *Flight International*, 9 September 2003, URL: <http://www.flightglobal.com/articles/2003/09/09/171000/airbus-adapts-a320-for-florence.html> [cited October 2010].
- [137] Phillips, W. F., *Mechanics of Flight*, 1<sup>st</sup> ed., John Wiley & Sons Inc., Hoboken, NJ, 2004.
- [138] Pohl, Ulrich, Renken, Jürgen, European Patent for a "Flaps system for aircraft wing," EP19860108915, Publication 4 January 1987.
- [139] Pompl, W., *Luftverkehr*, 5<sup>th</sup> ed., Springer Verlag, Berlin, 2007.
- [140] Pototzky, Anthony S., Moses A., Robert W., "A Method to Analyze Tail Buffet Loads of Aircraft," *RTO AVT Symposium on Flow-Induced Unsteady Loads and the Impact on Military Applications*, RTO-MP-AVT-123, Budapest, Hungary, 25 - 29 April 2005.

- [141] Rae, W. H., Pope, A., *Low Speed Wind Tunnel Testing*, 3<sup>rd</sup> ed., John Wiley & Sons Inc., New York, 1984, p. 11.
- [142] Rakhshani, B., Filippone, A., "Large-Eddy Simulation for Aerodynamic Noise from High-Lift Device," 47<sup>th</sup> *AIAA Aerospace Sciences Meeting Including The New Horizons Forum and Aerospace Exposition*, AIAA-2009-0281, AIAA, Orlando, Florida, 5 - 8 January 2009.
- [143] Rakhshani, B., Filippone, A., "Three-Dimensional CFD Analysis of Slat Noise," 46<sup>th</sup> *AIAA Aerospace Sciences Meeting and Exhibit*, AIAA-2008-0015, AIAA, Reno, Nevada, 7 - 10 January 2008.
- [144] "Reach for the ground," *Flight International*, 12 March 1997, URL: <http://www.flightglobal.com/articles/1997/03/12/137/reach-for-the-ground.html> [cited October 2010].
- [145] Recksiek, Martin, "Hochauftriebssysteme - von der Flugzeugkonfiguration zur Systementwicklung," *Presentations of DGLR-Bezirksgruppe Hamburg*, Hamburg, 16 December 2004.
- [146] Reckzeh, Daniel, Hansen, Heinz, "High Reynolds-Number Wind tunnel Testing for the Design of Airbus High-Lift Wings," in *New Results in Numerical and Experimental Fluid Mechanics V*, Notes on Numerical Fluid Mechanics and Multidisciplinary Design, edited by Rath, Hans-Josef and Holze, Carsten and Heinemann, Hans-Joachim and Henke, Rolf and Hönlinger, Heinz, Springer Berlin / Heidelberg, Vol. 92, 2006.
- [147] Ren, L., "Flight-Test Evaluation of the Tool for Analysis of Separation and Throughput," *Journal of Aircraft*, Vol. 45, No. 1, January – February 2008.
- [148] Rizzi, Arthur, Jirásek, Adam, Lamar, John E., Crippa, Simone, Badcock, Kenneth J., Boelens, Okko J., "Lessons Learned from Numerical Simulations of the F-16XL Aircraft at Flight Conditions," *Journal of Aircraft*, Vol. 46, No. 2, March–April 2009, pp. 423 - 441.
- [149] Rudnik, R., Germain, E., "Reynolds Number Scaling Effects on the European High-Lift Project Configurations," *Journal of Aircraft*, Vol. 46, No. 4, July–August 2009, pp. 1140 - 1151.
- [150] "Saab evolves 2000 for Darwin," *Flight International*, 3 August 2004, URL: <http://www.flightglobal.com/articles/2004/08/03/185356/saab-evolves-2000-for-darwin.html> [cited October 2010].
- [151] Sakaliyski, K. D., Hileman, J. I., Spakovszky, Z. S. "Aero-Acoustics of Perforated Drag Plates for Quiet Transport Aircraft," 45<sup>th</sup> *AIAA Aerospace Sciences Meeting and Exhibit*, AIAA 2007-1032, AIAA, Reno, Nevada, 8 - 11 January 2007.
- [152] Sarfield, Kate, "VistaJet seeks to expand reach," *Flight International*, 14 July 2008, URL: <http://www.flightglobal.com/articles/2008/07/14/225801/vistajet-seeks-to-expand-reach.html> [cited October 2010].

- [153] Schenck, H., "Theories of Engineering Experimentation," 3<sup>rd</sup> ed., McGraw Hill, New York, 1979, p. 237.
- [154] Schmiderer, A., "Service Bulletin No.: AT01-001," Aquila GmbH, Do No.: LBA.NSD.004, 28 April 2004, URL: <http://www.aquila-aviation.de/fileadmin/pdf/gemeinsam/service/techn-mitteilungen/TM-001-03.pdf> [cited October 2010]
- [155] Seoud, R. E., Vassilicos, J. C., "Dissipation and decay of fractal-generated turbulence," *Physics of Fluids*, Iss. 19, 105108, DOI: 10.1063/1.2795211, 17 October 2007.
- [156] Sepstrup, James L., US Patent Application for an "Aircraft Wings with Aileron Supported Ground Speed Spoilers and Trailing Edge Flaps," Patent No. 4,717,097, filed 3 March 1986.
- [157] Shmilovich, Arvin, Yadlin, Yoram, Pitera, David M., "Wing Leading Edge Concepts For Noise Reduction," 27<sup>th</sup> Congress of the International Council of the Aeronautical Sciences, edited by I. Grant, ICAS 2010-5.2.2, Nice, France, 19 - 24 September 2010.
- [158] Shovlin, Michael D., Cochrane, John A., "An Overview of the Quiet Short-Haul Research Aircraft Program," NASA-TM-78545, November 1978.
- [159] Smith, A. M. O., "High-Lift Aerodynamics," *Journal of Aircraft*, Vol. 12, No. 6, June 1975, pp. 501 - 530.
- [160] "Sophisticated Skyhawk," *Flight International*, 22 Januar 1997, URL: <http://www.flightglobal.com/articles/1997/01/22/1501/sophisticated-skyhawk.html> [cited October 2010].
- [161] Spalart, P. R., "Trends in Turbulence Treatments," *AIAA Fluids Conference and Exhibit*, AIAA-2000-2306, Denver, CO, 19 - 22 June 2000.
- [162] Stansfeld, Stephen A., Matheson, Mark P., "Noise pollution: non-auditory effects on health," *British Medical Bulletin*, Vol. 68, 2003, pp. 243 – 257.
- [163] "Statistical Summary of Commercial Jet Airplane Accidents - Worldwide Operations 1959 – 2009," *Aviation Safety Boeing Commercial Airplanes*, July 2010, URL: [www.boeing.com/news/techissues/pdf/statsum.pdf](http://www.boeing.com/news/techissues/pdf/statsum.pdf) [cited October 2010].
- [164] Strouhal, V., "Über eine besondere Art der Tonerregung," *Annalen der Physik und Chemie*, 1987, pp. 216 – 251.
- [165] Taylor, Barry N., Kuyatt, Chris E. "Guidelines for Evaluating and Expressing the Uncertainty of NIST Measurement Results," National Institute of Standards and Technology, Technical Note 1297, 1994.

- [166] Tong, K., Warren, A., "Development of Continuous Descent Arrival (CDA) Procedures for Dual-Runway Operations at Houston Intercontinental," *6<sup>th</sup> AIAA Aviation Technology, Integration and Operations Conference (ATIO)*, PV2006-7750, AIAA, Wichita, Kansas, 2006.
- [167] Tropea, Cameron, Yarin, Alexander L., Foss, John F., (Eds.), *Springer Handbook of Experimental Fluid Mechanics*, Springer, Berlin, 2007, p. 36.
- [168] Truckenbrodt, E., *Fluidmechanik*, Band 1. 2. Auflage. Springer-Verlag Berlin Heidelberg New York, 1980.
- [169] Turner, Aimée, "How will Europe achieve its Clean Sky goals?," *Flight International*, 2 February 2008, URL: <http://www.flightglobal.com/articles/2008/09/09/315691/how-will-europe-achieve-its-clean-sky-goals.html>, [cited October 2010].
- [170] Valarezo, Walter O., Dominik, Chet J., Mcghee, Robert J., Goodman, Wesley L., "High Reynolds number configuration development of a high-lift airfoil," *AGARD High-Lift System Aerodynamics*, N94-18415 04-01, 1993, p 8.
- [171] van Dam, C. P. "The aerodynamic design of multi-element high-lift systems for transport airplanes," *Progress in Aerospace Sciences*, Vol. 38, 2002, pp. 101 - 144.
- [172] Vèque, Sophie, "A318 – Steep Approach Operation," *OLM FBW 2006*, Toulouse, France, 26 – 28 September 2006, URL: [http://www.smartcockpit.com/data/pdfs/plane/airbus/A320/misc/A318\\_Steep\\_Approach\\_Operations.pdf](http://www.smartcockpit.com/data/pdfs/plane/airbus/A320/misc/A318_Steep_Approach_Operations.pdf) [cited January 2010].
- [173] Vetter, Bernd, Vetter, Frank, *Der Eurofighter*, Motorbuch Verlag, 2008.
- [174] Wallis, T. E., Ellis, D. R., Wentz, Jr., W. H. "The Use of Small Strakes to Reduce Interference Drag of a Low Wing, Twin Engine Airplane," *9<sup>th</sup> Atmospheric Flight Mechanics Conference*, AIAA, San Diego, CA, 9 - 11 August 1982.
- [175] Willert, C., *Vector field operators*, notice, DLR, Göttingen, 1998.
- [176] "Wind Tunnel A," *Institute of Aerodynamics - Technische Universität München*, [website], URL: <http://www.aer.mw.tum.de/windkanal/A.en.php> [cited 09 April 2010].
- [177] WS Atkins Consultants And members of the NSC, *Best Practice Guidelines for Marine Applications of Computational Fluid Dynamics*, report of MARNET-CFD Thematic Network, 9. April 2005.
- [178] Zimmerman, N.H.; Ferman, M. A., Yurkovich, R. N. and Gerstenkorn, G.: "Prediction of Tail Buffet Loads for Design Application," AIAA paper No. 89-1378, 1989.